Characterization of semiconductor nanostructures by spin-flip Raman spectroscopy

Dissertation

presented to the Faculty of Physics of the
TU Dortmund University, Germany,
in partial fulfillment of the requirements
for the degree of

Doktor rer. nat.

by

Dennis Kudlacik

technische universität
dortmund

Dortmund, July 2018

Accepted by the Faculty of Physics of the TU Dortmund University, Germany.

Day of the oral examination: 31th August 2018

Examination board:
Dr. Jörg Debus
Prof. Dr. Heinz Hövel
Prof. Dr. Kevin Kröninger
Dr. Ulf Berges

Contents

Summary

The main goal in the research field of spintronics is to take full advantage of the spin and charge of quantum mechanical particles in order to display and process information. In this regard, a major requirement in the realization of solid-state quantum information applications is robust quantum coherence, which represents the essence of entanglement. How to control quantum decoherence due to perturbing interactions within the semiconductor is, therefore, the fundamental question that challenges the semiconductor spintronics. The key to achieve novel spin effects or to improve existing spin phenomena is based on a better understanding of quantum mechanical interactions, in particular those between carriers themselves as well as carriers and a second system, such as thermal phonons, fluctuating charges or nuclear spins. In the framework of this thesis the fundamental question is tackled by means of spin-flip Raman scattering, which is a fundamental technique in order to study spin interactions of carriers confined in low-dimensional semiconductors. The thesis covers studies of spin effects and interactions in (In,Ga)As/GaAs self assembled quantum dots, in (Zn,Mn)Se/(Zn,Be)Se diluted magnetic semiconductors and CdSe colloidal nanocrystals.

In the first part, the focus is directed towards the thermal efficiency enhancement of the coherent spin-flip Raman scattering of resident electrons in quantum dots. In particular, it is demonstrated that thermal phonons do not disturb the coherent spin-flip scattering process based on electron exchange interaction, thus emphasizing that it is worth to pursue coherent spin physics at high temperatures. It is further shown that spin-flip Raman scattering is not only used to manipulate carrier spins but also to sensitively indicate the coupling of carrier spins to the surrounding nuclear spin bath, hence the central spin problem is investigated. The second part of the thesis addresses the impact of crystal-field splittings on paramagnetic Mn^{2+} spin-flip resonances in dilute magnetic quantum wells. It is shown that a significant quadrupole correction of a few tens of GHz affects the exchange interaction, leading to a strong asymmetry of the scattered light frequency. In the final part of the thesis the spin properties of resident electrons in CdSe nanoplatelets are investigated, demonstrating a strong dependence on the quantum confinement potential and magnetic field confinement. In summary, the thesis outlines the advances and problems of semiconductor spintronics, highlighting different ways to identify, manipulate and monitor carrier spin properties and, thus, to study the quantum mechanical nature of the spin.

Zusammenfassung

Das wesentliche Ziel im Forschungsfeld der Spintronik ist die volle Ausnutzung von Spin und Ladung quantenmechanischer Teilchen, um Informationen darzustellen und zu verarbeiten. Eine Grundvoraussetzung für die Realisierung von Festkörper-Quanteninformationsanwendungen ist die robuste Quantenkohärenz, die die Essenz der Verschränkung darstellt. Die fundamentale Frage mit der sich die Halbleiter-Spintronik auseinandersetzt ist daher, wie die Quantendekohärenz durch störende Wechselwirkungen innerhalb von Halbleiterstrukturen kontrolliert werden kann. Entscheidend für die Erforschung neuer Spin-Effekte oder zur Verbesserung bestehender Spin-Phänomene ist das Erlangen eines besseren Verständnisses quantenmechanischer Wechselwirkungen, insbesondere zwischen Ladungsträgern untereinander als auch zwischen Ladungsträgern und sekundären Systemen. Zu sekundären Systemen zählen zum Beispiel thermische Phononen, fluktuierende Ladungen oder Kernspins. Im Rahmen dieser Arbeit wird die fundamentale Frage mit Hilfe der Spin-Flip-Raman-Streuung in Angriff genommen, die eine grundlegende Technik darstellt, um Spin-Wechselwirkungen von niederdimensionalen Halbleitern zu untersuchen. In diesem Hinblick widmet sich diese Arbeit verschiedenen Forschungsschwerpunkten, wobei Spin-Effekte und Wechselwirkungen in selbstorganisierten (In,Ga)As/GaAs Quantenpunkten, in verdünnt magnetischen (Zn,Mn)Se Halbleitern und CdSe kolloidalen Nanokristallen untersucht werden.

Im ersten Teil der Arbeit liegt der Schwerpunkt auf der thermischen Effizienzsteigerung der kohärenten Spin-Flip-Raman-Streuung an residenten Elektronen in Quantenpunkten. Insbesondere wird demonstriert, dass thermische Phononen den kohärenten Spin-Flip-Streuprozess auf Basis der Elektronenaustausch-Wechselwirkung nicht ausschließlich stören. Dies unterstreicht, dass es lohnenswert ist, die kohärente Spinphysik bei hohen Temperaturen voranzutreiben. Es wird ferner gezeigt, dass die Spin-Flip-Raman-Streuung nicht nur zur Manipulation von Ladungsträgerspins eingesetzt werden kann, sondern auch, um die Kopplung von Ladungsträgerspins an das umgebende Kernspinbad sensibel anzuzeigen. Auf dieser Basis lässt sich auch das zentrale Spin-Problem untersuchen. Der zweite Teil dieser Arbeit befasst sich mit dem Einfluss von Kristallfeldaufspaltung auf paramagnetische Mn^{2+} Spin-Flip-Resonanzen in einem verdünnt magnetischen Quantentrog. Es wird nachgewiesen, dass eine signifikante Quadrupolkorrektur von einigen Dutzend GHz die Wechselwirkung beeinflusst, was zu einer starken Asymmetrie der gestreuten Lichtfrequenz führt. Im letzten Teil dieser Arbeit werden die Spin-Eigenschaften von residenten Elektronen in CdSe Nanoplättchen untersucht, welche eine starke Abhängigkeit vom Quanteneinschlusspotential und der Magnetfeldeinschränkung aufzeigen. Zusammengefasst weist diese Arbeit die Fortschritte und Probleme der Halbleiter-Spintronik auf und fast verschiedene Möglichkeiten zur Identifizierung, Manipulation und Beobachtung von Ladungsträger-Spin-Eigenschaften zusammen.

Chapter 1

Motivation

In the past few decades of research and development, no other material system has aroused such a technological revolution as the semiconductor. The historic development of semiconductor physics and technology began in the second half of the 19th century. With the invention of the first prototype semiconductor, the field-effect transistor by J. E. Lilienfeld in 1925 [1] and its commercial realization in 1947, a fast paced development towards smaller and faster electronic devices began. Semiconductor-based transistors, which constitute the building-blocks of complex electronic systems, are used as logic switches in almost every electronic device of every day life. They fulfill the requirement of modern technologies, which demand a fast transfer and processing of information. [2]

In the pursuit of further miniaturization of semiconductors, in order to place transistors and functionality on a single chip, nanoscale engineering as well as an improved understanding of the physical phenomena at the nanometer scale have facilitated a rapid development of novel semiconductor structures fabricated with subnanometer accuracy. A recent example are thin field effect transistors with sizes of about 7 nanometers as well as hot electron transistors, which may be used for ultra-high frequency operation in the THz range. [3] Both types of transistors uphold Moore's law declaring an exponential growth in the microprocessor chip performance as a function of time. [4] However, the reduction of the structural size of a semiconductor down to the nanoscale leads to a confinement of carriers (electrons), in turn, having an decisive impact on the electronic structure and optoelectronic properties of the semiconductor, due to quantum confinement effects. [5]

In search of an alternative to conventional transistors, a paradigm shift has been initiated by the development of the research field of spin electronics (spintronics). This is a branch of science and technology which employs both the charge and the spin of the carrier (electron). The studies of spin effects in the solid-state physics goes back to the Stern-Gerlach experiment performed in the early 1920s. [6] In this experiment O.

Stern and W. Gerlach observed that passing silver atoms through an inhomogeneous magnetic field are deflected either up or down by the same amount, thus, demonstrating the space quantization of the electron spin for the first time. In addition to the discovery of the splitting of atomic spectral lines in an external magnetic field by P. Zeeman in 1897[7], it prompted physicists to develop a quantum mechanical explanation that could describe these phenomena. In particular, the formulation of the quantum mechanics of many-electron systems by P. A. M. Dirac[8] as well as the theoretical work by W. Pauli[9], who postulated the connection between arbitrary half-integral spins and the Einstein-Bose statistics, contributed to a deeper insight. By the end of the 1920s, physicists developed a fundamental understanding of the essential role of the electron spin in explaining the electronic structure of the atom.[10]

The intimate connection between the charge and spin degrees of freedom of the electron, linked by the Pauli principle, are the underlying basis for spintronics. A decisive implication of this relationship is that spin effects can often be accessed via the orbital properties of the electron in the solid state. In this regard, the most fundamental phenomenon in the field of spintronics, which utilizes both properties, is the giant magnetoresistance effect, which results from spin-dependent scattering of electrons propagating through thin metallic films.[11,12] In this way, information can be encoded both in the charge of the electron and in its spin state, i.e. by aligning a spin (either "up"-↑ or "down"-↓) relative to a given reference. A further very interesting suggestion for a novel device, which is based on spin injection into non-magnetic semiconductors, is the spin transistor. It has been proposed by S. Datta and B. Das at the end of 1989[13] and latter theoretically described by A. S. Sheremet et al. in 2016.[14]

The field of semiconductor spintronics is recently at an exciting stage. Despite the successful study of many spin phenomena, major fundamental problems and open questions are still being addressed by experiment and theory. These issues include the spin coherence in nanoscale structures, the optimization of electron spin lifetimes, transport of spin-polarized carriers, and the manipulation of both electron and nuclear spins. Especially, the dimension of the structure is of crucial relevance. In this regard, low-dimensional semiconductor structures have aroused a lot of attention, as they offer promising properties for spin-based applications.

The new era of research on electronic structures of lower dimensions began with the invention of semiconductor quantum wells and superlattices by L. Esaki and R. Tsu[15,16] in the 1970s, allowing one to probe the fundamentals of quantum mechanics. Confining electrons in all three spatial dimensions denotes the ultimative miniaturization in semiconductor technology. These low-dimensional structures, called quantum dots (QDs), are considered the solid-state equivalent of atomic systems. The versatility of QDs for a variety of applications results from their uniqe electronic and optical properties, which can be influenced by changes in their size and composition.[5,17] Due to three-dimensional spatial confinement the number of perturbing interactions is reduced in a QD, preventing electron spin states from relaxing and, thus, losing their

coherence. In this respect, the spin lifetime describes the time during which a spin can serve as information carrier until reaching its thermal equilibrium. Recent studies reported electron spin lifetimes of about 10 μs in CoFe nanoparticles.[18] It is suggested that the storage time of quantum information encoded in spins can be even further extended through the interplay of optically spin-polarized electrons with the surrounding nuclear spin environment.[19] This interaction, which is called contact hyperfine interaction, plays an essential role in manipulating and controlling nuclear spins.[20] A direct consequence of this hyperfine interaction is the occurrence of Overhauser fields with persistence times of about one hour. A probed electron spin polarization may thus survive in the direct environment of nuclei as long as the underlying Overhauser field.[21]

In the context of spintronics, materials which exhibit both magnetic and semiconductor properties proved to be a very interesting model system as well, as they combine permanent magnetic storage and the conventional electronics of semiconductors. In particular, researchers focused in the past decade on diluted magnetic semiconductors (DMS), i.e., substitutional alloys of either II–VI or, for example, IV–VI semiconductors that have been partially substituted by a small amount of transition-metal ions like Mn^{2+}. The ensembles of spins in these magnetic materials originate a magnetization, which can be reversed between two opposite orientations. This targeted manipulation is facilitated by the strong coupling of the localized ion-spins with the spins of the free charge carriers. If the localized spins are polarized, e.g. by a magnetic field, optically injected carriers may become polarized as well due to spin coupling.[22,23] Recent theoretical and experimental studies aimed at the coherent dynamics of localized spins (E.g.: Mn^{2+}-ions) coupled with a two-dimensional hole gas, highlighting a reduction of the Mn-ion Larmor frequency under the influence of an oscillating effective field of valence band vacancies, known as holes.[24,25] While these investigations consider a large ensemble of spins, the analysis of a single semi-magnetic quantum dot provides access to the interaction between the spin of a single charge carrier and a few spins in its direct environment.[26] The potential functionalities of such efficient spin injection, using diluted magnetic semiconductors as spin aligners, have been outlined by M. Oestreich et al..[27] Furthermore, DMS have aroused particular interest since the discovery of pronounced magneto-optical effects like the giant Faraday rotation, whose origin lies in the giant Zeeman splitting of the photoexcited states.[28] In this respect, the closely associated effect of the strong exchange interaction between the magnetic ion spins and the carrier spins has been in focus of research.[29,30]

One of the most powerful and most widely used optical techniques for the study of the spin properties of the confined carriers and the interaction processes in low-dimensional semiconductors is the resonant spin-flip Raman scattering. It is based on inelastic scattering of an incident electromagnetic wave with carriers, whose spin is reversed in the progress. The change of the spin states is accompanied by a variation in the energy of the carrier, which is reflected in the frequency of the scattered light. The analysis of the radiation characteristics via spectroscopic instruments allows conclusions

to be drawn on the splitting of spin states in an external magnetic field and, thus, to determine the Landé factor of the carrier under study. In particular, the sensitivity of the spin-flip Raman scattering to various external parameters, such as the temperature, the external magnetic field, the geometry, the energy of the electromagnetic light wave and the polarization of the light, can be used to study different carrier properties embedded in low-diemsional structures and their interaction processes. One of the first SFRS experiments on bound electrons and holes in CdS has been preformed by Thomas and Hopfield [31]. Since then, this technique is successfully applied to various semiconductor structures, such as quantum wells [32–34], nanocrystals [35], as well as indirect band-gap QDs. [36] Raman scattering is also applied in the field of biological applications [37] or chemical and mechanical engineering [38]. The method of spin-flip Raman scattering forms the basis of all experiments and analyses presented in this thesis. Essential features of low-dimensional semiconductors and the principle of inelastic light scattering are overviewed in Chap.2. A detailed description of the experimental realization of spin-flip Raman scattering in low-dimensional semiconductors is described in Chap.3.

In order to realize solid-state quantum information applications robust quantum coherence is a major requirement. A possibility to achieve quantum coherence is offered for example by carrier spins in ensembles of self-assembled (In,Ga)As QDs. [39] However, a major adversary is decoherence, that is the process by which quantum information is lost due to coupling of the system to other hard-to-control degrees of freedom in the environment, such as thermal phonons, fluctuating charges, nuclear spins etc. To what extent thermal phonons contribute to spin manipulation within the limits set for maintaining coherence has not yet been explored. In the framework of this thesis this unsolved issue will be addressed by means of spin-flip Raman scattering, whose efficiency intrinsically depends on phonons, as they mediate spin-flips and thereby orient spins. In this prospect, in Part II of this thesis, the effect of temperature-dependent changes in the electron spin-flip scattering in self-assembled (In,Ga)As/GaAs QD ensembles will be discussed. Furthermore, the fundamental carrier exchange interactions are described, which depend on their angle-dependent Landé factors, and the localization degree of the carriers inside a quantum dot. As noted above, it is well known that nuclear spins act collectively on the electron spin via hyperfine interaction. However, even though the coupling of the nuclear spin bath to a central spin has been studied for many years the complexity arising from the many-body character is still not well understood. One of the aims of this thesis is to provide a more comprehensive picture. In this regard, the second half of Part II addresses this issue, highlighting the interplay between the dynamic nuclear polarization and the resonant spin-flip Raman scattering of resident electrons in an ensemble of singly charged (In,Ga)As/GaAs quantum dots. It will be illustrated that the Overhauser field can directly be measured by the spin-flip Raman shift demonstrating a new method to study electron-nuclear effects in quantum dot ensembles.

A substantial amount of effort is also devoted towards the II-VI diluted magnetic quantum well structures (Cd,Mn)Te and (Zn,Mn)Se. One of the key issues, here, is the

study of their magnetic and optical properties, in order to obtain a deeper understanding of the strong exchange interaction between the magnetic ion spins and the carrier spins. Spin-flip Raman scattering on free electrons or those bound to donor states provides a direct access to the magnetic field induced electron spin splitting energy and, thus, allows one to study the *s*-*d* exchange interaction between the 3*d* electrons of the Mn^{2+} and the *s*-like electrons and *p*-like holes of the photoexcited excitons. However, up to now it has been not studied how far the nuclear quadrupole moments coupled with the electric field gradients at the magnetic ion sites impact the paramagnetic Mn^{2+} spin-flip resonances. This issue is addressed in Part III. In particular, the spin-flip Raman scattering technique is used to determine the dependence of the spin-flip scattering on many external parameters. It turns out that a significant quadrupole correction of a few tens of GHz affects the exchange interaction, leading consequently to a strong asymmetry of the scattered light frequency.

An essential aspect of nanosciences, which has led to enormous research efforts and great advances in recent decades, is to understand the origin of quantum confinement and its influence on the electronic and spin properties of semiconductor nanocrystals (NCs). Colloidal NCs are one of the novel type of semiconductor nanostructures that have been theoretically and experimentally thoroughly investigated for this purpose. Their unique size- and shape-dependent optoelectronic properties revealed their great potential for application in lasers [40–42], optical amplifiers [40], light emitting devices [42,43], biomedical imaging [44] and photocatalysis [45,46]. Recent studies have shown that at low temperatures NCs, e.g. CdSe/CdS QDs or nanoplatelets (NPLs) [47], can be charged under illumination. This optical charging of the colloidal NCs allows one to create resident carriers in the NPLs that can be optically addressed, controlled and manipulated. [48] For developing optical manipulation algorithms, the study and understanding of the spin related phenomena, such as the exchange interaction between the resident carriers is of central importance. With the goal of achieving even more knowledge on the spin properties of the resident electrons in CdSe NPLs these structures are investigated by means of the spin-flip Raman scattering technique in terms of NPL-thickness, selection rules, geometry and temperature dependence. The results and discussions are presented in the final Part IV.

Basic spin interactions of confined carriers in various types of semiconductors are characterized with respect to their dependence on external perturbations and the local structure symmetry using the resonant spin-flip Raman scattering technique. The studies highlight various possibilities of identifying, monitoring and manipulating carrier spins, addressing various major fundamental problems and open questions of semiconductor spintronics. The results of this basic research represent the first step on the way of developing new promising structures towards the realization of spin-based applications.

Part I

Theoretical background and experimental methods

This thesis focuses on the study of a variety of spin phenomena in low-dimensional semiconductors. In particular, the investigation of the dynamics of carrier spins and the carrier-spin-dependent interactions between electron spins and/or nuclear spins are in the center of attention. The most elegant and informative technique for investigating spin phenomena in semiconductors is based on the optical orientation of spins. In order to characterize the spin properties of confined carriers and interaction processes in low-dimensional semiconductors the resonant spin-flip Raman scattering (SFRS) technique is used. It is based on the inelastic light scattering under involvement of a carrier whose spin orientation is reversed.[33] The method of SFRS forms the basis of all experiments and analyses presented in this thesis. To facilitate the presentation and understanding of the results discussed in the parts II to IV, this chapter focuses on the theoretical background, describing the properties of low-dimensional semiconductors and the principle of inelastic light scattering.

A decisive characteristic of quantum mechanical objects such as electrons and holes is the density of allowed states, which markedly differs between three-, two-, and zero-dimensional semiconductor structures. The reduced dimensionality, i.e. higher quantum confinement, has a major impact on the electronic structure and optoelectronic properties of a semiconductor. For instance, in a three-dimensional confined structure the density of electron states takes the form of a δ-function, resulting in discrete energy levels of electrons and holes.[49–51] The quantum confinement effect and crystal symmetry of the semiconductor band structure are discussed in Sec. 2.1 and Sec. 2.2 of the first Chap. 2. As the experimental results refer to optical properties of two-dimensional quantum wells (QWs) and zero-dimensional quantum dots (QDs), the main emphasis is placed on these two types of structures. In particular, the effect of spatial confinement on the carrier wave functions as well as the influence of magnetic interactions on the fundamental and measurable properties is discussed.

Diluted magnetic semiconductors (DMS) are the second research focus of this thesis. A DMS is defined as a diamagnetic semiconductor doped with a few to several atomic per cent of some transition metal with unpaired d electrons. A well-known example is the Mn-doped diluted magnetic quantum well structure (Zn,Mn)Se which is in the spotlight of this thesis. An overview on its structural, electronic, magnetic and optical properties is provided in Sec. 2.3.

As DMSs reveal great potential for efficient spin injection and magnetization manipulation by optical methods, the investigation of their magnetic and optical properties is one of the main research topics in recent years. Their optical properties originate from carrier-mediated exchange interaction in which the dopant spins are coupled with confined electrons and/or holes in the host semiconductor. In particular, the localized spins of the semi-filled d-shell of the Mn ions induce two types of exchange interactions. On the one hand, the Kondo-like s/p-d-exchange interaction between the band electron spins and the localized moments of the magnetic ions, which strongly affects the electronic properties of the DMS, and on the other hand, the Heisenberg inter-ion

d-*d*-exchange interaction which defines the static and dynamic magnetic properties of a DMS. The different exchange interactions are introduced briefly in Sec. 2.3.3. In the vicinity of an external magnetic field, neutral excitons in the quantum well experience the giant Zeeman splitting, which originates from the strong *s*/*p*-*d*-exchange interaction.[28,52] The effect of the giant Zeeman splitting of exciton states is discussed in Sec. 2.3.4. A further important aspect of DMSs is the heating of the magnetic ion system, which may be facilitated by additional photoexcited carriers and/or phonons, thus, influencing its magnetic and optical properties. The key aspects of this process are described in Sec. 2.3.5.

The third Sec. 2.4 addresses the physics of light scattering. The focus is placed on the inelastic light scattering or Raman scattering, as it provides important information about the properties of semiconductor nanostructures. The macroscopic and microscopic views of Raman scattering are discussed and in particular the principle of SFRS is presented, on the basis of which carrier spins and fundamental carrier-spin interactions in semiconductor nanostructures are studied. The descriptions will highlight why spin-flip Raman scattering is a highly promising technique to investigate the fundamental properties of low-dimensional semiconductor structures.

A detailed description of the experimental realization of SFRS in low-dimensional semiconductors is described in Chap. 3. An overview of the basic principles of the experimental setup, the function and interplay of the equipment, and the experimental methods is provided. In particular, the experimental requirements in regard of the properties of SFRS are highlighted and all necessary arrangements to meet the experimental requirements are described.

Chapter 2

Fundamentals of low-dimensional semiconductor structures

The interest in low-dimensional quantum systems has been tremendous in the last decade, fueled by a constant stream of remarkable discoveries, revealing the potential for new state-of-the-art electronic devices. Modern material and technical science especially focused on the investigation of nanometer-scaled structures, which have established as basis materials, thus, giving rise to semiconductor-based spintronics.

In general, when the motion of carriers is restricted in one or more directions in space, the resulting structure is then called a low-dimensional structure (or system). Its physicochemical characteristics notably depart from those of a bulk solid. In particular, if the outer dimensions of a crystal solid are reduced to the size of the de Broglie wavelength of electrons, the charge carriers become spatially confined. The confinement of the charge carriers has a great influence on the band structure and the density of the solid states, and, thus, influences significantly the electrical, mechanical, chemical, magnetic, and optical properties of the semiconductor. An overview about the changes taking place with the reduction of the crystal dimensions is provided in this chapter. In addition, the carrier wave functions, which are spatially confined in two or three dimensions, are discussed.

2.1 Fundamentals of semiconductors

Semiconductors are materials whose electrical conductivity levels between those of a conductor and an insulator. They are characterized by an energy gap that separates the electronic states of the valence band (VB) from those of the conduction band (CB). The occupation of these bands depends on the absolute energy position and

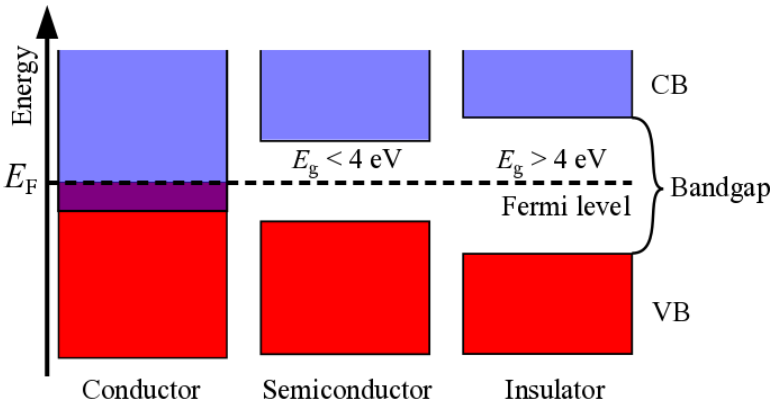

Figure 2.1: The band-gap diagram of a conductor, semiconductor and an insulator. The conduction (CB) and valence bands (VB) represent the energy states, which are allowed to be populated by carriers. The Fermi energy (E_F) is the energy of the highest level of quantum state which may be occupied by the electrons at the absolute zero temperature, thus, determining the intrinsic band population at low temperatures. For a conductor, the CB and VB are not separated and, therefore, there is no energy gap (E_g).

the value of the Fermi energy E_F describing the accessible energy of electrons without additional excitation. Hence, the intrinsic population of these bands defines whether the semiconductor is insulating or conducting. A description of the three solid state classifications is illustrated in Fig. 2.1.

At low temperatures near $T = 0$ K, the valence band is the energetically highest fully occupied band, whereas the conduction band is the lowest unoccupied band. The absence of free charge carriers in the VB provides that the material is insulating. However, in contrast to isolators, semiconductors have only small energy gaps in the region of a few eV. By definition, the Fermi energy of an undoped semiconductor lies within the band-gap.[53] Nonzero conductivity can be induced, e.g. by the application of external excitations such as optical illumination or electric potential as well as by increasing the temperature. If the temperature rises up to a value of $T = E_g/k_B$, the lattice electrons have enough kinetic energy to overcome the band-gap energy (E_g), thus, providing conductivity.[53] Here, k_B is the Boltzmann constant.

Another possibility to induce a large number of conduction electrons is by introducing suitable impurity atoms in a semiconductor. This process is called doping of a semiconductor. For instance, by the implementation of an element that posses one valence electron more as compared to the replaced host material, an additional electron is supplied which does not take part in the lattice binding. This electron may escape to the conduction band and, thus, can be treated as a free (quasi-)particle. The left behind positive ion is called a donor. Semiconductors containing many mobile electrons are called n-type semiconductors. In these types of systems the donator energy level is

close to the conduction band edge, so that the band-gap to be overcome is very small. In the opposite case, if the dopant element has one electron less than the replaced host element, it is referred to as acceptor. Here, the semiconductor is called p-type. In both cases the doping leads to an increased conductivity.

The typical band-gap energy in semiconductors corresponds to the energy of electromagnetic waves in the visible spectral range. This particular feature makes semiconductors attractive for optical and magneto-optical spectroscopy, allowing to establish the characteristics of light absorption processes, the electronic band structure, and the transport as well as spin properties of the carriers in a semiconductor.

The fundamental optical excitation in a semiconductor is based on the excitation of an electron from the valence band into the conduction band under absorption of a photon whose energy exceeds the energy of the band-gap: $\hbar\omega_\mathrm{i} > E_\mathrm{g}$. Here, $\hbar$ is the reduced Planck constant and ω_i the frequency of the incident photon. The excitation of an electron leaves behind an unoccupied state in the valence band, which may be treated as a positively charged particle in an otherwise empty band. This concept results in the definition of a quasi-particle known as hole.[54] This hole is not bound to the lattice, but can move freely and, like the electron, contributes to the conductivity through the crystal lattice. The hole is in many aspects comparable to an electron. While the electron in the conduction band can be described by the charge (e^-), spin ($s = 1/2$), and effective mass (m_e^*), the hole in the valence band is characterized by the positive charge (e^+), spin ($s = 1/2$ or $s = 3/2$), and effective mass (m_h^*). Because of their charge, electrons and holes are referred to as charge carriers.

Negatively charged electrons in the conduction band and positively charged holes in the valence band are subject to Coulomb interaction. Due to the Coulomb force, which consists of an attractive and a repulsive part, these charges form electron-hole pairs, known as excitons (X) and trions. With regard to an exciton, one electron and one hole are bound together. In the case of a trion, predicted by Lampert in 1958,[55] an exciton is additionally bound to a resident electron (negatively charged exciton, X^-) or hole (positively charged exciton, X^+) in the semiconductor.[56] The three basic complexes of quasiparticles are schematically illustrated in Fig. 2.2.

Excitons have been first proposed theoretically by Frenkel[57] and a few years later experimentally confirmed in cuprous oxide.[58] Frenkel excitons have large binding energies of up to 1 eV and tend to be strongly located in their host materials. Their typical size is comparable to the crystal unit cells. Frenkel excitons are mostly seen in materials with small dielectric constants.[57] Another class of excitons are Mott-Wannier excitons.[59] These represent the case of excitons with large spatial gaps and small binding energies. Mott-Wannier excitons are found in semiconductors with small band-gaps, which have a large dielectric constant reducing the Coulomb interaction between the conduction band electrons and valence band holes.[59] Both types of excitons have been the subject of extensive research in various materials and structures in the

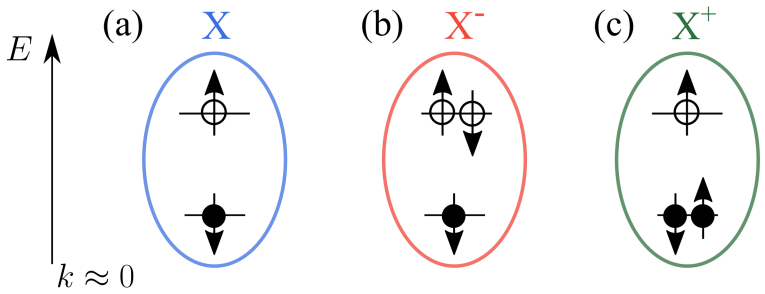

Figure 2.2: Scheme of optically excited complexes. (a) The optical excitation of a generally undoped semiconductor results in the formation of a bound electron-hole pair, known as exciton (X). (b) In the case of n-doped semiconductors, a resident electron is bound to the electron-hole pair, forming a quasiparticle, known as negatively charged exciton (X^-). Here, the electron spins align antiparallel. (c) In a p-doped semiconductor, two holes are bound to one electron, forming a complex, called positively charged exciton (X^-). The open circles symbolize electrons, and the full circles symbolize holes. Adapted from Ref. [39].

past decade.[33,48,60,61]

The existence and properties of atoms as well as the movement of an electron or hole in a crystal can not be understood exclusively in the sense of classical laws. Since many phenomena exhibited on the atomic or subatomic level reveal underlying quantum phenomena, which need to be explained within the framework of the quantum mechanical laws. By means of quantum mechanics, which form the basis of the present understanding of all natural phenomena studied and exploited in chemistry, physics, materials science, etc., the physical behavior of a particle at the nanoscale can be accurately predicted. The fundamental equation of physics used to describe quantum mechanical behavior is the Schrödinger equation. It provides a quantitative understanding of the properties of low-dimensional structures. In the Schrödinger description an elementary particle, e.g. an electron or a hole, is described by a wave function $\psi(\vec{r},t)$, which depends on the variables that describe the degrees of freedom of the particle and contains all of the information that may be obtained about its physical entity. The amplitude of the wave oscillation as that point and time is written as $|\psi(\vec{r},t)|$. The probability distribution of the particle at the spatial location $\vec{r} = (x,y,z)$ and at time t can be determined by the complex square of the quantum mechanical wavefunction. For a normalized wavefunction

$$\int_{-\infty}^{\infty} |\psi(\vec{r},t)|^2 \, \mathrm{d}r = 1, \tag{2.1}$$

the probability density is given by:

$$\rho(\vec{r},t) = \psi(\vec{r},t)^* \cdot \psi(\vec{r},t) = |\psi(\vec{r},t)|^2 . \tag{2.2}$$

This means that $|\psi(\vec{r},t)|^2\,\mathrm{d}V(\vec{r})$ is the probability that at time t the particle is in the small volume, $\mathrm{d}V(\vec{r})$ centred at the point $\vec{r}$.

The Schrödinger equation actually refers to two separate equations, often called the time-dependent and time-independent Schrödinger equations. The most general form is the time-dependent Schrödinger equation,

$$\hat{H} \mid \psi(\vec{r},t)\rangle = i\hbar \frac{\partial}{\partial t} \mid \psi(\vec{r},t)\rangle, \tag{2.3}$$

which gives a description of a system evolving with time.[62] Here, $i = \sqrt{-1}$ is the imaginary unit, $\hbar$ is the reduced Planck constant and $\hat{H}$ is the Hamiltonian operator, characterizing the total energy of the particle or system. For a single particle moving in an electric field one obtains the nonrelativistic Schrödinger equation:

$$\left[-\frac{\hbar^2}{2m^*} \bigtriangledown^2 + V(\vec{r},t)\right] \psi(\vec{r},t) = i\hbar \frac{\partial}{\partial t}\psi(\vec{r},t), \tag{2.4}$$

where $\bigtriangledown^2 = \frac{\partial^2}{\partial x^2} + \frac{\partial^2}{\partial y^2} + \frac{\partial^2}{\partial z^2}$ is the Laplacian operator and m^* is the particle's reduced mass. In this Schrödinger equation, the first part of the Hamilton operator ($-\frac{\hbar^2}{2m^*}\bigtriangledown^2$) expresses the kinetic energy of the particle and the second part ($V(\vec{r},t)$) its spatiotemporal varying potential. For time independent potentials $V(\vec{r})$, the position and time dependences of the Schrödinger equation can be separated. In this case the wavefunction $\psi(\vec{r},t)$ can be written as $\psi(\vec{r},t) = \mathrm{Re}\,[\exp(-iEt/\hbar)\psi(\vec{r})]$, with $\psi(\vec{r})$ describing the complex-valued function of space, and E the particle's energy. Analytical solutions of the time-harmonic Schrödinger equation, providing an insight into the nature of quantum phenomena, can be obtained for a variety of relatively simple conditions, offering a reasonable approach to the behavior of more complex systems.

The concept of effective mass is introduced in Eq. (2.4) to take into account the interaction of the particle with the periodic crystal lattice. The effective mass can be expressed by the second-rank tensor in terms of the second derivative of the energy dispersion ($E(k)$)[53]:

$$m^* = \hbar^2 / \frac{\partial^2 E(k)}{\partial k^2}. \tag{2.5}$$

Here, $\hbar$ describes the reduced Planck constant and $|\mathbf{k}| = k$ the absolute wave vector. With this concept the electrons and holes can be mathematically described as free (quasi-) particles in a semiconductor. In comparison to an electron in vacuum, the effective mass reflects the increased or decreased mobility of an electron or hole in the semiconductor. Within the single particle approximation, the properties of the charge carriers are defined by the band structure of the semiconductor.

2.1.1 Band structure of bulk and low dimensional semiconductors

The characteristics of the energy bands can be better understood when considering the periodicity of semiconductor crystals. When an electron travels through a semiconductor, it experiences the periodic potential caused by the atoms in the crystal lattice. Simplified to one dimension the crystal can be described by the following Hamilton:

$$H = H^0 + V(x) = -\frac{\hbar^2}{2m}\frac{\partial^2}{\partial x^2} + V_{\text{lattice}}(x). \tag{2.6}$$

Here, H^0 is the kinetic energy operator and $V_{\text{lattice}}(x)$ describes the periodic potential of the underlaying Bravais lattice. Since the potential is periodic to the lattice constant a, the Schrödinger equation after a translation of the wave function $\psi(x)$ by a ($\psi(x+a)$), can be written as:

$$-\frac{\hbar^2}{2m}\frac{\partial^2}{\partial x^2}\psi(x+a) + V_{\text{lattice}}(x)\psi(x+a) = E_{n\vec{k}}\psi(x+a). \tag{2.7}$$

The eigenvalues are characterized by the eigenstates $E_{n\vec{k}}$ with the wave vector $\vec{k}$ and band index n. These eigenstates for fixed n in solid states are called energy bands. After a translation of the wave function by the lattice constant a, $\psi(x)$ and $\psi(x+a)$ still have the same eigenvalue $E_{\vec{k}}$, and, thus, differ only by a phase factor. A wave function that obeys this criterion and, moreover, is an eigenfunction of Eq. (2.7), according to Bloch's theorem, can be expressed by the modulated Bloch-wavefunctions [63]:

$$\psi_{nk}(\mathbf{x}) = u_{nk}(\mathbf{x}) \cdot \mathrm{e}^{i\mathbf{k}\cdot\mathbf{x}}. \tag{2.8}$$

Here, k defines the wave vector in the Brillouin zone and $u_k(\mathbf{x})$ describes the Bloch amplitudes, which are a function that has the periodicity of the lattice. The Bloch amplitudes are invariant under symmetry transformations of the crystal. [64]

Considering more than one dimension, one notices that the periodicity is not the same for different directions. In this case, the Bloch-wavefunctions are given by:

$$\psi_{nk}(\vec{r}) = u_{n\vec{k}}(\vec{r}) \cdot \mathrm{e}^{i\vec{k}\cdot\vec{r}}. \tag{2.9}$$

In this regard, it is worthwhile to note that in a three-dimensional crystal, the Bragg reflections are more complex. For instance, the first Brillouin zone of a face-centered cubic (fcc) lattice (e.g. the rock salt lattice of PbSe, or the zinc-blende lattice of ZnSe) has the shape of a truncated octahedron. For illustration the first Brillouin zone, which is also called the Wigner Seitz cell, is shown in Fig. 2.3 (a), with the points of high symmetry labeled in k-space. The Wigner Seitz cell of this lattice has multiple points of high symmetry, e.g. the point of origin Γ, or the center of the big hexagonal face L and the small square face X. Between the center of the Brillouin zone Γ and any symmetry point the wave vector of a well defined direction changes its magnitude $|\mathbf{k}|$. The usual way of plotting the energy dependence of electrons in a three-dimensional

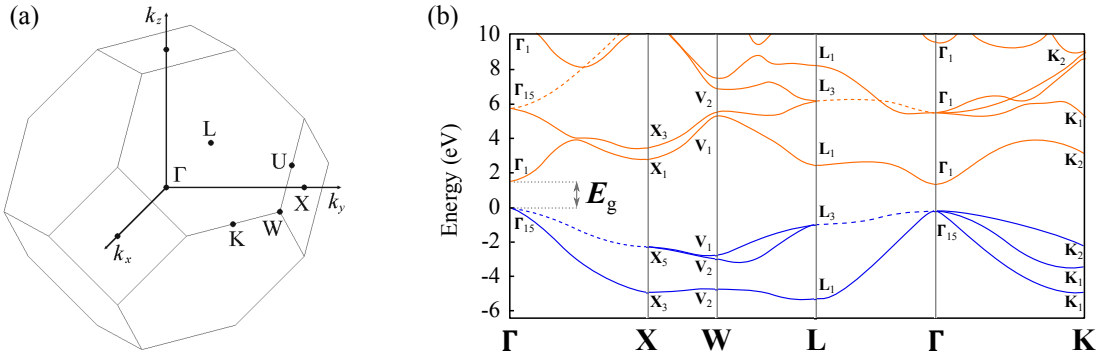

Figure 2.3: (a) The first Brillouin zone of a fcc crystal structure, with the points of high symmetry labeled in k-space. Adapted from Ref. [5]. (b) Nonrelativistic self-consistent local-density band structure of ZnSe calculated with the Ceperley-Alder exchange correlation.[65] Dashed lines show doubly degenerate bands. The minimum of the conduction band is separated by an energy gap $E_g = 1.83$ eV from the maximum of the valence band at the Γ-point. Adapted from Ref. [65]. For cubic zinc-blende ZnSe the lattice parameter is $a = 5.668$ Å.[66]

semiconductor crystal is depicted in Fig. 2.3 (b), which shows the electronic band structure of ZnSe as a representative example. Here, the bands at points of high symmetry are labeled by their irreducible representations in the double group notation of the T_d crystal symmetry.[65]

In order to determine the optical properties of a semiconductor, knowledge of the electronic band structure, which is closely related to the crystallographic symmetry, is necessary. In particular, the region in the vicinity of the energy dispersion close to the fundamental band-gap at the Γ-point is of major importance. To outline the important characteristics, the focus next is directed towards the band structure in this region. To classify the different states some group theoretical aspects will be introduced in the discussion.

All of the systems to be considered in this thesis involve direct band-gap semiconductors. In these types of semiconductors the maximum in energy of the valence band and the minimal energy of the conduction band are situated near the Γ-point ($k = 0$) in the middle of the Brillouin zone.[53,67] At this symmetry point, the band dispersion follows the effective mass approach:

$$E_{\mathrm{v}}(\vec{k}) = -\frac{\hbar^2 k^2}{2m_{\mathrm{v}}} \quad \text{and} \quad E_{\mathrm{c}}(\vec{k}) = E_{\mathrm{g}} + \frac{\hbar^2 k^2}{2m_{\mathrm{c}}}, \tag{2.10}$$

with the absolute wave vector $|\mathbf{k}| = k$ and the effective masses of the valence and conduction band m_{v} and m_{c}, respectively. The band-gap of the bulk material is given by E_{g}. To improve the single-band effective-mass approximation, one can consider more bands and allow the coupling between the different bands. These models are referred to as $\mathbf{k} \cdot \mathbf{p}$-models. For instance, the Kohn-Luttinger Hamiltonian for a zinc-blende

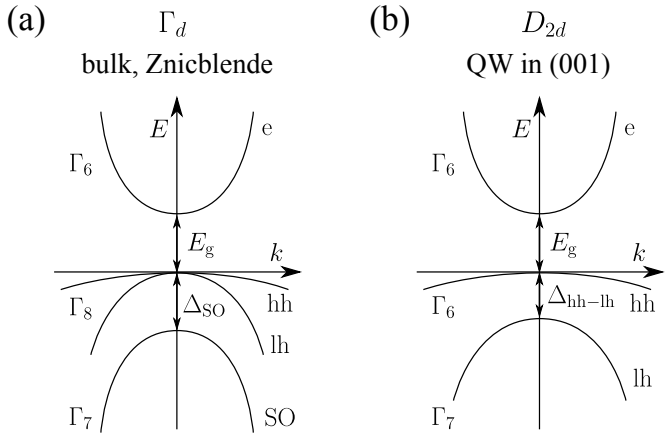

Figure 2.4: Schematic representation of the electronic band structures for different point group symmetries near the Γ-point ($k = 0$). The conduction band and valence sub-bands are indicated by the group-specific irreducible representation Γ_i. For the sake of clarity, the energies are given on an arbitrary scale and, moreover, spin splittings at $k \neq 0$ as well as nonparabolic effects are omitted.

structure includes the contributions of the second- and third highest valence bands to the hole Hamiltonian.[68] This operator also comprises the coupling between the three different valence bands, which are referred to as heavy-, light- and split-off hole band.

A scheme of the band structure around the Γ-point of a typical direct-band gap bulk semiconductor like ZnSe, GaAs or CdTe with zinc-blende lattice is shown in Fig. 2.4 (a). In this systems the conduction band at the center of the Brillouin zone consists of one band and the valence band comprises three sub-bands. For a better overview the bands of the bulk zinc-blende crystal are labeled in Fig. 2.4 (a) by their irreducible representations in the tetrahedral point group notation of the T_d crystal symmetry.[65,69]

The valence and conduction bands evolve from the hybridization of atomic orbitals. In a system with cubic symmetry, the conduction band originates from the *s*-like atomic states, whereas the valence bands emerge from the *p*-like states. The orbital electronic wave functions are classified according to the orbital angular momentum L as *s*, *p*, *d* etc.. In order to describe the energy states, taking into account the spin-orbit interaction, one has to consider the total angular momentum J = L + s, where s denotes the spin. The eigenstates of J can be classified according to J and m_J ($\mid J,m_J\rangle$), where m_J takes $2\,J+1$ values. The spin function transforms as the irreducible representation $D_{1/2}$, which is given by the irreducible representation Γ_6.[67,70,71] The total wave function of the electron and hole transform like the direct product of their single group representation with $D_{1/2}$.[70]

Considering the *s*-like conduction band, the spin part χ_s of the electron (e) wave function is defined by the basis functions of the irreducible representation Γ_6.[67] The

corresponding angular momentum is L = 0, and, thus, the band is characterized by $J = 1/2$ and $m_J = \pm 1/2$. Hence, the parabola-shaped conduction band is twofold spin-degenerate, and, therefore, the Bloch states of the conduction band take the form:

$$| u_{1/2}\rangle = | s\rangle \, |\uparrow\rangle \quad \text{and} \quad | u_{-1/2}\rangle = | s\rangle \, |\downarrow\rangle. \tag{2.11}$$

Here, $u_{\pm 1/2}$ describes the Bloch amplitudes and $| s\rangle$ the coordinate part of the s-type Bloch amplitude.[64,70] As noted above the Bloch amplitude is invariant under symmetry transformations of the crystal.[64]

According to the spin-statistics theorem[9], the behavior of electrons, which have a half-integral spin, is determined by the Fermi-Dirac statistic.[72] These electrons are called "fermions". In quantum physics, the Pauli exclusion principle restricts the number of fermions per quantum state to one. This restriction has a decisive impact on the structure of atoms, their chemical properties and the condensed matter physics in general.[39]

In regard of the p-like ($L = 1$) valence band states, the coupling of the carrier spins and the orbital angular momentum alters the band structure. The multi degenerate states belong to the Γ_4 representation.[73] Hence, the symmetry of the hole wave function $\psi_\mathrm{h} = \chi_\mathrm{h} \cdot \chi_\mathrm{s}$ is defined by the direct product $\Gamma_4 \otimes D_{1/2} = \Gamma_7 + \Gamma_8$.[49,70] Due to the spin-orbit coupling the valence band splits into the fourfold degenerate Γ_8- and twofold degenerate Γ_7-states. The spin-orbit splitting is induced by the interaction of the intrinsic magnetic moment of the electron spin with the magnetic field generated by the electron motion. It is known that the size of the spin-orbit splitting influences the position of the lowest hole levels in the valence band. Hence, the spin-orbit splitting may affect the luminescence properties of semiconductors.[74] The Dirac-equation yields the spin-orbit interaction

$$\widehat{H}_\mathrm{SO} = -\frac{\hbar}{4m^2c^2}\vec{\sigma} \cdot \vec{p} \times (\vec{\bigtriangledown} V), \tag{2.12}$$

from which can be concluded that the total angular momentum J can take the two possible values $J = 3/2$ and $J = 1/2$ at $k = 0$. Thereby, $\vec{\sigma}$ is the spin operator and $\vec{p}$ describes the electron momentum operator. According to J and m_J the valence band eigenstates can be classified by:

$$| J,m_J\rangle = \begin{cases} | \frac{3}{2}, \pm \frac{3}{2}\rangle_\mathrm{hh} \\ | \frac{3}{2}, \pm \frac{1}{2}\rangle_\mathrm{lh} \\ | \frac{1}{2}, \pm \frac{1}{2}\rangle_\mathrm{SO}. \end{cases} \tag{2.13}$$

The fourfold spin degenerate $J = 3/2$ states belong to the irreducible representation Γ_8, whereas the twofold spin degenerate $J = 1/2$ state belongs to the Γ_7 representation.

The Γ_8-states split into the twofold Kramers degenerate heavy-hole (hh) and light-hole (lh) sub-bands. Kramers degeneracy means that the energy levels of a system,

such as an atom that contains an odd number of spin-1/2 particles, are at least double degenerate in the absence of an external magnetic field.[75] Spin-degeneration of electron and hole states requires simultaneous spatial inversion symmetry ($E_\uparrow(\vec{k}) = E_\uparrow(-\vec{k})$ and time reversal symmetry (Kramers-degeneration: $E_\uparrow(\vec{k}) = E_\downarrow(-\vec{k})$). While in a free atom the spin-orbit interaction can cause degeneration of states with the same orbital wave function but opposite spins, spin splitting in solids with inversion symmetry is not allowed. The designation as heavy and light holes stems from the concept of effective mass (m^*) as introduced above. Since the effective masses for a heavy and light hole differ, their quantization energies are different and the levels are split (including at $k = 0$). Hence, the curvatures of their sub-bands diverge for $k \neq 0$. The splitting of the heavy hole and light hole states ($\Delta_{\text{hh-lh}}$) at $k = 0$ typically amounts tens of meV. The associated heavy-hole and light-hole Bloch states read:

$$
\begin{aligned}
&| u_{3/2}\rangle = -\tfrac{1}{\sqrt{2}} \mid x + iy\rangle \mid\uparrow\rangle, \mid u_{-3/2}\rangle = \tfrac{1}{\sqrt{2}} \mid x - iy\rangle \mid\downarrow\rangle, \\
&| u_{1/2}\rangle = -\tfrac{1}{\sqrt{6}}(\mid x + iy\rangle \mid\downarrow\rangle - 2 \mid z\rangle \mid\uparrow\rangle) \quad \text{and} \\
&| u_{-1/2}\rangle = \tfrac{1}{\sqrt{6}}(\mid x - iy\rangle \mid\uparrow\rangle + 2 \mid z\rangle \mid\downarrow\rangle).
\end{aligned}
\tag{2.14}
$$

Here, $\mid x\rangle$, $\mid y\rangle$ and $\mid z\rangle$ describe the p-type coordinate parts of the Bloch amplitudes. Since the p-like coordinate part $\mid z\rangle$ is present in the light-hole Bloch states ($\mid u_{\pm 1/2}\rangle$), this means that the interband transitions are not only circularly but also linearly polarized. The optical selection rules of interband transitions are described in detail in Sec. 2.2.

As noted above, due to the spin-orbit interaction the twofold degenerate Γ_7-states are decoupled from the Γ_8-quadruplet. The Γ_7-states ($\mid 1/2, \pm 1/2\rangle_{\text{SO}}$) are called spin-orbit split-off bands (SO). These bands are shifted by Δ_{SO} to lower energies in relation to the Γ_8-band. At low temperatures the split-off band is almost always fully occupied, and, therefore, it has no effect on the optical properties in the region of the fundamental band-gap. For instance, the split off energy in GaAs amounts about $\Delta_{\text{SO}}^{\text{GaAs}} = 0.34$ eV which is considerably smaller than the corresponding band-gap energy of $E_{\text{g}}^{\text{GaAs}} \approx 1.42$ eV.[76]

The band structure of crystals with a lower symmetry than T_d can be deduced with an equivalent group-theoretical approach. For instance, the symmetry of well-balanced doped ideal two-dimensional quantum wells grown along a (001)-oriented substrate belongs to the $D_{2\text{d}}$ point group. In the $D_{2\text{d}}$ point group, the two lowest valence band levels are represented by the direct product $\Gamma_5 \otimes \Gamma_6 = \Gamma_6\,(\text{hh}) + \Gamma_7\,(\text{lh})$, in which Γ_6 and Γ_7 relate to the twofold spin degenerate heavy-hole and light-hole band, respectively. Moreover, the conduction band is described by the basis functions of the irreducible representation Γ_6. The corresponding band structure is schematically illustrated in Fig. 2.4 (b). Similar to the bulk zinc-blende crystal structure at the center of the Brillouin

zone ($k = 0$) the hole bands are separated by $\Delta_{\text{hh-lh}}$. The splitting between the heavy- and light-hole states typically amounts to tens of meV.[76]

When additional asymmetry is introduced, e.g. by nonequivalent interfaces, by asymmetrical growth conditions or by doping profiles, the symmetry of the system is reduced further to C_{2v}.[70] For instance, lens-shaped self-assembled quantum dots with a zinc-blende structure are typically described in terms of the C_{2v} point group. If a structure is part of this group, its conduction band is represented by Γ_5, and, thus, the valence band is described by the direct product $(\Gamma_2 + \Gamma_4) \otimes \Gamma_5 = \Gamma_5\,(\text{hh}) + \Gamma_5\,(\text{lh})$. Here, the heavy-hole and light-hole band are defined by the irreducible representations Γ_5. Taking the spin into account, every state in a system with C_{2v} symmetry is double degenerate. In the case of an elongation of the semiconductor structure in the xy-plane, e.g. along the (110) direction, the symmetry is further reduced to C_2, which is the lowest symmetry of a zinc-blende structure. The C_2 point group includes only the identity and the mirror reflection operation. In comparison to C_{2v}, due to the low symmetry of C_2 the electron, heavy-hole and light-hole sub-bands are split into the Γ_3- and Γ_4-levels. The optical properties associated with these symmetries are outlined in Sec. 2.2.

The influence of quantum confinement on the density of the solid states, determining significantly the electrical, mechanical, chemical, magnetic, as well as optical properties of the semiconductor is described in the following section.

2.1.2 Semiconductors of reduced dimensionality

In today's semiconductor technology, the miniaturization of electronic devices is continuously progressing. In this regard, nanotechnology made it feasible to create structures that have at least one of its dimensions smaller than one micron. Structures of this kind are called nanostructures. In nanostructures the movement of electrons and holes is spatially restricted in one or more dimensions yielding unique mechanical, electrical and optical properties at the nanoscale, e.g. quantized excitation [77,78], Coulomb blockade [79], and metal-insulator transitions [80]. Besides extensive efforts in the fabrication of nanostructures, the focus of current research and development focuses on the exploration of their fundamental material properties and the development of novel applications in a wide range of technical fields. However, most phenomena occur in structures small enough for quantum mechanical effects to dominate. For instance, the confinement of electrons in three dimensions is currently reaching the regime in which the quantum mechanical description of the system is of great importance as it gives rise to quantum effects. To provide a better understanding, the physical properties of nanostructures are presented and discussed below.

2.1.2.1 Fabrication of low-dimensional nanostructures

In almost all applications of nanostructures, manufacturing is the first and greatest challenge. In recent years many technologies have been explored to fabricate nanostructures in order to realize a controllable confinement of carriers. In general, two different methods can be used to realize small scale nanodevices: the "top-down" and the "bottom-up" method. [81,82]

In the top-down approach, the macroscopic starting material is subjected to a mechanical, physical grinding process in order to reduce the structure size by fragmentation. The disadvantage of this method is the resulting wide particle size distribution and the loss of control over the shape of the resulting particles. In contrast, the bottom-up approach is based on the formation of colloidal systems from the atomic level, using low-dimensional quantum nanostructures such as quantum dots or quantum wells. This method allows a precise control of the particle shape and particle size distribution. [81] The selection of the chemical-physical manufacturing process of nanoparticles depends on the desired chemical composition as well as the required properties of the material. [82]

The fabrication of nano-devices on the basis of the bottom-up approach is based on the method of self-assembly. This can be achieved either by chemical or by epitaxial synthesis. Chemical synthesis processes offer a cost-efficient and fast technique with which almost perfectly crystalline clusters of a few hundred to ten thousand atoms can be produced in a variety of shapes and materials. These nanostructures, which

are called nanocrystals, are synthesized in solution and covered by organic molecules, which on the one hand ensure solubility and on the other hand prevent aggregation. The possibility of drying these nanocrystals and applying them to substrates, made of other materials, opens up a variety of different applications. For example, colloidal nanocrystals are used as sensitizers in devices such as photovoltaic cells [45] or as markers in biological applications [44]. The properties und peculiarities of colloidal nanocrystals are described in detail in Part IV.

The second commonly used technique to fabricate low dimensional heterostructures is epitaxial synthesis. In what follows this method of epitaxial growth is described in more detail as it is used for the majority of semiconductor materials investigated in this thesis. The general concept of epitaxial synthesis is based on the combination of materials with different band-gap energies E_g, in order to create a potential landscape in which charge carriers are spatially confined. Epitaxial deposition of semiconductor materials on each other that differ slightly in their lattice constant, induces lattice strain, which may be exploited to obtain multi-dimensional structures such as quantum wells or arrays of three-dimensional islands or quantum dots. The most popular methods used to create these nanostructures, which may contain layers of different semiconductor materials, are dip-coating* and epitaxial growth.

The most common fabrication technique used for creation of nanostructures is enabled by epitaxial deposition techniques such as molecular beam epitaxy (MBE). [84,85] Thanks to the invention of MBE by J. R. Arthur and A. Y. Cho in the 1960s [85], thin-films of single crystals can be deposited on any surface via the interaction with several molecular beams, thus, making it possible to create multilayered heterostructures with atomically abrupt interfaces of various semiconductor materials. The main features that distinguish the MBE from other growth techniques are the precise reproducibility of all parameters involved during the epitaxial process and the ability to precisely control the kinetic evolution of the outer layers of epitaxial film.

The MBE bases on the arrangement of several thermal particles on top of a heated and ordered crystalline substrate to form a thin layer whose crystalline structure matches that of the substrate even though the composition of the materials may differ. [86] In this context, the epitaxial growth occurs via the interaction of one or more molecular or atomic beams. In order to deposit thin-films of various elements on any desired surface, atomic or molecular beams† are emitted towards a highly pure semicon-

*Dip-coating found its way into chemistry around 1940 and has been later on commercially marketed by Schott Glass Technologies Inc. in 1959 [83]. It is based on chemical solution deposition. In this process, a substrate is immersed in a solution of the coating material and afterwards pulled out of the solution at a constant speed, so that a thin film deposits on the surface.

†The term "beam" means that evaporated atoms do not interact with each other or vacuum chamber gases, which is ensured by the long mean free path of the atoms, until they reach the substrate. The atomic beams are created in separate quasi-Knudsen effusion cells attached to the vacuum chamber. In these cells the source materials are evaporated using a heater plate. The shape of the cells and their direction allow to produce beams with homogeneous material densities.

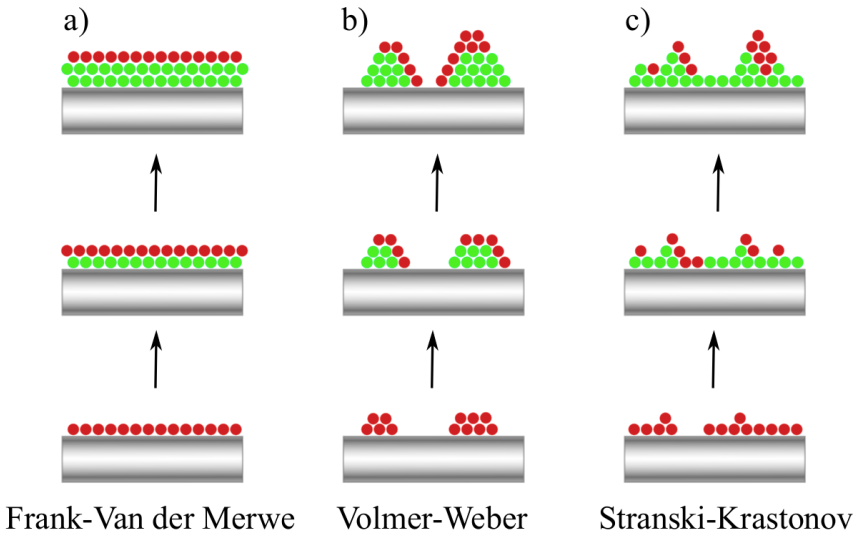

Figure 2.5: Different types of classical growth models. Depending on the surface energies of the materials, the substrate and their common heterointerface, three growth modes (a) - (c) can be distinguished. (a) The Frank-van der Merwe mode represents the "layer-by-layer" growth. (b) The Volmer-Weber mode represents the case of "islands" growth. (c) The Stranski–Krastanov mode represents an intermediate case between the first two modes. Here, the interface energy is comparable to the materials energy, from which follows that new layer formation competes with nuclei formation. Adapted from Ref. [89].

ductor substrate placed inside an ultra-high vacuum chamber. The gaseous elements impinging on the surface are absorbed by the substrate, thus, allowing to grow layers of single crystals. The evaporated materials attach to the substrates surface finally forming thin films on a nanometer scale.

The most important aspect of MBE is the deposition rate that allows one to grow epitaxially. To control the deposition rate during epitaxial growth, mechanical shutters with tenth of seconds operation time in front of the evaporation cells are used, allowing one to tailor the composition of the constituents with single monolayer growth accuracy.[87] Alternation of the evaporated materials allows one to form from multiple heterojunctions a quantum heterostructures. The growth of a single monolayer typically takes a few seconds, depending on the materials used as well as the heating temperatures during the growth process. However, depending on the surface energies of the deposited material and the substrate, as well as their common heterointerface, the basic growth type differs. In this respect, one distinguishes between three basic growth modes, called Frank-van der Merwe, Volmer-Weber and Stranski-Krastanov.[88,89] These three modes are schematically illustrated in Fig. 2.5. When two different semiconductor materials are combined by means of MBE, a comparative study of their surface energies (E_{γ_1},E_{γ_2}) and their interfaces ($E_{\gamma_{1,2}}$) allows one to predict which is the dominant growth mode.

The most common growth model is Frank-van der Merwe growth, also known as "layer-by-layer" growth. This model assumes that attachment of atoms to the edge of a growing layer is far more likely than attachment to the top of the layer. For this mode to be possible, the substrate surface energy needs to be higher than the sum of the deposited material and the heterointerface surface energies ($E_{\gamma_1} > E_{\gamma_2} + E_{\gamma_{1,2}}$). If this conditions are fulfilled, the deposited material is attracted more by the substrate than by itself. The direct opposite to this type of growth mode is the Volmer-Weber mode, where nucleation of islands is favored over extended growth at layer edges. For instance, this type of mode may occur, when two semiconductor materials that differ slightly in lattice constant are grown on top of each other. In this case, the material will strain to conform to the substrate in the plane of the junction. This in turn leads to a reduction of the lattice constant in the plane while the lattice constant along the direction of growth is extended due to the elastic response of the material.[90] This distortion of the active layer causes an accumulation of elastic energy, which is relaxed when a critical thickness depending on the respective heterostructure is reached.[90] When the substrate surface energy is smaller than the combined material and interface surface energy ($E_{\gamma_1} < E_{\gamma_2} + E_{\gamma_{1,2}}$), new precipitating atoms will tend to cluster, causing the two-dimensional growth to change into a three-dimensional growth. As a consequence, defect-free islands or quantum dots of the deposited material will form spontaneously on the substrate surface as illustrated in Fig. 2.5.

The third growth mode, called Stranski-Krastanov growth, represents an intermediate case, where growth is initiated as a "layer-by-layer" mode, but shifts to the formation of nano-islands on top of a thin two dimensional layer for a certain critical film thickness.[88,89] Such a process has been described as early as 1938 by Stranski and Krastanow[91], and is, therefore, called the Stranski-Krastanow growth mode. The evolution of the growth process can be explained by considering the fact that in the initial condition the substrate energy is larger than the cumulative energy $E_{\gamma_2} + E_{\gamma_{1,2}}$. Hence, at the initial stage, the growth occurs layer by layer to form a wetting layer with the microscopic thickness of one or two monomolecular layers.[17] With increasing layer thickness the interface surface energy increases, so that the sum of the deposited material and interface surface energies finally exceeds the substrates attraction, which leads to nucleation of islands which can have the shape of a pyramid with a square base.

The formation of islands due to the aforementioned growth modes depends mainly on the growth conditions and the resolution of the particular lithographic technique. Hence, the growth parameters can be adapted in order to create quantum structures of various shapes and sizes. This is evidenced by numerous previous studies, which have investigated self-assembled InAs quantum dots, grown on a GaAs matrix, by means of atomic force microscopy (AFM). Depending on the growth conditions quantum dots in the shape of square-based pyramids with a typical base length and height of 120 and 60 Å[92] or 240 and 30 Å[93], respectively, or in the shape of lens-shaped (hemispherical) islands with base diameters and heights of 200 and 60 Å[94], respectively, have been

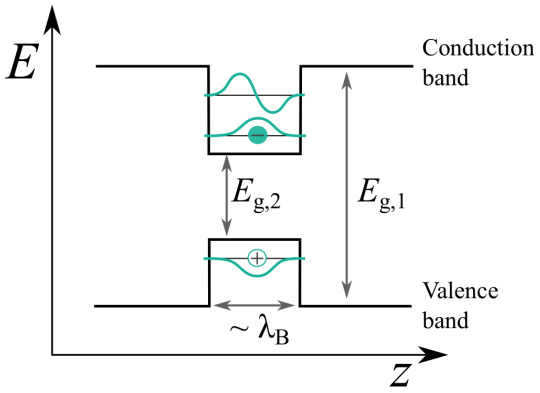

Figure 2.6: Potential profile of a single heterojunction along the growth direction. Here, a semiconductor with smaller band-gap ($E_{g,2}$) is embedded in two semiconductor layers with larger band-gap ($E_{g,1}$). Free charge carriers are localized in the region with smaller band-gap.

observed[‡]. However, by using suitable growth conditions, it is possible to fabricate arrays and stacks of nanometer-sized self-assembled quantum dots, ordered in size and shape, with high optical quality and high area density ($> 10^{11}$ cm^2).

It is important to emphasize at this point that both shape and size of nanometer-sized structures significantly influence the electronic bands of the semiconductor and, thus, its optical properties. In order to gain an understanding of the influence which a low-dimensional nanostructure can have on the electronic conduction and valence bands and therewith on the wave function of enclosed electrons, the case of a simple quantum well, i.e. a two-dimensional semiconductor structure, will first be discussed.

Epitaxial growth on the basis of the Frank-van der Merwe growth mode facilitates the creation of two dimensional structures. For instance, alternating layers of two dissimilar semiconductor materials can be grown on each other, e.g. $In_xGa_{1-x}As$ on GaAs, so that the material with smaller band-gap ($E_{g,2}$) is embedded in between two layers of a semiconductor material with a larger band-gap ($E_{g,1}$), providing a potential landscape for electrons and holes. The one-dimensional potential $V(z)$ as a function of the growth direction z in the conduction and valence band is sketched in Fig.2.6. When the lattice constant mismatch between the two dissimilar materials is small (mismatch ≤ 5 %) and both materials have a similar chemical composition, the interface will be very sharp and well defined. As a consequence, the band-gap will show a discontinuity at the interface. The illustrated structure in Fig.2.6 is a typical example of a type-I heterostructure system. For this type, the material with smaller band-gap is completely embedded within the wider band-gap material. In consequence, electrons and holes

[‡]The formation of very complex shapes and compositions is possible. In this regard, recent studies reported that due to a nonuniform composition, quantum dots with truncated pyramid shape and an In-rich core having an inverted-triangle shape can form. [95]

relax into the material with the smaller band-gap and are, therefore, localized in the same region of space. If the encased layer is sufficiently thin for quantum properties to be exhibited, then such a band alignment is called a single quantum well. The impact of quantum confinement on the properties of the charge carriers is addressed in the next section.

2.1.2.2 Quantum confinement in low-dimensional Systems

Quantum confinement effects on the electronic and optical properties become important when the physical size of the confinement potential is comparable to the de Broglie wavelength (λ_B) of the electrons or holes.[96] The de Broglie wavelength is the wavelength associated with a matter wave which represents any aspect of the behavior or properties of a material object that varies in time or space in conformity with the mathematical equations that describe waves. Considering the thermal motion of an electron of mass m_e^* along a single direction in a crystal with lattice temperature T, the de Broglie wavelength is given by:

$$\lambda_\mathrm{B} = \frac{h}{\sqrt{2m_\mathrm{e}^* E_\mathrm{kin}}} = \frac{h}{\sqrt{m_\mathrm{e}^* k_\mathrm{B} T}}. \tag{2.15}$$

Here, k_B is the Boltzmann constant, h is the Planck constant and E_kin is the kinetic energy of the electron. At room temperature ($T = 300$ K), free electrons have an kinetic energy of approximately $E_\mathrm{kin} \approx k_\mathrm{B}T = 0.026$ eV. However, their effective mass m_e^* varies widely in different semiconductors as the degree of the electron interaction with the periodic crystal lattice varies. For instance, in GaAs the effective mass amounts $m_e^* \approx 0.068 m_0$ and in ZnSe it equals $m^* \approx 0.017 m_0$, where m_0 is the rest mass of free electrons. In respect to Eq. (2.15) the de Broglie wavelength can be determined to $\lambda_\mathrm{B} \approx 29$ nm (for GaAs) and $\lambda_\mathrm{B} \approx 18$ nm (for ZnSe). For the observation of quantum size effects, it is important that the mean free path of the electrons is larger than the geometric dimensions of the object under consideration and, furthermore, that the object boundaries are sufficiently smooth. By epitaxial growth techniques spatial confinement can be realized for up to three dimensions. Depending on the dimension of the resulting structure, one speaks of bulk semiconductors (3D), quantum wells (QW/2D), quantum wires (1D), or quantum dots (0D). In Fig. 2.7 the systems of reduced dimensionality in real space are schematically illustrated.

To provide a description of the changes caused by the confinement potential, the undisturbed states observed in bulk semiconductors are considered as reference point. As described in the previous section, the effective mass approximation allows one to give an elementary description of the energy state characteristics. Using the Schrödinger equation (see Eq. 2.7) the band dispersion, and, thus, the energy eigenvalues, can be determined. In the simplest case, the confinement potential of the three-dimensional bulk semiconductor corresponds to $V(r) = 0$, which implies that the movement of the

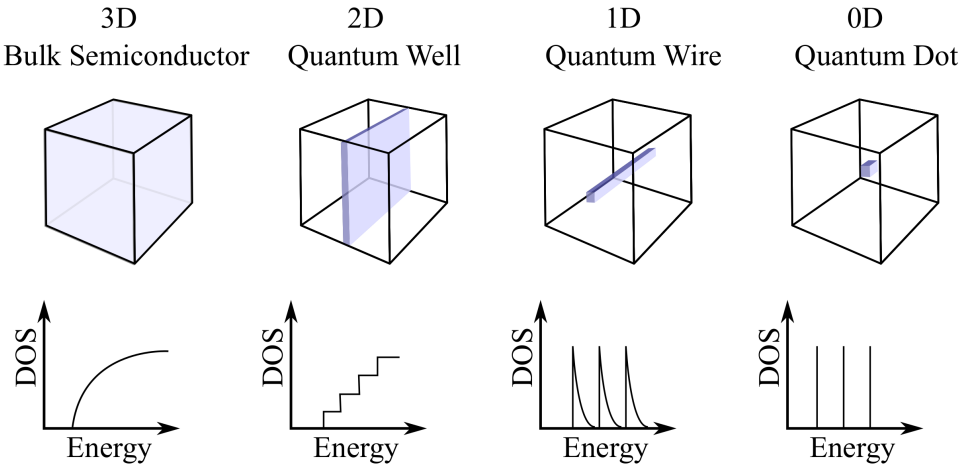

Figure 2.7: Illustration of the spatial elongation of a bulk semiconductor (3D), quantum well (2D), quantum wire (1D), and quantum dot (0D) and the respective energy dependence of the density of states ($D(E)$). The density of states changes by the confinement effect. While in bulk semiconductors the DOS follows a $\sqrt{E}$-dependence, in structures of reduced dimensionality the quantization of the energy states induces a change of the DOS function. In a structure with confinement along one direction, as in the case of QWs, $D(E)$ follows the Heavyside step function. In the case of quantum wires, i.e. structures with two-dimensional confinement, $D(E)$ displays a $1/\sqrt{E}$-dependence, with singularities at the energy positions which coincide with the quantized energy states. The energy levels in QDs are completely quantized and, therefore, only result in discrete energy states. The DOS function is accordingly a sequence of δ-functions. Figures have been drawn after Ref. [97].

electrons is not restricted in any direction. Consequently, for a bulk semiconductor the resulting energy eigenvalues correspond to the parabolic energy dispersion, as depicted for the valence band and conduction band near the Γ-point in Eq. 2.10. With regard to structures of reduced dimensionality, it is necessary to adapt the inclusion potential in order to solve the Schrödinger equation.

In addition to the energy eigenvalue, the density of states (DOS) is of key importance. It is defined essentially as the number of different states N between two successive energies E and $E + dE$ of infinitely small distance that electrons are allowed to occupy. Mathematically it is expressed by [90]:

$$D(E) = \frac{\mathrm{d}N}{\mathrm{d}E}. \tag{2.16}$$

The calculation of electronic processes like absorption, emission, or the general distribution of electrons in a material requires knowledge of the DOS. Material properties like specific heat, paramagnetic susceptibility, and other transport phenomena of conductive solids depend on it. [97] In general, calculations allow one to determine the general distribution of states as a function of energy ($D(E)$). [97,98] The DOS for an electron

gas in different systems of reduced dimensionality in the energy range including the first three sub-bands is sketched in Fig.2.7. In the case of a bulk semiconductor the calculation of the DOS yields:

$$D_{3D}(E) = \frac{2}{V_0} \sum_k \delta[E(\vec{k}) - E] = \frac{1}{2\pi^2} \left(\frac{2m^*}{\hbar^2} \right)^{3/2} \cdot \sqrt{E}, \tag{2.17}$$

with V_0 describing the unit cell volume. It becomes immediately evident, that the DOS follows a square root dependence with increasing energies. How the inclusion potential, the resulting energy eigenvalues and the DOS changes in regard of QW and QD structures is the central issue below.

2.1.2.3 Two dimensional systems - Quantum wells

In the case of a two-dimensional QW structure, as sketched in Fig.2.6, quantization of the carriers may occur in the perpendicular direction to the QW plane. The prerequisite for this is that the thickness of the well is considerably smaller than the transverse dimensions (i.e. $L_z \ll L_x$,L_y), and moreover, that the width of the well is comparable to the de Broglie wavelength of the confined carriers. For ideal quantum wells, the confinement potential is infinite in one direction (here z-direction) and zero in the other two directions. The quantization of the carrier motion in one dimension has to be considered in the dispersion carrier dynamics. Motion in the non-confined plane is not quantized, i.e. the electron can still be described as a free particle with an effective mass and its motion is defined by the Bloch waves (see Eq.(2.9)). The resulting wave function ($\psi_n(\vec{r},\vec{k}_{||})$) is and, thus, the product of the Bloch function describing the bulk properties of the semiconductor, and the envelope function ($\phi(z)$) that describes the confinement effects of the charge carriers (here in z-direction).[99,100] In the case of a QW, the electron (or hole) wave function reads:

$$\psi_n(\vec{r},\vec{k}_{||}) = u_{n\vec{k}_{||}}(\vec{r}) \cdot \mathrm{e}^{i(k_x \cdot x + k_y \cdot y)} \cdot \phi(z). \tag{2.18}$$

Inserting this wave function in the Schrödinger equation (see Eq.(2.7)) provides solutions for the energy levels of a confined electron (or hole) in a QW. Herewith one obtains for the energy eigenvalues of the system:

$$E_{n\vec{k}} = E_{n_z} + E_{\vec{k}_{||}} = E_{n_z} + \frac{\hbar^2}{2m^*} \cdot (k_x^2 + k_y^2). \tag{2.19}$$

The quantized energy E_{n_z} results from the calculation of the wave function $\phi(z)$ in a potential well and represents the energy of an electron (or hole) in the corresponding state. The energy levels in the k_x and k_y directions form a continuum, and for each discrete energy E_n, a two-dimensional energy band in the k_x-k_y plane will form. In the limit of a square well with infinite high barriers and a finite width of the well (L_z) the quantization energy reads:

$$E_{n_z} = \frac{\pi^2 \hbar^2}{2m^* L_z^2} n_z^2. \tag{2.20}$$

Here, m^* is the effective mass of the electron (or hole) and n is the principal quantum number ($n_z = 1,2,3,\ldots$), describing the states of rising energy. The energy E_n depends mainly on n and, thus, increases quadratically. Hence, the separation of the energy levels increases for higher quantum numbers. The lowest possible energy of a particle, which is also called the zero point energy, is obtained for $n = 1$. It is obvious that in the realistic case of finite potential wells only a finite number of quantized states is bound in the well. From Eq. (2.20) it can be further concluded that the QW thickness is inverse proportional to the confinement energy. Hence, for decreasing QW widths, the quantized energy increases. In the limit of finite potential wells, the first excited state may merge from the well and become a virtual state, when the width of a single quantum well is decreased.[101]

The effect of quantization also influences the density of states, as the maximum number of carriers that can occupy one energy state is limited and the energy levels itself are separated from each other. According to Eq. 2.16, for a single confined state the DOS function is given by[90]:

$$D_{\mathrm{2D}}(E) = \frac{1}{2\pi}\left(\frac{2m^*}{\hbar^2}\right)^1 \cdot E^0. \tag{2.21}$$

If there are many (n) confined states within the quantum well, then the density of states at any particular energy is the sum over all the sub-bands below that point. Hence, with the transition from a bulk semiconductor to a two-dimensional QW, the DOS function changes from the smooth parabolic shape function to a Heaviside step function, consistently increasing the density of states by one when the threshold energy, i.e. quantized energy (E_i), is exceeded.[101] The corresponding DOS function in a two-dimensional electron system reads[102]:

$$D_{\mathrm{2D}}(E) = \frac{m^*}{\pi\hbar^2}\sum_{i=1}^{n}\Theta[E - E_i], \tag{2.22}$$

with $\Theta[E \geq E_i] = 1$ and $\Theta[E \leq E_i] = 0$. The cumulative density of states is step-like up to the energy at which the discrete bound state spectrum merges into the continuum of free (unbound) states.[101] For visualization, the energy dependence of the DOS is depicted in Fig. 2.7. The changes in the energy spectrum discussed above occur for low-dimensional semiconductor crystals, including the spectrum of electrons in the conduction band and the spectrum of holes in the valence band. The confinement of electrons and holes also affects the band-gap. In comparison to bulk semiconductors the band-gap increases in low-dimensional semiconductors, leading, in particular, to a blue-shift in the optical absorption spectrum of low-dimensional systems.[103] For instance, in previous studies on InGaN/GaN periodic structures it has been shown that the absorption edge shifts to lower energies as the well width increases.[104] Furthermore, it has been demonstrated that the oscillator strength for the optical transition significantly decreases with the QW width.[104]

It is important to point out, that ascribing to the wave-particle duality the solutions of the Schrödinger equation for electrons confined in a QW indicates the occurrence of standing waves, for which the allowed values of k are expressible in terms of the nonzero integers n_x, n_y and n_z. Standing waves form at the quantization energies E_n within the confining potential. Here, the principal quantum number n corresponds to the number of nodes, i.e. points at which the displacement along the vertical axis is zero. For each discrete energy E_n in a potential well the total number of nodes equals $n-1$. Since the wave function of the electrons (or holes) has always to satisfy the Schrödinger equation, it has to be continuous inside the well as well as at the barrier. In result the wave function penetrates into the barrier where its amplitude drops exponentially. [101] Hence, there is a finite probability that the particle may tunnel through the barrier and escape from the QW.

2.1.2.4 One dimensional systems - Quantum wires

It has been shown that the reduction in dimensionality produced by confining electrons (or holes) to a thin semiconductor layer leads to a change of the energy eigenvalues and, therefore, to a change of the DOS. By further reducing the dimensionality of the electron's environment to one-dimension, artificial structures are created that are described as quantum wires. The charge carriers are still confined along the heterostructure growth z-axis, as they are in the quantum well, but in addition they are now also confined along an additional direction, either along the x- or the y-axis, characterized by an additional quantization number n_x or n_y, respectively. For simplicity's case, the electron motion can be regarded as movement in a two-dimensional, infinitely deep potential well. Due to this property, quantum wires are of particular importance in the research of transport phenomena. [105,106]

Within the effective mass approximation the motion along the unconfined direction of the quantum wire is defined by the parabolic dispersion (see Eq. (2.10)). Assuming that the confinement occurs in the yz-plane, the total energy of the electron reads:

$$E = E_{n_z,n_y} + \frac{\hbar^2 k_x^2}{2m^*} = \frac{\pi^2\hbar^2}{2m^*}\left(\frac{n_y^2}{L_y^2} + \frac{n_z^2}{L_z^2}\right) + \frac{\hbar^2 k_x^2}{2m^*},\ (n_y,n_z = 1,2,3,\ldots), \tag{2.23}$$

with L_y and L_z describing the wire dimensions in the transverse plane (L_z,$L_y \ll L_x$). In this example, the confined states are described by the two principle quantum numbers n_y or n_z specifying the sub-bands. The lowest sub-band has $n_y = n_z = 1$, defining the zero point energy of the system.

In analogy to both the bulk and quantum well cases, the DOS for a one-dimensional wire can be determined via Eq. (2.16). Hence, the corresponding DOS function in a

one-dimensional electron system is given by:

$$D_{1\mathrm{D}}(E) = \frac{1}{\pi}\left(\frac{2m^*}{\hbar^2}\right)^{\frac{1}{2}} \cdot \frac{1}{\sqrt{E}}. \tag{2.24}$$

In the case of several confined states within the quantum wire with the sub-band minimum E_i, the DOS at any particular energy is given by the sum over all the sub-bands below the point, which is given by [90]:

$$D_{1\mathrm{D}}(E) = \sqrt{\frac{2m^*}{\hbar^2}} \sum_{i=1}^{n} \frac{1}{\pi\sqrt{(E-E_i)}} \Theta[E-E_i]. \tag{2.25}$$

As can be concluded from $D_{1\mathrm{D}}(E)$, the cumulative DOS follows the product of a Heaviside step function and a $1/\sqrt{E}$-dependence with singularities at the energy positions that are equal to the quantized states E_i. An example of the one-dimensional density of states is shown in Fig.2.7. In contrast to the bulk and quantum wells, quantum wires have maxima in the DOS at the energy of the subband minima, i.e. at the point where the charge carriers are expected to accumulate. A comparison of the energy dependence of the DOS for bulk (see Eq. (2.17)), quantum wells (see Eq. (2.21)) and quantum wires (see Eq. (2.24)) demonstrates that a gradual reduction in the degrees of freedom of the electron movement leads to a reduction in the functional form of $D(E)$ by factors of $\sqrt{E}$. However, the situation changes, when the dimensionality of the electron's environment is further reduced to zero dimensions. As discussed in Sec. 2.1.2.2, nanostructures in which the carrier is confined in all directions are referred to as quantum dots. In what follows the focus is set on the impact of quantum confinement on the electron and hole wave functions in zero-dimensional structures and in this regard, the respective energy levels as well as their respective DOS.

2.1.2.5 Size quantization in quantum dots

Semiconductor quantum dots (QDs), epitaxially grown or chemically synthesized, have attracted great interest in current research, as they provide charge carrier confinement in all three directions and, thus, offer the possibility to study fundamental quantum phenomena. In the first approximation, a QD can be considered an artificial atom, since its state density consists of a series of very sharp peaks and its physical properties in many respects resemble those of an atom in a box. However, since QDs are filled with electrons and holes, they are expected to have significantly different properties than real atoms. The confined carriers in a QD are strongly localized and, thus, experience the competing effects of quantum confinement and Coulomb-induced electron-hole correlations. To fully comprehend the interplay of these two factors, a detailed understanding of the electronic structure is essential, which additionally provides the link between the structural and optical properties of these systems.

The calculation of the energy levels of a single quantum dot is a major challenge as these systems are to large to be treated as simple molecules. In this regard, the translational invariance, which is the most fundamental symmetry of solid state physics, is not fulfilled. Therefore, neither the standard methods of theoretical chemistry nor those of solid state theory such as the ab initio methods based on density functional theory (DFT) and local density approximation (LDA) can be applied to these systems.[90] However, when the atomistic details of the underlying crystal structure are negligible, the formation of bound electron and hole states can be deduced from a simpler model, based on an effective-mass approximation[107] or a multi-band $k \cdot p$ model[108,109], describing the QD by a confinement potential caused by the band offsets.

It is important to note that in all the aforementioned methods of energy level calculation due to the three-dimensional confinement of carriers in QD structures, it must be taken to account that the electronic states depend considerably on the dot shape and size, which in turn are determined by the growth conditions.[110] Theoretically the shape of a dot can be modeled by spheres[111], pyramids[108,112] or lenses[107]. A description based on a parabolic potential is used to describe dots, which are made from a QW heterostructure through a series of masking and etching steps.[113] In what follows the focus is set on the last mentioned, since it best describes the (lens-shaped) self-assembled (In,Ga)As/GaAs QDs formed on a nano-meter thin wetting layer, studied in the framework of this thesis. It is important to note, that all considerations are idealistic, as uniaxial deformations can cause a further decrease of the symmetry and, thus, a decisive change of the energy levels.

Parabolic QDs, fabricated by layer epitaxy in the Stranski-Krastanov mode, are artificial atoms with a lateral confining potential. In these structures, the confinement along the growth direction z is stronger than in the xy-plane. This allows one to separate the vertical (z) and the in-plane (x, y) motion of the electrons and holes and, thus, allows one to use a single-band approximation that is consistent with the generalized Kohn theorem[§]. The Khon theorem is an important basis of DFT, used, for instance, in quantum chemical calculations of molecules and solids.[114] The basis wave function of the electron and hole is expressed by the product of the in-plane and the vertical envelope functions, $\Phi_{\mathrm{e,h}}(x,y)$ and $f_{\mathrm{e,h}}(z)$, respectively.[17] The basis wave function ($\psi_{\mathrm{e,h}}(\vec{r})$) reads:

$$\psi_{\mathrm{e,h}}(\vec{r}) = \Phi_{\mathrm{e,h}}(x,y) f_{\mathrm{e,h}}(z). \tag{2.26}$$

The vertical part $f_{\mathrm{e,h}}(z)$ describes one of the electron or hole subband functions in the two-dimensional QW. This function can be considered a linear combination of in-plane waves ($\exp(\pm i k_{\mathrm{e,h}} z)$) inside the QD, which decay exponentially into the surrounding

[§]Originally, W. Kohn has shown that for all electrons moving in a parabolic confinement potential, the electron-electron interaction does not affect the cyclotron resonance frequency and, moreover, a homogeneous excitation field couples only to the center of mass motion of the electrons.[114] In the limits of the generalized Kohn theorem, i.e. a parabolic confinement potential and a homogenous excitation field, the response of electrons in a many-electron system is easily described as the response of their center of mass motion, which also applies to the case of a parabolic quantum dot confinement.[115,116].

wetting layer.[17] The respective, confining potential in the vertical direction can be supposed as a rectangular quantum well, which results from the band offset between the QD and the barrier material.

The function $\Phi_{\mathrm{e,h}}(x,y)$ in Eq.(2.26) describes the in-plane confinement. The respective confining potential, can be considered, in good approximation, to have a cylindrical symmetry with a parabolic profile. Therefore, the confinement function $\Phi_{\mathrm{e,h}}(x,y)$ has to satisfy the Schrödinger equation for a two-dimensional oscillator, depicted in Eq.(2.7). This Schrödinger equation can be rewritten in terms of the azimuthal ϕ and radial ρ coordinates:

$$\left[-\frac{\hbar^2}{2m^*}\left(\frac{1}{\rho}\frac{\partial}{\partial\rho}\rho\frac{\partial}{\partial\rho}+\frac{1}{\rho^2}\frac{\partial^2}{\partial\phi^2}\right)+\frac{1}{2}m^*\omega_0^2\rho^2\right]\Phi_{\mathrm{n,l}}(\phi,\rho)=E\Phi_{\mathrm{n,l}}(\phi,\rho). \tag{2.27}$$

Here, m^* is the in-plane electron or hole effective mass. The last term in the square brackets describes the two-dimensional parabolic confinement potential $V_0(\rho)=\frac{1}{2}m^*\omega_0^2\rho^2$, expressed via the oscillator characteristic frequency ω_0. Because of the rotational symmetry of the Hamiltonian, the wave function $\Phi_{\mathrm{n,l}}(\phi,\rho)$ is separable into a azimuthal and radial part. The energy eigenfunction of the Hamiltonian, and, thus, reads:

$$\Phi_{\mathrm{n,l}}(\phi,\rho)=\frac{e^{im\phi}}{\sqrt{2\pi}}R(\rho), \tag{2.28}$$

where $n\in\mathbb{N}_0$ is the radial quantum number and $l\in\mathbb{Z}$ the angular momentum component along z. The solutions for the radial function R, which satisfy the Schrödinger equation in (2.27), are determined by:

$$R_{n,l}(\rho)=\sqrt{\frac{2l}{(n+|l|)!}}\left(\frac{\rho}{l_0}\right)^{|l|}\exp\left(-\frac{\rho^2}{2l_0^2}\right)\mathrm{L}^{|l|}_{n+|l|}\left(\frac{\rho^2}{l_0^2}\right), \tag{2.29}$$

with the effective natural harmonic oscillator length scale $l_0=\sqrt{\hbar/(m^*\omega_0)}$ and the associated Laguerre polynomials $\mathrm{L}^{|l|}_{n+|l|}(\xi)$[¶]. Based on Eq.(2.27), the eigenenergies of the two-dimensional oscillator in its simplest form are given by:

$$E_{n,l}=(2n+|l|+1)\hbar\omega_0. \tag{2.30}$$

It follows from this result that the two-dimensional parabolic potential forms shells ($N=1,2,3\ldots$) including $\pm l$ and spin degeneracy. The shells are equally spaced in energy with the intershell spacing $\hbar\omega_0$ and the degeneracy $2N$.[17]

An important aspect of the analytical derivation of the charge distribution in a quantum dot is the analysis of the probability distributions $|\Phi_{\mathrm{l,n}}(\phi,\rho)|^2$ of the electron

[¶]Solutions to the associated Laguerre differential equation $\xi y''+(1-\xi)y'+\lambda y=0$ with the integer k are called associated Laguerre polynomials $\mathrm{L}^m_k(\xi)$. The Rodrigues representation for these polynomials is $\mathrm{L}^m_k(\xi)=\frac{e^\xi\xi^{-k}}{m!}\frac{d^m}{d\xi^m}\left(e^{-\xi}\xi^{m+k}\right)$. From this equation one obtains for $m=0$ and $m=1$ the first two associated Laguerre polynomials $\mathrm{L}^0_k(\xi)=1$ and $\mathrm{L}^0_k(\xi)=-\xi+k+1$, respectively.

and heavy-hole wave functions $\Phi_{\mathrm{l,n}}(\phi,\rho)$. Visualizing the variation of an electron wave function in terms of r, ϕ, and ρ is important, as the absolute square of the wavefunction depicts the charge distribution in the low-dimensional structure. It follows from Eq. (2.29) that the ground state $|n = 0,l = 0\rangle$ of both the electron and heavy-hole is described by a radial-symmetric Gaussian, which is characteristic for a s-type wave function.[117] In contrast, the first excited states $|n = 0,l = \pm 1\rangle$ reveal the presence of a radial node in the function. A radial node occurs when the radial function equals zero other than at $r = 0$ or $r = \infty$. In a QD the probability distribution tends to zero at the center of the xy-plane because it is modulated by a coefficient linear in the radial coordinate ρ. It is worthwhile to note, that nodes of atomic orbital functions are both useful in identifying which orbital is being described by which wavefunction. For instance, all of the s functions have non-zero wavefunction values at $r = 0$, whereas p, d, and all other functions converge towards zero at the origin. Principally, the wave function probabilities of s- and p like distributions only marginaly overlap.[117] Moreover, it is important to point out that the composition profile as well as dot size and shape might decisively influence the in-plane directions and, thus, the charge distribution.[112,113]

The general distribution of electrons in a material requires knowledge of the DOS. In analogy to the higher dimensional cases, the DOS is determined via Eq. (2.16). Herewith, the DOS function for a zero-dimensional system is given by:

$$D_{\mathrm{0D}}(E) = \sum_{n} 2\delta(E - E_n). \tag{2.31}$$

Since, in contrast to QW or QWR, the electron and hole motion in the case of a QD is restricted in three spatial dimensions, there is no k space that could be filled with electrons. Consequently, each quantum state at the energy $E_{n,l}$ is occupied by only two electrons. For this reason the DOS function is described by a series of δ-functions. The zero-dimensional density of states is schematically illustrated in Fig.2.7.

In the closing remarks of this section the competing effects of quantum confinement and Coulomb induced electron-hole correlations for an confined electron or hole in a quantum dot will be addressed. According to Heisenberg's uncertainty principle the confinement of a particle into an area with length Δz introduces an uncertainty in its linear momentum p_z given by $\Delta p_x \sim \hbar/\Delta z$. This uncertainty causes an additional kinetic energy $(\Delta p_z)^2/2m^*$ which may become significant if it is greater than the thermal motion of the particle $k_{\mathrm{B}}T/2$.[96] In general two length scales are characteristic for an exciton (electron-hole pair) confined in a QD. Firstly, the size of the quantum dot, which can be approximated by the length $R = \sqrt{(\hbar m^*)/\omega}$, and secondly the effective Bohr radius $a^*_{\mathrm{B}} = (\epsilon m^* \hbar^2)/e^2$ [54]. Here, $m^* = (1/m^*_{\mathrm{e}} + 1/m^*_{\mathrm{h}})$ marks the reduced mass of the exciton with the effective masses m^*_{e} and m^*_{h} of electron and hole, respectively, e is the electron charge and ϵ is the dielectric constant of the semiconductor. The exciton Bohr radius provides a very useful length scale to describe the spatial extension of excitons in semiconductors. It typically ranges from ~ 2 to ~ 50 nm, depending on

the semiconductor material.[54,118]

The relation between the QD radius and the exciton Bohr radius defines the strong and weak confinement regimes. In the so-called strong confinement regime, the Coulomb interaction between electron and hole is no longer sufficiently strong to form a bound exciton, which holds for QDs where the Radius is smaller than the exciton Bohr radius ($R \ll a_{\mathrm{B}}^{*}$).[119] In this regime, the confinement potential is greater than the Coulomb interaction and the electron-hole pairs occupy the lowest energy single-particle states. It is important to point out that the direct Coulomb interaction is actually much larger than in a bulk crystal, as it is induced by a stronger confinement of an electron and a hole in a quantum dot. However, the kinetic energy of the electrons and holes increases as well and, thus, becomes much larger than the Coulomb interaction for a small QD radius. In this case, the electron and hole do no longer correlate to form an exciton.[119] If the QD radius is larger than the exciton Bohr radius, which is the case in the so-called weak confinement regime ($R \gg a_{\mathrm{B}}^{*}$), the quantum energy caused by the localization of charged carriers ($\hbar\omega = \hbar^2/(m^* R^2) \sim R^{-2}$) can be neglected against the Coulomb attraction ($e/(4\pi\epsilon R) \sim R^{-2}$). Hence, an electron-hole pair is strongly correlated.

In general the exciton Bohr radius a_{B}^{*} provides a convenient length scale to evaluate the impact of quantum confinement on the properties of semiconductor nanostructures. When the size of the nanostructure approaches a_{B}^{*}, which differs widely within the semiconductor materials, the confinement begins to affect the exciton wave function, thus, having large effect on the optical properties of the nanostructure. The band-gap E_g and and a_{B}^{*} are correlated, so that materials with narrower E_g have larger a_{B}^{*}, thus, experiencing quantum confinement at larger nanostructure sizes.[54]

2.1.3 Electron-hole oscillator strength in a quantum dot

In general, the oscillator strength defines the probability of absorption or emission of electromagnetic radiation in transitions between different energy levels. As shown by Wang and Herron[120], who investigated the dependence of the oscillator strengths on crystallite size, both exciton banding energies and oscillator strengths can increase in small scale nanostructures. The reason for this is the quantum confinement of both electrons and holes, which provides an increased spatial overlap of the electron and hole wavefunctions. The oscillator strength f of an exciton in terms of the matrix elements of the momentum $\vec{p}$ is defined by[103]:

$$f_{n,k} = \frac{2}{m_{\mathrm{e}}^{*}} \frac{|\langle n|\hat{\vec{p}}|k\rangle|^2}{E_n - E_k}. \tag{2.32}$$

Here, m_{e}^{*} is the effective mass of an electron and $E_n - E_k$ reflects the energy in regard of a transition from a lower state $|n\rangle$ to an upper state $|k\rangle$. The amplitude of the optical transition is given by the corresponding dipole matrix element

$$M_{\mathrm{if}} = \langle i|e \cdot r|f\rangle, \tag{2.33}$$

where r is the modulus of the position vector and e is the elementary charge. In terms of M_{if} Eq. (2.32) can be rewritten to $f = \frac{2m_{\mathrm{e}}^*}{\hbar^2}(E_n - E_k) \cdot |M_{\mathrm{if}}|^2 |U_(0)|^2$, with U_0 defining the probability of an electron and hole wavefunction overlap. As noted above the exciton oscillator strength depends significantly on the quantum confinement and, thus, it is important to distinguish between the weak and strong confinement regime.

In the weak confinement regime ($R \gg a_{\mathrm{B}}^*$), the probability $|U(0)|^2$ does not depend on the size of the nanostructure. Hence the macroscopic transition dipole moment determines f. In the strong confinement regime ($R \ll a_{\mathrm{B}}^*$), there is an increased overlap of the electron and hole wavefunctions, leading to an increase of $|U(0)|^2$. In this case, the oscillator strength per unit volume f/V increases with decreasing QD radius R, scaling roughly with $(a_{\mathrm{B}}^*/R)^3$. With increasing oscillator strength, the exciton absorption becomes stronger, yielding the possibility to observe excitonic-type features in the absorption spectra even at room temperature.[121] With regard to parabolic QDs, owing to the large effective hole mass, the hole is more confined in the vertical direction than the electron, resulting in a smaller overlap of the electron and hole wave functions. Hence, for this specific example the exciton oscillator strength decreases.

In summary, quantum confinement enhances principally the exciton kinetic and direct Coulomb energies and reduces the electron-hole separation, in turn increasing the spatial overlap of electron and hole wavefunction, which leads to an amplification of the exciton oscillator strength. As shown by Bryant[121], even in the transition regime between weak and strong confinement, the enhancement of exciton oscillator strengths can enhance optoelectronic properties.

2.1.4 Impact of magnetic field and quantum confinement on the electron g factor

In what follows, the impact of an external magnetic field on a system of quasi-two-dimensional electrons and holes confined in a QD is discussed. So far, the spin of a charge carrier has been treated in the context of band structure, and, thus, it has been sufficient to consider the angular momentum that is associated with it. However, the angular momentum of a charged particle gives rise to a magnetic moment, which is the fundamental object of magnetism. The polarization of magnetic moments causes magnetism, which also applies to electron spins, as experimentally demonstrated by the discovery of electron spin resonance.[122] The magnetic properties of an carrier spin are defined by its magnetic moment[123]

$$\vec{\mu}_{\mathrm{S}} = g\frac{\mu_{\mathrm{B}}}{\hbar}\vec{S}_{\mathrm{e(h)}}, \tag{2.34}$$

with the Bohr magneton $\mu_{\mathrm{B}} = 5.7884 \cdot 10^{-5}$ eV/T, the effective carrier spin $\vec{S}_{\mathrm{e(h)}}$ and the Landé factor g, which defines the response of a spin to an external magnetic field. The Landé factor of a free electron is $g_0 \approx 2$.[17]

For the action of an external magnetic field $\vec{B}$ on the spin magnetic moment $\vec{\mu}_{\mathrm{S}}$ the relative orientation has to be taken into account. An important aspect in this context is the Zeeman effect, which describes the splitting of exciton as well as single particle spin states in dependence of the magnetic field strength. In general it is defined by the corresponding Zeeman Hamiltonian.[124,125] For a magnetic field B of arbitrary strength and orientation it is given by[17]:

$$\hat{H}_{\mathrm{Z}} = \mu_{\mathrm{B}} \sum_{\alpha,\beta} g_{\alpha,\beta} \sigma_{\alpha} B_{\beta}, \tag{2.35}$$

with the Pauli spin matrices σ_{α}[‖] and the Landé factor tensor $g_{\alpha,\beta}$ as a function of the spatial coordinates α,β = x,y,z. The Electron-Spin Resonance (ESR) frequency, which is determined by the electron effective Landé factor, characterizing the Zeeman splitting of the electron (hole) spin levels, is found from $\hbar\omega = \Delta E_{\mathrm{Z}}$, where the Zeeman splitting of the spin sublevels equals

$$\Delta E_{\mathrm{Z}} = \mu_{\mathrm{B}} \sqrt{\sum_{\alpha} (\sum_{\beta} g_{\alpha,\beta} \sigma_{\alpha} B_{\beta})^2}. \tag{2.36}$$

For a low-symmetry system, the real tensor $g_{\alpha,\beta}$ comprises nine linearly independent components. However, when the system has a uniaxial symmetry, the tensor $g_{\alpha,\beta}$ is reduced to only two linearly independent components, which are traditionally denoted by $g_{\parallel} = g_{zz}$ and $g_{\perp} \equiv g_{yy} = g_{xx}$ with z being the quantization axis. The subscripts $\parallel$ and $\perp$ denote components in and perpendicular to the xy-plane, respectively. In this case Eq.(2.36) reduces to[17]

$$\Delta E_{\mathrm{Z}} = \mu_{\mathrm{B}} \left|\vec{B}\right| \sqrt{g_{\parallel}^2 \cos^2(\theta) + g_{\perp}^2 \sin^2(\theta)}, \tag{2.37}$$

where $\vec{B}$ and the quantization axis z enclose the angle θ. In the simple case of a magnetic field applied along the growth direction of the semiconductor ($\vec{B} \parallel z$), the Hamiltonian in Eq.(2.35) simplifies to

$$H_{\mathrm{Z}}(B) = \mu_{\mathrm{B}} \sum_{n} g^n_{\parallel,\mathrm{e(h),z}} S^n_{\mathrm{e(h),z}} B_z, \tag{2.38}$$

where $S^n_{\mathrm{e(h),z}}$ denotes the nth effective carrier spin and $g_{\mathrm{e(h),z}}$ describes the electron (hole) effective Landé factor. As explained in Sec. 2.1.1, the effective carrier spins for electrons and holes differ. In this respect, the particle spin of an electron is defined as $S^n_{\mathrm{e},z} = \pm 1/2$, whereas for heavy-holes and light-holes it is given by $S^n_{\mathrm{hh},z} = -1/3 j_{i,\mathrm{hh}}$

[‖] The Pauli matrices, also called the Pauli spin matrices, are complex matrices that arise in Pauli's treatment of spin in quantum mechanics. They are defined by

$$\sigma_x = \begin{pmatrix} 0 & 1 \\ 1 & 0 \end{pmatrix}, \sigma_y = \begin{pmatrix} 0 & -i \\ i & 0 \end{pmatrix}, \text{and } \sigma_z = \begin{pmatrix} 1 & 0 \\ 0 & -1 \end{pmatrix}.$$

and $S^n_{\mathrm{lh},z} = -j_{i,\mathrm{lh}}$, with the total angular momentum projections $j_{i,\mathrm{hh}} = \pm 3/2$ or $j_{i,\mathrm{lh}} = \pm 1/2$.[126]

Within the terms of second-order $k \cdot p$ perturbation theory the Zeeman Hamiltonian for the conduction band electrons in a bulk semiconductor can be expressed as[17]:

$$H_{\vec{B},ss'} = \frac{1}{2}\mu_\mathrm{B} \sum_\gamma B_\gamma \left(g_0 \sigma_{\gamma,ss'} - \frac{2i}{m_0} \sum_{n \neq c} \sum_{\alpha\beta} \delta_{\alpha\beta\gamma} \frac{p^\alpha_{cs,n} p^\beta_{n,cs'}}{E_c - E_n} \right). \tag{2.39}$$

Here, $\delta_{\alpha\beta\gamma}$ is the unit antisymmetric tensor of the third rank and $p_{cs,n}$ is the momentum matrix element between the Γ-point electron states in the conduction band c and the band n. The respective electron energies at the bottom of the conduction band and in the lower or higher band ($n \neq c$) are E_c and E_n . For an electron, occupying the lowest s-antibonding conduction band Γ_6 in a zinc-blende semiconductor with T_d symmetry, the g factor is isotropic and reads[17]:

$$g_\mathrm{e} = g_{zz} = g_0 + \frac{1}{m_0} \sum_{n \neq c} \frac{|p^+_{c,s;n}|^2 - |p^-_{c,s;n}|^2}{E_c - E_n}. \tag{2.40}$$

The g factor is determined by the coupling matrix element $p^\pm_{c,s;n} = \langle c\,\Gamma_6, s | \hat{p}_x \pm i\hat{p}_y | n \rangle$, with the spin matrix index $s = \pm 1/2$ and the momentum operator $\hat{\vec{p}}$. In the case of a zinc-blende semiconductor the value of the electron g factor is mainly defined by the upper valence bands Γ_8 and Γ_7, as can be seen from the Roth-Lax-Zwerdling relation[127]

$$g_\mathrm{e} = g_0 - \frac{2E_p \Delta_\mathrm{SO}}{3E_g(\Delta_\mathrm{SO} + E_g)}. \tag{2.41}$$

It follows from this equation that the electron effective Landé factor depends strongly on the fundamental band-gap E_g, the Kane energy E_p as well as the spin-orbit splitting Δ_SO of the topmost valence band.

A similar equation to Eq.(2.39) and (2.40) can be applied to strongly confined systems, like in QWs or QDs. In this case, however, the index n runs not only over the different bands but also over subbands formed as a result of the quantum confinement. Moreover, the assumption of a purely isotropic electron g factor has to be abandoned. For instance, the electron g factor in an unstrained quantum well, with infinitly high barriers for both valence and conduction band, in which case only nonzero matrix elements $p^\pm_{c,s;n}$ for the quantum-confined states with the same quantum number are allowed, can be estimated by:

$$\frac{g_\perp - g_\parallel}{g_\perp} \approx \frac{3}{2} \frac{E_\mathrm{lh} - E_\mathrm{hh}}{\Delta_\mathrm{SO}} \frac{E_g + \Delta_\mathrm{SO}}{\eta E_g}, \tag{2.42}$$

where

$$\eta = 1 - \frac{3}{2} \frac{E_g(E_g + \Delta_\mathrm{SO}) m_0}{\Delta_\mathrm{SO} |p_{c,n}|^2}. \tag{2.43}$$

Here, the confinement energies in the lowest heavy-hole and light-hole subbands are denoted by E_{hh} and E_{lh}, respectively. It follows from this equation, that the electron g factor shall exhibit a decisive anisotropy. Furthermore, it is important to point out that so far only unstrained heterostructures with matching lattice constants have been considered. However, when the QW consists of two semiconductor materials with mismatched lattice constants the strain-induced energy shifts of the conduction and valence bands need to be taken into account. Hence, both the confinement and the strain affect the splitting and shift of the heavy-hole and light-hole states. [17]

2.1.5 Fock-Darwin spectrum of an electron-hole pair in a quantum dot

After the previous section has highlighted the impact of an external magnetic field on the g factors of the electron as well as hole, now the focus is shifted towards the calculation of the eigenenergies of the quasi-two dimensional single-particle electron and hole levels in the presence of a magnetic field. In this respect, the effective Hamiltonian is introduced first, in order to subsequently develop a description of the energy states in a QD.

In the framework of the effective mass approximation and with consideration of the electron (hole) interaction with an external magnetic field (see Eq.(2.38)), the effective Hamiltonian for electrons or holes is given by [17,128]

$$\hat{H} = \sum_i \frac{1}{2m^*} \left\{ \vec{p}_{\perp i} + (\vec{p}_{\parallel i} + e\vec{A})^2 \right\} + V_0(\vec{R}_i) + V_I(\vec{R}_i) + \frac{1}{2} \sum_{i \neq j} V(\vec{R}_i, \vec{R}_j) + g_{\mathrm{e(h)}} \mu_{\mathrm{B}} B_z S_z \tag{2.44}$$

Here, $\vec{A}$ is the magnetic vector potential, $\vec{p}$ is the momentum operator, $m^*_{\mathrm{e(h)}}$ and $g_{\mathrm{e(h)}}$ are the electron (hole) effective mass and Landé factor, $V_0(\vec{R}_i)$ is the three-dimensional confining potential, and $V(\vec{R}_i, \vec{R}_j)$ is the electron-electron interaction potential. The interaction of each electron with its own image charge is denoted by $V_I(\vec{R}_i)$. All terms are dependent on the spatial position $\vec{R} = (\vec{r}, z)$ through the in-plane position $\vec{r}$ and z coordinate.

For the sake of simplicity in the following a single electron and hole confined in a QD is considered. Hence, the Coulomb interaction between identically charged carriers as well as exchange based interactions or interactions between carriers localized in different quantum dots are omitted. However, it is important to note that in QDs with two electrons these interaction terms can be essential. [128,129] In further approximation, small deviations from the exceptional case of a strictly parabolic dot confinement, which can lead to a rich fine structure, strongly influenced by Coulomb interaction effects, are disregarded as well. [129] Without interaction, the eigenstates of the system are anti-

symmetrised products of the states of the one-electron Hamiltonian

$$\hat{H} = \sum_i \frac{1}{2m^*} \left\{ \vec{p}_{\perp i} + (\vec{p}_{\parallel i} + e\vec{A})^2 \right\} + V_0(\vec{R}_i) + g_{\mathrm{e(h)}} \mu_{\mathrm{B}} B_z S_z. \tag{2.45}$$

These states are also known as Fock-Darwin states whose mathematical form may be found in the literature.[130,131]

The effective one-electron (hole) Hamiltonian, written in terms of the azimuthal ϕ and radial ρ coordinates, is given by

$$\hat{H} = -\frac{\hbar^2}{2m^*} \left(\frac{1}{\rho} \frac{\partial}{\partial \rho} \rho \frac{\partial}{\partial \rho} + \frac{1}{\rho^2} \frac{\partial^2}{\partial \phi^2} \right) - i \frac{\hbar \omega_c}{2} \frac{\partial}{\partial \phi} + \frac{1}{8} m^* \omega_c^2 \rho^2 + \mu_{\mathrm{B}}\, g_{\mathrm{e(h)}}\, S_z^i\, B + V_0(\rho). \tag{2.46}$$

Here, $\omega_c = |e|\, B/m^*$ is the electron (hole) cyclotron frequency, written as function of the magnetic field B_z, and $V_0(\rho)$ denotes the QD confinement potential, that takes into account the shape of the nanostructure. In this equation the contributions of the bulk inversion asymmetry (the Dresselhaus term) and the system inversion asymmetry (the Rashba term**), describing the momentum-dependent splitting of spin bands due to the combined effect of spin–orbit interaction and asymmetry of the crystal potential, are neglected.[132]

The eigenenergies $E_{n,l}$ of the single-particle electron and hole levels, which follow from the effective Hamiltonian (see Eq.(2.46)), can be expressed by[131]:

$$E_{n,l} = (2n + |l| + 1)\hbar \sqrt{\omega_0^2 + \frac{1}{4}\omega_c^2} - \frac{l}{2}\hbar\omega_c + \mu_{\mathrm{B}}\, g\, S_z\, B. \tag{2.47}$$

In comparison to Eq. (2.30), the oscillator resonance frequency changes to $\sqrt{\omega_0^2 + \frac{1}{4}\omega_c^2}$ and two additional terms $-\frac{l}{2}\hbar\omega_c$ and $\mu_{\mathrm{B}}\, g\, S_z\, B$, which take into account the magnetic field induced shift and splitting of spin-states, are added to the eigenenergy values. Assuming that the condition: $m_{\mathrm{e}}^* \omega_0^{\mathrm{e}} = m_{\mathrm{h}}^* \omega_0^{\mathrm{h}}$ is fulfilled[133], which implies identical form of electronic and hole wavefunctions on their corresponding s, p, d, ... shells, the energy difference $\Delta E_{n,l}$ between the electron and hole single-particle can be written in terms of an electron-hole pair Fock-Darwin diagram[131]:

$$\Delta E_{n,l} = (2n + |l| + 1)\hbar \sqrt{(\omega_0^*)^2 + \frac{1}{4}(\omega_c^*)^2} - \frac{l}{2}\hbar\omega_c^* + \mu_{\mathrm{B}}\, B(g_{\mathrm{e}}\, S_{z,\mathrm{e}} + g_{\mathrm{h}}\, S_{z,\mathrm{h}}), \tag{2.48}$$

with $\omega_0^* = \omega_0^{\mathrm{e}} + \omega_0^{\mathrm{h}}$ and $\omega_c^* = (1/m_{\mathrm{e}}^* + 1/m_{\mathrm{h}}^*)\, |e|\, B/(2\pi)$.

The size of a Fock-Darwin state depends on the length parameter l_0 and on the quantum numbers l and n. Fock-Darwin states are localized on rings and, thus, a

**The Rashba Hamiltonian is defined by the coupling term $\hat{H}_{\mathrm{R}} = \alpha(\vec{\sigma} \times \vec{p}) \cdot \hat{z}$, where α is the Rashba coupling factor, $\vec{p}$ is the momentum and $\vec{\sigma}$ is the Pauli matrix vector.

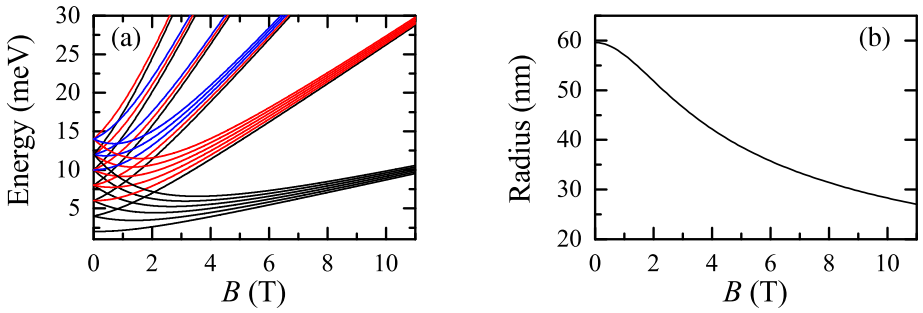

Figure 2.8: (a) Fock-Darwin states of a single electron in a (In,Ga)As QD ($m^* = 0.067\,m_0$) with lateral confinement energy of $\hbar\omega_0 = 2$ meV. The states $|n \geq 0, l \geq 0, +1/2\rangle$ are marked by a specific color (online), indicating orbitals with the same number of radial nodes. The levels with $n = 0$ are shown by black lines, with $n = 1$ by red lines, and with $n = 2$ by blue lines. The ground state $|0,0,+1/2\rangle$ has the lowest energy due to the negative electron Landé factor $g_e = -0.6$. (b) Magnetic field dependence of the effective size (radius) of the Fock-Darwin state $|n = 0, l = 0\rangle$, estimated by the squared radius from Eq.(2.49).

practical measure of the size is the mean square radius [134]

$$R^2 = \langle n,l|r^2|n,l\rangle \sim \frac{\hbar}{m^* \cdot \sqrt{(\omega_0^*)^2 + \frac{1}{4}(\omega_c^*)^2}}(2n + |l| + 1). \tag{2.49}$$

The size of the Fock-Darwin state $|n = 0, l = 0\rangle$ as a function of the magnetic field is depicted in Fig. 2.8 (b). Obviously the radius is proportional to the length l_0 and inverse proportional to the cyclotron frequency ω_c^*. Hence, the system size decreases with magnetic field. However, it follows from Eq.(2.49) as well that the size increases with angular momentum. For illustration the magnetic field dependence of the lowest few Fock-Darwin energies for a GaAs QD ($m^* = 0.067\,m_0$) with $\hbar\omega_0 = 2$ meV are shown in Fig.2.8 (a).

While at zero field the levels are equally spaced, with increasing field strength a complicated series of crossings occurs. From Eq. (2.48) follows for the lowest part of the Fock-Darwin spectrum that the energy of the electron states with zero orbital angular moment has a minimum at zero magnetic field, while for non vanishing orbital angular moment the energy minimum shifts to low magnetic fields. This can also be clearly seen in Fig.2.8 (a). This effect is attributed to the reduction in the effective natural harmonic oscillator length l_0.

It is obvious from Eq.(2.48) that at non-zero magnetic fields the overall energy $E_{n,l}$ increases, due to the increasing kinetic energy of the cyclotron motion. In addition, the magnetic field induces due to the Zeeman coupling a splitting of the Fock-Darwin levels into sublevels corresponding to the spin-up and spin-down states. The separation of these levels increases linearly with B. In the limit of a vanishing confinement potential

($\omega_0 \to 0$) or very high magnetic fields ($\omega_c \gg \omega_0$) the energy $E_{n,l}$ tends to $(2n + (|l| - l) + 1)\,\hbar\omega_c^*/2$, which coalesce into the free electron Landau levels, with the constant Landau quantum number $n + (|l| - 1)/2$. From this one may conclude that the energy $E_{n,l}$ for positive angular momentum values would be independent of l, even though it increase in the presence of an confinement potential with l. This is one of the key characteristics that allows one to distinguish between free and confined electrons. [134] Last but not least, it is worth emphasizing that there is significant broadening in high magnetic fields, as can be seen in Fig.2.8 (a). This broadening illustrates the effect of the angular momentum on the system size. Fock-Darwin states with larger angular momentum have a larger size, so electrons in these states experience a larger potential.

2.2 Interband transitions and optical selection rules

As described above, the effect of quantum confinement affects the optical properties of semiconductors, leading, for example, to a shift in the optical transitions to higher energies when the dimensions of a nanostructure are reduced. In order to understand how the optical transitions in low-dimensional nanostructures proceed, first the simple case of an optical transition in a two level system is considered.

Principally, the optical transition between two electronic states of a crystal is probed using an external electromagnetic (EM) wave (photon) varying periodically in time t at a specific frequency ω_l. When the energy of the incident monochromatic light wave $E(t) = E_{\mathrm{ip}} cos(\omega_{\mathrm{ip}} t)$ of amplitude E_i has sufficient energy ($\hbar\omega_{\mathrm{ip}} > E_g$), an electron is excited from the valence band to the conduction band, leaving behind a hole in the valence band. Electrons and hole are subject to the Coulumb interaction, which leads to the formation of an electron-hole pair, as has been explained in detail in the last sections. Hence, in the underlying process of excitation a mixing of the ground state and excited state orbitals occurs. This mixing of the two orbitals induced by the oscillating electric field of the photon can only occur when the mixed states have a dipole moment and according to the energy conservation principle the EM field corresponds to the frequency difference between the initial state $|i\rangle$ and the final state $|f\rangle$ at $\vec{k} = 0$. In this case the direct quantum transition is described by the classical dipole with the frequency $\omega_{if} = \omega_f - \omega_i = (E_f - E_i)/\hbar$, with E_i and E_f denoting the energies of the initial and final states, respectively. The lowest energy interband transition is between the lowest hole level and the lowest electron level.

The amplitude of the optical transition is given by the transition dipole moment M_{if} (see Eq.(2.33)). Taking into account only nonzero transition dipole moments ($M_{\mathrm{if}} \neq 0$), optical transitions in semiconductors can only occur, where the parity selection rule

$$\Delta l = \pm 1 \tag{2.50}$$

is fulfilled. With respect to atoms or molecules, transitions can only occur between

orbitals with different parity (e.g. $s \to p$, $p \to s$, or $p \to d$, etc.). Since a photon, which is the gauge boson[††] for electromagnetism, is a massless particle with spin $S = 1$, it can only have a spin angular momentum of $S_z = \pm\hbar m_z$, with $m_z = \pm 1$ defining its magnetic quantum number. Hence, due to the principle of angular momentum conservation all single photon transitions must obey

$$\Delta m_j = \pm 1, \tag{2.51}$$

where Δm_j is the difference between the projection of the total angular momentum m_j of the initial and the final state. [39]

Another possible type of transitions are intersubband optical transitions. In QWs or QDs, due to quantum-confinement effects, the free-carrier energy spectrum transforms into a series of subbands leading to an additional mechanism of intraband absorption associated with direct optical transitions of free carriers between the subbands. The transition rate from the electron states $|i\rangle$ to $|f\rangle$ is determined by Fermi's golden rule. In general, one can present the total transition rate $W_{e2,e1}$ between two electron states $e1 \to e2$ per unit area in the form [17]:

$$W_{e2,e1} = \frac{4\pi^2 e^2 I}{\hbar\omega^2 c n_\omega A} \sum_{ss'\vec{k}} \left| e \cdot \upsilon_{e2s',e1s}(\vec{k}) \right|^2 (f_{e1sk} - f_{e2s'k})\, \delta\left(E_{e2s'k} - E_{e1sk} - \hbar\omega\right). \tag{2.52}$$

Here, I is the incident light intensity, e is the elementary charge, s and s' are the spin indices, $\upsilon_{e2s',e1s}(\vec{k})$ is the matrix element of the velocity operator, f_{e1sk} is the electron distribution function, A is the sample area and $E_{e2s'k}$ or $E_{e2s'k}$ is the energy of the final or initial state, respectively.

In order to determine the entire spectrum of dipole-allowed optical transitions between the valence band and conduction band states, the band structure and, thus, the symmetry of an exciton in the corresponding structure must be taken into account. In what follows briefly in terms of group-theoretical aspects the symmetry of an exciton in a bulk crystal and in a QW is derived.

Principally, an exciton is primarily determined by the product of the electron (e) and hole (h) wave functions as well as the envelope function (env), which describes the relative motion of both charges. Its respective symmetry results from the direct product of the individual symmetries. In this regard, the envelope function of the ground state transforms like Γ_1. [67] For instance, in the bulk zinc-blende crystal with T_d crystal symmetry (see Fig. 2.4 (a)), the exciton is formed out of an electron in the Γ_6 conduction band and the hole in the Γ_8 valence band. Hence, its respective symmetry is given by:

$$\Gamma_{\mathrm{Ex},\ \mathrm{T}_d} = \Gamma_\mathrm{e} \otimes \Gamma_\mathrm{h} \otimes \Gamma_\mathrm{env} = \Gamma_6 \otimes \Gamma_8 \otimes \Gamma_1 = \Gamma_3 + \Gamma_4 + \Gamma_5. \tag{2.53}$$

[††]In particle physics, a gauge boson is a force carrier. This means a bosonic particle that carries any of the fundamental interactions of nature, commonly called forces.

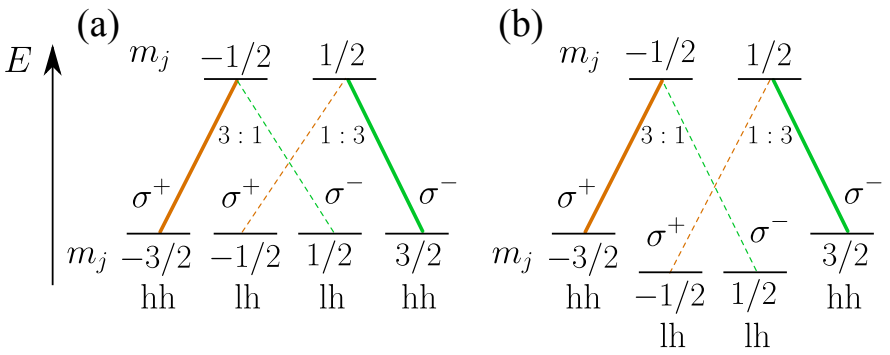

Figure 2.9: (a) Scheme of the electric dipole allowed transitions for $\vec{k} = 0$ of a bulk crystal with zinc-blende lattice. The corresponding band structure, illustrated in Fig. 2.3 (a), is characterized by the symmetry of the tetrahedral point group T_d. The different projections m_j for heavy- and light-holes result in different transition probabilities, denoted by the ratio 3 : 1, for the conduction band states for right-(σ^+) and left-handed(σ^-) circularly polarized light. The polarization of light is further denoted by orange (σ^+) and green (σ^-) lines. (b) Scheme of the optical selection rules of a two-dimensional QW structure, belonging to the D_{s2} point group (see Fig. 2.3 (b)). The confinement in the QW lifts the light- and heavy-hole degeneracy, and, thus, the light hole states are lower in energy than the heavy hole states at the Γ-point. The images are adapted from Ref. [39].

Within the three states, only the Γ_5-state can be reached from the ground state by an electric dipole transition. The Γ_3- and Γ_4-states with parallel electron and hole spins are dipole forbidden.

In the case of a QW structures with $D_{2\mathrm{d}}$ point group symmetry, the ground state heavy- and light hole excitons have multiplicities $\Gamma_1 \otimes \Gamma_2 \otimes \Gamma_5$ and $\Gamma_3 \otimes \Gamma_4 \otimes \Gamma_5$, respectively. In this case, the optically active states are the twofold degenerate Γ_5-state and the nondegenerate Γ_4-state. In the $D_{2\mathrm{d}}$ symmetry the transition to the doublet state Γ_5 is dipole allowed for the electric field vector perpendicular to the growth axis of the QW, while the singlet levels Γ_1 and Γ_2 as well as Γ_3 are dipole forbidden.[135]

Taking into account the quantum numbers of the involved states, the optical selection rules, and the band structure of the crystal, the scheme of dipole-allowed transitions can be determined. The dipole allowed transitions in a bulk and QW structure are schematically illustrated in the Figs. 2.9 (a) and (b).

In bulk and QW structures, the absorption of σ^+ polarized light can either lead to a transition between the $m_j = 3/2$ heavy-hole state and the $m_j = -1/2$ electron state or the $m_j = 1/2$ light-hole state and the $m_j = 1/2$ electron state. When the excitation has the opposite polarization σ^-, the signs of the total angular momentum m_j are reversed. The transitions occur with a probability of 3 : 1, indicated by the thickness of the respective lines in the Figs. 2.9 (a) and (b). In the case of a zinc-blende bulk crystal with T_d crystal symmetry the light- and heavy-hole states are not split at the

Γ-point. However, the situation changes for two-dimensional QWs, which belong to the D_{2d} point group. In these, the confinement and strain lifts the heavy- and light-hole degeneracy at the Γ-point, so that $\Delta E_{\text{hh-lh}} > 0$. Hence, the light-hole states have a lower energy than the heavy-hole states.[67,136]

As described above, electron and hole bind to form an exciton through their mutual Coulomb interaction. Due to their exchange interaction, which couples the spins of the electron and hole, the exciton fine structure at zero magnetic field arises. Description of this interaction yields the Heisenberg model.[137] Disregarding the light-hole states in the following, a comprising spin Hamiltonian describing the electron-hole exchange interaction of an exciton consisting of one electron with the possible spin states $j_e = \pm 1/2$ and one heavy-hole with $j_{hh} = \pm 3/2$ is given by[136]:

$$H_{\text{exchange}} = -\sum_{i=x,y,z} (a_i J_{h,i} S_{e,i} + b_i J_{h,i}^3 S_{e,i}). \tag{2.54}$$

Here, $S_{e,i}$ and $J_{h,i}$ ($i = x,y,z$) describe the electron and heavy-hole spin operators, and a_i and b_i denote the dimension of the nanostructure, and, thus, giving rise to a decrease of the crystal symmetry. From the single-particle states, four possible combinations of excitons can be formed. These states are characterized by their angular momentum projections $M_i = S_{e,i} + J_{h,i}$. Since the optical selection rules do only allow transitions with $\Delta m = 1$, exciton states, which have an angular momentum of $|M| = 2$, cannot couple to the light field and are, therefore, optically inactive. These states are referred to as dark excitons.[136] In contrast, exciton states with $|M| = 1$, which can be excited or can recombine under the absorption or emission of a single photon, are accordingly called bright excitons.[39,136] From these considerations on the basis of Eq.(2.54) and the exciton states ($|+1\rangle, |+2\rangle, |-1\rangle, |-2\rangle$), the matrix representation of the following expression for the exchange Hamiltonian is obtained[136]:

$$H_{\text{exchange}} = \frac{1}{2}\begin{pmatrix} +\delta_0 & +\delta_1 & 0 & 0 \\ +\delta_1 & +\delta_0 & 0 & 0 \\ 0 & 0 & -\delta_0 & +\delta_2 \\ 0 & 0 & +\delta_2 & -\delta_0 \end{pmatrix}. \tag{2.55}$$

For a better overview, the abbreviations $\delta_0 = 1.5 \cdot (a_z + 2.25 b_z)$, $\delta_1 = 0.75 \cdot (b_x - b_y)$, and $\delta_2 = 0.75 \cdot (b_x + b_y)$ are introduced. The matrix has a block diagonal form, indicating that bright and dark excitons do not mix with each other and their respective energies are separated by the electron-hole exchange energy δ_0. In respect of the (In,Ga)As/GaAs QDs investigated in this thesis, the electron-hole exchange energy is estimated to be in the range of 100 μeV.[138,139]

The exchange energy in its most general form is given by[136]:

$$E_{\text{exchange}} \propto \int\int d^3r_1 d^3r_2 \, \psi_X^*(r_e = r_1, r_h = r_2) \times \frac{1}{|r_1 - r_2|} \psi_X(r_e = r_2, r_h = r_1), \tag{2.56}$$

with the exciton wave function ψ_{X} and the electron and hole coordinates $\vec{r}_{\mathrm{eh}}$. The exchange energy comprises two parts, the short-ranged part, which describes the splitting of the exciton multiplet into bright and dark pairs of states, and the long-ranged part, which on one hand contributes to the splitting of the bright and dark excitons and on the other hand induces a fine structure splitting of the bright excitons in transverse and longitudinal components in structures with lower symmetry than $D_{2\mathrm{d}}$.[136] The latter has no influence on the dark exciton states.

The concluding remarks of this subsection deal briefly with the possible mechanisms of exciton relaxation and recombination. As described above, after the absorption of a photon an electron-hole pair is created within the conduction and valence bands. If the energy of this photon is greater than the energy of the semiconductor ground state, a hot exciton is formed, in which the electron and the hole occupy excited states. After the excitation process the single-particles relax within less than a 1 ps into their respective ground states by means of a cascade of intraband non-radiative relaxation steps. The excess energy is transferred to the crystal lattice, e.g. by coupling to phonons, i.e. lattice vibrations, of suitable energy. It is important to note that optical selection rules do not constrain this relaxation processes.

Once electron and hole reached the ground state of the semiconductor, further relaxation can take place by radiative electron-hole recombination. In this case the electron returns to the valence band, releasing its excess energy through the emission of a photon. For instance in (In,Ga)As/GaAs QDs, the emission spectra comprises well-defined peaks in the region of the lowest energy absorption transitions.[139] Moreover, a careful analysis of the peak widths allows one to primarily determine the size and shape of the QD ensembles as these fundamentally affect the emission spectra. As with absorption, the optical selection rules also apply to the recombination of electron-hole pairs. In low-dimensional nanostructures this is referred to as spontaneous emission. The radiative decay rate Γ_{rad} for spontaneous emission deduced from Fermi's Golden Rule reads[17,39]:

$$\Gamma_{\mathrm{rad}}(\omega) = \frac{\omega_f^3\, n\, |M_{if}|^2}{3\,\pi\, \text{œ}_0\, \hbar c^3}. \tag{2.57}$$

Here, n is the refractive index, $\text{œ}_0 = \epsilon_0$ is the permittivity of free space, c is the speed of light, and ω_f is the frequency of the outgoing photon. As can be deduced from this relation, the rate of spontaneous emission does not only dependent on the magnitude of the transition dipole moment M_{if}, which is proportional to the oscillator strength (see Sec. 2.1.3), but also on the density of optical modes that can couple to the transition.

An alternative pathway of recombination of two charge carriers is the non-radiative energy transfer between, for example, two QDs. This process, which bases on dipole-dipole interaction, is called resonant exciton energy transfer (ET).[140] Instead of emitting a photon like in the radiative recombination of the carriers, here, the oscillating dipole in one QD induces the oscillation of a dipole in another QD. This process is equivalent to a physical displacement of an exciton between neighbouring QDs. How-

ever, for this excitation to be possible the distance between the two interacting QDs must be sufficiently small and moreover a spectral overlap must be present. The interaction between two magnetic dipoles μ_1 and μ_2 separated by $r = |\vec{r}|$ is defined by the energy that the system has respective to the values of the separation of the dipoles and the angle that the dipoles make. The energy of the magnetic dipolar interaction is given by:

$$E = \frac{\mu_0}{4\pi r^3} \cdot [\boldsymbol{\mu}_1 \cdot \boldsymbol{\mu}_2 - \frac{3}{r^2}(\boldsymbol{\mu}_1 \cdot \boldsymbol{r})(\boldsymbol{\mu}_2 \cdot \boldsymbol{r})]. \tag{2.58}$$

The respective total energy transfer rate (Γ_{ET}), derived by Förster[141], between the two oscillating dipoles μ_1 and μ_2 is expressed by:

$$\Gamma_{\mathrm{ET}} = \frac{2\pi}{\hbar} \frac{\mu_1^2 \mu_2^2 \kappa^2}{r^6 n^4} \Theta. \tag{2.59}$$

Here n is the refractive index, $\Theta = \int \chi_1(\lambda)\chi_2(\lambda)\mathrm{d}\lambda$ represents the spectral overlap of the emission ($\chi_1(\lambda)$) and absorption ($\chi_2(\lambda)$) spectra of the two QDs, and κ denotes the orientational average of the dipoles, which is 2/3 for quantum dots, assuming that the dipoles are randomly oriented.

In fact, the long-range interaction of magnetic moments is dominated by the exchange interaction between electron spin and crystal anisotropy, which is based upon the spin-orbit interaction. In this respect the magnetic dipole-dipole interaction is by a factor of 10^{-3} weaker and can be neglected.[39]

2.3 Diluted magnetic semiconductors: characteristics and optical properties

One focus of this thesis is the study of Diluted Magnetic Semiconductors (DMS), a new class of magnetic materials that fills the gap between ferromagnets and semiconductors.[39] In general, DMS's are semiconducting alloys ($\mathrm{A}^{II}_{1-x}\mathrm{M}_x\mathrm{B}^{IV}$) in which the fraction x of the semiconductor crystal lattice is partially and randomly occupied by magnetic transition metal ions, thereby introducing magnetic properties into the host semiconductor AB. Among the principal DMS families, II–VI semiconductors, with Mn^{2+} as the magnetic impurity, are the best-known examples of such alloys (e.g. $Zn_{1-x}Mn_xSe$, $Zn_{1-x}Mn_xTe$ or $Cd_{1-x}Mn_xTe$). In contrast to typical ferromagnetic materials, DMS exhibiting semiconductor-like transport properties, retaining most of its classical semiconducting properties. The presence of randomly distributed localized magnetic ions leads to an exchange interactions between the *sp* band electrons and the $3d$ Mn^{2+} electrons, resulting in novel, important magnetic effects, e.g. extremely large Zeeman splittings of electronic levels, the formation of spin-glass-like phase at low temperature[142] and magnetic-field-induced metal–insulator transitions. These properties, which occur solely in DMS systems, are extensively described in literature.[143–145] In

particular, they demonstrate great potential for efficient spin injection and magnetization manipulation by electrical and optical methods.[142]

To facilitate the presentation and understanding of the results devoted towards the II-VI diluted magnetic quantum well structures (Cd,Mn)Te and (Zn,Mn)Se, discussed in part III, in what follows a brief overview about the structural, electronic and magnetic properties of DMS as well as related interactions will be provided. In this respect, the first Sec.2.3.1 focuses on the crystal structure as well as on the calculation of electronic states of the binary II-VI semiconductors. In the following section the effects of incorporated manganese ions, especially of the Mn 3*d*-electrons, on the electronic states are addressed with particular reference to the half-filled Mn $3d^5$-shells. By introducing Mn ions to the semicconductor, localized spins and magnetic moments are simultaneously integrated into the crystal. These spins of the semi-filled *d*-shell of Mn ions cause two types of interactions: On one hand the strong Kondo-like *sp*-*d*-exchange interaction between the band electron spins and the localized moments of the magnetic ions, which significantly influences the electronic properties, and on the other hand the Heisenberg inter-ion *d*-*d*-exchange interaction, which affects the static and dynamic magnetic properties. These exchange interactions and the magnetic properties of DMS are discussed in more detail in Sec. 2.3.3. A direct consequence of the strong *sp*-*d*-exchange interaction between the magnetic ion spins and the carrier spins, is the induction of an extraordinarily large spin splitting in the conduction and valence band. This unique feature in a DMS is the so-called giant Zeeman effect. It is described in more detail in Sec.2.3.4. The last Sec. 2.3.5 addresses the heating effect of the Mn spin system, facilitated, e.g. by photoexcited carriers. The heating effect causes a suppression of the giant Zeeman splitting, due to elevation of the magnetic ions spin temperature.

2.3.1 Crystal and band structure of (Cd,Mn)Te and (Zn,Mn)Se

Solids in crystalline phase have a spatial symmetry, which results from the continuous arrangement of the atoms in the crystal lattice. As discussed in Sec. 2.1.1, the crystallographic symmetry is closely related to the electronic band structure, which mainly defines the optical properties of a semiconductor. The materials studied in this thesis are the II-VI diluted magnetic quantum well structures (Cd,Mn)Te and (Zn,Mn)Se. This DMS's have the tendency to crystallize in a hexagonal wurtzite or cubic zincblende structure.[146] The type structure depends on different conditions, which are discussed in more detail next.

In the ternary compounds $Zn_{1-x}Mn_xSe$, $Zn_{1-x}Mn_xTe$, $Cd_{1-x}Mn_xSe$, and $Cd_{1-x}Mn_xTe$ a small amount of the Zn^{2+}-ions and Cd^{2+}-ions is exchanged by likewise bivalent Mn^{2+}-ions. Despite maintaining the crystallographic structure of the semiconductor during the replacement of a few to several atomic per cent of the cations, the lattice constant is altered. Therefore, the crystallographic structure depends mainly on the exchanged amount of cations. In the special case of $Zn_{1-x}Mn_xSe$, the crystal

structure even transforms from cubic zinc-blende to a hexagonal wurtzite, when the concentration of cations exceeds $x = 0.3$. To provide a better overview, the composition ranges and the corresponding crystal structure are summarized in Tab.2.1. For very high concentrations ($x > 0.57$), a mixture of wurtzite and rocksalt structures is observed in $Zn_{1-x}Mn_xSe$.[147] In the case of $Cd_{1-x}Mn_xTe$ a zinc-blende structure is maintained up to maximum Mn-concentration of about $x = 0.77$.[148] A pure MnTe bulk material has a NiAs structure.[149] However, the main focus of this thesis is on the investigation of DMS with low Mn-concentrations of up to $x = 0.03$. In this region, the (Cd,Mn)Te and the (Zn,Mn)Se compound-semiconductors have a zinc-blende crystal structure, as shown in Fig. 2.10.

The zinc-blende crystal consists of two face-centered-cubic (fcc) lattices, with two atoms at each lattice site. The two fcc lattices are displaced relative to each other by one quarter of the body diagonal along the [111] direction. Moreover, each atom is surrounded by four nearest neighbors, thus, forming a tetrahedron. In this composition, each cation has four nearest neighbour anions at a distance of $a\cdot\sqrt{3}/4$ and twelve nearest neighbour cations at a distance of $a \cdot \sqrt{2}/2$, with a describing the lattice constant. For instance, in ZnSe the lattice constant constitutes 5.668 Å[150,151] and in CdTe 6.487 Å.[151] The lattice constant of ternary materials a_t can be calculated by Vegard's law[152]

$$a_t = (1 - x) \cdot a_1 + x \cdot a_2, \tag{2.60}$$

as linear interpolation between values of the corresponding binary semiconductors a_1 and a_2. However, it is more convenient for general characterization to calculate the mean cation distance $d(x) = \sqrt{2}a$.[143] The corresponding cation distances as a function of the Mn-concentration x are listed in Tab. 2.1.

Important conclusions regarding physical and chemical properties of zinc-blende crystals can be derived from their symmetry. The space group of the zinc-blende structure is symmorphic and is denoted by T_d^2 (or $F\bar{4}3m$ in international notation). The point group symmetry operations of the zinc-blende crystal are defined with respect to the three mutually perpendicular crystallographic axes with the origin placed at one of the two atoms in the primitive unit cell. Hence, the T_d^2 point group contains 24

Compound	Crystal structure	Mn ion concentration x	$d(x)$ (Å)
$Zn_{1-x}Mn_xSe$	Zinc-blende	$0 < x < 0.3$	$4.0090 + 0.1645\,x$
	Wurtzite	$0.3 < x < 0.57$	$4.0090 + 0.1645\,x$
$Cd_{1-x}Mn_xSe$	Wurtzite	$0 < x < 0.50$	$4.296 - 0.123\,x$
$Zn_{1-x}Mn_xTe$	Zinc-blende	$0 < x < 0.86$	$4.315 + 0.168\,x$
$Cd_{1-x}Mn_xTe$	Zinc-blende	$0 < x < 0.77$	$4.587 + 0.105\,x$

Table 2.1: Crystal structure, the composition ranges, and the mean cation distance $d = \sqrt{2}a$ of different DMS ternary materials.[143,148]

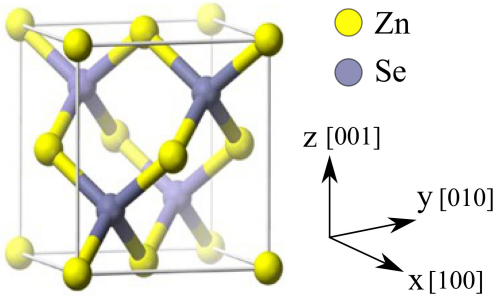

Figure 2.10: Unit cell representation of the cubic zinc-blende ZnSe crystal. The blue spheres represent the metallic Se cations and the golden spheres the semi-metalic Zn anions. The two sublattices are displaced against each other by a quarter of the space diagonal. There is no inversion centre due to point group symmetry T_d. Adapted from Ref. [153].

proper and improper symmetry-conserving rotations[‡‡]. [143] In contrast to monatomic semiconductors with a diamond structure, crystals with zinc-blende structure are not invariant under inversion with respect to the origin at an atom. Hence, the physical properties of zinc-blende crystals may depend on the direction. For this reason zinc-blende crystals are piezoelectric. [150]

In what follows, the band structure of DMS will be described in greater detail. The qualitative devolution of the band structure, which is described in depth in Sec.2.1.1 and is shown in Fig. 2.4, remains unaltered for ternary compounds like (Cd,Mn)Te or (Zn,Mn)Se, as long as the concentration of Mn^{2+}-ions is rather low. [148] Hence, zinc-blende or wurtzite semiconductors possess a direct band-gap at the Γ-point. But in addition, the *d*-states of the Mn atoms, with a more or less localized character, contribute to the total density of states. This has a direct influence on the magnetic properties of DMS, as will be elaborated in the following sections.

In a typical II-VI semiconductor like ZnSe the chemical bond takes place between the *s*-electron of the cation (Zn) and the *p*-electron of the anion (Se) of neighboring ions, i.e. sp^3 hybridisation of the electron states with four equivalent orbitals in tetrahedral order. The bond sp^3 states in the crystal constitute the valence band, while the conduction band originates from their antibonding counterpart. After replacing a cation by Mn^{2+}, the two $4s$-electrons of the iso-electronic Mn atoms start to participate in the covalent sp^3-bonding. This purely stochastic implantation affects both the symmetry of the cubic unit cell and the translation invariancy. However, the $(3d)^5$ electrons of the

[‡‡]The symmetry-conserving rotations include the identity operation $\{E\}$, the $C2$ rotation about each of the three equivalent [100] axes $\{3C_2\}$, the two $C3$ rotations about each of the four equivalent [111] axes $\{8C_3\}$, the two four-fold improper rotations about each of the three equivalent [100] axes $\{6S_4\}$, and the reflection on each of the six equivalent (110) planes $\{6\sigma_d\}$.

Mn^{2+}-ions are not influencing the band structure, but their effects superimpose on the band structure of the host semiconductor. For this reason, the semiconducting properties of DMS in zero magnetic field are almost identical to those of non-magnetic II-VI alloys. The energy of the narrow band, originating from the ground state of the $(3d)^5$ electrons, lies approximately 3.5 eV below the valence band edge (E_V).[154] The ground state of the valence band edge is an orbital singlet which is neither split by the crystal field of the semiconductor matrix nor by the spin-orbit interaction.

It is important to note that the fundamental band-gap at the Γ-point shifts with increasing Mn concentration.[30] The variation of the fundamental band-gap with the manganese content can be described by a linear dependence. Estimated by the virtual crystal approximation (VCA) the band-gap energy for a given composition reads[39]:

$$E_g(x) = (1 - x) \cdot E_g(x = 0) + x \cdot E(x = 1). \tag{2.61}$$

In regard of the ternary compounds (Cd,Mn)Te and (Zn,Mn)Se the energy gaps at liquid helium temperature ($T = 4.2$ K) are determined by:

$$\mathrm{Cd}_{1-x}\mathrm{Mn}_x\mathrm{Te} : E_g(x) = 1.606 + 1.592\,x[\mathrm{eV}]\,(x < 0.77)\,[39] \tag{2.62}$$

and

$$\mathrm{Zn}_{1-x}\mathrm{Mn}_x\mathrm{Se} : E_g(x) = 2.82 + 0.48\,x[\mathrm{eV}]\,(x < 0.3).\,[39] \tag{2.63}$$

When a magnetic field is applied, or a spontaneous magnetization appears, magnetic properties of DMS become relevant. In this respect, the *p-d* hybridization is essential, as this leads to a strong exchange interaction between holes in the valence band and Mn atoms. This exchange interaction and the positions of *d*-levels in the host band structure influence significantly the magnetic and magneto-optical properties of DMS. In general, the energy of the *d*-levels determines the energy needed to promote an electron from the occupied *d*-level to the top of the valence band.

A further significant aspect in DMS is the existence of spin-flip excitations within the Mn *d*-shell, observed at 2.2 eV and above in CdMnTe.[39] The lowest energy states of the Mn 3*d*-shell are schematically illustrated in Fig.2.11. According to HUND's rule the $(3d)^5$ manganese electrons form a ${}^6S_{5/2}$-multiplet in the ground state with $J = 5/2$, $S = 5/2$, and zero orbital angular momentum ($L = 0$).[148] The induction of a spin-flip of one *d* electron leads to an excited state of the *d*-shell with the total spin $S = 3/2$ and non-zero total angular momentum. In contrast to the expectations based on parity rule and spin conservation, optical transitions between these excited states and the ground state are electric dipole active due to the lack of inversion symmetry of the tetrahedral crystal field, described above, and the mixing of $S = 5/2$ and $S = 3/2$ states by spin-orbit interaction.[155] In Fig.2.11 the excited states are labeled by ${}^4\mathrm{P}(L = 1)$, ${}^4\mathrm{D}(L = 2)$, ${}^4\mathrm{F}(L = 3)$, and ${}^4\mathrm{G}(L = 4)$, corresponding to $S = 3/2$. The states of the free Mn atom have a degeneracy of $2L + 1$, and, thus, the ground state of the Mn-ion splits into six equidistant sublevels. The transition with the lowest energy is ${}^6\mathrm{S}\rightarrow{}^4\mathrm{G}$.

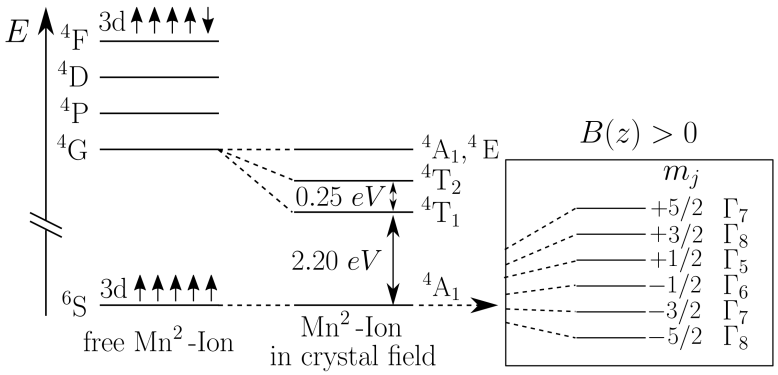

Figure 2.11: Scheme of the lowest energy states of the Mn 3d-shell. Shown are three cases: On the left the splitting of the free Mn^{2+} with spectroscopic notation $(2S+1)L$, in the middle the splitting of Mn^{2+} in crystal field (symmetry T_d), and on the right the splitting of the ground state $^4A_1$ in an external magnetic field (symmetry S_4). The internal Mn transition $^4A_1 \rightarrow ^4T_1$ amounts to 2.2 eV. Adapted from Ref. [143].

In comparison to a free Mn^{2+}-ion, the ninefold degenerated excited state ^{4}G is lifted in a cubic crystal field and splits into four levels: The $^4T_1$, the $^4T_2$, the $^4A_1$, and the ^{4}E state.[156,157] In the vicinity of a crystal field the $^4T_1$ and $^4T_2$ states are energetically lowered while the ^{4}E and $^4A_1$ coincide almost in energy, practically being unaffected by the crystal field.[158]

2.3.2 Magnetic properties of diluted magnetic semiconductors

Most magnetic properties in a solid state system emerge from the occurrence of a magnetic order. As postulated by Weiss in 1907[159], a magnetic ordering, i.e. an internal 'molecular' field, occurs, which is proportional to its magnetization, when an externally field H applied. The origin of this molecular field has been quantum-mechanically explained by Heisenberg in 1928[137], who attributed it to the exchange interaction of spins. As direct consequence of the Bohr-van-Leeuwen theorem, magnetic phenomena can only have a quantum-mechanical origin, as the magnetism of classical systems vanishes in thermal equilibrium.

The origin of magnetism in matter is to be found in the magnetic moments of electrons. These are induced by the spin and orbital angular momecntum, as is described in Sec.2.1.1. An alignment of the magnetic moments can occur either spontaneous or enforced by an external magnetic field. The spontaneous occurrence of long-range order results from the competition between the energetically favorable ideal alignment of spins, i.e. a minimum of the internal energy, and the entropically favorable overall disturbance of spins, i.e. a minimum of entropy. When the individual magnetic mo-

ments of the electrons align, due to the exchange interaction with one another, and, thus, point in the same direction, magnetic domains may form. Herein, several types of magnetic ordering can be distinguished, which can be generally classified into two groups. Firstly, the dia- and paramagnetism, which do not exhibit any long-range magnetic ordering in absence of external magnetic fields, and secondly, the ferro-, ferri- and antiferromagnetism, revealing a spontaneous long-range magnetic ordering.[155] The magnetic state of a solid state depends on several parameters, e.g. the magnetic field or the temperature. Latter is significant, because when the thermal energy is larger than the ordering energy then the material will lose its magnetic properties.

The magnetization $\vec{M}$ and the magnetic field strength $\vec{H}$ are related to another via the magnetic susceptibility $\hat{\chi}_m$:

$$\vec{M} = \hat{\chi}_m \cdot \vec{H} = (\mu_r - 1) \cdot \vec{H}, \tag{2.64}$$

where the magnetic susceptibility is defined as the difference of the relative permeability of a material μ_r and the relative permeability of vacuum ($\mu_r = 1$). The magnetic susceptibility is one measure of the magnetic properties of a material, indicating whether a material is attracted into or repelled out of a magnetic field. If $\hat{\chi}_m > 0$, the material is referred to be paramagnetic, while in the reverse case ($\hat{\chi}_m < 0$) the material is diamagnetic. Although diamagnetism is in all solid states existent, it can be observed only in atoms or ions with complete filled electron shells, since otherwise the diamagnetism would be masked by other types of magnetic ordering. Principally, the susceptibility in diamagnets is rather small ($10^{-9} < |\hat{\chi}_{\mathrm{Dia}}| < 10^{-5}$).[160]

In contrast to diamagnetism, paramagnetism refers to the magnetic state of an atom or ion with one or more unpaired electrons. In these systems uncompensated magnetic moments can occur. However, in absence of magnetic fields or long-range interactions, the magnetic moments are randomly oriented and, thus, an average macroscopic magnetic moment is not present. In the vicinity of an magnetic field the magnetic moments can align. The susceptibility in paramagnets is positive and in the order of $10^{-3} < |\hat{\chi}_{\mathrm{Para}}| < 10^{-2}$.[160] Assuming the case of noninteracting magnetic moments $\mu = -g\mu_{\mathrm{B}}J$ at low temperatures the macroscopic magnetization reads:

$$M = -n\, g\, \mu_{\mathrm{B}}\, J\, \mathfrak{B}_J \left(\frac{g\mu_{\mathrm{B}} J B}{k_{\mathrm{B}} T} \right), \tag{2.65}$$

with the Landé factor of electrons

$$g = 1 + \frac{J(J+1) + S(S+1) - L(L+1)}{2J(J+1)}, \tag{2.66}$$

the Bohr magneton μ_{B} and the Brillouin-function $\mathfrak{B}_J(x)$. The latter is determined by:

$$\mathfrak{B}_J(x) = \frac{2J+1}{2J} \coth\left(\frac{2J+1}{2J} x \right) - \frac{1}{2J} \coth\left(\frac{x}{2J} \right). \tag{2.67}$$

The magnetic properties in (Cd,Mn)Te and (Zn,Mn)Se are attributed to the parallel aligned, unpaired spins of the half-filled Mn^{2+}-ion d-shell. The spin and angular momentum of the $(3d)^5$-electrons induce a magnetic moment, which leads to a macroscopic magnetization in the presence of an external magnetic field. The total magnetization in regard of noninteracting magnetic $(3d)^5$-electron spins in a magnetic field applied along the direction $B = B_z$ is expressed by:

$$M = -n\, g_{\mathrm{Mn}}\, \mu_{\mathrm{B}}\, \langle S_z \rangle, \tag{2.68}$$

with the thermal average value of the Mn spin along the direction of magnetic field $\langle S_z \rangle$ and the number of magnetic moments $n = xN_0$ per inverse unit-cell volume N_0. The z-component of the thermal average $\langle S_z \rangle$ is determined by the Brillouin function $\mathfrak{B}_{5/2}$:

$$\langle S_z \rangle = -\frac{5}{2}\, \mathfrak{B}_{5/2} \left(\frac{5\, g\, \mu_{\mathrm{B}}\, B}{2\, k_{\mathrm{B}}\, T_{\mathrm{Mn}}} \right). \tag{2.69}$$

Here, T_{Mn} is the manganese spin temperature, which is equal to the lattice temperature in equilibrium condition. According to literature the Mn Landé factor constitutes $g_{\mathrm{Mn}} \approx 2$.[155]

2.3.3 Exchange interactions in DMS

Since the early stage, paramagnetic II–VI DMSs[145,148,157,161] have been studied extensively, as they exhibit the peculiarity of two types of exchange interactions associated with the presence of the magnetic ions in the lattice. On the one hand, there is the antiferromagnetic superexchange coupling among Mn ions (d-d-exchange interaction), due to which most of II–VI DMS's reveal a spin-glass phase[162] or antiferromagnetic phase at low temperatures, and on the other hand, there is the strong spin-dependent coupling (sp-d exchange interaction) between the delocalized s- and p-orbitals of the band electrons and the localized d-electrons of the Mn^{2+}-ions. The sp-d exchange interaction is mainly responsible for the enhanced magneto-optical properties of DMS. In the following, the two types of interactions are discussed, with particular regard to exchange interactions at the Brillouin zone center, as most optical transitions involve the direct energy gap of the semiconductor.

2.3.3.1 sp-d Exchange interactions

A simple example of a direct exchange interaction is the s-d exchange interaction. Due to the Pauli exclusion principle, which states that two fermions are forbidden entering the same quantum state, electrons with the same spin orientation avoid each other, in result reducing their Coulomb interaction energy. When the electrons have opposite half-integer spin projections and their total wave function antisymmetric, then they can

occupy the same orbital and, therefore, approach each other. From this one can draw the conclusion that the *s-d* exchange interaction is ferromagnetic and is most effective on the short range because it only occurs when the *s* and *d* orbitals overlap.

One of the most important features of DMS is the strong exchange interaction between the localized $3d$-electrons of the Mn^{2+}-ions and the delocalized *p*-like valence band electrons. When the $3d$-electron levels are found within the valence band, as it is the case in II-VI based DMS, due to *p-d* hybridization the additional exchange interaction mechanism called kinetic exchange arises.[163] Kinetic exchange may be viewed as a second-order perturbation-theory effect involving virtual transitions of an electron between the band states and the ionic orbitals. This interaction is called the *p-d* exchange interaction. Theoretical models describing this exchange mechanism are presented in several theoretical papers for the most extensively studied Mn based DMS's as well as other transition metal based materials.[148,155,164,165]

The contribution of both the *s-d* and *p-d* exchange interaction to the band structure can be expressed by the Kondo-like exchange Hamiltonian[148]

$$\hat{H}_{sp\text{-}d} = \sum_{\vec{R}} \left[\hat{J}_{sp\text{-}d}(\vec{r} - \vec{R}_i) \right] \vec{S}_i \cdot \vec{J}, \tag{2.70}$$

where $\hat{J}_{sp\text{-}d}$ designates the positive exchange coupling integral, $\vec{J}$ and $\vec{r}$ are the spin and coordinate of the carrier, and $\vec{S}_i$ and $\vec{R}_i$ are the spin and position of the magnetic impurity. The summation is over all lattice sites occupied by Mn^{2+}-ions. Hence, it follows for the total Hamiltonian H_T, which formally describes a semiconductor containing localized magnetic moments:

$$\hat{H}_T = \hat{H}_0 + \hat{H}_{sp\text{-}d}, \tag{2.71}$$

with $\hat{H}_0$ defining the effective electron Hamiltonian (see. Eq.(2.44)), consisting of the Landau quantization as well as the intrinsic Zeeman effect.

In consideration of extremely extended wave functions of the band electrons in the lattice, which provide interaction with a large number of Mn^{2+}-ions, it is, thus, possible to average over several lattice sites. In this case the Kondo-like exchange Hamiltonian in Eq. (2.70), can be simplified by the Virtual Crystal Approximation (VCA) and the molecular field approximation (MFA). In VCA, the sum over all Mn lattice sites is replaced by a sum over all cation lattice sites and moreover, weighted by the value of the Mn-content x, which, simplified, means that $\vec{S}_i$ is replaced by $x\vec{S}$. In the MFA considers that the single spins $\vec{S}_i$ is replaced by the thermal average value $\langle \vec{S} \rangle$ taken over all Mn^{2+}-ions. Considering the VCA and the MFA the exchange Hamiltonian reads:

$$\hat{H}_{sp\text{-}d} = -x\langle \vec{S} \rangle J \sum_j \hat{J}_{sp\text{-}d}(\vec{r} - \vec{R}_j). \tag{2.72}$$

The resulting Hamiltonian has the periodicity of the lattice and allows, therefore, to use the same Bloch state wave functions as in the case of the crystal lattice Hamiltonian,

introduced in Sec.2.1.1. It follows from Eq.(2.72) that the *sp-d* exchange interactions are primaraily determined by the values of the exchange constant $\hat{J}_{sp\text{-}d}$. Thereby, two different interactions have to be distinguished at the center of the Brillouin-zone. First the interaction between the $3d$-electrons and the s-like electrons ($|S\rangle$), which belong to the Γ_6 representation and secondly, the interaction between the $3d$-electrons and the p-like electrons ($|P\rangle$), which belong to the Γ_8 representation. The *s-d* interaction is denoted by $\alpha = \langle S|J|S\rangle$, whereas The *p-d* interaction is given by $\beta = \langle P|J|P\rangle$.[148]

The matrix elements of of the exchange constant $\hat{J}_{sp\text{-}d}$, can be evaluated between the Bloch states $|\vec{k},m_s\rangle$, of the wave function $\langle\vec{r}|\vec{k}\rangle = u_{c,\vec{k}}(\vec{r})\exp(i\vec{k}\cdot\vec{r})$. This way one obtains:

$$\langle\vec{k}',m'_J|\hat{H}_{sp\text{-}d}|\vec{k},m_J\rangle = -x\sum_i J_{\vec{k}',\vec{k}}e^{i(\vec{k}-\vec{k}')\vec{R}_i}\,\langle\vec{S}\rangle\langle m'_J|J|m_J\rangle. \tag{2.73}$$

Considering a Bloch state at the bottom of the conduction band ($u_{c,0}(\vec{r})$), the exchange integral is generally denoted by $N_0\,\alpha$, which is defined by[148]:

$$N_0\,\alpha = J_{0,0} = \frac{\int|u_{c,0}(\vec{r})|^2\hat{J}_{sp\text{-}d}(\vec{r})\mathrm{d}^3r}{\int|u_{c,0}(\vec{r})|^2\mathrm{d}^3r}. \tag{2.74}$$

In general $N_0\,\alpha$ defines the magnitude of the giant Zeeman effect, which will be described in more detail in Sec.2.3.4. Neglecting any $\vec{k}$-dependance the effective *sp-d* exchange Hamiltonian simplifies to

$$\hat{H} = -\alpha\cdot x\sum_i\langle\vec{S}\rangle\cdot J\cdot\delta(\vec{r}-\vec{R}_i). \tag{2.75}$$

Next the focus is shifted towards the mechanism of kinetic exchange as it is one of the important features of DMS. Kinetic exchange can be simply understood by considering the energy levels of the hybridized $3d$-electrons of the Mn^{2+}-ion and the valence band states, under the assumption that all electron spins are fully polarized. From this it follows that close to the valence band maximum the spin up antibonding states are shifted to high energy, while spin down bonding states are shifted to low energy. In second order perturbation theory these shifts are given by

$$\partial E_\uparrow \simeq \frac{(V_{pd})^2}{\epsilon_v-\epsilon_d} \text{ and} \tag{2.76}$$

$$\partial E_\downarrow \simeq -\frac{(V_{pd})^2}{\epsilon_d+U_{\text{eff}}-\epsilon_v-}, \tag{2.77}$$

where V_{pd} is the *p-d* hybridization parameter, ϵ_v and ϵ_d are the energies of the valence band maximum and the $3d$-electron states, respectively, and U_{eff} is the intra d-shell Coulomb energy. The *p-d* exchange integral is defined by the energy difference between spin up and spin down states: $-N_0\beta S = \partial E_\uparrow - \partial E_\downarrow$. A parametrization of the *p-d* hybridization mechanism can be, thus, achieved by the Schrieffer-Wolff expression:

$$N_0\beta \simeq -\frac{(4V_{pd})^2}{S}\left[\frac{1}{\epsilon_v-\epsilon_d}+\frac{1}{\epsilon_d+U_{\text{eff}}-\epsilon_v-}\right]. \tag{2.78}$$

The exchange integral values for α and β in (Cd,Mn)Te and (Zn,Mn)Se can be experimentally determined, e.g. by magneto photoluminescence (PL) and magneto Raman measurements, by comparison of magnetization and optical measurements of the Zeeman-splitting. The proportionality between magnetization of the Mn spins and the Zeeman shift of the excitons has been checked in previous works in various $(Zn_{1-x}Mn_x)Se$ as well as in $(Cd_{1-x}Mn_x)Te$ QW's for different Mn-concentrations, temperatures and magnetic fields.[166] Hence, the presence of both heavy-hole and light-hole excitons, which split proportionally to $N_0(\alpha - \beta)$ and $N_0(\alpha - \frac{\beta}{3})$, respectively, allowed one to determine the *s-d* exchange constants $N_0\alpha$ and $N_0\beta$. In the case of $(Zn_{1-x}Mn_xSe)$ the values of the exchange integrals amounts

$$N_0\alpha = 0.26 \text{ eV} \text{ and } N_0\beta = -1.32 \text{ eV},^{[30]} \tag{2.79}$$

and respectively, for $(Cd_{1-x},Mn_x)Te$

$$N_0\alpha = 0.22 \text{ eV} \text{ and } N_0\beta = -0.88 \text{ eV}.^{[30]} \tag{2.80}$$

Generally $N_0\alpha$ assumes a positive value in all II-VI DMS and $N_0\beta$ has a large negative value, which is proportional to N_0.

It is important to note that according to $\langle\vec{S}\rangle$ in Eq. (2.69) the energy splitting induced by *sp-d* exchange interaction is dependent on the temperature of the Mn-ion spin system. This aspect is dealt with in more detail in Sec. 2.3.5. In summary the exchange integral $\hat{J}_{sp\text{-}d}$ is determined on one hand by the direct exchange interaction induced by the 1/r-Coulomb potential among the valence band electrons and the $3d$-electrons of the Mn^{2+}-ions, resulting in a parallel (ferromagnetic) alignment of band electron spins and Mn-ion spins. On the other hand the exchange integral is affected by the kinetic exchange, originating from the hybridization of the $3d$-electrons and the p-orbital electrons. This exchange interaction leads to a antiferromagnetic alignment of the spins. In regard of the center of the Brillouin zone, *s-d* hybridization is not possible due to symmetry conditions at the Γ-point, and, thus, the conduction band splitting is only caused by the ferromagnetic direct potential exchange. This splitting is qualitatively identical to spin splittings of nonmagnetic semiconductors, which are described in detail in Sec. 2.1.1. However, since the splitting in DMS depends primarily on the properties of the magnetization the magnitude of the spin splitting scales with temperature and Mn-concentration, and, thus, becomes extremely large.[148] This effect is referred to as giant Zeeman splitting. It is further discussed in Sec. 2.3.4.

It is worthwhile to note, that in the case of an antiferromagnetic exchange interaction a qualitatively new situation can establish, especially if not all spins can be energetically aligned in the most favorable way. This phenomenon is called frustration. Considering, e.g. three spins that are inserted into a crystal lattice, only two of them can be aligned antiferromagnetically. The third will always be ferromagnetic to one of the first two. This situation favors the formation of the spin glass. In fact, the susceptibility or specific heat of diluted magnetic semiconductors is often observed to be characteristic for spin glasses.[162]

2.3.3.2 *d*-*d* Exchange interactions

The magnetic moments of localized Mn^{2+}-ions in DMS may interact not only with delocalized valence and conduction band carriers but also either indirectly or directly with one another. From the theoretical side the question of the inter-ion exchange interaction has been addressed by Larson et al.[167], who has shown that in typical DMS materials the dominating exchange coupling is that of superexchange, which is proportional to *p*-*d* hybridization.[168] In contrast to typical transition metals, where the overlap between *d*-orbitals is large and, thus, leads to the formation of *d*-bands, direct exchange interactions between Mn atoms in DMS are negligible, since their *d*-orbitals do not overlap. The effective spin Hamilton-Operator, which takes the *d*-*d* exchange interaction into account is given by:

$$\hat{H}_{d\text{-}d} = -\sum_{i\neq j}\sum_{\alpha,\beta} \vec{S}_{i,\alpha} \vec{J}^{d\text{-}d}_{\alpha,\beta}(\vec{R}_{ij}) \vec{S}_{j,\beta}. \tag{2.81}$$

Here, $\vec{J}^{d\text{-}d}_{\alpha,\beta}(\vec{R}_{ij})$ is the exchange coupling tensor and $\vec{R}_{ij} = \vec{R}_i - \vec{R}_j$ is the distance between the spins $\vec{S}_{i,\alpha}$ and $\vec{S}_{j,\beta}$ of the Mn spin i at the coordinate $\vec{R}_i$ and the Mn spin j at the coordinate $\vec{R}_j$, respectively. The Hamilton comprises three parts, which describe the isotropic exchange interaction, the Dzyaloshinsky-Moriya exchange interaction, and the pseudo-dipolar (PD) interaction.

The most important part of this exchange coupling, is the isotropic exchange term, which is described by the Heisenberg-Hamilton operator[167]:

$$\hat{H}_{\mathrm{H}} = -\sum_{i\neq j} J^{d\text{-}d}(\vec{R}_{ij}) \vec{S}_i \vec{S}_j. \tag{2.82}$$

Here, the coupling constant $J^{d\text{-}d}(\vec{R}_{ij})$ of the *d*-*d* exchange interaction, denotes the overlap of the wave functions of both interacting spins. The Heisenberg superexchange relies on coupling of two adjacent Mn-ions by virtual hopping-processes via the $4p$-orbitals of intermediate anions. Following from literature[168], superexchange is a consequence of kinetic exchange, which is, as described above, the determining factor that leads to antiferromagnetic coupling between local spins. The superexchange coupling parameter can be obtained in second order of perturbation as $J^{d\text{-}d} \sim \partial E_{\downarrow\uparrow} = -b^2/U_{\mathrm{eff}}$, where b defines the hopping integral between the Mn atoms and U_{eff} is the intra *d*-shell Coulomb energy.

In magnetically ordered systems the Dzyaloshinskii-Moriya interaction favors a rotation of otherwise (anti)parallel aligned magnetic moments. It can be seen as the source of weak ferromagnetic behavior in an antiferromagnet. The Dzyaloshinsky-Moriya exchange interaction for two adjacent Mn-ions is determined by:

$$\hat{H}_{\mathrm{DM}} = -\sum_{i\neq j} \vec{D}_{ij}(\vec{R}_{ij})(\vec{S}_i \times \vec{S}_j). \tag{2.83}$$

Here, the Dzyaloshinsky-Moriya vector $\vec{D}_{ij}(\vec{R}_{ij})$ is perpendicular to the plane, which is spanned by two Mn-ions. Finally, the Hamiltonian of the pseudo-dipolar interaction is given by:

$$\hat{H}_{\mathrm{PD}} = \hat{H}_{d\text{-}d} - \hat{H}_{\mathrm{H}} - \hat{H}_{\mathrm{DM}}. \tag{2.84}$$

In general, the accepted terminology distinguishes between two interactions: On one hand, the indirect exchange, which is mediated by the polarization of the intervening medium, and on the other hand the superexchange, which is due to covalent mixing of magnetic (d) and non magnetic (s-p) orbitals. This two categories include four main mechanisms leading to inter-ion exchange interactions. Firstly, the Bloembergen-Rowland interaction, which implies a virtual excitation of conduction pairs of holes and electrons.[167,168] Secondly, the Ruderman-Kittel-Kasuya-Yosida interaction (RKKY), which refers to a coupling mechanism of localized inner d-shell electron spins by means of an interaction through the conduction electrons.[39,169] This interaction becomes efficient when a high density of free carriers is present in the sample. Thirdly, the double exchange, which proceeds via virtual hopping of a d-electron from one Mn-ion to another. The gain in kinetic energy is simply given by the hopping integral b, which is described above.[39,170] And finally, the superexchange, which is most dominantly in Mn-based II-VI DMS. A more detailed overview on different exchange interactions in DMS is provided in Ref. [170] and [39].

2.3.4 Magneto-optical properties of DMS

As outlined in the previous sections, the magnetic properties of DMS are governed primarily by the sp-d exchange interaction, i.e. the interaction between the valence band electrons and the $3d$-electrons of the Mn^{2+}-ions, as well as by the inter-ion exchange interactions. In this respect, the probability of exchange interactions depends significantly on the number of Mn-ions embedded in the semiconductor as well as the temperature. In particular, for higher concentrations, where the d-d exchange interaction prevails, the magnetization cannot be expressed by the standard Brillouin-function any longer, even though the behavior of the magnetization versus magnetic field strength is qualitatively similar. To include the aforementioned effects, the two empirical parameters S_{eff} and T_0 are introduced, in order to modify the Brillouin-function in Eq.(2.67)[171]:

$$\langle S_z \rangle = -S_{\mathrm{eff}}\, \mathfrak{B}_S \left(\frac{g\mu_{\mathrm{B}}\, S_{\mathrm{eff}}\, B}{k_{\mathrm{B}}(T_0 + T_{\mathrm{Mn}})} \right). \tag{2.85}$$

Here, S_{eff} is referred to as the effective spin ($S_{\mathrm{eff}} < S$) and T_0 is called the antiferromagnetic temperature ($T_0 \geq 0$). In the case of small Mn-concentrations these parameters can be physically interpreted. Hence, $n \cdot S_{\mathrm{eff}}$ describes the saturation magnetization of antiferromagneticly aligned spins of nearest-neighbor Mn-spins and T_0 defines the antiferromagnetic temperature, which is a measure of the long-range interaction, acting

against this alignment. It is important to note further, that the spin value $S = 5/2$ for the Mn^{2+}-ion spin is only valid for isolated spins.

One of the key features in diluted magnetic semiconductors is the giant Zeeman effect. It results directly from the *s/p-d* exchange interactions, which are described in the previous section 2.3.3. To determine the spin splitting of the conduction band arising from the giant Zeeman effect the exception value of the effective *s-d* exchange Hamiltonian (Eq. (2.75)) has to be calculated. By means of this approach one obtains a spin splitting which equals $\alpha\langle\sum_i S_i\delta(\boldsymbol{r}-\boldsymbol{R}_i)\rangle$. The average over all spins S_i of the magnetic impurities epitomizes the definition of the magnetization of the Mn spins. This expression demonstrates that the bands split proportionally to the Mn magnetization.

For a general case of a parabolic conduction band, the eigenenergies of the electrons in the lth Landau level obtained from solving the effective electron Hamiltonian (see Eq.(2.44)) are expressed by [39]:

$$E_l(m_s) = E_g + E_{\text{Landau}}(l) + E_{\text{Zeeman}}(m_s) + E_{\text{giantZeeman}}(m_s) \tag{2.86}$$

$$= E_g + \hbar\omega_c(l+\frac{1}{2}) + m_s(g_e\mu_{\text{B}}B - xN_0\alpha\langle S_z\rangle), \tag{2.87}$$

where $l \in \mathbb{N} = \{0,1,2\ldots\}$ is the Landau quantum number, $m_s = \pm 1/2$ is the z-component of the electron spin, ω_c is the cyclotron frequency, and g_e is the electron Landé factor. A More convenient way to express the eigenenergies $E_l(m_s)$ is in terms of an effective g-factor including the *sp-d* exchange effect [39]:

$$E_l(m_s) = E_g + \hbar\omega_c(l+\frac{1}{2}) + m_s g_e^{\text{eff}}\mu_{\text{B}},B \tag{2.88}$$

where the effective g-factor is defined as [39]:

$$g_e^{\text{eff}} = g_e - xN_0\alpha\frac{\langle S_z\rangle}{\mu_{\text{B}}B}. \tag{2.89}$$

In general, the effective Landé factor g_e^{eff} in II–VI DMSs is of the order of unity and the corresponding effective masses m_e^{eff} are large. Hence, the splitting due to the *sp-d* exchange interaction ($\hat{H}_{sp\text{-}d}$) is much greater than the ordinary Zeeman splitting of the *sp*-band ($m_s(g_e\mu_{\text{B}}B)$ and also the orbital Landau splitting ($\hbar\omega_c(l+\frac{1}{2})$). Most significance for small Mn-ion concentrations is attributable to the Landau splitting $E_{\text{Landau}} = \hbar\omega_c^e(l+\frac{1}{2}) - \hbar\omega_c^{hh}(l+\frac{1}{2})$, whereas for high Mn-concentrations ($x > 0.02$) the giant Zeeman-splitting contribution $E_{\text{giantZeeman}} = xN_0\langle S_z\rangle(m_s\alpha - 1/3m_j\beta)$ is dominant.

To evaluate the average of the splitting theoretically for light and heavy-hole excitons and, furthermore, to distinguish the Mn temperature of the Mn spins, the virtual-crystal field approximation over the Zn and Mn distribution and a mean-field approximation for the Mn spins is used. [172] In this way the energy of QW heavy-hole excitons

with the total spin ±1 can be described by

$$E^{\pm 1}_{\text{hh-X}}(B) = E_{\text{hh-X}}(B=0) \pm \frac{1}{2}(\delta_e \alpha - \delta_h \beta) N_0 x \langle S_z \rangle, \tag{2.90}$$

and for the light-hole excitons by

$$E^{\pm 1}_{\text{lh-X}}(B) = E_{\text{lh-X}}(B=0) \mp \frac{1}{2}(\delta_e \alpha - \delta_h \frac{\beta}{3}) N_0 x \langle S_z \rangle. \tag{2.91}$$

Here α and β are the exchange constants for conduction and valence bands, respectively, N_0 is the inverse unit-cell volume and $\langle S_z \rangle$ is the thermal average of the Mn spins given by the modified Brillouin function along the magnetic field direction z. The parameters δ_e and δ_h account for the leakage of the electron and hole wave functions into the nonmagnetic barriers. In regard of the $(Zn_{1-x}/Mn_x)Se/(Zn,Be)Se$ heterostructures, which have been investigated in this work, approximately 96% ($\delta_e = \delta_h = 0.96$) of the carrier wave functions are localized in the DMS layers of the QW's.[30,173] This value is calculated from the electron and hole envelope wave function, with a valence-band offset of $Q_V = 0.22$.[173] For DMS structures with a Mn mole fraction x of up to 0.02, the thermal average of the Mn spins $\langle S_z \rangle$ can be well described by the modified Brillouin-function $\mathfrak{B}_S$ (see Eq.(2.85)).

It follows from the linear relationship between Zeeman-splitting and magnetization in terms of $\langle S_z \rangle$ in the Eqs.(2.75) and (2.88) that the Zeeman-splitting closely resembles the magnetization of a paramagnet. Due to the decisive influence of $\langle S_z \rangle$, the giant Zeeman-splitting is non-linear in B and, moreover, strongly depends on the temperature of the spin system $T_{\text{eff}} = T_0 + T_{\text{Mn}}$ (see Eq.(2.85)). Due to the inverse proportionality of the effective temperature and the eigenenergies $E_l(m_s)$, already a slight increase in spin temperature leads to a reduction of the giant Zeeman splitting. The suppression of the giant Zeeman splitting of excitonic states due to an elevated spin temperature of the magnetic ions has also been experimentally observed in photoluminescence and reflectivity spectra by D. Keller[30] and B. König[29]. The temperature related effects in DMS are in the focus of the next section.

2.3.5 Heating of the magnetic ion system

As described above elevated spin temperatures cause a suppression of the giant Zeeman splitting. This heating effect of the Mn spin system can also be facilitated by additional photoexcited carriers. This has been described in the publications by D. Keller[30] and B. König[29] for DMS structures with and without two-dimensional electron gas (2DEG). The heating effect is a peculiarity of DMS and has a significant influence on the magnetic and optical properties of DMS's. In the papers addressing this issue it is shown that the system of free carriers plays an important role in the energy transfer between the phonons and the magnetic ions.[29] The key aspects of the exchange interactions

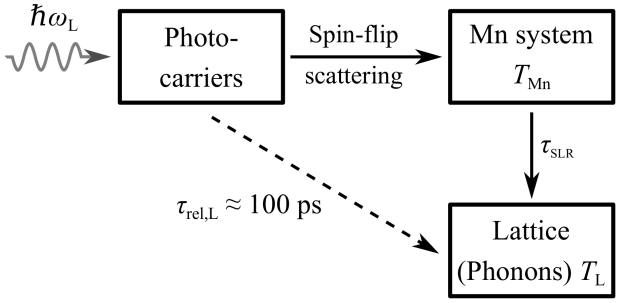

Figure 2.12: Scheme of the energy reservoirs that participate in the Mn system heating process. Relaxation channels responsible for the heating of the Mn spin system are denoted by arrows. Photocarriers transfer their excess energy ($\hbar\omega_L$) to the electron and to the phonon system. The spin-lattice relaxation time is denoted by τ_{SLR}. Less effective channels for the energy transfer from the photocarriers to the Mn spin system are shown by dotted arrows. Adapted from Ref. [30].

between the energy reservoirs of the DMS heterostructures, which participate in the Mn heating process are described briefly in the following.

It is assumed in literature that DMS have primarily three interacting systems characterized by its own heat capacity, its total angular momentum and temperature [29,30]. Those systems are the (i) phonon system (i.e., lattice phonons), (ii) the magnetic ion system and (iii) the photoexcited carriers. Between these energy reservoirs an exchange of energy and magnetic momentums occurs. The relations between the three systems are illustrated schematically in Fig. 2.12.

The photocarriers which are generated by optical excitation ($\hbar\omega_{\mathrm{L}}$) of the DMS are characterized by an excess energy and a finite lifetime caused by diverse recombination processes. As shown in the scheme they can transfer their energy on two possible routes into the magnetic system. Either indirectly through the phonon system or directly in the form of spin-flip exchange scattering. The first possibility requires a strong coupling between the phonons and the magnetic system. Its decisive in DMS with large concentration of magnetic ions ($x > 0.05$), but inefficient in very dilute systems ($x < 0.01$) due to isolated Mn ions and, therefore, a low spin-lattice relaxation rate (τ_{SLR}). [30] However, the coupling between the lattice phonons and the Mn system can be increased by several orders of magnitude when there is a formation of magnetic ion clusters. [174] In the case of spin-flip exchange scattering, the excess energy and momentum of the photocarriers is transferred directly through coupling to the magnetic ions elevating its spin temperature. [29] This mechanism has been investigated by different approaches, e.g. by time-resolved photoluminescence [175], by pump-probe techniques [176] or by optically induced magnetization, where optical pumping and superconducting quantum interference detection have been combined. [177,178]

2.4 Inelastic light scattering in low-dimensional semiconductors

In the last decade inelastic light scattering spectroscopy has developed into one of the most powerful and most widely used optical techniques for the study of the properties of elementary quantized excitations inside an optical medium. In general, under light scattering in a system, illuminated by an external source, one understands the appearance of electromagnetic waves (photons) with frequencies and/or propagation directions different from those of the initial wave.[17] In this respect, a scattering process is called inelastic when the internal state of the particles involved is changed. In bulk and low-dimensional semiconductors the light can be scattered, for instance, by free carriers, by optical phonons(Raman scattering*), by acoustic phonons (Brillouin or Mandelstam-Brillouin), or by static imperfections and inhomogeneities (Rayleigh scattering) inside the optical medium. It is important to point out that the term electrons does not only include (free) electrons and holes, but also bound excitation complexes like excitons, trions, or quasi-particles like magnons.

This section has the dual purpose of giving a description of the basic mechanisms of inelastic light scattering processes of electrons and phonons as well as that of discussing the properties of the first-order Raman scattering of collective excitations of non-magnetic semiconductors. In particular, the spin-flip Raman scattering, which forms the basis of all experiments in this thesis, is discussed in more detail.

2.4.1 The fundamentals of light scattering

To illustrate the elastic and inelastic scattering of light by means of a simple model, we consider a localized electric dipole with the moment P exposed to an external electric field $E(t)$ varying periodically in time t. The electric dipole with the eigenfrequency ω_0 satisfies the equation of motion for an externally perturbed oscillator

$$\left(\frac{\mathrm{d}^2}{\mathrm{d}t^2} + \omega_0^2\right) P(t) = \gamma(t) E_0 \cos(\omega_i t). \tag{2.92}$$

Here, ω_i and E_0 are the frequency and electric-field amplitude of the incident monochromatic light wave, and $\gamma(t)$ is a coefficient, which characterizes the interaction between the dipole and the electric field. Assuming this coefficient varies periodically in time,

*The Raman effect has been first reported by C. V. Raman and K. S. Krishnan in 1928 [179], who studied the scattering properties of different kinds of liquids by use of collimated sun light and complementary light filters. In the same year, G. Landsberg and L. Mandelstam [180], who performed scattering experiments on quartz crystals illuminated by light of a mercury lamp, independently observed the same effect, but denoted it as combinatorial scattering of light. C. V. Raman received the Nobel Prize in 1930 for his work on the inelastic light scattering from molecules.

it can be expressed by:

$$\gamma(t) = \gamma_0 + \gamma_t \cos(\Omega t), \tag{2.93}$$

with the constant coefficients γ_0 and γ_t and the modulation frequency Ω ($\Omega \ll \omega_0$). The solution of the inhomogeneous linear differential equation (2.92) with $\gamma(t)$ is given by:

$$P(t) = \frac{\gamma_0}{\omega_0^2 - \omega_i^2} E_0 \cos(\omega t) + \frac{\gamma_t}{\omega_0^2 - (\omega_i + \Omega)^2} E_0 \cos((\omega_i \pm \Omega)t). \tag{2.94}$$

The solution for the electric dipole moment $P(t)$ consists of a triple-harmonic oscillation at the initial frequency ω_i and the combinational frequencies $\omega_i \pm \Omega$. The secondary light wave with frequency ω_i is accordingly caused by elastic scattering (Rayleigh scattering), while the inelastic light scattering leads to the emission of electromagnetic waves with the modulated frequencies $\omega_i \pm \Omega$ (Raman scattering). In an optical medium, the modulation energy $E_\mathrm{A} = \hbar\Omega$ can either correspond the energy of a phonon or a single particle excitation, e.g. spin-flip processes.[17] In Fig. 2.13 (a) the Stokes process is illustrated by a Feynman diagram.

The elementary excitations resulting out of the inelastic scattering process can either be generated (Stokes process S) or annihilated (Anti-Stokes process AS). Correspondingly, the energy of the scattered light $\hbar\omega_f$ is shifted by the energy value of the elementary excitation, i.e. by the modulation energy E_A in relation to the incoming energy of the incoming electromagnetic wave $\hbar\omega_i$. In Fig. 2.13 (b) a schematic description of the Stokes transition ($\hbar\omega_f = \hbar\omega_i - \hbar\Omega$) is shown. In the case of generation and annihilation of an elementary excitation the energy and momentum are conserved:

$$\hbar\omega_f = \hbar\omega_i \pm \hbar\Omega \tag{2.95}$$

$$\vec{k}_f = \vec{k}_i + \vec{q}. \tag{2.96}$$

Here, the wave vector of the initial and scattered electromagnetic waves is denoted by $\vec{k}_i$ and $\vec{k}_f$, respectively. The wave vector of the generated or annihilated elementary excitation is denoted as $\vec{q}$. The magnitude of the scattering wave vector is determined by the scattering geometry. In this respect, the minimum value of $|\vec{k}| = k$ is obtained in forward scattering, i.e. for $\theta = 0°$, with θ defining the scattering angle. In isotropic media it is given by

$$k_\mathrm{min} = \frac{[\eta(\omega_i)\omega_i - \eta(\omega_f)\omega_f]}{c}, \tag{2.97}$$

where $\eta(\omega_i)$ and $\eta(\omega_f)$ are the refractive indices of the crystal for the incident and scattered light. The maximum value of $|\vec{k}|$ is obtained in back-scattering, i.e. for $\theta = 180°$, and is given by

$$k_\mathrm{max} = \frac{[\eta(\omega_i)\omega_i + \eta(\omega_f)\omega_f]}{c}. \tag{2.98}$$

The conservation of the wave vector is one of the most important selection rules for light scattering processes in crystals.

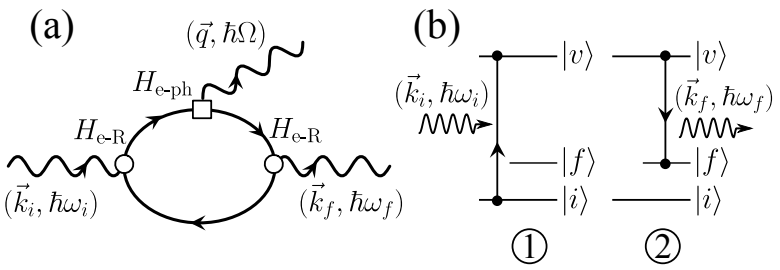

Figure 2.13: (a) Feynman diagram which describes the first-order Raman scattering by lattice vibrations involving intermediate electron-hole pair states. $H_{\text{e-R}}$ denotes the electron-photon interaction and $H_{\text{e-ph}}$ denotes the electron-phonon interaction. In the inital step a photon is absorbed, creating an electron-hole pair. In the intermediate stage the electron-hole pair changes its state via scattering with an elementary excitation. In the final step, the electron-hole pair recombines, emitting a scattered photon. (b) Schematic description of the optical transitions during the inelastic light scattering process. The numbers 1 and 2 indicate the time order of transitions. The first transition to a virtual state $|v\rangle$ is accompanied by an annihilation of a photon, whereas the second transition leads to a creation of a scattered photon. Adapted from Ref. [181].

Furthermore, it is important to point out that the wave vector of light is much smaller than the Brillouin zone boundary wave vector. Hence, first order inelastic light scattering allows only the study of excitations in the vicinity of the Γ-point.[181] This turns out to be one major limitation of inelastic light scattering spectroscopy. However, it yet enables to determine in a straightforward way the energy, lifetime and symmetry properties of elementary excitations.

Apart from the conservation of energy and momentum, which determines the relation to the homogeneity of time and space, the rotation invariance, which governs the conservation of angular momentum plays a decisive role in the inelastic scattering process. The rotation invariance arises from the isotropy of space. As described in Sec. 2.2, optical transitions in semiconductors can only occur, where the parity selection rule $\Delta l = \pm 1$ is fulfilled. However, not only optical excitations are involved in the scattering process. Hence, in what follows a total angular momentum l_m will be considered, which comprises the entity of particles participating in the scattering. From this follows for the conservation law of the angular momentum for Stokes and anti-Stokes processes:

$$l_f = l_i \pm l_m, \tag{2.99}$$

where l_i and l_f denote the angular momentum of the incident and scattered electromagnetic wave. With regard to scattering processes in which phonons and photons are involved, it is difficult in first approximation to consider the conservation of angular momentum, as phonons, which represent quantized lattice vibrations, are quasi-particles without spin. Nevertheless phonons can change the momentum $\vec{k}$ of an electron. The fact that a phonon can also transfer an orbital angular momentum of $\Delta l = 1$ has been outlined in recent studies, which investigated the angular momentum of phonons

in a magnetic crystal.[182,183] In the presence of a spin-phonon interaction, a nonzero angular momentum of phonons has been observed, which is an odd function of magnetization.[182] However, the main contribution to the phonon-assisted light scattering comes from the indirect interaction of photons with the lattice through the electron subsystem rather than from the direct photon-phonon interactions. For instance, an initially photoexcited electron can recombine with a ground state hole after the transfer of angular momentum via electron-phonon scattering.

In what follows, the focus is directed towards the light scattering, associated with the coupling of electromagnetic waves to the electric or magnetic moments of a crystal. It is well known that many optical phenomena originate due to electron-photon coupling, which is defined by the Hamiltonian:

$$H_{\text{e-R}} = -\frac{e}{c}\int \vec{j}\cdot\vec{A}\mathrm{d}^3r, \tag{2.100}$$

where $\vec{A}$ is the vector potential of light and $\vec{j}$ the electron current density operator. By first-order perturbation theory applied to Eq. (2.100), the absorption coefficient for a photon with specific frequency ω_i, wave vector $\vec{\kappa}_i$, and polarization unit vector $\vec{e}_i$ is obtained[184]:

$$I(\omega_i,\vec{\kappa}_i,\vec{e}_i) = \vec{A}\sum_{if}|\langle f|\vec{j}_{-k}\cdot\vec{e}|i\rangle|^2 2\pi\delta(E_i+\hbar\omega-E_f). \tag{2.101}$$

Here, $\vec{j}_k$ is the kth Fourier component of the current operator $\vec{j}(\vec{r})$ and the indices i and f denote the initial and final states of the system with energy E_i and E_f, respectively.

Theoretical estimates have shown that the light scattering processes associated with the magnetic moment of the crystal electronic transitions is rather weak.[181] A direct measure of the inelastic light scattering is provided by the scattering cross section ζ. The scattering cross section sets the number of scattered photons N_f in relation to the incident number of photons N_i, integrated over all directions and frequencies. However, one has to consider in experiments that only photons are detected which are scattered into a cone with a solid angle ϑ along a specified direction. Hence, the differential scattering cross section is determined by $\frac{\mathrm{d}^2\zeta}{\mathrm{d}\omega_f\mathrm{d}\vartheta}$, with the scattered frequency ω_f. The relation between the differential scattering efficiency η_s and the differential cross section ζ is defined as[17]

$$\frac{\mathrm{d}^2\eta_s}{\mathrm{d}\omega_f\mathrm{d}\vartheta} = \frac{\hbar\omega_f}{J_1 V}\frac{\mathrm{d}^2\zeta}{\mathrm{d}\omega_f\mathrm{d}\vartheta} = \frac{2\pi\omega_f}{\hbar J_1\omega_i V}|M_{if}|^2\delta(\Delta E), \tag{2.102}$$

where V is the emitting volume, M_{if} is the dipole scattering matrix element (see Eq.(2.33)), andJ_1 is the energy-flux density of the primary radiation, which is related with the mean number of initial photons N_i and the dielectric constant ε through

$$J_1 = \frac{c\hbar\omega_i}{V\sqrt{\varepsilon(\omega_i)}}N_i. \tag{2.103}$$

The δ-function in Eq. (2.102) accounts for the conservation of energy $\Delta E = E_i - E_f \pm \hbar\Omega$ in regard, of a transition between the two quantum systems $|i\rangle$ and $|f\rangle$. The respective scattering rate w_{if} between these states is defined by Fermi's golden rule [39]:

$$w_{if} = \frac{2\pi}{\hbar}|M_{if}|^2\delta(E_i - E_f \pm \hbar\Omega). \tag{2.104}$$

The spectral intensity of the scattered light I_f propagating in vacuum in a unit solid angle is directly proportional to the scattering rate: $I_f \propto w_{if}$.

In the last step, the contributions of resonant secondary emission will be discussed. This comprises the resonant photoluminescence and resonant Rayleigh scattering. In order to explore this process, a two-level system is considered, which is excited by an incident photon with specific frequency ω_i, wave vector $\vec{k}_i$, and polarization unit vector $\vec{e}_i$. This excitation leads to the formation of an electron-hole pair (exciton) with lifetime τ_f and energy $\hbar\omega_i$. In the next step, the electron and hole recombine under emission of a photon, defined by the parameters ω_f, $\vec{k}_f$ and $\vec{e}_f$. A Feynman diagram of this three-step scattering process is depicted in Fig. 2.13 (a). In this case, the intensity of the secondary emission in terms of the dipole-moment matrix element $\vec{\mathfrak{d}}_{if}$ for the optical transition between the inital and final state is determined by:

$$I_f \propto |M_{if}|^2\delta(E_f - E_i) \propto \left|\frac{(\vec{e}_f \cdot \vec{\mathfrak{d}}_{fi})(\vec{e}_i \cdot \vec{\mathfrak{d}}_{if})}{\omega_0 - \omega_i - i\Gamma}E_i\right|^2 \delta(\omega_f - \omega_i), \tag{2.105}$$

with the damping parameter Γ, which corresponds to $(2\tau_f)^{-1}$. The positive damping parameter is originally introduced, in order to damp the second order correction $M^{(2)}$ by:

$$\lim_{t\to\infty} \exp(-\Gamma t) \to 0, \tag{2.106}$$

so that convergence within the second order time-dependent perturbation theory is ensured. [185] It follows from Eq.(2.105) that the secondary emission, which can be attributed to resonant photoluminescence, depends on the incident frequency and the corresponding intensity I_f is inversely proportional to the square of ω_i. When the frequency of initial and final photon are in resonance ($\omega_i = \omega_f$), which is referred to as resonant Rayleigh scattering, the photocreated exciton and photon interact elastically. It is obvious that the spectral properties are primarily determined by the optical absorption and radiative recombination. An experimental analysis of the spectral properties, however, does not allow one to gain information about an optical medium in a direct way, as the analysis basis exclusively on the study of incident and scattered photons. In addition, it is obvious that secondary emission involves only real excited states and is moreover coherent with exciting electromagnetic wave. Finally, it is essential to emphasize that a correlation between the incident and scattered $\vec{k}$-vectors is characteristic for the resonant Raman scattering in bulk semiconductors. Considering low-dimensional quantum structures like QW or QD, due to quantum confinement effects the wave vector is no longer conserved.

2.4.2 Inelastic scattering processes

Before the mechanism of spin-flip Raman scattering (SFRS) can be elaborated in greater detail, this section briefly focuses on the most relevant inelastic scattering processes of electrons in optical media that related to SFRS. In general, two types of interactions can be distinguished: On the one hand the inelastic scattering between photons and electrons, and on the other hand the acoustic electron-phonon scattering. This inelastic scattering mechanisms are predicated on the three-step scattering process, which is addressed under various aspects in the previous sections and which is shown in the Feynman diagram in Fig. 2.13 (a). Following the three-step scattering process, a Hamilton can be assigned to each interaction. Hence, the total Hamiltonian $\hat{H}_{\mathrm{T}}$ comprises the electron-radiation interaction $\hat{H}_{\text{e-R}}$, the electron-hole-lattice interaction $\hat{H}_{\text{e-ph}}$, and the unperturbed $\hat{H}_0$ Hamiltonian, which includes the free electron, photon, and phonon contributions. Written in the second-quantization representation $\hat{H}_0$ is expressed by:

$$\begin{aligned}\hat{H}_0 &= \hat{H}_{\mathrm{R}} + \hat{H}_{\mathrm{ph}} + \hat{H}_{\mathrm{e}} \\ &= \sum_{\kappa,e} \hbar\omega_\kappa \left(\hat{c}^\dagger_{\kappa,e}\hat{c}_{\kappa,e} + \frac{1}{2}\right) + \sum_q \hbar\Omega(\vec{q}) \left(\hat{b}^\dagger_q \hat{b}_q + \frac{1}{2}\right) + \sum_{n,\vec{k}} E_{n,\vec{k}} \left(\hat{a}^\dagger_{n,\vec{k}}\hat{a}_{n,\vec{k}} + \frac{1}{2}\right),\end{aligned}$$

where, $\hat{a}^\dagger_{n,\vec{k}}$ and $\hat{a}_{n,\vec{k}}$ are the electron creation and annihilation operators acting on the band state, which is characterized by the wave vector $\vec{k}$, the quantum number n, and the energy $E_{n,\vec{k}}$. The creation and annihilation operators for the photons are $\hat{c}^\dagger_{\kappa,e}$ and $\hat{c}_{\kappa,e}$ and those for the phonons are $\hat{b}^\dagger_q$ and $\hat{b}_q$. Furthermore, the photon is described by the wave vector $\vec{\kappa} = \kappa$, the polarization vector $\vec{e} = e$ and the frequency ω_κ. Respectively the phonon has the frequency Ω and wave vector $\vec{q}$.

An expression for electron-photon interaction can be obtained from equation (2.100), which written in the second-quantization representation has the following form

$$\hat{H}_{\text{e-R}} = \frac{e^2}{m^* c^2}\hat{c}_{\kappa_1}\hat{c}^\dagger_{\kappa_2}(A_1 \cdot A_2^*) \sum_{\vec{k},s,s'} \Pi_{s,s'}\hat{a}^\dagger_{\vec{k}+\vec{q},s}\hat{a}_{\vec{k},s}, \tag{2.107}$$

where

$$A_i = \left(\frac{2\pi\hbar c^2}{V\text{œ}(\omega_i)\omega_i}\right)^{1/2} e_i \quad (i = 1{,}2), \tag{2.108}$$

and Π is the matrix comprising the unit matrix $\hat{I}$ and the Pauli matrix σ, which considers the upper valence bands Γ_8 and Γ_7 of a zinc-blende structure. Latter is defined by:

$$\Pi = C(e_i \cdot e_f^*)\hat{I} - iD(e_i \times e_f^*) \cdot \sigma. \tag{2.109}$$

The explicit expressions for the coefficients C and D can be found in Ref. [17]. Substituting Eq. (2.109) into (2.107), one obtains for the electron-photon interaction:

$$\hat{H}_{\text{e-R}} = \frac{e^2}{m^* c^2}\hat{c}_{\kappa_1}\hat{c}^\dagger_{\kappa_2}(A_1 \cdot A_2^*)[C(e_i \cdot e_f^*)\rho_{\vec{q}} - 2iD(e_i \times e_f^*) \cdot s_q], \tag{2.110}$$

with the charge-density operator $\rho_{\vec{q}}$ and the the Fourier component of the electron-spin density operator

$$s_q = \frac{1}{2V} \sum_{\vec{k},s,s'} \sigma_{s',s} \hat{a}^{\dagger}_{\vec{k}+\vec{q},s} \hat{a}_{\vec{k},s}. \tag{2.111}$$

The first term of (2.110) describes the change of the electron momentum for parallel-orientated polarization vectors of the incident and scattered light, while the second term accounts for the electron spin-dependent scattering. It becomes apparent from this equation as well that photons can be scattered not only by fluctuations of the electron density, but also by those of the spin density as well. In this respect the cross-section of spin-dependent scattering is given by:

$$\frac{\mathrm{d}^2\eta_s}{\mathrm{d}\omega_i \mathrm{d}\vartheta} = \frac{e^4}{(m^* c^2)^2} D^2 \left(\frac{\omega_f}{\omega_i}\right)^2 |e_i \cdot e_f^*|^2 \frac{\hbar q^2}{\pi e^2} (1 + N_i) \mathrm{Im}\{\chi_{\mathrm{el}}(\omega,q)\}, \tag{2.112}$$

with the electronic susceptibility $\chi_{\mathrm{el}}(\omega,q)$. From Eq. (2.110), one further derives, in regard of the in-plane components of the polarization cross product, that electrons are scattered within the same band by changing their spin and momentum, due to spin-flip scattering:

$$\vec{k}, \pm 1/2 \rightarrow \vec{k} + \Delta\vec{k}, \mp 1/2 \quad \propto |(e_i \times e_f^*)_{\pm}|^2. \tag{2.113}$$

On the other hand, along the quantization axis z the spin of the electron is conserved. Hence, a spin-dependent spin-conserving scattering occurs, due to which only the wave vector changes:

$$\vec{k}, \pm 1/2 \rightarrow \vec{k} + \Delta\vec{k}, \pm 1/2 \quad \propto |(e_i \times e_f^*)_z|^2. \tag{2.114}$$

When a magnetic field B is applied along the quantization axis z, the electron spin states split and the transferred frequency in spin-flip scattering $s \rightarrow -s$ is given by:

$$\hbar\omega = E_{\vec{k}+\vec{q}} - E_{\vec{k}} - 2j g_e \mu_{\mathrm{B}} B_z, \tag{2.115}$$

where g is the electron Landé factor. It is apparent that contributions to light scattering in the vicinity of a quantizing magnetic field also result from transitions between different Landau levels.

The second important interaction Hamiltonian is based on electron-hole-lattice interaction $\hat{H}_{\text{e-ph}}$. As mentioned before the main contribution to this light scattering process originates from the indirect interaction through the electron and hole subsystem, rather than from the direct photon-phonon interaction. The respective Hamiltonian, written in the second-quantization representation in terms of phonon ($\hat{b}^{\dagger}$,$\hat{b}$) and electron-hole (exciton) ($\hat{A}^{\dagger}$,$\hat{A}$) operators is given by[186]:

$$\hat{H}_{\text{e-ph}} = \sum_{n',n,\vec{k},\vec{q}} S_{n,n'}(\vec{q}) \hat{A}^{\dagger}_{n',\vec{k}+\vec{q}} \hat{A}_{n,\vec{k}} (\hat{b}_q + \hat{b}^{\dagger}_{-q}). \tag{2.116}$$

Here, $\vec{q}$ is the phonon wave vector and $S_{n,n'}$ is the matrix element for the electron-hole-pair phonon coupling, which depends on the quantum numbers n and n'. The matrix element for electron-phonon interactions is expressed by [186]:

$$S_{n,n'}(\vec{q}) = \int \mathrm{d}^3 r \phi_n^*(\vec{r}) \phi_n'(\vec{r}) [u_q^e e^{-i\vec{q}\cdot\vec{r} m_e/(m_e+m_h)} - u_q^h e^{i\vec{q}\cdot\vec{r} m_h/(m_e+m_h)}], \tag{2.117}$$

where m_e and m_h are the electron and hole effective masses, respectively. The term u_q^e and u_q^h relate to interactions with acoustic and optical phonons. Here, three cases can be distinguished: On the one hand, the Fröhlich interaction with longitudinal phonons [186], on the other hand, the deformation-potential interaction with acoustic phonons [187] and finally, the piezoelectric interaction with acoustic phonons. [188]

The main contribution to the electron-hole-phonon interaction is given by the deformation-potential interaction with acoustic phonons. In this respect the term $u_q^{e,h}$ reads [186]:

$$u_q^{e,h} = \sqrt{q \frac{\hbar}{2\rho\nu V}} D_{e,h}. \tag{2.118}$$

Here, ν is the speed of sound and $D_{\mathrm{e,h}}$ are the deformation potential constants. It is worth noting, that the longitudinal acoustic phonons dominantly contribute to this scattering process, since their deformation potential exceeds that of the transverse acoustic phonons. [189]

The Hamiltonian in (2.116) reveals that the electron-hole-phonon interaction is linear in the phonon operator and bilinear in the electron-hole operator. At the onset of an interaction, the phonon scatters the electron-hole-pair from a quantum state n to n', increasing or decreasing its energy by the energy difference of the two quantum states involved. The transfer between the two quantum states can also be accompanied by a reversal of the exciton spin state. For this reason the exciton-phonon scattering may be regarded as an inelastic spin-flip scattering mechanism.

The efficiency of scattering η_s by acoustic phonons is inherently connected with the respective cross-section ζ of scattering. The differential scattering cross section within a scattered frequency range $\mathrm{d}\omega_f$ and scattered into a cone with a solid angle ϑ is given by:

$$\frac{\mathrm{d}^2\eta_s}{\mathrm{d}\omega_f \mathrm{d}\vartheta} = \frac{\omega_i^2 V}{4\pi\hbar^2 c^4} \nu(\omega_i) \nu^3(\omega_f) |w_{fi}(\omega_f, \vec{e}_f, \omega_i, \vec{e}_i)|^2, \tag{2.119}$$

where w_{fi} denotes the scattering rate from the initial state $|i\rangle$ to the final state $|f\rangle$. According to the three-step Feynman diagram shown in Fig. 2.13 (a), the scattering rate in terms of the electron-radiation interaction $\hat{H}_{\text{e-R}}$ as well as the electron-hole-phonon interaction $\hat{H}_{\text{e-ph}}$, can be written as

$$w_{fi} = \sum_{X,X'} \frac{\langle f|\hat{H}_{\text{e-R}}|X\rangle\langle X|\hat{H}_{\text{e-ph}}|X'\rangle\langle X'|\hat{H}_{\text{e-R}}|i\rangle}{(\hbar\omega_f - E_X + \Gamma_X)(\hbar\omega_i - E_{X'} + \Gamma_{X'})}. \tag{2.120}$$

The scattering rate includes the intermediate electron-hole pair states $|X\rangle$ and $|X'\rangle$, with the respective lifetime broadenings Γ_X and $\Gamma_{X'}$ as well as the respective electron-hole pair energies E_X and $E_{X'}$.

2.4.3 Spin-flip Raman scattering

The SFRS is based on the inelastic scattering of an incident electromagnetic wave with carriers or complexes, whose spin is reversed in the process. In general, the SFRS is initiated by the excitation of carriers through an incident light wave, whose energy has to be in resonance with an interband electron-hole transition. Subsequently, the spin of an electron, hole, or both carriers is reversed in a scattering process induced either by acoustic phonon or carrier-carrier interaction. In the final step, due to an interband transition the electron and hole recombine under the emission of a photon. The SFRS interband transitions follow the electric dipole selection rules, described in Sec.2.2.

In regard of a single electron spin-flip induced by photon-electron scattering, as described in (2.113), the magnitude of the transferred energy $\hbar\Omega$ depends on the energy difference between the states with oppositely orientated spins. As outlined in Sec.2.1.5 an external magnetic field influences the splitting of these spin states, and may lift restrictions imposed by selection rules, thus, making SFRS processes possible. Furthermore, the magnetic confinement can enhance the exciton oscillator strength, and in turn increase the scattering efficiency. For instance, in the presence of an external magnetic field B, the incident photon energy ω_i changes, due to the effect of the Zeeman splitting of spin states, to $\omega_i - |g|\mu_B B$ and $\omega_i + |g|\mu_B B$ for the Stokes and anti-Stokes shifted waves, respectively. Here g is the electron Landé factor of the scattered carrier. The energy difference between incident and scattered photon is referred to as Raman shift $\Delta E_R = |g|\mu_B B$. It follows from this that the SFRS provides a direct measure of the g factor of electrons as well as holes in low-dimensional semiconductors. [17]

It is important to point out that the Raman shift of a carrier does not necessarily provide enough information to distinguish the origin of a SFRS process. Under certain conditions, g factors of different carriers can be very similar. It is, thus, necessary, to study the SFRS from various points of view. For instance an analysis of the temperature of the Raman intensity can be used to describe the localization energy of the scattered particle complex. Further, from the magnetic field and angular dependence of the Raman shift conclusions can be drawn on deviations from the linear Zeeman behavior and the g factor tensor components, as described in Sec. 2.1.5. In order to determine the type of SFRS an analysis of the Raman shift as function of the resonant excitation energy, which affects mainly the scattering efficiency, should be used.

In the analysis of interband transitions and, thus, the designation of the scattering mechanism, the polarization characteristics of the SFRS are of major importance. As underlined in Sec. 2.1.5, from the comprising spin Hamiltonian (see Eq. (2.54)), which

describes the electron-hole exchange interaction, four possible combinations of excitons can be derived, which are characterized by their angular momentum projections $M_i = S_{e,i} + J_{h,i}$. On this basis, the SFRS mechanism can be evaluated from the circularly polarized SFRS spectra by analyzing the selection rules of electric dipole transitions in an external magnetic field. In regard of a quantum state $|\, j\,, j_z\,, l\,, S\,\rangle$, characterized by the quantum numbers of the total angular momentum j, its projection on the quantization z-axis j_z, the orbital angular momentum l, and the spin S, the electric dipole selection rules are given by $\Delta j = (0,\pm 1)$, $\Delta j_z = (0,\pm 1)$ and $\Delta l = 0$. The scheme of the electric dipole allowed transitions for $\vec{k} = 0$ of a bulk crystal with zinc-blende lattice is depicted in Fig. 2.9.

The efficiency of SFRS η_{sf} is inherently connected with the respective cross-section ζ_{sf}. According to Eq. (2.109) the spin-flip scattering cross-section for backscattering Faraday geometry is proportional to

$$\frac{\mathrm{d}^2\zeta_{sf}}{\mathrm{d}\omega \mathrm{d}\vartheta} \propto \left| (e_i \times e_f^*) \times \frac{\vec{B}}{B} \right|^2 . \tag{2.121}$$

It follows from this relation that scattering is only allowed, if the magnetic field has a nonzero component perpendicular to the light propagation direction. For instance, in Faraday geometry with $B \parallel z \parallel \vec{k}_i$), the angular momentum component projected onto the quantization z-axis should be conserved

$$s_{i,z} + \mathfrak{m}_i = s_{f,z} + \mathfrak{m}_f, \tag{2.122}$$

where $s_{i,z}$ and $s_{f,z}$ are the electron spin components $S = \pm 1/2$ in the initial and final states and $\mathfrak{m}_i$ and $\mathfrak{m}_f$ are the angular momentum components of the circularly polarized photon before and after the scattering ($\mathfrak{m} = \pm 1$). In the backscattering process, where the propagation directions of the incident and scattered light are opposite, the electron changes the z component of its spin by $\Delta s_z = \pm 1$, whereas the photon angular momentum either remains unchanged ($\Delta\mathfrak{m} = 0$) or changes by $\Delta\mathfrak{m} = \pm 2$. It is obvious, that for both cases the angular momentum component is no longer conserved in Faraday geometry, meaning that spin-flips of an electron or a hole are principally forbidden. However, according to (2.121) the scattering becomes allowed at tilted magnetic fields, which lift the restrictions of the selection rules. In oblique magnetic field geometries ($B_x \neq 0$, $B_y \neq 0$) a mixing between the optically bright and dark excitons occurs and, thus, the spin quantization direction differs from that of the incident light. The mixing is established generally via the transverse electron g factor and not via the heavy-hole, as it does not have a magnetic moment perpendicular to the quantization z-axis.[190] Another possibility to induce a mixing optically bright and dark excitons is via strain. For instance, in structures with low symmetry, e.g. in lens-shaped self-assembled QD, which are described in terms of the C_{2v} point group, light-hole and heavy-hole states are mixed due on strain.[135,191] states are mixed due to strain. In general, it can be said that the light scattering involving the spin of a carrier becomes allowed, when the symmetry of the electron-hole pair complex is lowered.

The SFRS experiments, which are presented in this thesis, are typically performed in the backscattering geometry. In this regard, the polarization configuration of the incident light is denoted by σ^{λ} and of the scattered light by σ^{ν}.[17] The signs λ or ν are determined by the sign of the angular momentum component of the photon on the quantization z-axis. Using this nomenclature the conventional specular reflection of right- (σ^{+}) or left-handed (σ^{-}) circularly polarized light from an medium is denoted by the term (σ^{λ},σ^{ν}).

In order to illustrate the specific features of inelastic resonant Raman scattering, in what follows, an example of a typical acoustic-phonon based SFRS process, i.e. the resonant excitation of a neutral excitation in the QW and a subsequent spin-flip scattering process, is discussed. This spin-flip scattering process is elaborated in the following for Faraday geometry. Hence, it is assumed that a high magnetic field is applied along the quantization z-axis, lifting the spin degeneracy of the electron and heavy-hole states. The lowest unexcited exciton ground state is assumed to be $\mid 0\rangle$. For resonant probing of the heavy-hole exciton by circularly polarized light, e.g. σ^{+}, the optical state $\mid +1\rangle = \mid s_{\mathrm{c,hh}},s_{\mathrm{c,e}}\rangle = \mid +3/2,-1/2\rangle = \mid\Uparrow\downarrow\rangle$ is excited. Here, $s_{\mathrm{z,i}}$ denotes the projection of the electron spin or heavy-hole angular momentum on the quantization z-axis. A single spin-flip of either the electron or heavy-hole induced by an acoustic phonon leads to a dark exciton state of $\mid\Uparrow\uparrow\rangle$ or $\mid\Downarrow\downarrow\rangle$, respectively. These states are two fold degenerate dark states with an angular momentum projection of $\Delta L = \pm 2$. The optical excitation or annihilation of these states is forbidden in the electric dipole approximation. Hence, Raman scattering of a single spin can not be observed. However, if the electron and heavy-hole reverse both their spins the momentum conservation requirement is fulfilled and a optical transition is possible. Accordingly, the exciton is scattered from $\mid\Uparrow\downarrow\rangle$ to $\mid\Downarrow\downarrow\rangle$. The annihilation of the final exciton state yields a photon with an opposite circular polarization to the incident one. In the presented example this would be σ^{-}.

The described spin-flip scattering process in Faraday geometry demonstrates that a spin-flip Raman shift is only observable when a simultaneous spin-flip of the electron and heavy-hole occurs. A single spin-flip of either an electron or a heavy-hole are forbidden due to the electric dipole selection rules. As noted above, there are possibilities to bypass these limitations, as, e.g. by tilting of the magnetic field with respect to the z-axis, which leads to a mixing of the bright and dark exciton states. Another possibility are anisotropic exchange interactions with carriers bound to an acceptor state. The anisotropic exchange is attributed to a spatial separation of the localization centers of both the photo-exciton and acceptor-bound carrier. This difference reduces the symmetry of the coupled carrier complex, hence, the selection rules are relaxed. Further SFRS mechanisms and influencing factors are discussed in the context of this thesis.

Chapter 3

Experimental methods

The knowledge of how to manipulate and store information in the form of electronic and nuclear spin states have attracted considerable interest in current research as it may lead to pioneering applications in spin electronics and quantum information technologies. Electron spin polarization in a semiconductor can be prepared optically and then manipulated by taking advantage of optical selection rules that allow a preferred excitation of electrons and holes with certain spin orientations. In this regard, coherent optical spectroscopy has proven to be an efficient method to perform such operations, and, thus, to investigate the energy levels, vibrations and spin states in condensed matter systems. [192]

The various established techniques can roughly be classified into two categories. The first one is based on the study of the temporal dynamics of the system's response to coherent spin rotation with ultrashort laser pulses. A prominent example, for this purpose, are spin echo experiments in semiconductors. For instance, these are used to investigate the exciton dynamics in GaAs QWs. [193]

The second category of techniques is based on continuous wave (cw) lasers, which are used as a source of the monitoring light and for excitation in steady state measurements. The main advantage of this approach is the narrow wavelength band and, respectively, the high spectrum resolution, making it possible to characterize precisely the energy level structure of carriers in semiconductor nanostructures. One established nondestructive spectroscopic technique, in this respect, is photoluminescence (PL) spectroscopy. It is based on the generation of excitons (electron-hole pairs) by nonresonant laser excitation and the detection of their luminescence, after the photoexcited electron makes a transition from the valence band back to the conduction band. The energies of these luminescence photons provide information on the energy level structure and the optical properties of low-dimensional semiconductors.

In the research field of spintronic, the understanding of the fundamental interactions between confined carrier spins is essential, as it allows one to reveal novel spin effects or to improve existent spin phenomena. One appealing optical technique to study the spin properties of confined carriers and interaction processes is the resonant spin-flip Raman scattering (SFRS). The SFRS-spectroscopy is a powerful and sensitive tool to coherently initiate and manipulate carrier-spins.[34,35,194] It is used to directly determine the g factors of the confined carriers, thus, supporting the identification of the type of carriers involved in the scattering. Moreover, by means of SFRS one can characterize the spin interactions between carriers themselves as well as a carrier and a second system, e.g. the nuclear spin system or a lattice vibration (phonon). The experimental technique of SFRS is used in the framework of this thesis to investigate different spin phenomena in (In,Ga)As/GaAs QDs (see Part II), ZnMnSe QWs (see Part III), as well as CdSe colloidal nanocrystals (see Part IV).

The main idea of Raman scattering, which has been discovered in 1928 by Indian physicist C.V. Raman[179], is simply based on the comparison between the energies of the incident and scattered photons. The frequency shift of the Raman scattered light, denoted as Raman shift, is directly related to the structural properties of the material. In the specific case of SFRS, the inelastic light scattering is based on the participation of a carrier whose spin orientation is reversed, giving a direct measure of the splitting of spin states induced by a strong external magnetic field.[32,33] Useful information about the spin-flip scattering mechanism can furthermore be derived from the dependence of the intensity and spectral width of the SFRS on various external parameters such as temperature, optical excitation polarization, or excitation energy dependence. One of the first SFRS experiments on bound electrons and holes in CdS has been preformed by Thomas and Hopfield[31]. Since then, this technique is successfully applied to various semiconductor structures, such as quantum wells[32–34], nanocrystals[35], as well as indirect band-gap QDs[36].

A detailed description of the experimental realization of SFRS in low-dimensional semiconductors is described in this chapter. It provides an overview of the basic principles of the experimental setup, the function and interplay of the equipment, and the experimental methods. Its realization is not simple, and, thus, requires sophisticated equipment which fulfills the experimental requirements in regard of the properties of SFRS that will be briefly described in Sec. 3.1. The basic SFRS setup and all necessary arrangements to meet the experimental requirements are described in the subsequent Sec. 3.2. In this respect, two possible implementations will be discussed in detail and various experimental modifications will be presented. Another important part of this work included time-resolved SFRS measurements which addressed the temporal evolution of the nuclear spin polarization in singly charged (In,Ga)As/GaAs quantum dots by using a two-color laser excitation scheme. The description of these experiments is given in the last Sec. 3.3 and, thus, completes the chapter about the experimental methods.

3.1 Basic experimental requirements for spin-flip Raman scattering

The spin-flip Raman scattering of an electron and/or a hole is typically triggered by the inelastic scattering of an incident photon whose energy is in resonance with the bound electron-hole pair (exciton). In this scattering process, the spin-flip of the carrier is induced, for example, by a phonon or carrier-carrier interaction. However, it requires the reduction of the exciton symmetry and lifting of the energy degeneracy, so that the angular momentum conservation is removed and, thus, the final scattering state is optically active. A possibility to meet this requirement is by tilting of the magnetic field with respect to the QW or QD growth axis, which on one hand lifts the spin degeneracy and on the other hand provides a mixing of the electron and, respectively, light- and heavy-hole states. When the respective spin states are nondegenerate, in agreement with the electric-dipole selection rules, also in the absence of an external magnetic field an SFRS process should be possible.

These highlighted aspects suggest that the spin-flip scattering of a carrier should be observable in every semiconductor, which meets the mentioned requirements.[49] However, the scattering process is closely linked to various external parameters, which may either reduce or enhance the spin-flip scattering probability. These are the temperature, the magnetic field geometry, as well as the energy and polarization of the exciting light. Each of these factors has a decisive influence.

For instance, the temperature causes an increase of multiple interactions of the photoexcited carriers in the many-body environment, in particular, with thermal phonons, typically resulting in a rapid loss of spin coherence, in turn, decreasing the spin-flip scattering probability. However, recent studies have demonstrated that confined electron spins in QDs may reveal a robust electron spin coherence for a wide temperature range (up to $T = 20$ K).[139] Furthermore, the e-SFRS efficiency may even significantly enhance at higher temperatures due to interaction with acoustic phonons. The temperature dependence of the e-SFRS is the subject of Part II. Despite the temperature, the spin-flip scattering probability increases, as mentioned above, also in tilted magnetic field geometry where the symmetry of the exciton complex is reduced, in turn allowing the spin-flip of electrons and holes. The type of the SFRS process is classified with respect to the excitation energy, which is the third crucial parameter. Here, it is important that the excitation energy satisfies the resonance conditions.

To meet the presented requirements, the experimental setup must ensure that the SFRS measurements can be carried out at low temperatures and in a strong magnetic field with adjustable orientation. In addition, a precisely tunable laser excitation with a spectrally narrow laser line, to achieve high spectral resolution, is required. However, these conditions are not yet sufficient. To observe a SFRS signal, one has to overcome further obstacles. Here, the spin-flip efficiency (η_{SF}), the Raman shift (ΔE_{SF}) of the

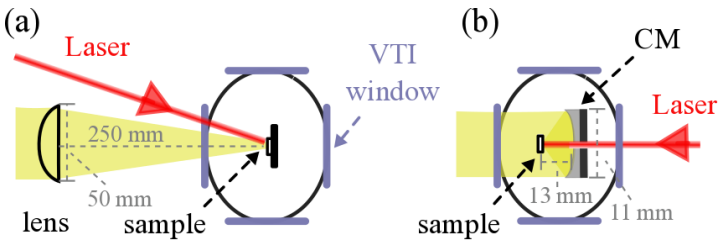

Figure 3.1: Schemes showing two ways to collimate the light emitted from a sample, which is located in the variable temperature insert (VTI) of a split-coil superconducting magnet system. The laser excitation is illustrated by the red line. (a) The emitted light is collimated with a large-diameter plano-convex lens ($f = 250$ mm, $D = 50$ mm) positioned in front of the cryostat. The respective light cone is about 12°. (b) The collimation is realized inside the cryostat sample chamber, by the use of a holder with a concave mirror (CM). Here, the sample is positioned in the focus of the CM ($f = 13$ mm, $D = 11$ mm). The light cone encloses an angle of 50°.

SFRS line, as well as the signal to background ratio ($I_{\mathrm{SF}}/I_{\mathrm{BG}}$) play a key role. The significance of these factors is described in detail in the work of J. Debus (see Ref. [49]), and, thus, will be briefly pointed out in the following, highlighting the most important aspects which have to be met by the experimental setup.

The first obstacle that has to be overcome, in order to detect an SFRS signal, is the intrinsically low spin-flip scattering efficiency, which ranges between 10^{-9} and 10^{-12}.[17,195] This low efficiency demands an efficient collection of the light scattered from the sample. Since the sample is located inside a split-coil magnet-cryostat and is optically accessible only through small-sized windows, the technical possibilities are rather limited. In the experiments carried out, the collimation of the light scattered from the sample is realized in two ways: Either via a long-focus lens which is positioned in front of the cryostat window or it is realized inside the cryostat sample chamber by the use of a holder with a concave mirror (CM), which serves as light collimation element. Both methods are illustrated schematically in the Figs. 3.1 (a) and (b). To compare the collimation efficiency of both optical systems, the intensity I_{L} of the collimated light is estimated by the numerical aperture N_{A} or, respectively, the f-number N_f which is defined as the ratio of the focal length f to the diameter of the objective D[49,196]:

$$I_{\mathrm{L}} \propto N_f^{-2} = (2N_{\mathrm{A}})^2 = \left(\frac{f}{D}\right)^{-2}. \tag{3.1}$$

The f-number describes the light-gathering ability of the objective, i.e., lens or focussing mirror. For lower f-number, i.e. a high numerical aperture, the gathered light power enhances.

In the case of configuration (a) (see Fig.3.1), in which the sample is in the focal plane of a plano-convex lens with a diameter of $D = 50$ mm and a focal length of $f = 250$ mm, the respective f-number equals $N_f = 5$. This corresponds to a numerical

aperture of $N_A = 0.22$. In this configuration the light cone is not larger than 12° and, thus, only a small part of the light scattered can be effectively collected. The situation differs in the concave mirror system (see Fig.3.1 (b)). Here, the sample is positioned in the vicinity of the focusing mirror ($f = 13$ mm) which has a diameter of $D = 11$ mm. In this case the f-number equals $N_f = 1.18$ ($N_A = 0.46$) and the respective light cone encloses an angle of approximately 50°. Hence, the concave mirror system has a 18 times higher light-gathering efficiency than the long-focus lens system.

It is worthwhile to note that the numerical aperture of an optical system such as an objective lens or focusing mirror linearly depends on the refractive index. Their numerical aperture is defined by:

$$N_A = \nu \cdot \sin(\varphi), \tag{3.2}$$

where ν is the refractive index of the medium in which the objective is working and φ is the maximal half-angle of the light cone originating from the sample area illuminated by the laser. When the sample holder is immersed in liquid helium, which has a refractive index of $\nu = 1.03$, the light-gathering efficiency will further improve.[197] In addition, reflections at the interface between different media are reduced by the liquid helium, since its refractive index is comparable to that of the VTI window (quartz, $\nu = 1.54$)[198] and the sample surface (e.g. ZnSe, $\nu = 2.61$ or CdSe, $\nu = 2.54$).[199,200]

In addition to sufficient light collimation, the efficiency of the final detection system, consisting of a spectrometer and photon detector, is crucial to observe a weak spin-flip Raman line. Furthermore, one has to consider, as mentioned above, that the SFRS is characterized by a particularly low Raman shift ΔE_{SF} which is about four orders of magnitude smaller then the excitation energy E_{exc}. For this reason, the spin-flip Raman line appears as a weak satellite in close vicinity of the laser line and may, therefore, be obscured by either strong Rayleigh scattering or photoluminescence background caused by resonant excitation. Hence, these aspects demand a strong stray light suppression. To meet this requirements a double Raman spectrometer (Jobin Yvon, U1000) which provides a high spectral resolution, wide-ranging tuneability and improved stray light rejection, is used. The design of this spectrometer is shown in Fig. 3.2 (a).

The arrangement of this device is similar to a conventional double Czerny-Turner (CZ) monochromator system,[202] operating in the double additive mode. Its optical scheme is presented in Fig. 3.2 (b). As shown in this scheme, the incoming light from the sample crosses the input slit of size d_1 and is then collected by a spherical mirror with a focal length of $F = 1$ m. This mirror is positioned at the distance of its focal length from the entrance slit and, thus, creates a flat wave front which is subsequently directed to the grating. The diffracted light from the grating is collected by a second spherical mirror and focused to the output slit of size d_2. In this regard, the monochromator dispersion equation is defined by[203]:

$$\lambda = \alpha \frac{(1 + \cos(\phi))}{m \cdot g} + \frac{\sin(\phi)}{m \cdot g}. \tag{3.3}$$

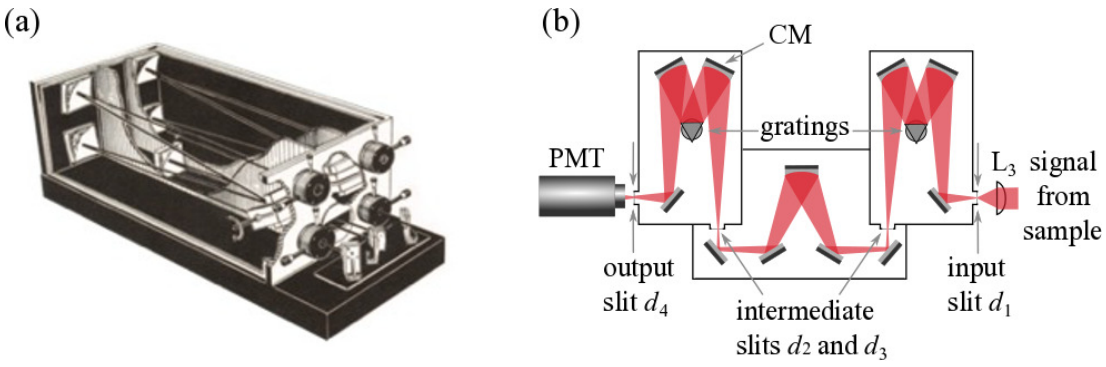

Figure 3.2: Design (a) and optical scheme (b) of the double Czerny-Turner (CZ) monochromator system (U1000). The sizes of the input, intermediate and output slit widths are denoted by d_i. Fig. (a) is adapted from Ref. [201].

Here, α is the incident angle of the light on the grating, ϕ is the angle between the incident and diffracted beams, m is the diffraction order and g describes the grooves number, which is defined as reciprocal of the grating period. Before entering the second monochromator stage, which works the same way as the first stage, the light is directed via two mirrors onto a spherical intermediate mirror located in the focus of the slits d_2 and d_3. This additional light path helps to suppress the stray light more effectively. In the second monochromator stage the light is dispersed further and finally directed through output slit d_4 to the photon counter.

In order to resolve a spin-flip Raman line the spectral resolution of the spectrometer has to be sufficiently high. The resolution is mainly determined by the alignment and quality of the spectrometer optics as well as the finite widths of the entrance and exit slits. Furthermore, it linearly depends on the grating width as one can derive from the monochromator dispersion equation (see Eq. 3.3). Hence, to achieve a high resolution one has to use small slit widths d_i and gratings with high grooves number. However, this literally decreases the amount of light, reducing the monochromator efficiency gradually. The double spectrometer (U1000) contains two holographic 1800 grooves/mm gratings, whose synchronized rotation leads to the light dispersion. The average quantum efficiency of this non-blazed holographic gratings is about 45% at 800 nm and 60% at 475 nm.[201] The double additive mode of this monochromator provides a spectral resolution of about 0.1 cm^{-1} and a high stray light rejection of 10^{-14} at 20 cm^{-1} from the Rayleigh line.[201]

Due to the strong light attenuation of the double monochromator, a sensitive detector with high quantum efficiency and a high signal-to-noise ratio is required. Therefore, at the output of the spectrometer, the light enters the detector system consisting of a Photomultiplier tube (PMT) with housing cooled by a Peltier element. The PMT is an electronic device which converts the incoming photons to current. It is composed of

a photo-cathode (material: GaAs), which converts photons to electrons, and an electron multiplication system which amplifies the electric signal. The main advantage of a PMT is its relatively big photo-sensitive area of about 2 cm in diameter, providing a high sensitivity, which may reach a value of 10^4 A/W. The wavelength range of the PMT which is defined by the GaAs photo-cathode ranges from 300 up to 920 nm. Its peak quantum efficiency at 700 nm amounts 15%. The response time of the PMT equals a few nanoseconds, while the dark counting rate is approximately 2 counts/s. The output of the photomultiplier is connected to a discriminator (F100T, Advanced Research Instruments), which rejects low amplitude pulses due to thermal electrons, and forms fixed duration and amplitude pulses for each detected photon. The pulses from the discriminator are directed to the control unit of the U1000 which functions as a photon counter.

A further important factor, which significantly influences the efficiency of the SFRS detection, is the polarization of the light scattered from the sample. Depending on whether the light wave is polarized parallel (p) or perpendicular (s) to the the grating grooves, the monochromator grating efficiency changes. This is particularly evident from the solutions of the Helmholtz equation with boundary conditions differing for p- and s-polarized waves.[204] If the wavelength of the incoming light is higher than the blaze-wavelength of the grating, the diffraction efficiency for p-polarized light is smaller than that for s-polarized light. The highest possible efficiency with the above described gratings implemented in the U1000 is obtained for s-polarized light.[201] How the polarization of the incoming light is set to meet the experimental requirements is described in Sec. 3.2.

In order to demonstrate the importance of sufficient spectral resolution and stray light rejection exemplary SFRS spectra measured at different conditions are presented in Figs. 3.3 (a) and (b). When all experimental requirements are fulfilled, SFRS lines can be monitored on top of a background contributed by resonant excited PL and stray light, originating from the laser or sample surface (see Fig. 3.3 (a)). During the laser line measurement the PMT photocathode is protected from the intensive laser light by a neutral filter (NF) which is manually inserted into the detection path. The laser line cut-off is indicated by the grey dashed line in Fig. 3.3 (a). It is worthwhile to note that the spin-flip line profile is contributed by the natural and laser line widths. If the slit widths d_i of the monochromator are increased, the spin-flip Raman line profile does not change whereas the light quantity is greatly enhanced. When the experimental SFRS requirements are not fulfilled, e.g. when efficient stray light suppression is not provided, the spin-flip Raman line is not distinguishable any more from the high background as illustrated in Fig. 3.3 (b). In the case of a spectrally broad laser line, the detection of a spin-flip Raman line in the vicinity of a laser is impeded and, moreover, itself can be decisively broadened.

Before shifting the focus towards the basic SFRS setup, a further important aspect, namely the competition between the resonant excited PL background and a spin-flip

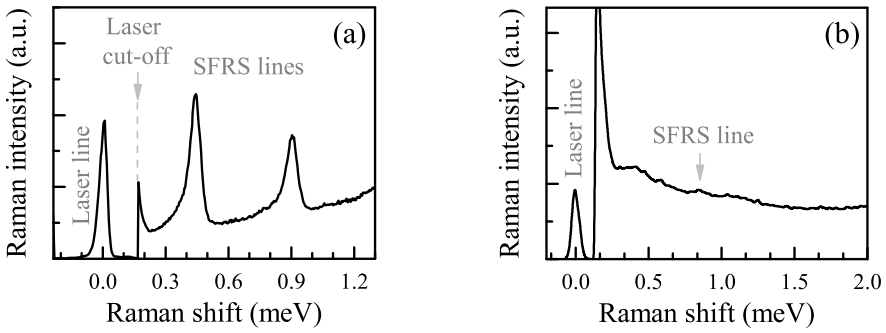

Figure 3.3: Exemplary SFRS spectra for satisfied and unsatisfied experimental requirements. (a) In the case of efficient stray light rejection, high spectral resolution, and sufficient light collimation, in close vicinity of the narrow laser line, SFRS lines can be monitored. These spin-flip Raman lines, which are characterized by their Raman shift, sensitively respond to different external parameters like the magnetic field, temperature, geometry, or exciting light. Analyzing their properties provides information on the carrier spin and interaction process. (b) If the experimental requirements are not fulfilled, e.g. in the case of not efficient stray light suppression, the spin-flip lines are screened by the PL or acoustic phonon background. The SFRS line is marked by an arrow.

Raman signal, is to be addressed. As pointed out above, a high PL background may potentially obscure the spin-flip Raman line. A way to bypass this obstacle is by taking advantage of the different optical properties of PL and SFRS. For instance, their respective intensities reveal principally a dissimilar dependence on the optical power density or polarization characteristics, thus, offering the possibility to identify the SFRS line on top of the background contributed by PL. Another approach is by tuning the excitation energy to the edge of the PL spectrum. In consequence the SFRS spectrum is less screened by the resonantly excited PL. However, the SFRS efficiency generally depends on the resonance conditions, and, thus, its relative intensity for quasi-resonant excitation may decrease. In summary, there is no fundamental guideline which could specify how to proceed in order to achieve the best $I_{\mathrm{SF}}/I_{\mathrm{BG}}$ ratio. Depending on the optical properties of the samples under study, the experiment has, therefore, to be individually optimized to obtain the best results. In the following chapters, experimental realization and methods will be highlighted.

3.2 Spin-flip Raman scattering setup

Building on the last section, which has highlighted the SFRS requirements that have to be fulfilled by the experimental setup, next the realization of a basic SFRS experiment will be addressed. The setup for measuring SFRS is sketched in Fig. 3.4. One can divide the setup roughly into three segments, namely the excitation, sample, and

detection part. In general, the excitation, which is composed of a laser and various optical components to optimize and set the properties of the outgoing light, provides a laser beam that is used to excite the semiconductor sample exposed to cryogenic temperatures and high external magnetic fields. Afterwards, the light scattered from the sample is analyzed with a spectrometer and photon detector. Each of the three segments has alternative configurations, which will be briefly illustrated in this section. To provide an overview, the general experimental parameters used for the SFRS measurements are listed in Tab. 3.1.

For the optical excitation of the studied semiconductor samples, different laser sources are used. Here, the choice depends on the energy required for the resonant excitation of the bound electron-hole pair. The different laser paths are marked by the numbers (1) to (4) in Fig. 3.4. In the case of the single-beam SFRS experiments on InGaAs QDs, the beam path is denoted by (1), a continuous-wave Ti:sapphire laser (Tekhnoscan, T&D-scan) pumped by the second harmonic of a Nd:YVO_4 laser (532 nm$\sim$ 2.33 eV, Coherent, Verdi V10 or V8) is used. The active centers of the Ti:sapphire laser are Ti^{3+} ions incorporated into the sapphire (AI_2O_3) crystal. The Ti^{3+} ions provide a broad emission and amplification band which is the key feature of the Ti:sapphire laser. The laser covers a wavelength range from 680 up to 1100 nm (1.13 to 1.82 eV) and has a maximal output power of ≈ 900 mW at 800 nm.[205] The actual wavelength is measured by a fiber-coupled wavelength-meter device (Coherent Wavemaster). The recorded values are transferred to a computer, where these are stored while the measurement is being performed. A thick Fabry-Perot interferometer with high reflectance, which is inserted in the laser resonator, reduces the laser line width to about 0.03 cm^{-1} (2.3 pm) at the central wavelength.[205,206] The small width of the laser line is more than sufficient for the SFRS experiments.

With respect to the study of the diluted magnetic semiconductor $Zn_{1-x}Mn_xSe$ QW samples, an optical excitation is required, which is about 2.8 eV. For this purpose, the QWs are excited by the second harmonic of the tunable continuous-wave Ti:sapphire laser. The second harmonic is generated by a non-linear optical crystal, namely a β-barium borate (BBO) crystal, which is inserted in the laser resonator. By the use of this second harmonic generator (SHG) a wavelength range from 425 up to 475 nm ($2.61 - 2.92$ eV) is covered. The output power is approximately 5 % of the respective first harmonic.

In order to set the excitation light properties, the beam from the Ti:sapphire laser is profiled by different optical components which will be discussed in more detail next. Initially, the beam is directed through an edge-filter (EF), which absorbs the green background light of the pumping laser, to an iris diaphragm (ID). By means of the ID the central part of the beam cross-section is selected. Moreover, it serves as reference for the laser spot position. With the subsequent variable gradient filter (VF) the laser beam is roughly attenuated. For fine adjustment of the laser power the combination of an achromatic half-wave plate ($\lambda/2$) and a Glan-Thompson prism (GTP) is used. The

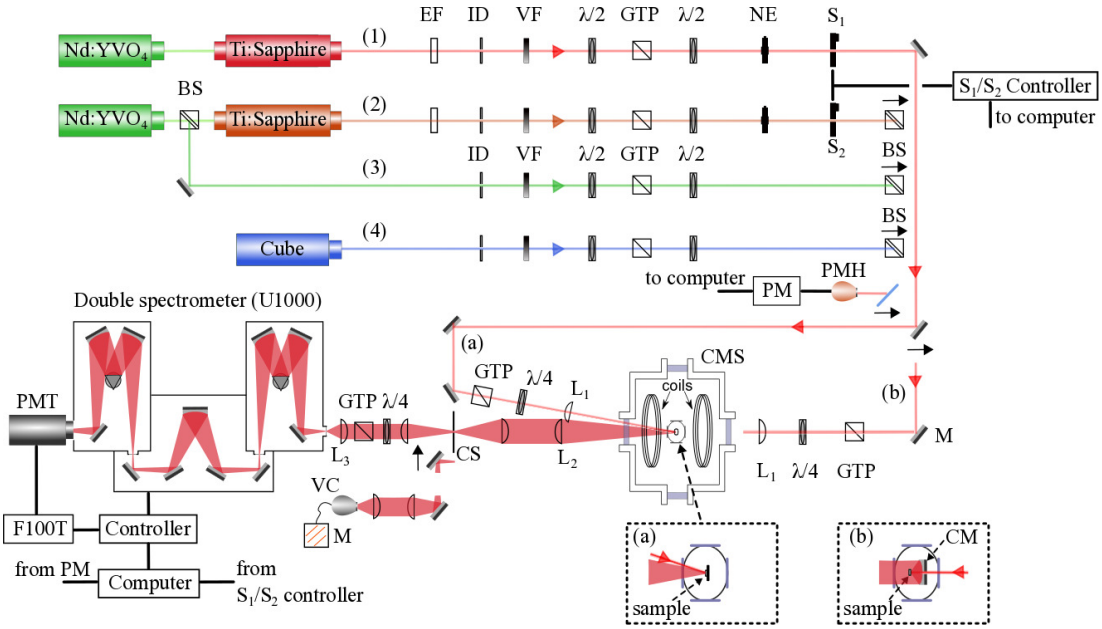

Figure 3.4: Scheme of the SFRS setup. In the single-beam SFRS experiments (1), the tunable continuous-wave Ti:sapphire laser provided the optical excitation of the studied samples. In regard of the two-color SFRS experiments, the SFRS setup can be extended by additional laser sources, denoted by (2) to (4). The laser beams are profiled by different optical components and then focused onto the sample surface. In the insets (a) and (b) the two different Raman-holders are depicted. Depending on the Raman holder selected the sample has to be excited either from the frontside (a) or backside (b) of the optical cryostat. Alternative light paths and optical components that may be inserted in the setup are indicated by the black arrows. The abbreviations are explained in the main text.

half-wave plate rotates the polarization of the linearly polarized laser light in respect to the polarizer which is horizontally polarized. The rotation of the half-wave plate allows one to regulate the amount of light transmitted through the polarizer.

To prevent undesired fluctuations in the laser intensity during a SFRS measurement, the laser power is stabilized and attenuated by the combination of a achromatic half-wave plate and a liquid-crystal noise eater (NE, Thorlabs). The block diagram of the noise eater is depicted in Fig. 3.5. The variable attenuator is composed of a liquid crystal retarder, a calibrated beam splitter, a photodiode and a servo controller to control the modulator.[207] This device requires linearly polarized light as an input which is set by the half-wave plate inserted after the Glan-Thompson prism. A light beam entering the noise-eater is attenuated by the liquid crystal retarder and output polarizer which together act as a variable retarder. A small part of the attenuated beam is sent by the subsequent beamsplitter to a feedback loop consisting of a photodiode and a Servo-controller. The controller unit compares the light intensity with the adjusted

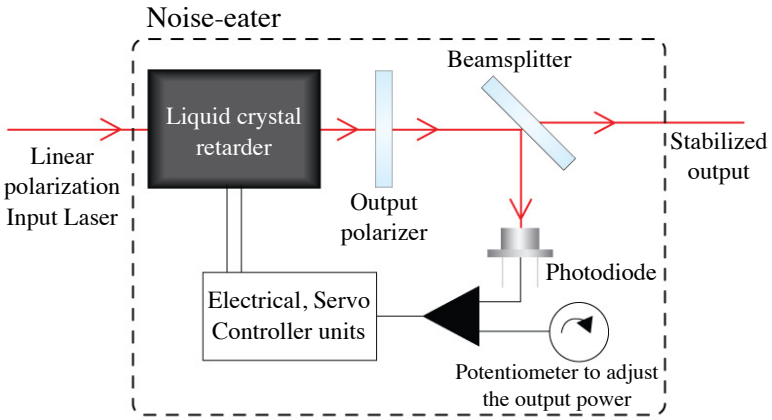

Figure 3.5: Block diagram of the liquid-crystal noise-eater. Adapted from Ref. [207].

power level and applies an appropriate adjustment voltage to the liquid crystal retarder. The desired output power is set manually by the potentiometer.

After the noise-eater, an automatic shutter (S_1) is integrated into the beam path, which makes it possible, if necessary, to block the laser beam while the measurement is being performed. The shutter is triggered by a controller which can be operated by the computer. The shutter-control is mainly used in the time-resolved SFRS experiments, which are described in detail in Sec. 3.3. To monitor the laser power during the measurements a glass plate can be inserted into the beam path which reflects a part of the beam to a photodiode sensor (PMH) connected to a digital handheld optical power and energy meter console (PM, PM100D Thorlabs). The PM provides calibrated measurements across a broad range of powers, energies, and wavelengths. The power density P_{exc} at the sample is varied from 0.001 up to ≈ 60 W/cm^2.

In addition to the single-beam SFRS experiments, denoted by (1) in Fig. 3.4, the SFRS setup can be extended by additional laser sources to perform two-color SFRS experiments. For this purpose, either a second continuous-wave Ti:sapphire laser (2), a Nd:YVO_4 laser with a photon energy of $E_{\mathrm{exc}} = 2.33$ eV (3) or a diode laser (Coherent CUBE) is utilized. High-energy illumination, which is used in addition to the resonant SFRS, can be an essential factor in influencing the SFRS mechanism. For instance, it may change the background carrier concentration and, thus, enhance the probability of charged exciton formation, which, in turn, affects considerably the SFRS efficiency in QDs or QWs. The nonresonant laser beams are profiled with comparable equipment in the same manner as the beam used for resonant SFRS. Their respective power density used in the measurements ranges from $1 \cdot 10^{-4}$ W/cm^2 to ≈ 2 W/cm^2. An important requirement for the two-color SFRS experiments is the spatial overlap of the resonant and nonresonant laser beams so that these hit the sample in the same spot on the sample surface. To overlap the two beams a nonpolarizing beamsplitter (BS) is inserted into the

main excitation path, as indicated by the respective black arrow in Fig. 3.4.The spatial coincidence of both laser spots on the sample surface is checked with an intermediate image of the illuminated sample area in the detection. This technique will be explained in more detail in the description of the detection segment.

The superimposed beams or the single beam, in the case of a simple SFRS experiment, can now be directed onto the sample in two ways, denoted by (a) and (b) in Fig. 3.4. For both options the beam is directed through a Glan-Thompson prism, which ensures a definite vertical-linear polarization, and a quarter-wave retardation plate ($\lambda/4$), by which the circular polarization of the laser light is set. In the last step a lens focuses the laser beam on the sample. The difference between the beam paths (a) and (b) is the chosen method of light collimation, described in the previous Sec. 3.1 (see Fig. 3.1), defining the incidence direction as well as angle of the laser beam. In this respect, the light scattered from the sample can either be collimated with a long-focus lens (a) or by a holder with a concave mirror (CM) in the vicinity of the sample (b), as illustrated in the small inserts shown in Fig. 3.4.

Since all measurements required cryogenic sample temperatures ($T \leq 70$ K) and a strong external magnetic field, the millimeter-sized sample (S) is positioned inside an optical cryostat with a split-coil superconducting magnet system generating magnetic fields of up to ± 10 T (Oxford-Instruments). The sample compartment, called variable temperature insert (VTI), consist of a long cylindrical tube with a diameter of about 25 mm with four windows near the bottom, allowing one to perform optical measurements. To achieve cryogenic temperatures a thin capillary tube connects the VTI to the helium volume of the cryostat. The flow of liquid helium through this capillary tube allows one to cool down the sample either by a controlled gas flow or by immersion in liquid helium. Moreover, the VTI temperature is regulated by electrical heating with an ohmic resistor composed of a copper cylinder which is located in the bottom part of the VTI. The temperature is read out by a calibrated semiconductor sensor which is connected to an electronic temperature controller. The available temperatures range from about 1.3 K up to 300 K.

Device/ mode	slit widths (μm)	B (T)	T (K)	λ_{exc} (nm)	max. P_{exc} (mW)
U1000 Additive	80/120/120/80	$\leq \pm 10$	$1.5 \leq T \leq 290$	$650 - 960$ (SHG) $425 - 475$	≤ 900 ≤ 45

Table 3.1: Experimental parameters for the SFRS measurements. The double spectrometer (U1000), which is used for this purpose, has a total focal length of 2 x 1 m, contains two non-blazed holographic 1800 grooves/mm gratings, and is operated in the double additive mode, providing a spectral resolution of 0.1 cm^{-1}. Besides the typically used slit widths ($\mathrm{d}_1/\mathrm{d}_2/\mathrm{d}_3/\mathrm{d}_4$) (see Fig. 3.2, the maximal magnetic field strength (B), temperature range (T), optical excitation wavelength (λ_{exc}) and maximal optical excitation density (P_{exc}) are listed.

The semiconductor sample is mounted to a sample holder consisting of a long tube that is inserted into the VTI. The tube allows one to adjust the vertical position of the sample and its angle with respect to the magnetic field direction $\vec{B}$. In this regard, the orientation of the sample normal $\vec{z}$ can be set to a specific angular position between 0° (Faraday geometry, $\vec{z} \parallel \vec{B}$) and ±45° with an accuracy of ±2°. When the optical cryostat is rotated by 90°, angles between ±45° and 90° (Voigt geometry, $\vec{z} \perp \vec{B}$) can be established. As mentioned above, the illumination of the sample can be realized either from the front- or back-side of the cryostat. In both configurations the lens L_1 ($f = 250$ mm) directly focuses the laser beam onto the sample.

In the case of method (a), the sample is evolved strain free in black paper and installed at a holder made of brass. In addition, the sample is covered by a mask having a hole of 300 μm diameter. This mask ensures that all measurements are preformed on the same sample spot. The light emitted/scattered from the sample is collimated by a long-focus lens (L_2; $f = 250$ mm, $D = 50$ mm) positioned in front of the cryostat window. For the concave mirror-based holder (b), the sample is fixed at a small brass-plate by silver conductive varnish. To provide an tilting angle between the external magnetic field direction and sample surface normal, the plate can be wedge-shaped. Here the light scattered from the sample is collimated by the annular area of the concave mirror. The collimated beam diameter is about 11 mm. The advantage of this mirror-based holder is the preservation of the polarization plane of the incident light as it is not rotated by a mirror. Moreover, this construction allows one to excite the sample with the wave vector of the exciting light being parallel the magnetic field direction as well as growth axis of the sample for Faraday configuration. However, due to the fact that the sample is mounted by silver conductive varnish to the brass-plate, it is not fully stress-free. This may, in turn, influence the properties of the studied semiconductor structures.

In the detection segment of the SFRS setup, the collimated light scattered from the sample is directed to the entrance of the U1000 spectrometer. On this main detection path the polarization of the light scattered is analyzed and the illumination position on the sample is controlled. The position of the laser spot is checked by means of an intermediate image of the illuminated sample surface. The intermediate image is coupled into the detection path via two plano-convex lenses ($f = 250$ mm) in combination with a cross slit (CS). A mirror that can be inserted into the beam path, as indicated by the black arrow in Fig. 3.4, reflects the light through two lenses onto a video camera (VC) connected to a monitor (M). The cross slit selects the homogeneously illuminated sample region. In the performed measurements, unless otherwise specified, the slit aperture is about 50 μm x 50 μm. After the intermediate image, the circular polarization of the scattered photons is studied. For this purpose, a large diameter quarter-wave plate and a Glan-Thompson prism, which generates horizontal-linear polarization in order to achieve the highest diffraction efficiency, are used (see Sec. 3.1). Finally, the light is focused by lens L_3 onto the entrance slit of the U1000 spectrometer. The functionality of this spectrometer and the attached PMT is described in detail in the previous sec-

tion. To achieve the best signal to noise ratio and to ensure a high spectral resolution as well as efficient stray light rejection the slit widths of the U1000 ($d_1/d_2/d_3/d_4$) (see. Fig. 3.2) are set to (80 μm/120 μm/120 μm/80 μm). To protect the PMT photocathode from the intensive laser light during the laser line measurements, a neutral filter is manually inserted in the detection path. The typical experimental parameters for SFRS measurements utilizing the U1000 double monochrometer are summarized in Tab. 3.1.

3.3 Time-resolved spin-flip Raman scattering setup

In current research ultrafast optical pump-probe spectroscopy has proven to be a powerful tool to investigate the dynamics of different interaction processes, e.g. electron-electron, electron-phonon, or electron-spin interactions, in various materials.[208–211] The basic idea of the pump-probe technique is to monitor the pump pulse induced changes of the reflectivity or transmissivity of probe pulses as a function of the probe delay time. A scheme illustrating the fundamental principle of the pump probe technique is presented in Fig. 3.6. The time evolution, which is related to the relaxation of carriers and the dynamics of phonons or spins, is derived by delaying the relative arrival time (τ) between the pump and probe pulses. For instance, in the case of ultrafast mechanisms this can be realized by a mechanical delay line. However, if the relaxation processes are considerably longer than milliseconds, a mechanical delay line is no longer sufficient, and, thus, it is necessary to generate the delay between pump and probe using alternative methods. A technique based on the automatized control of mechanical shutters is described below.

The pump-probe spectroscopy is an efficient tool to obtain information in the time and frequency domain simultaneously.[211] Hence, it is used to study the nuclear spin polarization in the electron spin-flip Raman scattering of (In,Ga)As/GaAs QDs in the stationary and time-resolved regime using a two-color laser pump-probe excitation scheme. For that purpose, a SFRS setup consisting of two tunable laser sources and a time-resolved detection system is required. The two lasers shall provide nonresonant and resonant excitation, i.e. pump and probe, in order to initially polarize the nuclei and then, after a delay time (τ), to stimulate an electron spin-flip. Proportional to the degree of the nuclear orientation an effective magnetic field acts back on the electron system and induces a shift of the electron spin-flip Raman line, which is known as the Overhauser shift.[212] In result, the temporal evolution of the Raman shift of the electron spin-flip line provides information on the amount of remaining nuclear spin polarization.

These time-resolved measurements are based on the SFRS setup sketched in Fig. 3.2. This setup configuration offers the possibility to control the properties of the laser light used for excitation, to apply high external magnetic fields, to vary the temperature

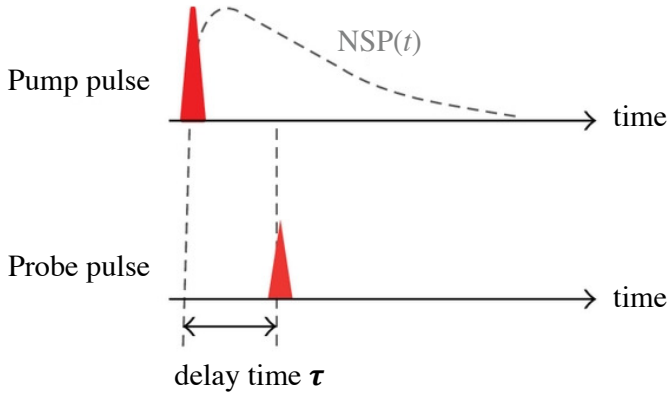

Figure 3.6: Scheme illustrating the fundamental principle of the pump-probe experiments. The time evolution of the nuclear spin polarization (NSP(t)) is derived by delaying the relative arrival time between the pump and probe pulse. The degree of the nuclear orientation is observed by detecting the Overhauser shift of the spin-flip line stimulated by the probe beam. Adapted from Ref. [211].

as well as to analyze the polarization of the light scattered from the QD sample. Here, in addition to the resonant excitation by a continuous-wave Ti:sapphire laser, denoted by (1) in Fig. 3.2, the sample is illuminated by nonresonant light from a second Ti:sapphire laser, denoted by (2). As described in the previous section both laser beams are profiled with comparable equipment in the same manner and then spatially overlapped by a nonpolarizing beamsplitter. The superimposed beams are directed from the backside of the optical cryostat, denoted by (b) in Fig. 3.2, onto the sample mounted on the Raman-holder with a concave mirror. The light scattered from the sample is collimated by the concave mirror and then sent to the U1000 double spectrometer. Polarization optics positioned in the beam path allow one to set the polarization of the incident laser beam and to analyze the polarization of the light scattered from the QD sample.

To investigate the temporal evolution of the nuclear spin polarization, which is on the time scale of several tens of seconds [21], the laser beams of the two continuous-wave Ti:sapphire lasers need to be chopped and additionally delayed in respect to each other. This is realized by the computer-controlled mechanical shutters S_1 and S_2 which are inserted in the beam paths of the resonant and nonresonant lasers, respectively. The pulse sequence is schematically illustrated in Fig. 3.7 (a). Initially, the nonresonant laser, denoted by (2), excites the sample for a time of $t_{\mathrm{exp}} = 60$ s. During this time period the shutter S_1 is closed, blocking the resonant laser, denoted by (1). The long exposure time is required to ensure that the maximally reachable nuclear spin polarization induced by nonresonant excitation could establish. After the exposure time t_{exp}, the shutter S_2 closes the beam path of the pump beam. Following a delay time of τ, S_1 opens the resonant probe beam for a time frame of $t_{\mathrm{m}} \approx 100$ ms. In this short time window the SFRS measurement is performed. After t_{m}, the probe beam is closed until

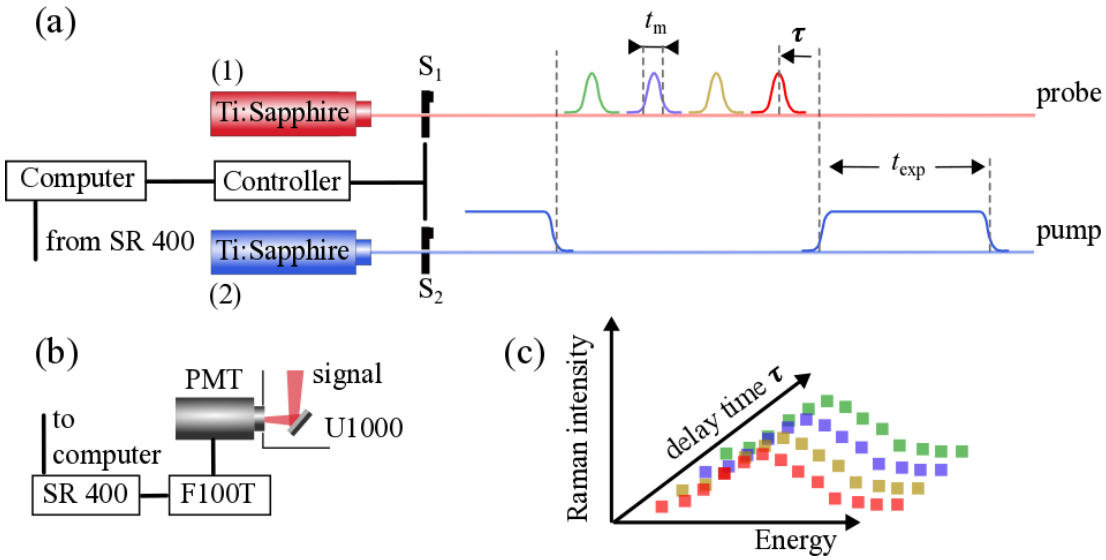

Figure 3.7: (a) Scheme of the pulse sequence in the SFRS pump-probe measurements. The pulse sequence is realized by the computer-controlled mechanical shutters S_1 and S_2, which are inserted in the beam paths of the probe (1) and pump (2) lasers. The exposure time of the pump beam is given by t_{exp}, the SFRS measurement time by t_m and the delay time of the probe beam by τ. The differently delayed probe pulses for each cycle are depicted by varying colors. (b) The light scattered from the sample is analyzed with the U1000 double spectrometer equipped with a PMT. The abbreviations and technical components are explained in the main text. (c) Scheme of the final three dimensional plot displaying the Raman intensity measured for a certain energy and delay time. The colors of the data measured at different delay times correspond to the probe pulses in (a).

the pump beam has restored back the nuclear spin polarization. The nonresonant laser repetition time is 60 s. In each cycle the delay time is increased until it reaches the repetition time of the pump beam. The differently delayed probe beams in each cycle are highlighted by varying colors in Fig. 3.7 (a). It is important to note here that both mechanical shutters have a response time of about 5 ms. The timing sequences are monitored with an oscilloscope (Tektronix, TDS2012).

The collimated light scattered from the sample is analyzed with the U1000 double spectrometer equipped with a PMT (see Fig. 3.7 (b)). As described in the previous sections, both devices ensure a high spectral resolution as well as efficient stray light rejection. The output of the photomultiplier is connected to a discriminator (F100T, Advanced Research Instruments) which rejects low amplitude pulses and forms fixed duration and amplitude pulses for each detected photon. These pulses are directed to the dual-channel gated photon counter (SR400, Stanford Research Systems) which counts the pulses at rates of up to 200MHz with a pulse-pair resolution of 5 ns. The photon counter is used instead of the U1000 control unit, as it provides a convenient way of

controlling the device via the computer and retrieving data. During the measurements, the photon counter receives a trigger signal from the computer when the shutter S_1 opens and closes, starting and, respectively, stopping the counting mode. Afterwards the data is transferred to the computer. It is worthwhile to note, that the computer works as master clock that temporally delays both the shutter pulse and starting pulse for the photon counter without external triggering. Internal delays caused by the finite lengths of the BNC connection cables, amplification and digitalization processes are negligibly small compared to the measurement times t_{m} and t_{exp}. The time resolution of the detection system is limited by the shutters response time of about 5 ms.

The decisive disadvantage of using the U1000 and PMT is that the scattering intensity can only be measured at a certain spectral wavelength for each measuring cycle. Hence, to receive a full spectrum the above presented technique has to be repeated for several spectral wavelengths (see Fig. 3.7 (c)). To ensure the laser line does not shift during this experiments, it is measured once between each spectral step. The drawback of this procedure is the huge amount of time required to investigate the time evolution of the nuclear spin polarization. Moreover, due to the short SFRS measurement time of 100 ms, the time resolved measurement has to be repeated over 10 times, in order to improve the signal to noise ratio.

If the resonant excitation does not alter the nuclear spin dynamics, the experiment can be modified to increase the measurement speed. In this respect, the probe pulse which is delayed by time τ is frequently repeated with a probe-pulse delay of t_n until the next pump pulse. In this way, the spin-flip scattering intensity can be monitored for a specific energy as function of the delay in just one cycle.

Part II

Spin-flip Raman scattering in (In,Ga)As/GaAs quantum dots

In the last decade semiconductor quantum dots (QDs) have attracted considerable interest in various scientific fields as they are considered as appealing material system for applications in spin electronics and quantum information technologies.[50,213] In order to realize solid-state quantum information applications robust quantum coherence is a major requirement. Quantum coherence in many-body systems represents the essence of entanglement and is an essential component of many intriguing phenomena in today's nanostructures.[214,215] For instance, the knowledge about quantum coherence is mandatory in order to understand the famous Aharonov-Bohm like interference oscillations of the conductance of metallic rings.[216] A possibility to achieve quantum coherence is offered for example by carrier spins in ensembles of QDs.[39]

In contrast to singly charged QDs, excitons which are usually considered for realization of quantum information applications are less convenient due to their short lifetimes.[217,218] As a result of the three-dimensional confinement of a QD to length scales small compared to the particle's wavelength the spin relaxation mechanisms related to free motion of electrons are suppressed, in turn yielding rather long spin coherence times of confined charges.[219,220] However, a major adversary, in this respect, is decoherence, that is the process by which quantum information is lost due to coupling of the system to other hard-to-control degrees of freedom in the environment, such as thermal phonons, fluctuating charges, nuclear spins etc.[21,139,221,222]

For exciton complexes in QDs, the interaction with acoustic phonons reduces the coherence even at liquid helium temperatures.[139,223,224] However, the situation differs for confined electron spins which reveal a robust electron spin coherence for a wide temperature range.[139] Previous studies on self-assembled (In,Ga)As QDs have shown that the electron spin coherence time is found to be constant up to about 20 K, while dropping fast into the nanosecond range for higher temperatures.[225,226] These results predict that coherent manipulations of carrier spins are performable also at elevated temperatures. However, only a few excitations in solid-state systems, primarily involving nuclear or carrier spins localized at deep defects, display the required robustness for coherent manipulation up to room temperature.[227,228] Nevertheless, through ultra-fast pumping of semiconductor QDs has been shown that coherent phonons can establish an interaction between quantum states in nanostructures.[229] To what extent thermal phonons also contribute to spin manipulation within the limits set for maintaining coherence has not yet been explored. In the framework of this thesis this unsolved issue is tackled by means of spin-flip Raman scattering (SFRS), whose efficiency intrinsically depends on phonons, as they mediate spin-flips and thereby orient spins. The focus of the study is placed on temperature-dependent changes in the electron-SFRS in self-assembled (In,Ga)As/GaAs QD ensembles. It is the continuation of the comprehensive studies carried out by J. Debus et al.[49,138] which investigated the spin interactions and spin dynamics in (In,Ga)As/GaAs QDs at low temperatures. The temperature-dependence of the e-SFRS is addressed in the first half of this part II.

In prospect for spintronics and applications in secure optical communications and

linear optics quantum computing, a major part of research is further directed towards the interaction mechanisms between electron and nuclear spins in QD semiconductors.[221,230–232] It is well known that nuclear spins act collectively on the electron spin via hyperfine interaction. As a result, fluctuations of the current as well as hysteresis effects due to dynamic nuclear polarization can be monitored.[233–235] In this respect, comprehensive studies of the nuclear spin dynamics have yielded spin coherence times ranging from hundreds of microseconds up to a millisecond.[236] However, despite some basic understanding, the central spin problem of a carrier spin in a nuclear spin bath, which is aggravated by its intrinsic multi-body character, is still not fully explored.[236–241]

As noted above, one common way to investigate carrier spins is spin-flip Raman spectroscopy. Recent experiments indicate though that circularly polarized laser light manipulation by resonantly exciting charged exciton complexes unavoidably affects the nuclear spins.[242–244] These nuclei spins in turn induce an effective nuclear spin-fluctuation field which depolarizes carrier-spins due to their precession around this field. This is a large drawback for SFRS which decisively depends on the manipulation of carrier spins by optical excitation. However, the reduction in the spin polarization can be suppressed by polarizing the nuclear spins. In this regard, previous studies have shown that optical pumping can be used to orient carrier spins confined in QDs whose polarization is than transferred to the nuclei spins through flip-flop processes, in turn resulting in a dynamic nuclear polarization.[245] The interplay between the dynamic nuclear polarization and the resonant SFRS of resident electrons in an ensemble of singly charged (In,Ga)As/GaAs quantum dots is addressed in the second half of this part II.

Chapter 4

Efficiency enhancement of the coherent electron SFRS

Semiconductor QDs, such as (In,Ga)As/GaAs QDs, are considered to be an attractive material system for spin electronics, as the geometric confinement leads to long spin coherence times of the confined charges. However, this spin coherence times are considerably affected by interactions in the many-body environment, e.g. with phonons. It is well known that thermal phonons play a crucial role in QW and QD semiconductors as they typically cause a rapid loss of coherence due to multiple electron-phonon interactions. These interactions occur because of the particle nature of phonons, in which the emission and absorption of phonons by electrons takes place. The probability of phonons occupying a phonon mode depends mainly on the temperature. Their distribution is determined by the Bose-Einstein statistics which states that the average number of phonons increases with rising temperature, in turn giving rise to electron-phonon interactions.

At high temperatures, excitons are unstable against collisions with thermal phonons. For instance, in GaAs/(Al,Ga)As QWs the LO-phonon energy ($\sim$ 36 meV) exceeds significantly the exciton binding energy ($\sim$ 9 meV). In the case of an exciton-phonon collision the exciton ionizes, releasing a free electron-hole pair with great excess energy. In this regard, previous studies have demonstrated that due to LO-phonon scattering at room temperature excitons live only $\sim$ 0.4 ps in GaAs/(Al,Ga)As and $\sim$ 0.3 ps in (Ga,In)As/(Al,In)As QWs.[246] Considering exciton complexes in QDs, the interaction with acoustic phonons causes a rapid loss of coherence even at liquid helium temperatures.[223] However, in the case of confined carrier spins, the spin coherence can be maintained up to temperatures of $\approx$ 20 K, as has been shown in studies on self-assembled (In,Ga)As QDs.[225,226] Therefore, also coherent manipulations of carrier spins shall be performable in this temperature range. However, to what extent thermal phonons can contribute to spin manipulation within the limits set for main-

taining coherence has not been explored so far. In this respect, this chapter of the thesis addresses the temperature-dependent changes in the electron-SFRS for self-assembled (In,Ga)As/GaAs QD ensembles.

For the sake of guidance, this chapter is divided into two sections. The first Sec. 4.1 is intended to serve as an introduction into the topic of e-SFRS in (In,Ga)As/GaAs QDs. Initially a brief description of basic properties of the e-SFRS under resonant excitation are presented. In particular, close attention is paid to the spin-flip scattering mechanism in n-doped and undoped QDs which bases on an isotropic electron-electron exchange interaction between the photogenerated and resident electron with the charged exciton complex as an intermediate scattering state. The spin-flip process becomes possible due to magnetic-field-induced symmetry reduction. Following this, in Sec. 4.2 the focus is set on the temperature-dependent changes in the e-SFRS. In this respect, the results and analysis of the SFRS are presented and afterwards the mechanism of the thermal enhancement of the e-SFRS efficiency is discussed. The enhancement is based on acoustic phonons which mediated interlevel transitions, and, thus, enhancing the spin-flip probability of the resident electron.

4.1 Characterization of the e-SFRS in (In,Ga)As/GaAs QDs

4.1.1 The experimental approach and sample details

Before addressing the basic characteristics of the SFRS, in this section a brief description of the QD samples studied is given. In the frame of this thesis three samples with self-assembled (In,Ga)As/GaAs QDs, fabricated by molecular beam epitaxy (MBE) on a (100)-oriented GaAs substrate, are investigated. These (In,Ga)As/GaAs QD samples were grown at the Ruhr-University in Bochum by Prof. Dr. A. D. Wieck's group. Their technological parameters are summarized in Tab. 4.1. The samples #1 and #2 contain 20 layers of lens-shaped QDs with a density of 10^{10} dots per cm^2. The distance between their adjacent layers amounts about 60 nm. Due to n-modulation doping with Si donors 20 nm below each QD layer, the QDs are charged by about one electron per dot

sample name	annealing Temp. (°C)	GaAs substrate	doping	density (dots/cm^2)	QD layers
14054b (#1)	920	(100)	n-doped	10^{10}	20
11955 (#2)	945	(100)	n-doped	10^{10}	20
11294 (#3)	980	(100)	undoped	10^{10}	1

Table 4.1: Technological parameters of the studied (In,Ga)As/GaAs quantum dots, which have been fabricated by MBE.

in average. The sample #3 contains only one layer of lens shaped quantum dots and is uncharged. After the growth the samples are annealed at temperatures of 920°C (#1), 945°C (#2), and 980°C (#3) leading to different QD sizes and composition profiles.

To study the spin related phenomena, i.e., the exchange interaction between the resident carriers and photogenerated excitons, the technique of SFRS is used. The general experimental approach to study the SFRS is presented in the previous chapter 3. In order to analyze the temperature-dependent changes in the electron spin-flip scattering, the measurements are performed in a wide temperature range from 1.6 K up to 80 K. The samples are attached strain free to a rotation holder and exposed to magnetic fields up to 10 T. Unless otherwise indicated, the QDs are excited by a tunable continuous-wave Ti:Sapphire laser with a typical power density of 0.5 W/cm^2. In order to minimize laser fluctuations, the laser power is stabilized by a liquid-crystal variable attenuator. The laser spot diameter is approximately 0.5 mm. Due to the spatial inhomogeneity of the QD size distributions and composition profiles which decisively influence the emission characteristics of the (In,Ga)As/GaAs QDs [49], it is necessary to ensure that all measurements are performed on the same sample spot. Therefore, each sample is covered by a mask having a hole of ≈ 150 μm diameter and the laser spot position on the sample surface is monitored during the experiments by checking the intermediate image of the sample surface (see Chap. 3). The backscattered SFRS experiments are performed in Voigt geometry ($\theta = 90°$) and in a tilted geometry, where the magnetic field $\vec{B}$ and the QD growth axis z enclosed an angle of $\theta = 15°$ within the xz-plane. The scattered light is analyzed by the double monochromator (U1000) equipped with a Peltier-cooled GaAs photomultiplier. The circular polarization characteristics of the SFRS spectra are described by the abbreviated expression ($\sigma_i^{\pm}/\sigma_s^{\pm}$). Here, $\sigma^{\pm}$ designates the circular polarization of the incident (σ_i) and scattered (σ_s) light, which is determined by the angular momentum projection on the propagation direction of the incident light.

4.1.2 (In,Ga)As/GaAs QD photoluminescence

Various optical approaches can be used to investigate the optical and electronic properties of low dimensional semiconductors as well as molecules. In this regard, one of the most commonly used techniques is photoluminescence (PL) spectroscopy. The analysis of the spectral distribution of PL emitted from a semiconductor allows one to determine nondestructively the electronic band-gap as well as radiative or nonradiative processes. It applies well to qualitatively monitor changes in material quality as a function of growth and processing conditions. For instance, it is used to study the shell structure of variably annealed QD ensembles.

The exciton PL spectrum of the studied (In,Ga)As/GaAs QDs (sample #1) at $T =$ 6 K is shown in Fig. 4.1 (a). The QDs are excited nonresonantly ($E_{\text{PL-exc}} = 1.530$ eV) above the band-gap of the wetting layer (WL). The excitation power density is set

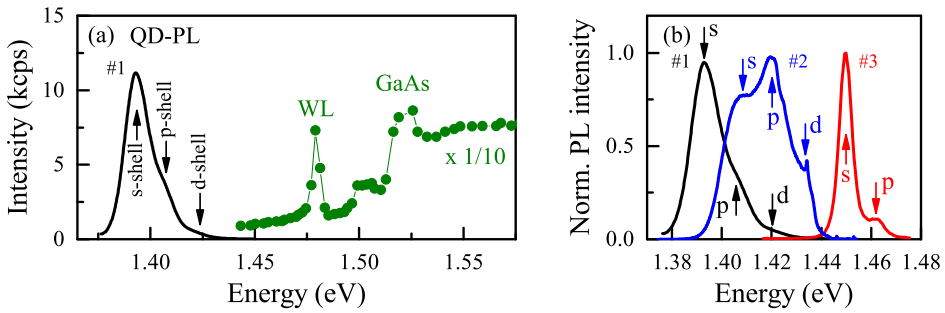

Figure 4.1: (a) PL spectrum of the (In,Ga)As/GaAs QDs (sample #1) for $B = 10$ T (Faraday, $\vec{B} \parallel z$) and $T = 6$ K. To obtain the PL spectrum the QDs have been excited nonresonantly at $E_{\text{PL-exc}} = 1.530$ eV. Further shown is the excitation-energy dependence of the intensity of the s-shell QD PL (green closed circles). To improve the overview, the PLE spectrum is downscaled by a factor of 10. The WL resonance is found at 1.480 eV, while the other PLE features can be attributed to the GaAs barrier. Adapted from Ref.[21]. (b) PL spectra of the three studied (In,Ga)As/GaAs QD samples, which have been fabricated at three different post-growth annealing temperatures. The QDs are excited above the band-gap of the WL at an energy of 1.520 eV. The measurements are performed at $B = 0$ T and $T = 6$ K. The arrows in (a) and (b) mark the s-, p-, and d-shell peaks.

to 10 W/cm^2. The depicted spectrum is measured in an external magnetic field of $B = 10$ T in Faraday geometry (Faraday, $\vec{B} \parallel z$). The QD emission due to ground state trion recombination (s-shell) is centered at 1.391 eV. The high-energy PL shoulder is attributed to the recombination of p-shell (1.406 eV) and d-shell (1.421 eV) trions. The spectral positions of these peaks are marked by arrows in Fig. 4.1 (a). The photoluminescence excitation (PLE) spectrum detected for the s-shell trion is depicted by green closed circles. By means of PLE the WL resonance of sample #1 is found at 1.480 eV. The additional features in the PLE spectrum can be assigned to the GaAs barrier.[138]

The alteration of the QD PL due to the effect of post-growth annealing is highlighted for the three studied (In,Ga)As/GaAs QD samples in Fig. 4.1 (b). As pointed out above, the PL of each QD ensemble is composed of s-, p- and d-shells which originate from the recombination of the ground and excited trion states. For a better overview, the shell structure for each QD ensemble is marked by arrows in Fig. 4.1 (b). The emission energy of the s-shell peak for the samples #1, #2, and #3 is 1.391 eV, 1.408 eV, and 1.449 eV, respectively. As can be deduced from these results, the PL spectrum shifts to higher energies with increasing annealing temperature (T_{an}). The shift is caused by an increase of the band-gap energy due to the diffusion of gallium atoms from the barrier into the QDs. This process is induced by the post-growth annealing.[247] The band-gap energy (E_{g})of the $\text{In}_x\text{Ga}_{1-x}\text{As}$ QDs with the average indium concentration

x is given by[248]:

$$E_{\mathrm{g}} = 0.417 \cdot x + 1.519 \cdot (1 - x) - 0.477 \cdot x \cdot (1 - x). \tag{4.1}$$

In order to estimate the indium concentration in the studied QD samples the s-shell peak energy is used in first approximation for the band-gap energy. Hence, the Indium concentration of the studied QDs amounts 0.084 (#1), 0.076 (#2), and 0.045 (#3).

It is well known from previous studies[247] that higher annealing temperatures facilitate the flattening of QDs, resulting in an increase of the QD diameter. In turn, this leads to a reduction of the lateral confinement. In first approximation the lateral confinement energy can be estimated from the energy difference between the trion s- and p-shell emission. Hence, the PL spectra shown in Fig. 4.1 (b) indicate confinement energies of 14.1 meV (#1), 11.2 meV (#2), and 9.8 meV (#3). This result underlines that the confinement energy decreases for higher T_{an}. The degree to which the confinement is influenced by the bath temperature is described in Sec. 4.2. It is worth to note that the displayed PL profiles demonstrate a narrowing of the PL line width with increasing annealing temperature. For instance, the FWHM of the s-shell peak decreases from 10.2 meV (#1) down to 5.0 meV (#3). This result indicates that the distribution of QD sizes is more homogenous for high T_{an}.

4.1.3 Spin-flip scattering mechanism of the resident electron spin in (In,Ga)As/GaAs QDs

After this rough analysis of the PL, next the focus is set on the basic properties of the SFRS under resonant excitation of the trion. In this regard, the initial emphasis is placed on the analysis and exploration of the SFRS mechanism in the n-doped QD ensembles. Following this, the SFRS in the undoped QDs will be discussed.

As described in Sec. 2.4.3, an SFRS spectrum is typically composed of lines which shift from the laser excitation energy in the vicinity of an external magnetic field. Here, the shift is described by the Zeeman splitting of spin states (see Sec. 2.1.5). For instance, typical SFRS spectra of the studied (In,Ga)As/GaAs QDs in regard of a resonant excitation ($E_{\mathrm{exc}} = 1.396$ eV) of the high-energy flank of the s-shell QD emission (sample #1) are presented in Fig. 4.2 (a). The depicted spectra are measured at $T = 6$ K and $B = 6$ T in the co-polarized (σ^+/σ^+) and (σ^-/σ^-) as well as cross-polarized (σ^+/σ^-) and (σ^-/σ^+) configurations in a tilted geometry, where the magnetic filed $\vec{B}$ and the QD growth axis z enclosed an angle of $\theta = 15°$.

For these excitation conditions, the spin-flip Raman lines on the Stokes and anti-Stokes side are observable on a background contributed by PL. The spin-flip Raman lines are dominant in the (σ^-/σ^-) and (σ^+/σ^+) polarization configuration on the anti-Stokes and Stokes side, respectively. The cross-polarized spectra demonstrate only

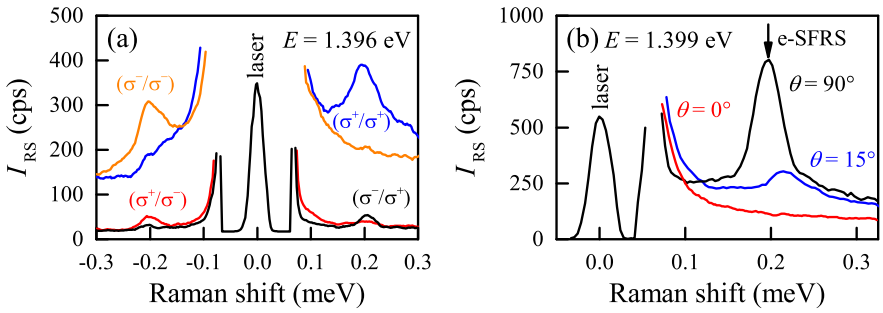

Figure 4.2: (a) Circularly cross- and co-polarized SFRS spectra of sample #1, excited resonantly on the high-energy flank of the s-shell QD emission ($E_{\mathrm{exc}} = 1.396$ eV) in tilted geometries ($\theta = 15°$). The laser line is at zero Raman shift. The most intensive electron spin-flip Raman lines are observed in co-polarized configurations. (b) SFRS Stokes spectra of sample #1 measured in Faraday ($\theta = 0°$, red curve), Voigt ($\theta = 90°$, black curve), and oblique magnetic geometry ($\theta = 15°$, blue curve). The QD ensembles are excited at the s-shell maximum of the QD emission ($E_{\mathrm{exc}} = 1.391$ eV). All spectra in (a) and (b) are measured at $T = 6$ K and $B = 6$ T. The laser power density is set to 0.5 W/cm^2.

weak SFRS intensities in both regimes. In this regard, the SFRS intensity on the anti-Stokes side is 3 times higher in (σ^-/σ^-) than in (σ^+/σ^-). However, the shift of the Raman lines exhibits no change. It equals $|\Delta E_{\mathrm{SF}}| = (0.22 \pm 0.01)$ meV for scattering to lower and higher energies. Taking into consideration the Zeeman splitting $|g|\mu_{\mathrm{B}}B$ (see Eq. (2.35)), these Raman shifts correspond to a g factor of (0.59 ± 0.03).

In order to further determine the origin of these Raman lines, the SFRS Stokes spectra are investigated for different geometries. The resulting spectra for Faraday, Voigt, and tilted geometries ($\theta = 15°$) are presented in Fig. 4.2 (b). The results pertain sample #1 and are measured in (σ^+/σ^+) polarization configuration at $T = 6$ K and $B = 6$ T. The excitation energy is tuned into resonance with the s-shell maximum of the QD emission ($E_{\mathrm{exc}} = 1.391$ eV). The resulting spectra demonstrate that an SFRS signal is absent in Faraday geometry. Only by tilting the magnetic field direction with respect to the QD growth axis a spin-flip Raman line becomes apparent on the Stokes side, as can be seen by the blue curve measured at small tilting angles of $\theta = 15°$ shown in Fig. 4.2 (b). A further increase of the tilting angle leads to a continuous increase of the SFRS intensity, while reaching the maximum in Voigt geometry ($\vec{B} \perp z$). From the results can be, furthermore, deduced that the geometry alters the Raman shift of the spin-flip Raman line. In Fig. 4.2 (b) one observes that the Raman shift amounts approximately (0.218 ± 0.005) meV in close to Faraday geometry, while decreasing down to (0.195 ± 0.005) meV in Voigt. Hence, the in-plane g factor equals in first approximation $|g_\perp| = 0.53$.

Beside the strong symmetry dependence of the spin-flip Raman line further the efficiency of interaction in dependence on the chosen excitation energy is important.

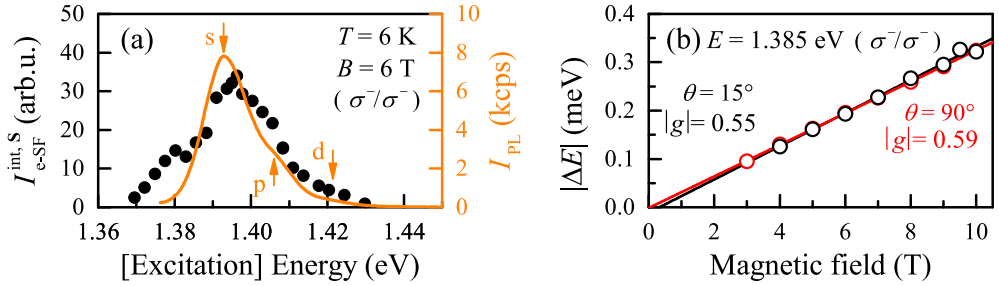

Figure 4.3: (a) SFRS resonance profile (closed circles, left y-axis) and the related QD PL (black solid line, right y-axis) for sample #1 at $B = 6$ T and $T = 6$ K in close to Faraday geometry ($\theta = 15°$). The integral spin-flip intensity ($I^{\mathrm{int,S}}_{\mathrm{e\text{-}SF}}$) is determined from SFRS Stokes spectra measured in (σ^+/σ^+) polarization configuration. The error in the integral SF intensity does not exceed the symbol size. The arrows mark the s-, p-, and d-shell PL peaks. The maximum of the SFRS profile centered at (1.398 ± 0.03) eV deviates slightly from the s-shell PL peak at (1.392 ± 0.02) eV. (b) Raman shift of the electron spin-flip Raman line in dependence on the magnetic field in tilted ($\theta = 15°$, black open circles) and Voigt geometry (red open circles). The depicted results pertain the QD ensemble #1 regarding a resonant excitation of the low-energy flank of the trion s-shell ($E_{\mathrm{exc}} = 1.385$ eV). The error in the Raman shift does not exceed the symbol size. The fitting (black and red-colored) curves based on Eq. (2.35) demonstrate that the zero-field offset is negligible.

Therefore, the SFRS resonance profile is investigated which represents the dependence of the spin-flip Raman line intensity on the excitation energy. The spin-flip Raman resonance profile of the QD ensemble #1 is shown in Fig. 4.3 (a). The related spectra are measured in close to Faraday geometry ($\theta = 15°$) at $B = 6$ T and $T = 6$ K. The closed circles indicate the SFRS intensities while the orange solid line gives the PL spectra. For a better overview, the shell structure of the QD ensemble is indicated by arrows. One can deduce from the spectral profile that the SFRS efficiency almost coincides with the PL intensity. In this regard, the spin-flip Raman line can be monitored over the whole width of the PL spectrum, i.e., from 1.37 eV up to 1.43 eV. This also applies to the QD samples #2 and #3 which are annealed at higher temperatures (not shown here). However, at $B = 6$ T, the maximum of the SFRS intensity is centered between the s- and p-shell of the QD PL. Here, one obviously monitors that the maximum of the PL and SFRS intensity profile do not coincide. In this respect, previous studies have reported that for small tilting angles and rising magnetic field the maximum of the SFRS efficiency shifts faster towards higher energies than the PL.[138] This shift, which follows the electron cyclotron energy, is enhanced for QD samples with smaller lateral confinement. Hence, it is assigned to a hybridization of s-shell singlet and p-shell triplet states of the negatively charged excitons. In the frame of the SFRS temperature dependence the origin of this effect will be investigated in more detail.

According to previous studies, it is furthermore reported that the g factor smoothly varies with the energy.[138] It is shown that the g factor increases for lower excitation

energies, i.e., for smaller QD diameters with stronger lateral confinement, underlining that it is predominantly determined by the band-gap.[249] In order to determine precisely the corresponding Landé factor, the Raman shift of the spin-flip line on the Stokes side is investigated for close to Faraday ($\theta = 15°$) and Voigt geometry as a function of the magnetic field. The results regarding a resonant excitation ($E_{\mathrm{exc}} = 1.385$ eV) of the low-energy flank of the trion s-shell (sample #1) in co-circular (σ^-/σ^-) polarization configuration are presented in Fig. 4.3 (b). As can be deduced from these results, the absolute Raman shifts ($|\Delta E|$) of the Stokes spin-flip Raman lines show approximately linear magnetic field evolutions. The data demonstrate only minor fluctuations of the Raman shift which are basically of the same order of magnitude as the measurement error. In spite of this, a discrepancy between the two geometries is monitored. One observes a through-out smaller Raman shift in Voigt than in close to Faraday geometry. To determine the corresponding Landé factors, a linear least square fit to the data according to Eq. (2.35) is conducted. This yields Landé factors of $g_{15°} = 0.55$ and $g_{\perp} = 0.59$. From the linear extrapolation of the experimental data, the zero-field offset can be deduced, amounting $\Delta E_{\mathrm{off},15°} = (-19 \pm 20)$ μeV and $\Delta E_{\mathrm{off},\perp} = (1 \pm 12)$ μeV. These offsets are in the range of the measurement error, indicating that the zero-field offset is negligible.

The anisotropy of the g factor and the angular dependence of the SFRS intensity indicate that the Raman line monitored is attributed to a spin-flip of an electron.[21,49,138,139] The estimated g factor is in good agreement with recently performed pump&probe measurements on (In,Ga)As/GaAs QDs.[250,251] Moreover, it is worth to note that the weak anisotropy of the electron g factor is characteristic for QDs, whereas heavy-hole and excitons typically exhibit strong anisotropic g factors.[251]

Based on the experimental results, which are presented above, the electron spin-flip scattering process can be exploited. The responsible mechanism is suggested by J. Debus et al. in a recent publication which addressed the SFRS of resident electron spins in singly charged QDs.[138] It is reported that due to a symmetry reduction for the negatively charged exciton, which is induced by the applied magnetic field, the spin-flip Raman scattering of the resident electrons trapped in a QD becomes allowed. Here, the electron spin-flip is mediated by the isotropic electron-electron exchange interaction, which requires the magnetic field induced mixing of the electron states in tilted geometries.[138] In more detail the mechanism of the e-SFRS will be elaborated next.

In general the SFRS process can be evaluated by analyzing the selection rules for electric dipole transitions, as it is theoretically described in Sec. 2.4.3. These selection rules can be deduced from the circularly polarized Raman spectra. As has been experimentally shown (see Fig. 4.2 (a)), the electron SFs are predominantly observed in the co-circular polarization configurations (σ^-/σ^-) and (σ^+/σ^+). This means that the polarization of the incident light is equal to that of the scattered light. Hence, the photogenerated excitons, i.e., electron-hole pairs, have the same spin orientation before

and after the spin-flip process. The experiments reveal further that a very weak spin-flip can be observed in cross-polarized configuration as well. However, the respective Raman shift in comparison to the spin-flip line in co-polarization is unaltered.

The first step is to explore the spin-flip process in Faraday geometry. Despite the fact that the admixture of light and heavy-holes is present in the studied QD ensembles[251], for simplicity it is assumed that the valence-band ground state has heavy-hole character. After photo excitation, e.g. by circularly polarized light (σ^+), an electron-hole pair, with an electron in the spin down state $|-1/2\rangle = |\downarrow\rangle$ and a heavy-hole in the spin up state $|+3/2\rangle = |\Uparrow\rangle$, is excited. This state reads $|\Uparrow\downarrow\rangle$. However, this excitation can only take place when the resident electron located inside the QD which is provided by the modulation doping with Si donors has the opposite spin orientation $|+1/2\rangle = |\uparrow\rangle$, since otherwise the excitation would be blocked by the Pauli exclusion principle. Hence, the exciton and resident electron form a trion state which can be expressed by $|+3/2,-1/2,+1/2\rangle = |\Uparrow\downarrow\uparrow\rangle$ with the total angular momentum projection $L = +3/2$. Since the two electrons form a singlet state, a spin-flip by one of the carriers is forbidden by Pauli exclusion principle. Therefore, in Faraday geometry an electron spin-flip shall not be experimentally observable. This is in good agreement with the results shown in Fig. 4.2 (b), which demonstrate that the spin-flip Raman line is absent in Faraday geometry.

The situation, however, changes when the magnetic field direction gets tilted with respect to the QD growth axis z. This is because of the fact that a quantum dot generally posses rotational symmetry about its growth axis and, therefore, its symmetry can be described by the irreducible representation D_{2d}. Hence, in oblique magnetic fields the restrictions of selection rules are lifted by mixing the optically bright and dark excitons, i.e., the electron spin basis eigenstates.[33,36,252] Since the heavy-hole does not poses a magnetic moment which is perpendicular to the growth direction z, the mixing is established via the transverse electron g factor.[190] Hence, the spin state of the resident electron in a tilted magnetic field can be written as

$$\alpha\,|\uparrow\rangle \pm \beta\,|\downarrow\rangle = \cos(\theta/2)\,|\pm 1/2\rangle \pm \sin(\theta/2)\,|\mp 1/2\rangle, \tag{4.2}$$

with $|\alpha|^2 + |\beta|^2 = 1$.[33] The mixing coefficients α and β depend on the tilting angle θ between the magnetic field $\vec{B}$ and the growth axis z. Assuming now an excitation with (σ^+) polarized light only one component of the resident electron is excited. The superposition state of the trion is given by $\alpha\,|\Uparrow\downarrow\uparrow\rangle + \beta\,|\downarrow\rangle$. Due to isotropic exchange interaction between the resident electron and the photo-excited electron, a spin-flip can occur in the second component, resulting in the intermediate state $\alpha\,|\Uparrow\uparrow\downarrow\rangle + \beta\,|\uparrow\rangle$. When the hole spin remains unaffected during this scattering process, the annihilation of the trion yields the emission of a photon with the same polarization as the incident. Due to this spin-flip process the electron spin has become obviously oriented ($|\uparrow\rangle$). The difference between the incident and scattered photon energies is equal to the Zeeman energy $|g|\mu_B B$ (see Eq. (2.35)). In this case the electron g factor is determined by the Zeeman splitting between the electron spin states ($|\uparrow\rangle$ and $|\downarrow\rangle$).

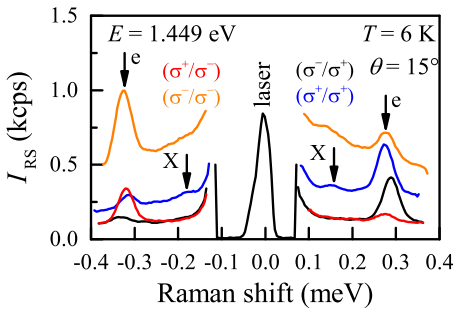

Figure 4.4: (a) Circularly cross- and co-polarized SFRS spectra of the undoped QD ensemble #3, excited resonantly on the low-energy flank of the s-shell QD emission ($E_{\mathrm{exc}} = 1.449$ eV) in tilted geometries ($\theta = 15°$). The spectra are measured at $T = 6$ K and $B = 10$ T. The laser power density is set to 1.1 W/cm^2. The laser line is at zero Raman shift. The arrows mark the peak positions of the electron (e) and exciton (X) spin-flips. Electron spin-flips can be monitored in all spectra, whereas the exciton is only apparent in both co-polarization configurations.

The illustrated spin-flip process is in good agreement with the experimental observations and, thus, highlights the origin of the co-polarized spin-flip Raman lines on the Stokes side as well as on the anti-Stokes side. However, it cannot be used to explain the spin-flip in cross-polarized configuration. According to Ref. [138] the process requires the flip of the heavy-hole spin, which is mediated by the anisotropic exchange interaction between the nonexcited electron and hole. The interaction strength is given by the product of the electron spin ($\mathbf{S}_{\mathrm{e}}$) and the third power of the hole angular momentum ($\mathbf{J}_{\mathrm{h}}$), $\mathbf{S}_{\mathrm{e}} \cdot \mathbf{J}_{\mathrm{h}}^3$.[138,191] After the flip-flop process the state in the intermediate scattering process reads $\alpha\,|\Downarrow\uparrow\downarrow\rangle + \beta\,|\uparrow\rangle$. In this case the annihilation of the trion yields the emission of σ^- polarized light. After this spin-flip process the resident electron is left in the reversed spin state ($\alpha\,|\downarrow\rangle + \beta\,|\uparrow\rangle$), while the shift of the Raman line is once again determined by the Zeeman splitting between the electron spin states.

Before turning the focus towards the temperature-dependent changes, in the following, briefly the spin-flip scattering in undoped QDs is discussed. In contrast to n-doped QD ensembles, the absence of resident electrons alters obviously the scattering mechanism. The scattering process can no longer be determined by charged excitons, but rather involves neutral excitons. In order to provide a better understanding of the underlying process the SFRS spectra of the studied undoped (In,Ga)As/GaAs QDs in regard of a resonant excitation ($E_{\mathrm{exc}} = 1.449$ eV) of the low-energy flank of the s-shell QD emission (sample #3) is shown in Fig. 4.4. The depicted spectra are measured at $T = 6$ K and $B = 10$ T in the co-polarized and cross-polarized configurations in a tilted geometry ($\theta = 15°$).

The results indicate that the electron spin-flip Raman line is visible in all polarized Raman spectra on the Stokes side as well as on the anti-Stokes side. The relative ratio of the SFRS intensities ($I^{+/+} : I^{+/-} : I^{-/+} : I^{-/-}$) for the different polarization

configurations is approximately given by (0.13 : 0.53 : 0.08 : 1), for the anti-Stokes regime, and (1 : 0.10 : 0.95 : 0.35), for the Stokes regime. This ratio indicates that the electron spin-flip is dominant on the anti-Stokes side when the angular momentum of the outgoing light equals $L = -1$, i.e., the emitted photon is (σ^-) polarized, whereas it is most pronounced on the Stokes side for light with the angular momentum of $L = +1$, i.e., the emitted photon is (σ^+) polarized. Furthermore, one can deduce from the depicted spectra that the electron spin-flip peak intensity in the Stokes regime is about a factor of 1.5 smaller than in the anti-Stokes regime. In regard of the phonon distribution which is determined by the Bose-Einstein statistics, the intensity ratio demonstrates that the electron spin temperature amounts about 5.5 K. This is in good agreement with the temperature of the surrounding He-gas of 6 K.

The Raman shift of the electron spin-flip line equals $|\Delta E^{\mathrm{S}}_{\text{e-SF}}| = (0.32 \pm 0.03)$ meV and $|\Delta E^{\mathrm{S}}_{\text{e-SF}}| = (0.29 \pm 0.03)$ meV for scattering to lower and higher energies, respectively. These values correspond to an electron g factor of about (0.55 ± 0.02) for the anti-Stokes regime and (0.52 ± 0.02) for the Stokes regime. This results are in good agreement with previous studies of undoped InGaAs QDs.[251,253] In addition to the electron spin-flip line in Fig. 4.4, one can clearly monitor a further spin-flip Raman line with a smaller Raman shift of about (0.16 ± 0.02) meV. This Raman line also demonstrates an linear magnetic field evolution, but tends to an offset of (0.09 ± 0.01) meV at zero magnetic field for $\theta = 15°$ (not shown here). The corresponding g factor amounts (0.12 ± 0.02). According to Ref. [251], the g factor value as well as the zero-field offset evidence that this Raman line stems from the neutral exciton (X).

As mentioned above the scattering mechanism of the electron spin-flip in undoped QDs is not determined by negatively charged excitons, but rather by neutral excitons as evidenced by the appearance of the exciton spin-flip in the Raman spectra shown in Fig. 4.4. The related SFRS process in a neutral exciton is described in-depth in Sec. 2.4.3. Herein, the spin-flip process of the electron and holes is mediated by acoustic phonons.[36] It competes with the electron-hole exchange interaction, which provides a stabilization of the electron spin along the QD growth axis. However, for tilted geometries the Zeeman splitting of the electron spin states becomes larger than the electron-hole exchange energy, in turn enhancing the probability of an electron spin-flip. Hence, the maximal SFRS efficiency is obtained for Voigt geometry.

In conclusion, the analysis of the basic SFRS properties has highlighted that in singly charged (In,Ga)As/GaAs QDs the spin-flip scattering of the resident electron is realized by isotropic electron-electron exchange interaction. In the case of undoped QDs the electron-phonon interaction, which exceeds greatly the electron-hole exchange, contributes to the spin-flip scattering. The major requirement for single spin-flip scattering processes in both types of QDs is the reduction of the trion or exciton symmetry by a magnetic field tilted with respect to the QD growth axis. The spin-flip scattering efficiency is maximal for magnetic fields applied perpendicular to the QD growth axis and furthermore gets greatly enhanced in the case of singly charged QDs. To which extent

the temperature influences the spin-flip scattering mechanism and e-SFRS efficiency is addressed in the next section.

4.2 Temperature dependence of the coherent electron SFRS in (In,Ga)As/GaAs QDs

In the following the effect of temperature induced enhancement of the coherent e-SFRS in singly charged and undoped (In,Ga)As/GaAs QDs will be discussed. To get a first impression of how an increase in temperature affects the optical properties of the studied QDs, initially the temperature dependent changes of the nonresonantly excited QD PL are analyzed (see Sec. 4.2.1). The focus is subsequently directed towards the polarization properties and efficiency enhancement of the spin-flip scattering at elevated temperatures (see Sec. 4.2.2 -4.2.3). In this regard, all factors which might impact the scattering process are assayed. Furthermore, it is analyzed to which extent the generation of additional carriers by additional high-energy illumination influences the efficiency of the e-SFRS. In the last Sec. 4.2.5, the mechanism of the thermal enhancement is discussed. Hereby close attention is directed towards phenomena in self-assembled QDs which could be excluded as relevant mechanisms. It is important to point out that a part of the results and conclusions presented in this section has been published (see Ref. [139]).

4.2.1 Temperature dependence of the QD photoluminescence

Following the basic description of the QD PL presented in Sec. 4.1.2, next its temperature dependence is analyzed. To illustrate briefly the influence of elevated temperatures, the nonresonantly excited QD PL of the singly charged (sample #1) and undoped (sample #3) QD ensembles are shown in Figs. 4.5 (a) and (b). In these measurements the QDs are excited nonresonantly ($E_{\text{PL-exc}} = 1.530$ eV) above the band-gap of the WL. The excitation power density is set to 1 W/cm^2. The depicted spectra are measured at $B = 6$ T in Voigt geometry.

Concerning the singly charged QDs at 6 K (see Fig. 4.5 (a)), the QD emission due to ground state (s-shell) trion recombination is centered at about 1.400 eV, while the emission of the first (p-shell) and second (d-shell) excited state is observable around 1.413 eV and 1.426 eV, respectively. For a better overview the shells are marked by arrows in Figs. 4.5 (a) and (b). When the bath temperature is increased up to 40 K, one monitors a shift of the QD PL to lower energies. In reference to the peak maximum of the trion s-shell at 6 K, the PL is redshifted in energy by approximately 2 meV for 40 K and 11 meV for 100 K. The energy shift of the trion s-shell is depicted in Fig. 4.5 (d).

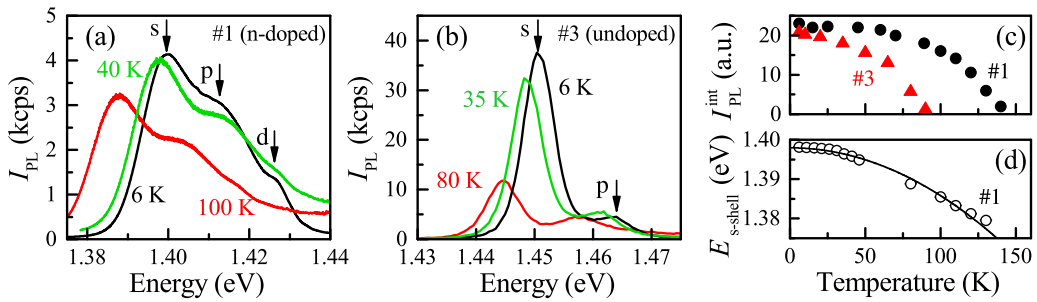

Figure 4.5: (a) PL spectra of the singly charged (In,Ga)As/GaAs QD ensemble #1 measured at $T = 6$ K, 40 K, and 100 K. Adapted from Ref. [139].(b) PL spectra of the undoped QD ensemble #3 measured at $T = 6$ K, 35 K, and 80 K. To obtain the PL spectrum in (a) and (b) the QDs are excited nonresonantly at $E_{\text{PL-exc}} = 1.530$ eV at $B = 6$ T in Voigt geometry. The excitation power density is set to 1 W/cm^2. The arrows mark the s-, p-, and d-shell peaks. (c) PL intensity integrated over the s-, p- and d-shell spectral range as function of the bath temperature. The closed black circles pertain the QD ensemble #1, whereas the closed red triangles are related to the undoped QD ensemble #3. (d) Emission energy of the trion s-shell of singly charged QD ensemble #1 (black open circles) in dependence on the temperature. The fitting curve (solid black line) is based on the Varshni's empirical expression depicted in Eq. (4.3).

In is well known that the band-gap energy of semiconductors decreases with increasing temperature, since the temperature significantly influences the phonon distribution due to the Bose-Einstein statistics, and, thus, enhancing the amplitude of atomic vibrations.[254] The interaction between phonons and electrons or holes affects markedly the band-gap energy in low dimensional systems. The relationship between the band-gap energy and temperature is theoretically described by Varshni's empirical expression[255]:

$$E_{\text{G}}(T) = E_0 - \frac{\alpha T^2}{(T+\beta)}, \tag{4.3}$$

where E_0 is the band-gap energy at $T = 0$ K and α, β are fitting parameters characteristic of a given material. By means of the Varshni equation the shift of the trion s-shell can be modeled. From a fit to the data, which is shown in Fig. 4.5 (d), one obtains a band-gap energy of $E_0 = (1.398 \pm 0.001)$ eV. As the results highlight the Varshni formula may be used with good effect to fit the temperature dependence of the band-gap.

In comparison to the singly charged QDs, the PL of the undoped QDs exhibits a similar temperature dependence (see Fig. 4.5 (b)). Here, the QD emission peaks at $T = 6$ K attributed to the s- and p-shell are centered at about 1.451 eV and 1.464 eV, respectively. Both lines demonstrate a redshift of 7 meV at 80 K. However, the peak intensity of the trion s- and p-shell decreases significantly faster. In order to highlight this, The PL intensity integrated over the s-, p- and d-shell spectral range for the n-

doped and undoped QD ensembles is shown as function of temperature in Fig. 4.5 (c). In the case of the n-doped QDs, one observes that the PL does not significantly vary with increasing temperature up to about 60 K. For larger temperatures, the QD emission weakens gradually and vanishes at about 145 K. On the contrary, for the undoped QDs the PL starts to decrease already at 6 K and finally vanishes at about 85 K. This temperature evolution of the PL intensity is associated with the thermally induced dissociation of the trions due to carrier escape from the QDs. According to Ref. [256], this process can be modeled by evaluating the rate equations for carrier capture and escape from a QD. This leads to the Arrhenius-like equation for the intensity [256]:

$$I(T) \propto \exp\left(\frac{E_a}{k_{\mathrm{B}}T}\right). \tag{4.4}$$

Here, E_a describes the activation energy and k_{B} the Boltzmann constant. Using this equation to model the decrease of the integral PL intensity as function of the bath temperature shown in Fig. 4.5 (c), one obtains for the n-doped and undoped QD ensembles the activation energy of $E_a = (15 \pm 3)$ meV and $E_a = (8 \pm 2)$ meV, respectively. In QD structures with a larger diameter, i.e., smaller lateral confinement energy, the dissociation of the trions occurs faster. If one estimates in first approximation the lateral confinement energy from the energy difference between the trion s- and p-shell emission, one obtains for the n-doped and undoped QDs at 6 K approximately 14.1 meV and 9.8 meV, respectively. These values are in good agreement with the activation energies.

4.2.2 Polarization properties of the e-SFRS at elevated temperatures

Following the brief analysis of the PL temperature dependence presented in the last section, the focus is shifted now towards the polarization properties of the e-SFRS at elevated temperatures. In this regard, the emphasis is placed on the analysis of the SFRS in the singly charged QD ensembles. In order to investigate the temperature dependence of the e-SFRS polarization properties, SFRS spectra at a bath temperature of $T = 22$ K and $T = 40$ K are investigated. In these experiments, care is taken to ensure that all parameters, i.e., excitation energy, power density and external magnetic field strength, remain constant.

The resulting SFRS spectra pertaining the singly charged QD ensemble #1 measured in co- and cross-polarized configurations are shown in Figs.4.6 (a) and (b) for $T = 22$ K and 40 K, respectively. The QDs are excited resonantly ($E_{\mathrm{exc}} = 1.396$ eV) on the low-energy flank of the s-shell QD PL in a tilted geometry ($\theta = 15°$). In comparison to the e-SFRS spectra presented in Sec. 4.1.3, one observes that the polarization properties of the e-SFRS are temperature independent. At all three temperatures the intensity ratio ($I^{+/+} : I^{+/-} : I^{-/+} : I^{-/-}$) of the e-SFRS intensities is given by approximately (1 : 0.19 : 0.27 : 0.19) for the Stokes regime and (0.19 : 0.30 : 0.16 : 1) for the anti-Stokes regime. Moreover, one observes that the electron spin-flip Raman line does not demonstrate a temperature-dependent energy shift. As can be deduced

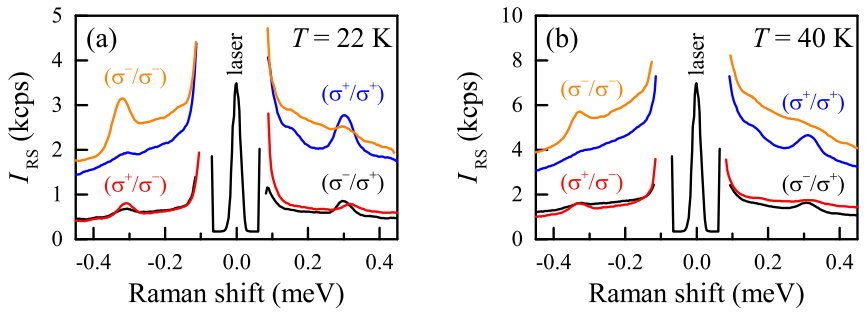

Figure 4.6: Circularly cross- and co-polarized SFRS spectra of sample #1 at $B = 10$ T for $T = 22$ K (a) and 40 K (b). The QD ensembles are excited resonantly ($E_{\mathrm{exc}} = 1.396$ eV) on the low-energy flank of the s-shell QD PL in tilted geometries ($\theta = 15°$). The laser line is at zero Raman shift.

from the SFRS spectra in Figs. 4.6 (a) and (b), the electron spin-flip is centered at about $|\Delta E| = (0.312 \pm 0.004)$ meV. The temperature independence of the Raman shift, Stokes-to-anti-Stokes scattering ratio and optical selection rules indicate that the spin-flip scattering mechanism in the investigated temperature range has not altered. However, if one compares the integral spin-flip intensity for the different temperature ranges, one finds that the spin-flip efficiency becomes greatly enhanced with increasing temperature. For instance, the SFRS intensity increases by a factor of about 7 from $T = 6$ K up to 22 K. This strong enhancement will be discussed in detail in Sec. 4.2.3.

It is worthwhile to mention, here, that the e-SFRS signal does not appear in exact Faraday geometry when the bath temperature is increased. Hence, one can conclude that a mixing of electron spin basis eigenstates, which might intensify the electron spin-flip efficiency and also give rise to an electron spin-flip in a scattering-forbidden symmetry, is not thermally activated.

For the undoped QDs investigated, a change in the spin-flip mechanism or an increase in SFRS efficiency may be expected, since the electron spin-flip scattering process is mediated by phonons whose probability of occurrence rises with increasing temperature. As described above, the temperature significantly influences the phonon distribution due to the Bose-Einstein statistics. Hence, it may provide the scattering of the electron spin-flip. However, this effect is not observed in the experiments. The undoped QDs demonstrate almost the same behavior as it is observed for singly charged QDs. For instance, the Raman shift, Stokes-to-anti-Stokes scattering ratio as well as the optical selection rules are not altered at higher temperatures. These findings indicate that the spin-flip scattering mechanism is also unaffected in regard of undoped QD ensembles.

4.2.3 Temperature dependence of the resident e-SFRS intensity

The above mentioned thermally induced increase in SFRS efficiency is the main topic within this section. To initially illustrate the impact of temperature on the e-SFRS, the Stokes and anti-Stokes electron spin-flip lines are presented as function of the bath temperature as image plots in Figs. 4.7 (a) and (b). The results pertain the singly charged QD ensemble #1. The related SFRS spectra are measured at $B = 6$ T in Voigt (a) and at $B = 10$ T in tilted (b) geometries, regarding a resonant excitation of the high-energy flank of the trion s-shell emission. The SFRS image plot on the Stokes side is shown for the co-polarized (σ^+/σ^+) configuration, whereas the one on the anti-Stokes side is presented for the (σ^-/σ^-) configuration.

From the evolution of the SFRS spectra, shown in Fig. 4.7 (a) can be deduced that the electron spin-flip reveals the same characteristics in the Stokes and anti-Stokes regime. The Stokes-anti-Stokes intensity ratio does not vary throughout the temperature range measured. For instance, the spin-flip intensity of the line on the Stokes side is approximately 10% smaller than the anti-Stokes line. Considering the spin-flip intensity, below $T = 10$ K the spin-flip Raman lines are relatively weak (≈ 200 cps), while intensifying decisively up to about 1400 cps at 28 K. Hence, the intensity gets enhanced by a factor of 7. When the temperature is increased further the intensity of the spin-flip Raman lines diminishes. Above 55 K, a electron spin-flip can no longer be monitored. Furthermore, the image plots highlight that the absolute Raman shift of about (185 ± 10) μeV does not change with increasing temperature. Considering the background in the SFRS spectra, one can obviously monitor that it enhances from ≈ 150 cps at 6 K up to ≈ 1200 cps at 60 K. The background is attributed to acoustic phonon scattering. It will be described in detail within the scope of Sec. 4.2.3. It is worthwhile to mention that the intensity demonstrates a sharp dip at about 18 K. This feature is reproducible and shows up only for probing the s-/p-shell and p-shell trion. The magnetic field dependence and origin of this dip will be discussed later.

To demonstrate the impact of the magnetic field geometry on the efficiency of the SFRS enhancement, the temperature evolution of the electron spin-flip line on the Stokes side in a tilted geometry is presented in the image plot in Fig. 4.7 (b). A direct comparison with the image plot in Fig. 4.7 (a) reveals immediately that the spin-flip intensity enhancement is significantly weaker. Below $T = 8$ K the spin-flip line demonstrates an intensity of about 250 cps, while intensifying up to about 500 cps at 25 K. For $T > 25$ K the spin-flip intensity diminishes gradually and vanishes above 50 K. The absolute Raman shift of the e-SFRS does not show any alteration throughout the temperature range measured, as it has been shown for Voigt geometry. One observes, further, that the SFRS background is less sensitive to a change of temperature. In this respect, the scattering background increases only weakly by about 200 cps from 6 K to 50 K.

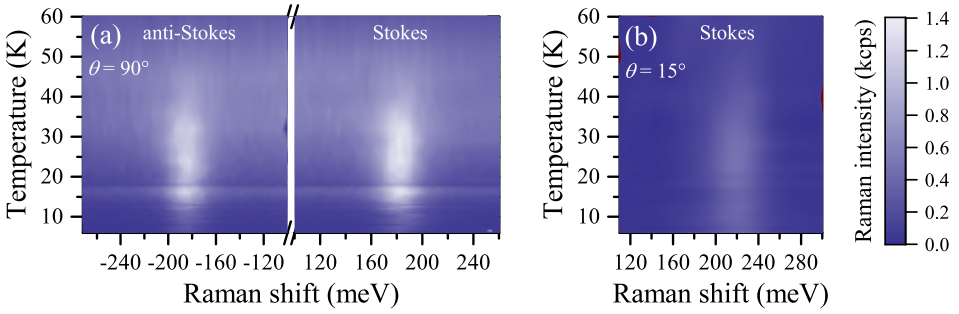

Figure 4.7: Image plots of the temperature-dependent intensity of the electron spin-flip line for the Stokes (σ^+/σ^+) and anti-Stokes (σ^-/σ^-) regime, measured at $B = 6$ T in Voigt (a) and at $B = 10$ T in tilted (b) geometries ($\theta = 15°$). The QD ensembles are excited resonantly ($E_{\mathrm{exc}} = 1.406$ eV) on the high-energy flank of the s-shell QD PL. The laser line area from -100 μeV to $+100$ μeV is excluded from the image plot. The image plot shown in (a) is adapted from Ref. [139].

To distinguish to what extent the excitation energy affects the enhancement of the e-SFRS, spin-flip resonance profiles of the singly charged and undoped QD ensembles are investigated at different temperatures. The results are presented in Figs. 4.8 (a) and (b). The resonance profiles are measured at $B = 6$ T in Voigt geometry. In the following the focus is shifted first towards the resonance profile of the singly charged QD ensemble (#1) (see Fig. 4.8 (a)). An analysis of the spin-flip resonance profile demonstrates that its shape coincides well with the PL spectrum shown in Fig. 4.5 (a) and, furthermore, clearly reflects the QD-shell structure. In this context, the maximum of the resonance profile centered at about 1.405 eV is attributed to the trion s-shell, while the high energy shoulder at about 1.421 eV belongs to the trion p-shell. The spin-flip Raman line can be monitored over the whole width of the PL spectrum from 1.37 eV up to 1.43 eV. Moreover, the results show that an increase of the bath temperature from 6 K to 25 K leads to a decisive enhancement of the integral e-SFRS intensity. However, the enhancement efficiency appears to depend on the chosen excitation energy. In regard of a resonant excitation of the trion s-shell, the efficiency is higher than in the case of resonant probing the trion p-shell or d-shell. When the temperature is increased up to 40 K the integral e-SFRS intensity at the s-shell maximum decreases down to approximately the same value as measured for 6 K. At this temperature, the high energy shoulder which is attributed to the trion p-shell vanishes. It is worthwhile to mention that the resonance profile width as well as the position of the QD-shells are not influenced by the temperature. Above 55 K the electron spin-flip Raman line disappears regardless of the excitation energy. Since the QD-PL can still be observed at 60 K, as shown in Fig. 4.5, evidences that the deactivation of the e-SFRS process occurs at temperatures, where the trion is far from being dissociated. Thus, the dissociation of the trion complexes is not to be associated as the only cause for the diminishing of the e-SFRS at elevated temperatures.

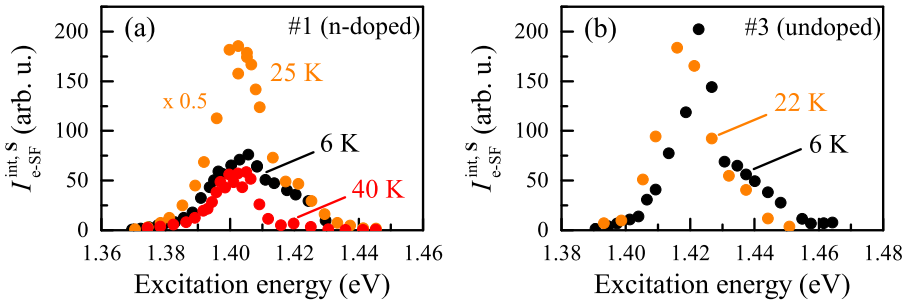

Figure 4.8: Resonance profile of the e-SFRS in singly charged (a) and undoped (b) QD ensembles measured at $B = 10$ T in Voigt geometry for different temperatures. The laser power density is set to 1 W/cm^2. The integral spin-flip intensity ($I^{int,S}_{e-SF}$) is determined from SFRS Stokes spectra measured in (σ^+/σ^+) polarization configuration. The error in the integral SF intensity does not exceed the symbol size. Fig. (a) is adapted from Ref. [139].

In comparison to the investigated singly charged QD ensembles, the analysis of the spin-flip resonance profile of the undoped QDs demonstrates a rather different evolution. The results presented in Fig. 4.8 (b) highlight that an increase of the temperature seems not to lead to an enhancement of the integral spin-flip intensity. Neither the shape of the resonance profile nor the absolute intensities significantly change. The shape of the resonance profile coincides well with the PL spectrum shown in Fig. 4.5 (b). At 6 K the s-shell maximum is centered at about 1.426 eV, and the p-shell can be found at about 1.439 eV. However, if one compares the resonance profile at 6 K with the one at 22 K, one can deduce a thermally induced shift of the s- and p-shell maximum to lower energies. In total the s- and p-shell are shifted by about 5 meV to 1.421 eV and 1.434 eV, respectively.

In order to highlight the degree of the temperature-dependent enhancement of the e-SFRS, the enhancement factor of the integral intensity (η_{SF}) and respective SFRS background (η_{BG}) are investigated in the following. The enhancement factors used here refer to the respective integral intensities normalized to the values measured at $T = 6$ K. Their dependence on the bath temperature as function of the excitation energy that is tuned across the different QD shells is presented in Figs. 4.9 (a)-(d). For the sake of demonstration the results relate to the resonant probing of the s-shell at 1.396 eV (a), s/p-shell at 1.407 eV (b), p-shell at 1.418 eV(c), and d-shell at 1.431 eV (d). The related e-SFRS spectra are measured at $B = 6$ T in Voigt geometry. The integral spin-flip intensity ($I^{int,S}_{e-SF}$) used to calculate the corresponding enhancement factors η_{SF} and η_{BG} is determined from SFRS Stokes spectra measured in (σ^+/σ^+) polarization configuration. The background integral intensities are evaluated from baseline fits of the Raman spectra between the lower and upper limits of 110 and 260 μeV, respectively.

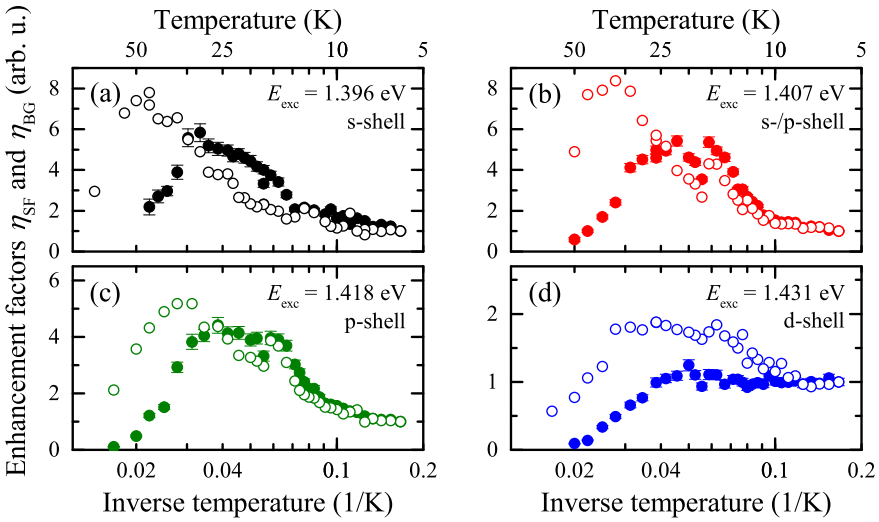

Figure 4.9: (a)-(d) Temperature dependence of the enhancement factors of the e-SFRS intensity (η_{SF}, closed circles), and acoustic phonon scattering background (η_{BG}, open circles). The enhancement factors refer to the respective integral intensities normalized to the values measured at $T = 6$ K. The related SFRS Stokes spectra are recorded at $B = 6$ T in (σ^+/σ^+) polarization configuration. The error of η_{SF} and η_{BG} does not exceed the symbol size. The results relate to the resonant probing of the s-shell at 1.396 eV (a), s/p-shell at 1.407 eV (b), p-shell at 1.418 eV(c), and d-shell at 1.431 eV (d). Adapted from Ref. [139].

The results shown in Fig. 4.9 demonstrate that the e-SFRS efficiency (closed circles) is enhanced up to 6 times with increasing temperature for resonantly exciting the trion in the s-shell and in the transition range of the s- and p-shell. When the excitation energy is tuned into resonance with higher QD shells η_{SF} weakens. For resonant probing of the d-shell almost no enhancement is present. The maximal η_{SF} is reached at 28 K for the s-shell and at 25 K for the s/p- and p-shell. Regardless of the selected excitation energy, the intensity of the e-SFRS gradually decreases above 28 K. The spin-flip signal vanishes at approximately 50 K. In comparison to η_{SF}, the integral intensity of the phonon scattering background (open circles) rises even up to 40 K. In this respect, the maximum attainable enhancement factor is $\eta_{BG} \approx 8$ for resonant probing of the s- and s/p-shell. For resonant excitation of the p- and d-shell η_{BG} decreases down to 5.2 and 2, respectively. It is furthermore worthwhile to mention that η_{SF} as well as η_{BG} demonstrate a sharp dip at about 18 K. This dip is apparent for excitation of all QD shells except for resonant probing of the s-shell. Its origin is discussed in Sec. 4.2.5.

The preliminary analysis of the temperature dependent electron spin-flip intensity, discussed above on the example of the image plots shown in Fig. 4.7, has highlighted that the e-SFRS exhibits a strong dependence on the geometry as well as the magnetic field. To what extent this influences the spin-flip intensity enhancement is analyzed in further detail next. In this respect, the temperature dependence of the enhancement

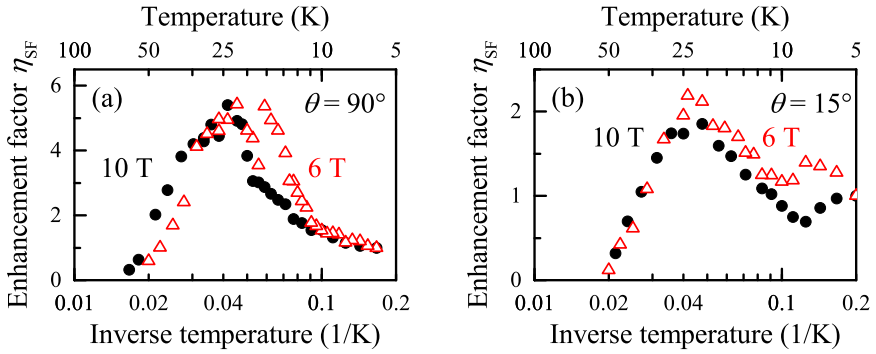

Figure 4.10: Temperature dependence of the enhancement factor η_{SF} of the singly charged QD ensemble #1 at $B = 6$ T (red open triangles) and 10 T (black closed circles) in (a) Voigt and (b) tilted geometry ($\theta = 15°$). The enhancement factors refer to the respective integral intensities normalized to the values measured at $T = 6$ K. The related SFRS Stokes spectra are recorded in (σ^+/σ^+) polarization configuration. The error obtained from the analysis does not exceed the symbol size. Adapted from Ref. [139].

factor η_{SF} is presented in Figs. 4.10 (a) and (b) as function of the magnetic field for Voigt and tilted geometries ($\theta = 15°$). The presented results pertain the singly charged QD ensemble #1 regarding a resonant excitation of the trion in the transition range of the s- and p-shell. As one can deduce from $\eta_{SF}(T)$ the thermal enhancement of the e-SFRS intensity is considerably smaller in tilted geometry than in Voigt geometry. In this regard, the maximal enhancement value in Voigt geometry amounts ≈ 5.8, whereas it decreases down to ≈ 2.1 in close to Faraday geometry. However, the magnetic filed only marginally influences the maximum obtainable value of $\eta_{SF}(T)$. Moreover, one observes that the dip in the evolution of η_{SF}, which is clearly evident in the image plot shown in Fig. 4.7 (a), vanishes at high fields ($B = 10$ T) in Voigt geometry. However, one may interpret this change of the profile also as an appearance of a local enhancement maximum at 6 T, since $\eta_{SF}(T)$ demonstrates a clear coincidence above 18 K at both magnetic fields. Hence, the local maximum is found between 10 K and 18 K for 6 T. Considering a tilted geometry, the dip can be monitored at about 10 K for $B = 6$ T, while shifting to 8 K at 10 T. The evolution of η_{SF} above 13 K coincides well for both high and low magnetic fields.

The temperature dependence of the integral spin-flip intensity has highlighted in singly charged QD ensembles that it is most efficient in the case of resonant probing of the s-shell and is significantly affected by the geometry. Another not yet addressed aspect is the temperature dependence of FWHM of the e-SFRS, which is of particular interest, since it reveals the decline mechanism of the e-SFRS process. The FWHM ($\hbar\omega_{SF}^{FWHM}$) of the e-SFRS in the Stokes regime is presented as function of the temperature in Fig. 4.11 (a). The depicted temperature dependence of $\hbar\omega_{SF}^{FWHM}$ pertains the singly charged QD ensemble #1 in regard of resonant probing of the trion in the

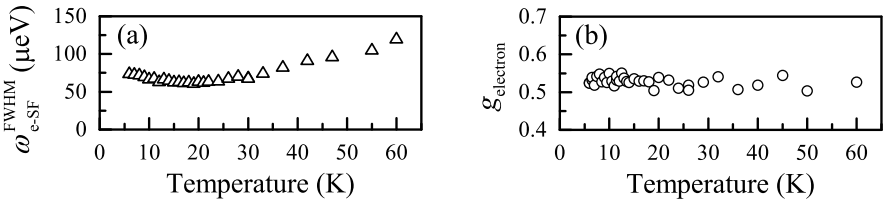

Figure 4.11: Dependence of the FWHM ($\hbar\omega_{\mathrm{SF}}^{\mathrm{FWHM}}$) (a) and the g factor (b) of the electron spin-flip Raman line in the Stokes regime on the bath temperature. The measurements refer to the singly charged QD ensemble #1. The related SFRS spectra are measured in Faraday geometry at $B = 6$ T and $P_{\mathrm{exc}} = 1$ W/cm^2 in co-circular polarization configuration (σ^+/σ^+) in regard of a resonant excitation of the trion s/p-shell ($E_{\mathrm{exc}} = 1.407$ eV). The error of $\hbar\omega_{\mathrm{FWHM}}$ and of the g factor do not exceed the symbol size.

transition range of the s- and p-shell at $B = 6$ T. The results highlight, that the FWHM of the electron spin-flip line decreases with rising temperature from $T = 6$ K ($\hbar\omega_{\mathrm{SF}}^{\mathrm{FWHM}} \approx 75$ μeV) to about 20 K ($\hbar\omega_{\mathrm{SF}}^{\mathrm{FWHM}} \approx 58$ μeV). For $T > 20$ K the electron spin-flip Raman line broadens gradually, reaching a FWHM of 122 μeV at $T = 60$ K. The shape which is well described by a Gaussian profile as well as the related g factor do not alter throughout the temperature range measured. For illustration purpose, the temperature dependence of the g factor is presented in Fig. 4.11 (b). The slight fluctuations of the g factor are within the range of the measurement accuracy. The g factor remains constant at about 0.53 over the entire temperature range.

Finally, for the sake of comparison, the focus will be directed towards the temperature-dependent enhancement of the e-SFRS in the undoped QD ensembles. The first analysis of the resonance profile which is described above has indicated that a clear enhancement as it is evidenced for the singly charged QDs is rather not observable. In order to analyze this more carefully, the temperature dependence of the enhancement factor is studied in tilted geometry ($\theta = 15°$). The enhancement factor of the integral spin-flip intensity (η_{SF}) and the respective SFRS background (η_{BG}) as function of the temperature are presented in Fig. 4.12. Here both enhancement factors refer to the respective integral intensities normalized to the values measured at $T = 5$ K. In order to obtain the maximal SFRS enhancement, according to the studies presented above, the excitation energy is tuned into resonance with the trion s-shell ($E_{\mathrm{exc}} = 1.449$ eV). However, in contrast to the singly charged QD ensemble #1, it become apparent for the undoped QDs that the polarization of the scattered light affects greatly the efficiency of e-SFRS. In co-circular polarized configuration (σ^+/σ^+) (closed black circles) η_{SF} is markedly higher than in cross-circular polarization (σ^-/σ^+) (closed red triangles). The e-SFRS efficiency is most enhanced for both polarizations at ≈ 12 K. Here, the enhancement in co- and cross-polarization configuration reaches a maximum value of $\eta_{\mathrm{SF}} \approx 3$ and ≈ 1.8, respectively. The e-SFRS intensity decreases rapidly above 12 K. In contrast to the evolution of the spin-flip intensity, the acoustic phonon scattering background intensity rises up to 20 K, reaching a maximum enhancement value of $\eta_{\mathrm{BG}} = 6$, and

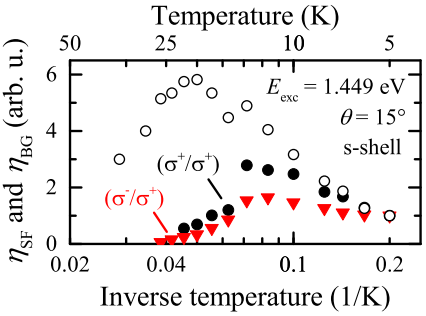

Figure 4.12: Temperature dependence of the enhancement factors of the e-SFRS intensity (η_{SF}, closed symbols), and acoustic phonon scattering background (η_{BG}, open symbols) pertaining the undoped QD ensemble #3. The related SFRS spectra are measured at $B = 6$ T for co-circular polarized (σ^+/σ^+) (closed black circles) and cross-circular polarized (σ^-/σ^+) (closed red triangles) configuration in tilted geometry ($\theta = 15°$). The enhancement factors refer to the respective integral intensities normalized to the values measured at $T = 5$ K. The error obtained from the analysis does not exceed the symbol size.

than diminishes gradually for increasing temperature. The spin-flip signal vanishes at about 28 K.

In summary, the singly charged and undoped QD ensembles reveal that the SFRS efficiency is thermally enhanced for probing the s- and p-shell trions. Thereby, the Raman shift, the SFRS polarization characteristics, and resonance profile demonstrate to be insensitive to a temperature change, and, thus, indicating that the spin-flip mechanism is thermally robust. Furthermore the strong enhancement of the SFRS background may be attributed to acoustic phonon scattering which on one hand facilitates the spin-flip probability at low temperatures but on the other hand also acts counterproductive, as it contributes to pure trion dephasing which suppresses the spin-flip Raman line. The responsible mechanism for the SFRS enhancement of the SFRS is discussed in detail in Sec. 4.2.5.

The last open question before the responsible mechanism of the SFRS is discussed in-depth in Sec. 4.2.5 is whether additional nonresonant above barrier excitation which provides additional carriers can further facilitate the SFRS. This issue is briefly addressed in the next section.

4.2.4 Impact of additional high-energy illumination on the e-SFRS efficiency

High-energy illumination, which is used in addition to the resonant SFRS, can be an essential factor in influencing the SFRS mechanism. For instance, an illumination can

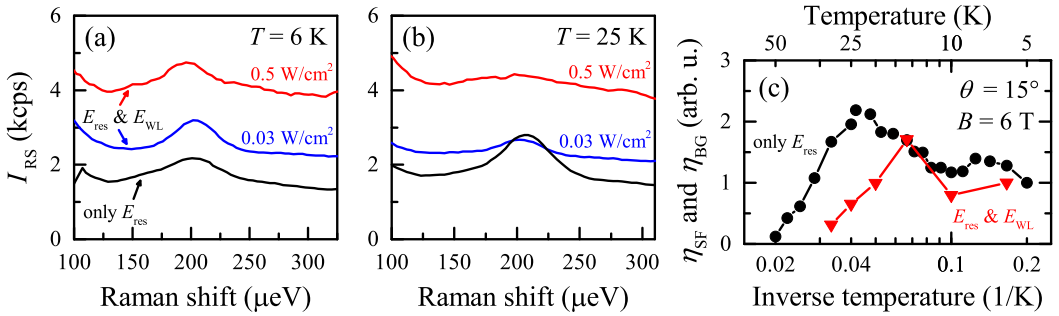

Figure 4.13: (a) and (b) SFRS Stokes spectra of the singly charged (In,Ga)As/GaAs QD ensembles #1 for resonant excitation of the trion s-shell at 1.396 eV, with (red or blue line) and without (black line) simultaneous WL illumination (E_{WL} = 1.480 eV). The spectra show the electron spin-flip in co-circular (σ^+,σ^+) polarization in the range from 100 μeV to 325 μeV, measured at B = 6 T in tilted geometry ($\theta = 15°$). The two laser beam SFRS spectra are shown for high (0.5 W/cm^2, red line) and low (0.03 W/cm^2, blue line) power density. (c) Temperature dependence of the enhancement factors of the e-SFRS intensity (η_{SF}), with (red closed triangles) and without (black closed circles) simultaneous WL illumination (P_{WL} = 0.5 W/cm^2). The related SFRS spectra are measured at B = 6 T for co-circular polarized (σ^+,σ^+) configuration.

change the background carrier concentration, which enhances the probability of trion formation, in turn affecting considerably the e-SFRS efficiency in QDs. However, it may also result in local heating, and, thus, lead to a decrease of the exciton lifetime and an enhanced violation of the electron spin-flip scattering.[138] The extent to which the generation of additional carriers by high-energy illumination influences the resonant e-SFRS in singly charged (In,Ga)As/GaAs QD ensembles is discussed in the following.

To investigate the impact of additional high-energy illumination the e-SFRS is studied for simultaneous resonant and WL excitation. In order to illustrate briefly the resulting effect of the two laser beam excitation, e-SFRS spectra in the vicinity of the electron spin-flip in the Stokes regime are presented in Figs. 4.13 (a) and (b) exemplarily for low (T = 6 K) and high (T = 25 K) bath temperature. The spectra shown in both figures are measured at B = 6 T in tilted geometry ($\theta = 15°$) for a high (P_{WL} = 0.5 W/cm^2, red line) and a low (P_{WL} = 0.03 W/cm^2, blue line) power density of the additional WL excitation.

In the case of resonant excitation only (black line), one monitors that the electron spin-flip Raman line, which is centered at about 205 μeV, obviously intensifies with rising temperature. For instance, the spin-flip intensity enhances by a factor of approximately 2 from 6 K to 25 K. The corresponding line width ($\approx$ 70 μeV), line shape as well as the Raman shift demonstrate almost no change. However, under application of additional unpolarized WL illumination the intensity of the electron spin-flip Raman line alters. One finds for T = 6 K that the SFRS efficiency enhances which is manifested in an increase of the absolute spin-flip intensity with respect to the phonon

scattered background. For instance, the absolute spin-flip intensity rises by a factor of 1.3 and 1.4 for low and high power density, respectively. If the temperature is increased to $T = 25$ K, the e-SFRS practically vanishes. For this temperature the spin-flip line is significantly broadened and the intensity is considerably reduced. The line width amounts about 110 μeV for $P_{\mathrm{WL}} = 0.5$ W/cm^2. By comparison, the additional illumination affects neither the Raman shift nor the line shape. Throughout the temperature range measured, the line is well described by a Gaussian profile.

In order to highlight the degree of temperature-dependent enhancement of the e-SFRS in regard of additional wetting-layer illumination, the enhancement factor of the integral intensity (η_{SF}) is studied in detail. The temperature dependence of η_{SF} is depicted in Fig. 4.13 (c). The enhancement factors refer to the respective integral intensities normalized to the values measured at $T = 6$ K in the case of two laser beam excitation and $T = 5$ K for only resonant excitation. In these measurments the singly charged QD ensemble #1 is probed resonantly on the low energy side of the trion s-shell at 1.396 eV. The evolution of η_{SF}, for resonant excitation only, is described in the frame of Fig. 4.10 (b) in Sec. 4.2.3. In recap, it demonstrates that the e-SFRS efficiency is enhanced up to 2.1 times at ≈ 25 K, whereas for temperatures above 25 K, the electron spin-flip diminishes gradually and finally vanishes at about 50 K. However, in the case of additional WL illumination the evolution of $\eta_{\mathrm{SF}}(T)$ appears to be shifted towards lower temperatures. In this regard, the maximal enhancement of $\eta_{\mathrm{SF}} \approx 1.7$ is reached at 15 K. Above 15 K the spin-flip integral intensity decreases. Hereby, the electron spin-flip Raman line can be monitored only up to 29 K.

In comparison to resonant only excitation, the maximal reachable enhancement η_{SF}, is slightly reduced and shifted by about 10 K to lower temperatures, while the profile shape of $\eta_{\mathrm{SF}}(T)$ remains unaltered. This effect may be attributed to local lattice heating by additional high power density applied to the QDs. As a result of this heating process, temperature-induced processes that have a beneficial effect on the e-SFRS occur earlier. Hence, the profile of $\eta_{\mathrm{SF}}(T)$ shifts to lower temperatures. In this respect, the charge fluctuations in the QD environment and also acoustic phonon interaction could enhance the pure trion dephasing. Moreover, high-energy illumination may also change the carrier-occupation of the QDs to more than one electron per dot. In this case the background based on photoluminescence may increase at the expense of the electron-SFRS intensity. In this regard, an increase of the background is clearly evident in Figs. 4.13 (a) and (b). Due to the optical charging of the QDs, amongst others also those which are initially undoped, an increase of the absolute SFRS intensity shall be facilitated. However, the results do not indicate any exceptional rise of η_{SF} with additional above barrier excitation.

4.2.5 Mechanism of the thermal enhancement of the e-SFRS efficiency

As pointed out in the introduction to this chapter, (In,Ga)As/GaAs QDs are considered to be an attractive material system for spin electronics as they provide the possibility of coherent manipulations of carrier spins at elevated temperatures, as it has been demonstrated in recent studies.[225,226] However, to what extent thermal phonons contribute to spin manipulation within the limits set for maintaining coherence has not been explored so far. To contribute to a better understanding, on the basis of the experimental results discussed in the last sections, the spin-flip scattering mechanism of the thermal enhancement of the e-SFRS efficiency will be described in the following.

In this respect, the interpretations extend the basic understanding of the resident e-SFRS process addressed in Sec. 4.1.3. In brief recap, the analysis has highlighted that in singly charged QDs the spin-flip scattering is realized by isotropic electron-electron exchange interaction, whereas in undoped QDs mainly the electron-phonon interaction is the driving force. In both cases the major requirement is the reduction of the trion or exciton symmetry which can be induced, for instance, by tilting the external magnetic field in respect to the quantum dot growth axis. As shown above this mechanism appears to be thermally robust, as neither the Raman shift, SFRS polarization characteristics, nor the resonance profile indicate any change. In this context, it is worthwhile to note that one can derive from the comparison of the thermal enhancement of the e-SFRS efficiency with the quantum yield of the resonant PL that about 10% of the incident photons initiate a spin-flip scattering process of the resident electron spin at 25 K.[36,139] This approximate value is achieved by estimating the average number of trions which have been created within a QD subensemble by the incident laser beam and approximate their contribution to the SFRS signal with respect to the resonant PL that has a quantum yield of about 90%.[36,139]

Following a general approach the origin of the e-SFRS efficiency enhancement is to be determined. In this respect, the electron spin-flip scattering intensity (I_{SF}) is given by the product:

$$I_{\mathrm{SF}} \propto I_{\mathrm{i}}\, W_{\mathrm{em}}\, \tau_{\bar{\mathrm{j}}}\, W_{\mathrm{SF}}\, \tau_{\mathrm{j}}\, W_{\mathrm{abs}}. \tag{4.5}$$

Here, the most cruicial factors, which define the spin-flip scattering intensity, are the lifetime (τ) of the exciton in a specific spin state with total angular momentum j, the probability rates for absorption W_{abs}, emission W_{em}, and spin-flip scattering W_{SF}, and the intensity of the incident light I_{i}. The latter mentioned I_{i} can be excluded as influencing factor, as it is kept constant during the measurements. Moreover, the absorption as well as emission probabilities, which depend on the resonance energy of the trion, can be neglected as these do not change in the temperature range up to 40 K (see Figs. 4.5 (a)-(d)). Hence, the determining factor is the spin-flip scattering probability.

In general the spin-flip scattering probability may be influenced in different ways. As described in Sec. 4.1.3, it is determined by the Pauli exclusion principle and the electric-dipole selection rules. Hence, it is very sensitive to the geometry, as this lifts the restrictions of selection rules by mixing the optically bright and dark excitons, i.e., the electron spin basis eigenstates. For instance, this explains the enhancement of the e-SFRS intensity with increasing tilting angle. Considering a rise of the temperature, thermal phonons begin to get involved in scattering processes and, thus, induce trion interlevel transitions.[257] In the singly charged QDs, these interlevel transitions are suggested to support the exchange-based electron-spin scattering in the negative trion.[139] Hence, the increase of the spin-flip scattering probability is attributed to the effective spin-orbit coupling. This coupling links the ground state with high-angular momentum states, in turn lifting the limitations given by the Pauli exclusion principle. In the case of undoped QD ensembles in which the electron spin-flip scattering process in a neutral exciton is mediated by acoustic phonons, the thermal phonons not only induce interlevel exciton transitions but also enhance the immediate electron-phonon scattering. For both, n-doped and undoped QD ensembles, the exciton interlevel transitions shall become even more pronounced in strongly tilted geometries, as the level spacing is considerably reduced in this case.[136,251,258] This suggested model would not affect the spin-flip mechanism and, therefore, the Raman shift as well as the SFRS polarization properties shall remain unchanged.

These theoretical assumptions are in good agreement with the experimental observations. As mentioned above the SFRS studies revealed that the Raman shift and the SFRS polarization characteristics are insensitive to the sample temperature (see Sec. 4.2.2). Furthermore, the thermal enhancement of the e-SFRS intensity increases almost by one order of magnitude for resonant probing of the s- and p-shell trions in Voigt geometry (see Sec. 4.2). This is in accordance with the model's prediction. The theoretical explanaitions are moreover underlined by the fact that the strong increase of the phonon related scattering background with rising temperature, demonstrates the same evolution as the e-SFRS intensity. The phonon scattering background is attributed to the increase in the density of populated acoustic phonon modes. Thus, it becomes clear that acoustic phonons which induce trion interlevel transitions with growing temperature, support the spin-flip probability of the resident electron. For instance, the SFRS studies indicate a stabilization of the trion coherence, evidenced by the slight narrowing of the spin-flip line, at the temperature of maximal SFRS efficiency. However, counterproductive mechanisms that counteract the spin-flip scattering process are also apparent. For instance, the strong line broadening for high temperatures, depicted in Fig. 4.11 (a), indicates a process counteracting the enhancement of the coherent e-SFRS. In this respect, it is important to note that the decrease in the e-SFRS intensity begins at temperatures, at which the line width starts to broaden.

The origin of the constructive and destructive effects, i.e., the broadening and intensity reduction of the electron spin-flip Raman line, may be attributed to two factors. On one hand to an acceleration of the transverse electron spin relaxation and on the

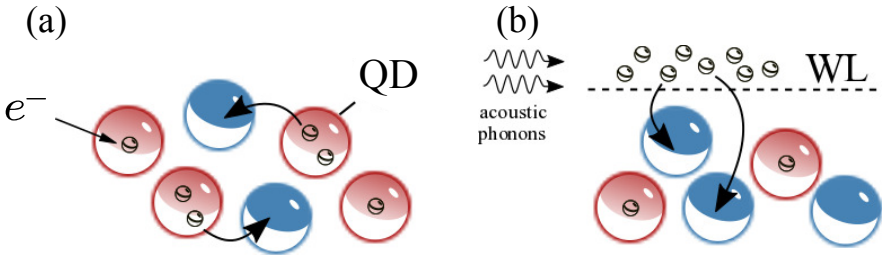

Figure 4.14: Model schemes of temperature-dependent phenomena in self ensembled (In,Ga)As/GaAs QDs. The small open circles represent electrons (e^-), whereas the large red and blue circles picture charged and undoped QDs. Both illustrated processes are excluded as relevant mechanisms. (a) A thermally activated transfer of electrons between differently strong confined, spatially adjacent QDs. (b) Thermal activation of trapped or wetting-layer electrons that relax into undoped QDs. Both processes may increase the total number of single-charged dots, in turn facilitating e-SFRS processes.

other hand to pure trion dephasing which is induced by charge fluctuations in the QD environment as well as acoustic phonon interaction [259,260] (see Sec. 4.2.1). In conclusion both, the constructive and destructive effects, are mediated by acoustic phonons, in turn significantly influencing the e-SFRS efficiency.

The temperature dependence of the e-SFRS enhancement factor η_{SF} has demonstrated that the diminishing of the e-SFRS is only weakly affected by the magnetic field strength and orientation. This is evidenced by the almost identical deactivation temperatures of the e-SFRS process (see Fig. 4.10). The reduction of the phonon scattering background intensity above 50 K can be attributed to the red-shift of the trion resonance. This effect occurs due to a decrease of the band-gap energy for increasing temperature. Furthermore, it is important to note that the dissociation of the trion complexes occurs at much higher temperatures, as the deactivation of the e-SFRS process. For instance, in the singly charged QD ensembles the electron spin-flip Raman line vanishes at about 55 K (4.7 meV), whereas the trion dissociates at 175 K (15.0 meV). In the case of the undoped QD ensembles the trion dissociation temperature is decisively lower (100 K, 8.0 meV) and, thus, the deactivation of the e-SFRS process decreases as well (28 K, 2.4 meV). In conclusion, this results demonstrate that the trion dissociation is closely linked to the diminishing of the e-SFRS.

For the sake of completeness in the following two temperature-dependent phenomena in self-assembled QDs will be discussed which, after careful analysis and comparison with the experimental results, can be excluded as relevant mechanisms.

The first conceivable mechanism is based on the thermally activated transfer of electrons between differently strong confined, spatially adjacent QDs. [261] This process is schematically illustrated in Fig. 4.14 (a). The transition of electrons between dots caused by tunneling or coupling would increase the total number of singly charged dots

and, thus, increase the amount of electron spin-flip processes that can occur. This in turn would enhance the spin-flip scattering efficiency. Furthermore, the reduced scattering efficiency in close to Faraday geometry, may be explained by the strong magnetic confinement which leads to an enhanced electron localization and, thus, less tunneling events. However, the mechanism requires a large number of doubly charged and undoped spatially adjacent QDs. This rare configuration of resident carrier occupations is highly unlikely. Especially in the case of undoped QD ensembles, where despite the absence of resident electrons, a significant increase of the SFRS efficiency is found. For these reasons, the mechanism proposed can be rejected.

The second possibility which may increase the spin-flip scattering efficiency is a thermal activation of trapped or wetting-layer electrons that relax into undoped QDs. [262] This model is schematically illustrated in Fig. 4.14 (b). This relaxation process by thermally activated electrons would increase the total number of singly charged dots and, therefore, enhance the e-SFRS efficiency. However, this process should not depend on the magnetic field geometry, which means that the relative enhancement shall be the same for Voigt and tilted geometries. This is experimentally disproved, as described in Sec. 4.2.3. Furthermore, this model requires the presence of a significant number of undoped QDs which may be probed at low- and high-excitation energies. In regard of the two-beam SFRS, this proposed mechanism would imply a significant increase of the e-SFRS intensity due to charging with additional carriers. However, the results reveal that additional unpolarized wetting-layer excitation leads only to a slight increase ($\eta_{\mathrm{SF}} \approx 1.3$) in the e-SFRS intensity at 6 K (see Sec. 4.2.4). Hence, this mechanism can be neglected as well.

Finally, the focus is placed on the outstanding feature, i.e., sharp drop in the e-SFRS and scattering background intensity at 18 K ($B \perp z$), observed in the temperature dependence of the enhancement factors of the singly charged QD ensembles. This dip is apparent for resonant probing of the trion s/p-, p- and d- shell and reveals a strong dependence on the magnetic field strength as well as magnetic field geometry. Considering a tilted geometry, i.e., for a strong in-plane magnetic confinement, the dip is monitored at about 10 K for $B = 6$ T, while shifting to 8 K at 10 T. This temperatures corresponds to 0.8 meV and 0.7 meV, respectively, which is significantly less compared to the lateral confinement energy of the QDs in the conduction and valence band. One may suggest that the decrease of the e-SFRS and background scattering intensity at specific temperatures is caused by a distorted trion coherence by acoustic phonons with energies between 0.5 to 2 meV, whose wave function fit into the QDs having an average diameter of 20 to 30 nm. A second alternative explanation is a p-orbital splitting in the conduction band resulting from the noncircular shape of the QDs. This splitting, which is dependent on the magnetic field strength and geometry, might open a loss channel for the electron spin-flip efficiency leading to dips in the e-SFRS efficiency. [139] It is worthwhile to note that both proposed mechanisms are in good agreement with the experimental results presented in this chapter.

In conclusion, the study of the temperature dependence of the SFRS efficiency for the resident electron in singly charged and undoped (In,Ga)As/GaAs quantum dots has demonstrated a significant enhancement of the scattering efficiency at elevated temperatures for resonant probing of the s- and p-shell trions. The thermal efficiency enhancement is mediated by acoustic phonons which induce trion interlevel transitions with growing temperature. However, they also lead in combination with charge fluctuations of the QD environment to pure trion dephasing in turn suppressing the e-SFRS at about 50 K. Hence, it is demonstrated that thermal phonons do not disturb the coherent SFRS process and, thus, contribute to spin manipulation within the limits set for maintaining coherence.

Chapter 5

Nuclear spin polarization in the e-SFRS of (In,Ga)As/GaAs QDs

The optical manipulation of QD carrier spins is found to be attractive in many applications in the research field of spin electronics and quantum information technologies, because it can be performed on time scales which are several times shorter than the spin coherence time.[263,264] In this respect, the spin coherence times are ranging from hundreds of microseconds up to a millisecond.[265,266] Since applications for quantum memories or quantum computation require yet unachieved control of the nuclear spins, new approaches are called for in order to understand and manipulate the dynamics of the nuclei spins.

One way to accomplish this is by optical spectroscopy. However, it is discovered that circularly polarized laser light manipulation by resonantly exciting charged exciton complexes inevitably influences the nuclear spins.[242–244] In order to bypass this effect strategies to manipulate the carrier spins, without obtaining feedback from the surrounding that is detrimental to the carrier spin state, have to be found. In this respect, it is well known that the electron-nuclear hyperfine interaction in semiconductor QDs leads to an electron spin decoherence, as the spin of the strongly localized electron inside a QD, is highly coupled to the spins of the lattice nuclei.[267] The impact of nuclei spins can be described by an effective nuclear fluctuation field about which the carrier spins may precess, resulting in a loss of spin polarization. However, one can suppress this effect by polarizing the nuclear spins. For instance, this can be achieved by optical pumping in a longitudinal magnetic field. This approach provides the possibility to orient carrier spins confined in QDs. The polarization of these spins is transferred to the nuclei spins through flip-flop processes, in turn providing a nuclear spin polarization, which in result decreases the random nuclei spin fluctuations.[245,268] The resident carrier spins may now be manipulated in a homogenized environment. However, despite some basic understanding, many details of this central spin problem of a carrier

spin in a nuclear spin bath is yet unexplored. In this respect, this chapter addresses the interplay between the dynamic nuclear spin polarization and resonant SFRS of the resident electron in an ensemble of singly charged (In,Ga)As/GaAs quantum dots.

For the sake of guidance, this chapter is divided into three sections. It is important to note, that a part of the results and conclusions presented in this chapter have been published (see Ref. [21]). Starting point in the first Sec. 5.1 are the basic properties of the e-SFRS under two-color laser excitation, in which resonant and nonresonant laser light stimulate an electron spin-flip and, respectively, polarize the nuclei spins dynamically. The nuclear spin effects are monitored through the Overhauser shift (OS) of the Raman line. In this respect, the mechanism of the dynamic nuclear spin polarization is discussed. The interpretations extend the basic understanding of the resident e-SFRS process addressed in Sec. 4.1.3. In the following Sec. 5.2 the focus is placed on the power dependence of the optically induced nuclear spin polarization and the temporal evolution of the OS. The Chapter is concluded with Sec. 5.3.

5.1 The effect of optically induced nuclear spin polarization on the e-SFRS

To explore the interplay between the dynamic nuclear spin polarization and the resonant SFRS of the resident electron a two-color laser excitation scheme is used. Here, the dynamical polarization of the nuclei spins is induced by quasi-resonant excitation and, in addition, the QDs are resonantly probed to detect the e-SFRS. The general experimental approach is presented in-depth in Chap. 3. The nuclear spin effects are monitored through the OS [212] of the Raman line in a slightly off longitudinal magnetic field. After briefly highlighting the effect of nuclear spin polarization on the e-SFRS in regard of the self-assembled singly charged (In,Ga)As/GaAs QD ensemble #1, the respective mechanism of the two-color spin-flip Raman scattering will be discussed. In particular, the electron-nuclear hyperfine interaction and Pauli exclusion principle will be addressed.

As discussed in the previous chapter, the spin-flip scattering process of the resident electron is realized by isotropic electron-electron exchange interaction. Furthermore, the scattering process requires, for single spin-flip scattering processes to be possible, a reduction of the trion symmetry. For instance, this can be realized by a magnetic field tilted with respect to the QD growth axis, leading to the mixing of electron spin basis eigenstates. In this way the restrictions governed by the Pauli exclusion principle are lifted.

In reference to Sec. 4.1.3, due to resonant excitation with σ_r^+ polarized light in tilted geometry, the resident electron, which is found in the lowest superposition spin state ($\alpha \left|\uparrow\right\rangle + \beta \left|\downarrow\right\rangle$), is excited to a trion in the state $\alpha \left|\uparrow\downarrow\Uparrow\right\rangle + \beta \left|\downarrow\right\rangle$ (see Sec. 4.1.3).

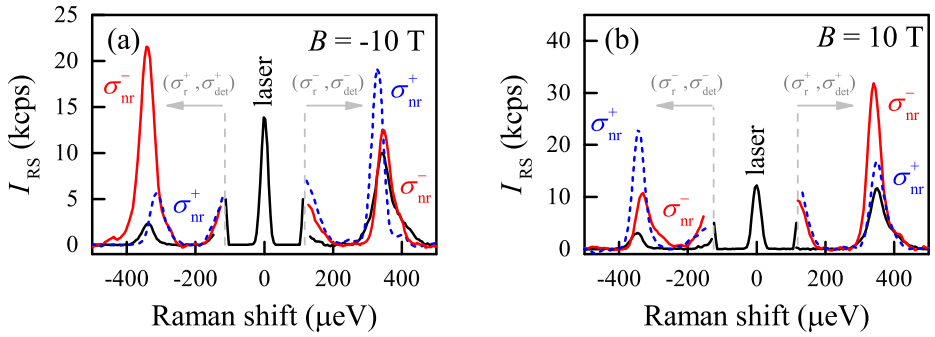

Figure 5.1: (a) and (b) SFRS spectra of the singly charged (In,Ga)As/GaAs QD ensembles #1 for resonant excitation of the trion s-shell at $E_\mathrm{r} = 1.409$ eV, with (red or blue line) and without (black line) simultaneous WL illumination ($E_\mathrm{WL} = 1.480$ eV). The spectra are shown for different excitation schemes and polarization configurations measured at $B = +10$ T (a) and $B = -10$ T (b) in tilted geometry ($\theta = 15°$). Each spectrum is smoothed and the PL background is subtracted. Adapted from Ref. [21].

Due to electron-electron interaction, the electrons exchange their spins and, thus, the intermediate state of the trion reads $\alpha\,|{\downarrow}{\Uparrow}{\uparrow}\rangle + \beta\,|{\uparrow}\rangle$. The annihilation of the trion results in scattered light, which has the same polarization as the incident one (σ^+_det). As a result of the SFRS process an electron is left in pure spin-up orientation ($\alpha\,|{\uparrow}\rangle + \beta\,|{\uparrow}\rangle$). After the SFRS process, the electron spin polarization may be transferred to the nuclear spin system via the hyperfine interaction, and, thus, leading to a dynamic nuclear spin polarization (NSP).[269] Proportional to the degree of the nuclear orientation an effective magnetic field acts back on the electron system, and energetically shifts the electron levels. This is also known as the Overhauser shift (OS).[212] The change in the electron energy can be described by the sum of the Zeeman energy of an electron spin $\vec{S}$ and the Zeeman energy of a system of nuclear spins $\vec{I}_n$.[39] The respective Hamiltonian is

$$\hat{H} = \hat{H}_\mathrm{Ze} + \hat{H}_\mathrm{ZN} = \mu_\mathrm{B} g_\mathrm{e} (\vec{B}\vec{S}) - \mu_\mathrm{N} \sum_n g_n (\vec{B}\vec{I}_n), \tag{5.1}$$

where $\vec{B}$ is the external magnetic field, μ_B is the Bohr magneton, g_e is the electron g-factor, $\mu_\mathrm{N} = 5.05 \times 10^{-27}$ J/T is the nuclear magneton, and g_n is the g-factor of the nth nucleus. As the Bohr magneton is approximately 2 000 times larger than the nuclear magneton, the splittings of the electron and nuclear spin levels differ by three orders of magnitude. The Raman shift of a spin-flip line is determined by $\Delta E = g_\mathrm{e}\mu_\mathrm{B}(B + B_\mathrm{N})$, with B_N denoting the nuclear hyperfine field which acts back on the electron system.

In order to illustrate briefly the impact of the dynamic nuclear spin polarization by a two-color laser excitation, SFRS spectra for resonant (r) excitation of the high-energy flank of the s-shell QD emission with (red and blue curves) and without (black curves) additional nonresonant laser excitation are presented in Figs. 5.1 (a) and (b). Here, the resonant laser energy is set to $E_\mathrm{r} = 1.409$ eV, whereas the nonresonant laser

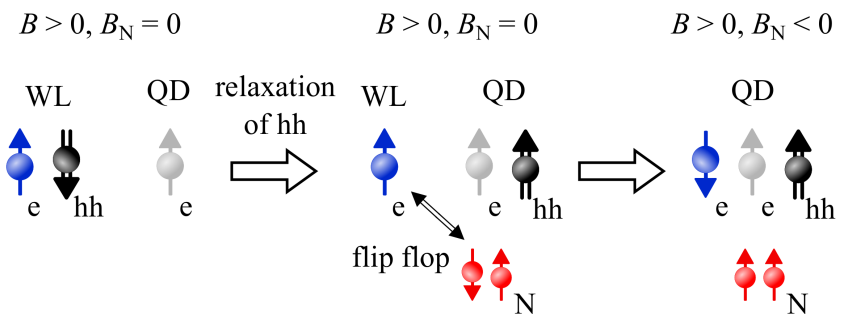

Figure 5.2: Model scheme of the dynamic nuclear spin polarization process. After nonresonant laser excitation (σ^-_{nr}) an exciton in the WL is created. Subsequently, the heavy-hole (hh, black) and electron (e, blue) relax into the QD. The relaxation of the WL electron requires, thereby, a change of its spin state as it cannot occupy the same spin state as the resident electron (e, grey) due to the Pauli exclusion principle. Accordingly, it undergoes a spin flip-flop with a nucleus (N, red) via the hyperfine interaction.

energy is probing the WL ($E_{\mathrm{WL}} = 1.480$ eV) with a laser power density of 16 W/cm^2. The spectra are measured at $B = \pm 10$ T for different polarization configurations. The circular polarization of light is denoted by $\sigma^{\pm}$, where the signs $\pm$ are determined by the sign of the photon angular momentum projection on the optical z-axis. The k vector of the incident light is parallel to z.

Considering first the case of $B = +10$ T (see Fig. 5.1 (b)), one obtains an electron spin-flip Raman line in co-polarized configuration ($\sigma^+_{\mathrm{r}}/\sigma^+_{\mathrm{det}}$) solely on the Stokes side, whereas for inverted polarizations it is apparent only on the anti-Stokes side. This is also shown in Fig. 4.2 (a) and described within the frame of Sec. 4.1.3. The Raman shift of the electron spin-flip Raman line amounts about $\Delta E_{\mathrm{SF}} = 347$ μeV. Taking into consideration the Zeeman splitting $|g|\mu_{\mathrm{B}}B$ (see Eq. (2.35)), this Raman shift is equivalent to a g factor of $g_{\mathrm{e}}^{15^\circ} = -0.60$. It is in good agreement with the results described in Sec. 4.1.3. A thorough analysis of the power dependence of the electron spin-flip Raman line for resonant excitation only (not shown here), has demonstrated that the Raman shift is insensitive to the resonant excitation power density P_{r}, since up to 30W/cm^2 no alteration of ΔE_{SF} is found. Hence, no appreciable nuclear spin effects can be identified. This result underlines that flip-flop process with nuclei spins may transfer the electron into the spin-down state. From this spin state, electrons cannot be excited efficiently due to the Pauli exclusion principle and, thus, are rather not induced by resonant excitation. It is furthermore obvious that the dynamic NSP is limited by the weak Raman scattering probability, which is why optical pumping by resonant excitation is very inefficient in the underlying SFRS process.

To effectively influence the NSP a nonresonant (nr) laser excitation with σ^+_{nr} polarized light can be used, while probing the QDs resonantly in order to stimulate the SFRS

process. In the case of nonresonant laser excitation, the nuclear spin pumping becomes more efficient, because the Pauli exclusion principle does not prevent the re-excitation. This process is shown schematically in Fig. 5.2 and proceeds as follows. By means of nonresonant excitation, e.g. with σ^-_{nr} polarized light, excitons ($|\uparrow\Downarrow\rangle$) are created in the WL. Subsequently, the WL heavy hole relaxes under reversal of $j_{\mathrm{z,hh}}$ into the QD. Here, it occupies the lowest spin up state, and, thus, leads to the creation of a dark exciton ($|\uparrow\Uparrow\rangle$), as the resident electron is mainly spin-up polarized. Since the resident and WL electron cannot occupy the same spin state due to the Pauli exclusion principle, for the relaxation of the WL electron into the QD a reverse of $j_{\mathrm{z,e}}$ is necessary. Accordingly, the WL electron undergoes a spin flip-flop with a nucleus via hyperfine interaction and than relaxes into the QD, leading to the formation of a trion in the state $|\uparrow\downarrow\Uparrow\rangle$. Due to this effect, the nuclear spin becomes polarized along the growth axis $+z$, thus, giving rise to an OS induced by the Overhauser field B_{N}, which is oriented along the $-z$ direction. In this example, the total external field strength is reduced. The dynamic NSP is followed and read out by the SFRS of the resident electron initiated by σ^+_{r} polarized excitation, as described in the example above. Finally, the SFRS process leaves a resident electron with spin-up orientation in the QD that, in turn, marks the initial situation for pumping the nuclear spins by σ^-_{nr} polarized WL excitation.

It is worthwhile to note that the orientation of the dynamically induced polarization of nuclei spins may be aligned either parallel or antiparallel to the external magnetic field B in Faraday geometry. This mainly depends on the polarization of the incident light. In the above mentioned example, a nonresonant excitation with σ^+_{nr} polarized light would induce no NSP, as the relaxation of the WL electron into the QD does not require a reversal of its spin state. However, one may obtain a positive Overhauser field for σ^+_{nr} polarized excitation when the heavy hole relaxes into the $|\Downarrow\rangle$ state and at the same time the WL electron reverses its spin orientation due to hyperfine interaction with the nuclei spins.

Referring to the SFRS spectra shown in Fig. 5.1 (b), one observes that for additional WL excitation with σ^+_{nr} polarized light (blue doted line), a spin-flip line is indeed apparent. However, the Raman line does not reveal any significant Raman shift on the Stokes side as well as on the anti-Stokes side in comparison to resonant excitation only. This result is in good agreement with the theoretical considerations, indicating that a NSP is absent for this excitation scheme. In the case of WL excitation with σ^-_{nr} polarized light, the electron spin-flip line clearly shifts to lower energies of about $\Delta E_{\mathrm{SF}} = 320\ \mu$eV both in the Stokes and anti-Stokes regime. According to Eq. (5.1), the respective OS is given by $\Delta E_{\mathrm{OS}} = (27 \pm 4)\ \mu$eV, which corresponds to an effective nuclear field of $B_{\mathrm{N}} = 0.78$ T. Moreover, one observes that the line width does not change under additional illumination. Both lines have a FWHM of $(60 \pm 5)\ \mu$eV. However, the electron spin-flip line shape is altered in the case of additional illumination. Here, it can be considered as a central line with pronounced sidebands. This reminds strongly of the spectral line shape which can be measured by four-wave mixing or PL. Here, the center line is identified as the zero phonon line and the wings are attributed to the

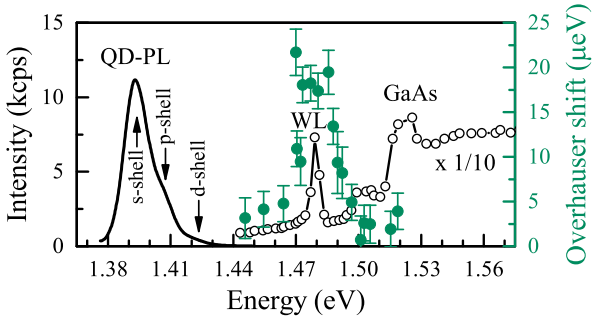

Figure 5.3: Dependence of the Overhauser shift on the nonresonant laser energy (green closed circles, right y-axis) for $B = 10$ T in Faraday geometry at $T = 6$ K. For a better overview, the PL (black line, left y-axis) and PLE (open black circels, left y-axis) spectrum, taken from Fig. 4.1, are presented, too. The results pertain the singly charged (In,Ga)As/GaAs QDs (sample #1). For detecting the OS, the resonant laser is tuned into resonance with the high-energy flank of the s-shell QD emission energy ($E_\mathrm{r} = 1.409$ eV). For excitation the $(\sigma^-_\mathrm{nr}/\sigma^+_\mathrm{r}/\sigma^+_\mathrm{det})$ polarization configuration is used. The power density of the nonresonant laser is set to $P_\mathrm{nr} = 16$ W/cm^2. The arrows mark the trion s-, p-, and d-shell peaks. Adapted from Ref. [21].

coupling with acoustic phonons.[270] With regard to the resonant SFRS, a similar line shape is expected, which shall result from the excitation of QDs via the zero phonon line or the acoustic sidebands. In general, the line width is determined by the g factor dispersion in the laser-excited QD ensemble, the trion spin relaxation rate, and the nuclear spin fluctuations.

When the external magnetic field is switched to $B = -10$ T, the effect of the nonresonant laser light polarization is reversed. This is highlighted by the e-SFRS spectra shown in Fig. 5.1 (a). Here, only for σ^+_nr polarized light the electron spin-flip line reveals a change of the Raman shift. The corresponding OS is about $\Delta E_\mathrm{OS} = (29 \pm 4)$ μeV. It is worthwhile to note that only for resonant excitation of the s- and p-shell trions, which become mixed by the tilted magnetic field, the OS becomes significant. According to previous studies this is attributed to the efficiency increase of the nuclear spin pumping at high magnetic fields near the s-/p-shell crossing, where electron-nuclear flip-flops are realized at negligible energy cost.[271]

Furthermore, the experiments have shown that for linearly polarized nonresonant excitation, a weak OS of about ≈ 9 μeV can be observed (not shown here). This is attributed to the mixed electron-spin states. In this respect, it is important to point out that the OS becomes smaller for tilting angles higher than $\theta > 15°$.

To explore for which nonresonant photon energy the dynamic NSP is most effective, the OS is investigated as function of E_nr. The results are presented in Fig. 5.3. In order to measure the OS, the resonant laser is exciting resonantly the high-energy flank of the s-shell QD emission energy ($E_\mathrm{r} = 1.409$ eV) in the $(\sigma^+_\mathrm{r}/\sigma^+_\mathrm{det})$ polarization

configuration, while for nonresonant excitation σ^-_{nr} polarization is used. The results highlight that a significant NSP is achieved when E_{nr} is tuned in resonance with the WL transitions between 1.471 and 1.474 eV. In the range of the WL the maximal OS amounts approximately $\Delta E_{\mathrm{OS}} = (20 \pm 3)$ μeV. When the excitation energy lies below the WL, the OS drops below $\Delta E_{\mathrm{OS}} = (4 \pm 2)$ μeV. Hence, one may assume that the absorption into excited QD shells is too weak to have a considerable impact on the NSP. Also in the case of higher energies ($E_{\mathrm{nr}} > 1.477$ eV) one monitors a rather low OS. Even though the absorption is strong, the optically excited carrier spins become quickly depolarized and, thus, no angular momenta can be transferred to the nuclei spins.

Another noticeable feature of the two-color laser excitation, is the strongly enhanced spin-flip intensity of the Stokes and anti-Stokes electron spin-flip Raman line. This effect primarily occurs for WL excitation that is counter-circularly polarized with respect to the circular polarization of the resonant excitation (see Figs. 5.1 (a) and (b)). One may assume, in reference to Sec. 4.2.4, that this effect is attributed to local lattice heating by additional high power density applied to the QDs. As discussed in the previous chapter, as a result of a laser induced heating, temperature-induced processes may occur which have a beneficial effect on the e-SFRS monitored at low temperatures. However, it is shown that in tilted geometries ($\theta = 15°$) the e-SFRS efficiency can be enhanced only up to 2 times. In comparison, the SFRS spectra shown in Figs. 5.1 (a) and (b) highlight that the e-SFRS intensity enhances for the above noted polarization configurations between 2 and 10 times. Hence, the increase of the e-SFRS intensity is notably higher than just in the case of a laser induced heating process. One may explain this effect by the preparation of initially charged and also empty QDs with an electron whose spin orientation is opposite to that of the resonantly excited electron, thus, allowing for the trion creation and a subsequent e-SFRS process. Here, it is assumed that the electron spin relaxation time is slow.

5.2 Temporal evolution and power dependence of the NSP

The assignment of the observed Raman shift alterations to nuclear effects is further substantiated by the temporal evolution of the NSP. It is monitored as function of the delay time after switching off the nonresonant laser. In this respect, it is worthwhile to note that it makes no difference whether or not the QD excitation by the resonant laser light is in a continuous or gated way, as both excitation schemes yield the same NSP decay times. The experimental approach is presented in detail in Chap. 3.3. The temporal evolution of the OS is presented in Fig. 5.4 as function of the bath temperature (a) and nonresonant excitation density (b). In the following, the focus will be first placed on the impact of temperature on the temporal decay of the OS. As shown in Fig. 5.4 (a), at helium temperatures ($T = 1.8$ K), the OS decreases from about 18 μeV to 8 μeV within several tens of seconds. When the temperature is raised

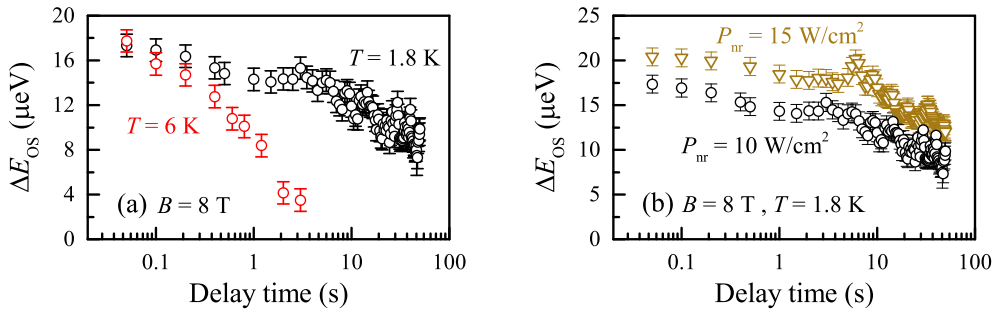

Figure 5.4: Temporal evolution of the OS as function of the bath temperature (a) and non-resonant excitation density (b) measured in the $(\sigma^{-}_{\mathrm{nr}}/\sigma^{+}_{\mathrm{r}}/\sigma^{+}_{\mathrm{det}})$ configuration. For detecting the OS, the resonant laser is tuned into resonance with the high-energy flank of the s-shell QD emission energy ($E_{\mathrm{r}} = 1.409$ eV), whereas the nonresonant laser energy is probing the WL ($E_{\mathrm{WL}} = 1.480$ eV). In (a) the temporal decay is depicted for $T = 1.8$ (black open circles) and 6 K (red open circles). The respective power density of the nonresonant laser is set to $P_{\mathrm{nr}} = 10$ W/cm^2. (b) The temporal evolution is shown for low (10 W/cm^2, black open circles) and high (15 W/cm^2, brown open triangles) WL excitation power densities. Fig. (a) is adapted from Ref. [21].

to $T = 6$ K, one observes that the decay time significantly decreases down to a few seconds.

To explain the long decay times the involvement of exchange interactions with the nuclei spins have to be considered. In this regard, the reduction of the initially induced NSP by optical WL excitation occurs due to resident electrons, which disturb the nuclear spin system. Herein, the anisotropic component of the nuclear dipole-dipole interaction plays a minor role at the B fields applied. For higher temperatures the involvement of acoustic phonons which randomly induce spin-flips of the resident electrons, in turn, leading to nuclear spin-flips, intensifies further the NSP decay. The decay times determined, here, are in good agreement with previous studies. For instance, by means of erase-pump-probe technique the nuclear spin diffusion in single self-assembled InAlAs QDs has been studied, demonstrating a relaxation of the OS on the time scale of a few tens of seconds.[272] Furthermore, in nuclei-induced frequency focusing experiments in a comparable (In,Ga)As QD ensemble an about one order of magnitude slower NSP depolarization time is determined.[273]

It is worthwhile to note that with decreasing NSP the electron spin-flip Raman line width is altered as well. The temporal evolution of the e-SFRS FWHM ($\omega^{\mathrm{FWHM}}_{\mathrm{e\text{-}SF}}$) is shown in Fig. 5.5. The results indicate that the spin-flip width decreases from 85 μeV at zero time delay to about 60 μeV after a delay of 50 s. This corresponds to a narrowing by about 29%. Note that these values are not limited by the instrumental broadening given by the laser line width or the monochromator resolution, which is less than 10 μeV. The narrowing of the electron spin-flip Raman line originates from a change

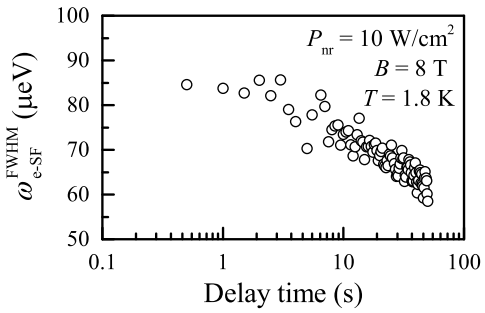

Figure 5.5: Temporal evolution of the electron spin-flip Raman line width for a temporally decreasing Overhauser field measured in the $(\sigma^-_{nr}/\sigma^+_r/\sigma^+_{det})$ configuration. The resonant laser is tuned into resonance with the high-energy flank of the s-shell QD emission energy ($E_r = 1.409$ eV), whereas the nonresonant laser energy is probing the WL ($E_{WL} = 1.480$ eV).

of the line shape. As mentioned above this is determined by the g factor dispersion in the laser-excited QD ensemble, the trion spin relaxation rate, and the nuclear spin fluctuations. Since the latter mentioned nuclear spin fluctuations shall increase with decreasing NSP, rather a broadening of the line would be expected. Therefore, it appears that either the trion spin relaxation rate increases or the g factor dispersion becomes smaller. However, on the basis of the presented data this question cannot be answered and, therefore, deserves further in-depth studies in the future.

The impact of an increase of the WL excitation power density on the temporal evolution of the NSP, is presented in Fig. 5.4 (b). The results demonstrate that with rising P_{nr} the overall value of the OS increases, while slightly prolongating the nuclei spin depolarization. In the case of $P_{nr} = 15$ W/cm^2, the OS has decreased from about 21 μeV to 12 μeV. Hence, in comparison to the NSP temporal evolution for $P_{nr} = 10$ W/cm^2, the OS is about 4 μeV higher throughout the complete measured time range. As these results indicate, the power of nonresonant excitation has a significant influence on the nuclear hyperfine field.

To highlight the impact of WL excitation power density (P_{nr}) on the NSP, the OS is investigated as function of P_{nr}. The results are presented in Figs. 5.6 (a) to (c). The OS of the SFRS Stokes-spectra as function of the power density are presented exemplarily for different nonresonant power densities and both circular polarizations in Fig. 5.6 (c). The spectra are measured at $B = 8$ T in tilted geometry ($\theta = 15°$). The resonant laser excites the QD ensemble on the maximum of the s-shell QD emission energy ($E_r = 1.401$ eV), whereas the nonresonant laser energy is probing the WL ($E_{WL} = 1.481$ eV). When the WL excitation is σ^+_{nr} polarized (orange curve) or when it is switched off (black curve), the Raman shift equals $\Delta E_{SF} = (274 \pm 2)$ μeV. Hence, no change of the Raman shift is observed for WL excitation which is counter-circularly polarized with respect to the circular polarization of the resonant excitation. This effect

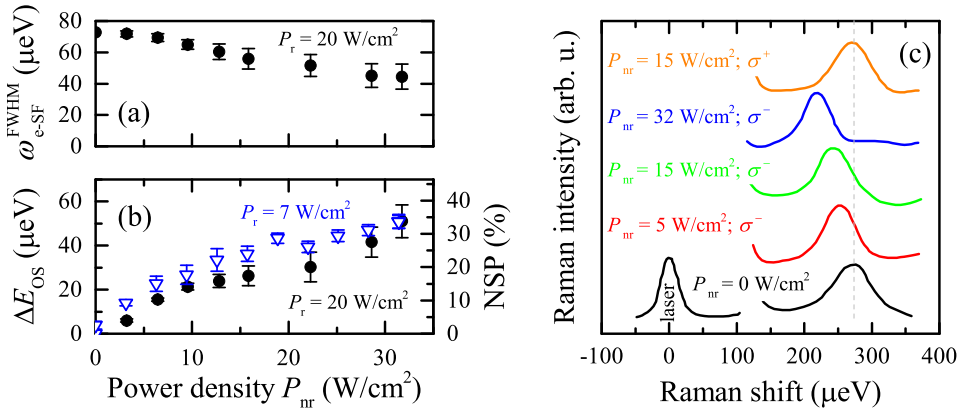

Figure 5.6: Dependence of the full width at half maximum of the electron spin-flip Raman line ($\omega_{e\text{-}SF}^{FWHM}$) (a), Overhauser shift (left y-axis) and the corresponding nuclear spin polarization (right y-axis) (b) on P_{nr} measured in the ($\sigma_{nr}^-/\sigma_r^+/\sigma_{det}^+$) configuration. The resonant laser is tuned into resonance with the high-energy flank of the s-shell QD emission energy (E_r = 1.409 eV), whereas the nonresonant laser energy is probing the WL (E_{WL} = 1.480 eV) at B = +10 T. Distinguishing the spin-flip Raman line from the PL background becomes more difficult for higher P_{nr}, which is reflected in a larger error of ΔE_{OS}. In (b) the dependence of the OS on P_{nr} is depicted for a low (7 W/cm^2, blue open triangles) and high (20 W/cm^2, black closed circles) power density of the resonant laser. (c) Electron spin-flip Raman Stokes-spectra for different polarizations and power densities of the WL excitation. The spectra are measured at B = +8 T in tilted geometry (θ = 15°). The power density of the resonant laser is set to P_r = 20 W/cm^2. Each spectrum is smoothed and the PL background is subtracted. The Figs. (a) and (b) are adapted from Ref. [21].

is described in the previous section and highlighted in Fig. 5.1. Moreover, one obviously observes that the use of high excitation power densities does not alter the process. The application of σ_{nr}^- polarized WL excitation leads to a decrease of the Raman shift due to the formation of an Overhauser hyperfine field induced by the NSP. Since the energy change is negative, the effective nuclear field B_N is aligned antiparallel to B. As the evolution of the spectra indicates further, this internal field is obviously strongly effected by the power density of the WL excitation. For instance, the Raman shift for P_{nr} = 32 W/cm^2 (blue curve) equals $\Delta E_{SF} = (233 \pm 2)$ μeV, which corresponds to an OS of $\Delta E_{OS} = (51 \pm 2)$ μeV and, thus, an effective nuclear field of $|B_N| = (1.5 \pm 0.1)$ T.

The dependence of the OS and the corresponding nuclear spin polarization on P_{nr} are highlighted in Fig. 5.6 (b). The results reveal that the OS of the Raman line increases continuously with rising power of the nonresonant laser. A saturation is not observed, so that for higher P_{nr}, even higher NSP degrees may be reached. When the excitation power density of the resonant laser is changed from P_r = 20 W/cm^2 to 7 W/cm^2 almost no alteration of the NSP is observable. The differences are within the accuracy of the measurement, and, thus, indicate that resonant optical pumping is

quite inefficient in the SFRS process in order to significantly probe the dynamic NSP.

It is furthermore interesting to analyze the width of the electron spin-flip Raman line. In this regard, the dependence of the FWHM of the electron spin-flip Raman line on P_{nr} is presented in Fig. 5.6 (a). It demonstrates that for increasing excitation power of the nonresonant laser a narrowing of the electron spin-flip line occurs. For instance the line width changes from (72 ± 2) μeV for only resonant excitation to (44 ± 8) μeV for $P_{\mathrm{nr}} = 32$ W/cm^2. This change of the line width corresponds to a narrowing of about 39%. As mentioned above the line width is influenced among other factors by the nuclear spin fluctuations. In the case of resonant excitation only these fluctuations are rather high, in turn, leading to a broadening of the spin-flip line. Due to nuclear spin pumping, and, thus, providing a NSP, the nuclear spin fluctuations are reduced. On the basis of the data shown here, one may expect that their influence is reduced at least by a factor of two.

The Overhauser shift ΔE_{OS} can be used to estimate the degree of nuclear spin polarization. According to previous studies which investigated the nuclear polarization created through optical pumping in $In_{1-x}Ga_xAs$ QDs, the NSP is given by [274,275]:

$$\frac{\left\langle \hat{I} \right\rangle}{I} = \frac{\Delta E_{\mathrm{OS}}}{\sum A_{\mathrm{hf}} I}. \tag{5.2}$$

Here, $\hat{I}$ denotes the nuclear spin operator, A_{hf} is the hyperfine constant, and $\sum A_{\mathrm{hf}} I = 147$ μeV reflects the Overhauser shift of fully polarized nuclei spins in the QDs studied. By means of Eq. 5.2 one obtains for the highest nonresonant laser power density ($P_{\mathrm{nr}} = 32$ W/cm^2) a NSP of 34 %. However, this value is smaller than it is reported in previous studies. For instance, in (In,Ga)As QDs a NSP of $\approx 40\%$ and for GaAs QDs a NSP of $\approx 65\%$ is reported. [245,274] However, the nuclear spin pumping efficiency in the underlying SFRS experiments performed in a tilted field geometry ($\theta = 15°$) is reduced due to the transverse component of the external magnetic field as this leads to a fast relaxation of the nuclei spins. Nevertheless, the electron-nuclear spin flip-flop rate is faster than the nuclear spin depolarization rate, which is suppressed at high magnetic fields and low temperatures. [276] It is worthwhile to note that the heavy-hole and electron generated by nonresonant optical excitation relax very efficiently into the QD, while the recombination of the WL exciton is inefficient. Hereby, the hole capture rate is supposed to exceed that of the electron and the hole spin relaxation rate is suggested to be faster than that of the electron. [270,277]

5.3 Conclusion

In this part of the thesis the thermally induced efficiency enhancement of the coherent electron spin-flip Raman scattering (Chap. 4.2) and the interplay between the dynamic

nuclear spin polarization and resonant SFRS (Chap. 5) in (In,Ga)As/GaAs quantum dots has been discussed.

The e-SFRS efficiency for probing the s- and p-shell trions is significantly enhanced due to acoustic phonons, which induce trion interlevel transitions at high temperatures. The trion interlevel transitions become even more pronounced in strongly tilted geometries, as the level spacing is considerably reduced.**??** Since the spin-flip scattering probability is determined by the Pauli exclusion principle and the electric-dipole selection rules, it is very sensitive to the geometry, which lifts the restrictions of the selection rules by mixing the electron spin basis eigenstates. In singly charged QDs the spin-flip scattering is realized by isotropic electron-electron exchange interaction, whereas in undoped QDs mainly the electron-phonon interaction is the driving force. The study of the temperature dependence of the e-SFRS demonstrates that up to 50 K neither the Raman shift, polarization characteristics, nor the spectral shape of the resonance profile are sensitive to the temperature, and, thus, indicating a thermally robust mechanism of the coherent electron spin-flip scattering based on exchange interaction. However, acoustic phonons, despite of enhancing the e-SFRS intensity, also additionally lead in combination with charge fluctuations of the quantum dot environment to pure trion dephasing, which broadens and ultimately suppresses the spin-flip Raman line. Thermal phonons can be exploited to support spin manipulation within the limits set for maintaining coherence.

The impact of dynamic nuclear polarization on the resonant SFRS of the resident electron due to the strong carrier-nuclear coupling is studied by using a two-color laser excitation scheme. Hereby, resonant and nonresonant laser light stimulates an electron spin-flip and, respectively, polarizes the nuclei spins dynamically. Proportional to the degree of nuclear spin orientation an effective magnetic field acts back on the electron system, which is monitored through the Overhauser shift of the Raman line in a slightly off longitudinal magnetic field. From this shift an optically induced nuclear spin polarization of up to 34 % that corresponds to an effective nuclear field of 1.5 T is derived. In this respect, it is demonstrated that the dynamic NSP increases with nonresonant excitation power density, while resonant optical pumping appears to be quite inefficient. Furthermore, the temporal evolution of the NSP indicates long nuclei spin depolarization decay times ranging up to several tens of seconds. However, the NSP rapidly decreases in time at a slightly elevated temperature of 6 K. This drop of NSP is caused by phonon-induced electron spin-flips that depolarize the nuclear spin system. In conclusion, the performed two-color SFRS has shown, that despite the possibility to manipulate carrier spins in an ensemble of (In,Ga)As QDs, it may further be used to sensitively indicate the coupling of carrier spins to the surrounding nuclear spin bath, i.e., to study the central spin problem.

Part III

Study of the diluted magnetic semiconductor $Zn_{1-x}Mn_xSe$

Diluted magnetic semiconductors (DMS's) have aroused remarkable interests in various scientific fields.[278] Particularly in the field of spin-physics, these structures play a major role, since they open new opportunities in spin-electronics and quantum information technologies. However, the ability to efficiently control spins in these semiconductors nanostructures has not yet been possible, since not all spin phenomena in these materials are well understood. Nonetheless, there are many major breakthroughs in the research of DMS's in recent years. One of the best examples of recent achievements is the great success related to quantum dots containing a single magnetic ion. In quantum dot material systems such as InAs/GaAs[279,280] and CdTe/ZnTe[281,282] doped by a single manganese atom, great progress has been made in studies of excitonic states and spin dynamics. In addition, II-VI-QD's first breakthrough advances in terms of optical control and manipulation of Mn spin states have been demonstrated experimentally and theoretically solved.[283–286] Based on these new insights, recently researchers successfully realized the electrical injection of spin-oriented electrons from (Zn,Mn,Be)Se into GaAs.[23]

A substantial amount of effort is also devoted towards the II-VI diluted magnetic quantum well structures (Cd,Mn)Te and (Zn,Mn)Se. In this regard, one of the key issues of research in the recent years is the investigation of their magnetic and optical properties.[142,148] Particular interest for these materials aroused from the recent discovery of pronounced magneto-optical effects like the giant Faraday rotation, whose origin lies in the giant Zeeman splitting of the excitonic states.[22,28,52] Especially the closely associated effect of the strong exchange interaction between the magnetic ion spins and the carrier spins is studied in-depth.[29,30,287,288]

For developing new optical manipulation algorithms, it is highly crucial to identify and tailor these exchange interactions. For that purpose various optical methods are used. The most promising is resonant spin-flip Raman scattering. This experimental technique makes it possible to study the Zeeman splittings of carriers and excitons and their selection rules, which provide information about the spin structure, their symmetries and spin interactions.[33] By means of SFRS in (Cd,Mn)Te QWs the spin interactions between the carriers and the paramagnetic impurities as well as their associated g factors are studied and theoretically described. Furthermore, researchers investigated the occurrence of multiple Mn^{2+} spin-flip resonances, which arise due to the presence of exciton magnetic polarons in oblique magnetic field geometries.[289–291] They demonstrated that a strong spatial confinement and low Mn^{2+} ion concentrations enhance the spin-flip scattering efficiency. However, despite the numerous studies the Mn^{2+} spin-flip scattering mechanism is discussed contrarily and not solved up to now.[194,290,292–294] This part III of the thesis addresses exactly this unsolved issue in prospect of contributing to a better understanding and unifying the different theoretical explanations in one common picture.

For the sake of guidance, this part is divided into two chapters. The first chapter 6 is intended to serve as an introduction to the topic of optical studies of the diluted

magnetic semiconductor (Zn,Mn)Se. Initially a brief description of the experiment and the samples studied is given and afterwards the investigation of the giant Zeeman splitting of excitonic states measured in photoluminescence and reflectivity is presented. The second chapter 7.3.3 the study of paramagnetic resonance spin-flips of single Mn^{2+} ions in $Zn_{1-x}Mn_xSe$ quantum wells by means of SFRS. In particular, high attention is paid to the spin-flip scattering mechanism and to an energetic asymmetry observed in SFRS of the Mn^{2+} SF resonances.

Chapter 6

Preliminary studies

DMS based on II-VI compounds, such as $Zn_{1-x}Mn_xSe$, have a high relevance for fundamental studies of magnetic, magneto-optical, and magnetotransport phenomena because they provide precise control of the spin dynamics as well as spin interactions by simply varying the magnetic Mn^{2+} ion content.[143] It is well known that the exposition of such a material to an external magnetic field induces an extraordinarily large spin splitting in the conduction and valence band induced by the strong *sp-d* exchange interaction between the magnetic ion spins and the carrier spins.[293] The level of the exchange interaction is material-specific. In addition, it is also influenced by parameters such as the given confinement, the charge carrier concentration or the manganese spin system temperature. The third mentioned is extensively analyzed, as it leads to a significant reduction of the giant Zeeman splitting of excitonic states.[30] The basic properties and a few remarkable physical phenomena related to (Zn,Mn)Se are in the focus of this chapter. As a brief introduction to the field of optical investigations of DMS structures, first the experimental methods and samples are presented and afterwards the analysis of reflection and photoluminescence is discussed.

6.1 The experimental realization and sample details

Different optical approaches can be applied to study the spin dynamics as well as spin interactions in DMS structures. The most famous techniques are reflectivity, transmission as well as spin-flip Raman spectroscopy. For instance, these are used to study numerous cubic (zinc-blende) large gap DMS, such as $Cd_{1-x}Mn_xTe$[28,29,52,175], $Zn_{1-x}Mn_xTe$ or $Zn_{1-x}Mn_xSe$[30,166,295]. The uniform properties and long spin lifetimes of the embedded manganese ions, demonstrate that these DMS structures are ideal candidates to probe interactions between the magnetic ion spins and carriers spins in a controlled manner.

sample code	Mn content, x	e^--concentration 10^{10} (cm^{-2})	QW width ($\AA$)	barrier width ($\AA$)	Be content, y	No. of periods
CB1542	0.004	undoped	100	200	0.06	5
CB1541	0.012	undoped	100	200	0.06	5
CB2422	0.020	undoped	100	–	0.06	1
CB2169	0.035	30	100	–	0.06	1

Table 6.1: Technological parameters for the $(Zn_{1-x},Mn_x)Se/(Zn_{1-y},Be_y)$ samples.

In this thesis the focus is placed on the $Zn_{1-x}Mn_xSe$ DMS QW compound. The main objective is to investigate the polarized reflectivity and photoluminescence of resonantly and nonresonantly excited heavy-hole excitons in high external magnetic fields as well as the analysis of the SF Raman scattering of paramagnetic resonance spin-flips of single Mn^{2+} ions. The experimental approach is presented in detail in the previous Chap. 3. Here, some additional details are briefly pointed out that are especially important for these studies. In this regard, in the following the method of reflection spectroscopy will be discussed first, subsequently the photoluminescence spectroscopy is thematized and finally the focus is placed on SFRS spectroscopy.

Reflectivity measurements are commonly used in DMS materials to determine the giant Zeeman splittings of the free exciton ground state. To measure the reflectance of a material, linearly polarized light is radiated in almost vertical incidence onto a surface and afterwards the reflected light beam is recorded. For excitation a simple white lamp with a a very wide homogeneous light spectrum of constant intensity in the energy range from 1.35 to 2.99 eV is used. The intensity of this light is adjusted with the help of natural gradient filters which are placed in the beam path. To avoid heating by photo carriers the power density of the light in the reflectivity measurements is set to 5 mW/cm^2.

To study the photoluminescence of the (Zn,Mn)Se QWs, it is of particular importance to excite the QW above the energy band-gap. For this purposes a continuous wave semiconductor laser (Coherent Cube) with a photon energy of $E_{\text{PL-exc}} = 3.061$ eV is used. To evade unwanted background heating of the QW sample, the laser power density of this laser is reduced by natural gradient filters down to 7 mW/cm^2. The experimental setup is pictured in Fig. 3.4.

The SFRS experiments are performed at high magnetic fields up to 10 T and at low temperatures ranging from 1.3 to 6.2 K. The QW samples are excited by the second harmonic of a tunable continuous wave Ti:Sapphire laser (Ti:Al_2O_3; 2.92 - 2.61 eV) with intra-cavity frequency doubling. Its power density on the sample is usually set to about 5 W/cm^2. In order to minimize laser fluctuations, the laser power is stabilized by a liquid-crystal variable attenuator. The backscattering SF experiments are performed in Faraday and in oblique geometries, where the magnetic field B and QW growth axis z enclosed an angle of (θ) within the xz-plane. The circular polarization of the exciting

photons is set by a Glan-Thompson prism combined with a quarter-wave retardation plate. In detection a similar set of polarization optics are used to analyze the circular polarization degree of the scattered light.

In the framework of this thesis various Zn_{1-x},Mn_xSe/Zn_{1-y},Be_y QW heterostructures, which were grown at the Institute of Semiconductor Technology, University of Braunschweig, by Prof. Dr. A. Waag's group, are investigated. The Mn content in the QW layers is varied from $x = 0.004$ up to 0.035, while the Be content in the barrier layers is at $y = 0.06$. The structural parameters for the studied (Zn,Mn)Se-based samples are collected in table 6.1. These QW structures have been grown by molecular beam epitaxy on (100) oriented GaAs[296]. This ultra-high vacuum process makes it possible to grow thin layers of structures with a certain orientation[297]. The samples comprise a single quantum well of 100 $\AA$ width, which are seperated by 500 $\AA$ barriers. In order to optimize the surface area and to adjust the lattice constant to the barrier of the quantum well structure, a sequence of BeTe, ZnSe and (Zn,Be)Se thin layers between the quantum well and the GaAs barrier is used.

To ensure that the same spot on the sample is excited in every measurement, each sample is covered by a mask having a hole of 300 μm diameter. Furthermore, the central part of 50x50 μm^2 size of the fully illuminated accessible sample area is selected by a cross slit.

6.2 Giant Zeeman shift in absorption and photoluminescence

As mentioned above, semimagnetic II-VI heterostructures are usually realized by the incorporation of Mn^{2+} ions in the crystal structure, resulting in a strong exchange interaction between the manganese ions and the electrons. Within the framework of this thesis this interaction is investigated by means of reflectance and photoluminescence for all $(Zn_{1-x}/Mn_x)Se/(Zn,Be)Se$ heterostructures with a Mn content of $0.004 \leq x \leq 0.035$. First, the emphasis is placed on the results and effects in absence of an external magnetic field and afterwards, the impact of an magnetic field is highlighted.

To begin with, the focus is set on the reflectance characteristics. In this regard, Fig. 6.1 (a) shows the reflectance and PL spectrum of the studied $Zn_{0.988}Mn_{0.012}Se$ quantum well sample at $B = 0$ T and 4 T. In absence of an external magnetic field the reflectance measurements reveal two resonances. They correspond to the exciton ground states involving the heavy holes (hh-X) and light holes (lh-X).[30,144] The resonance energy of the hh-X ground state equals $E = 2.8167$ eV and the resonance energy of the lh-X ground state $E = 2.8313$ eV. Both resonance lines have a Lorentzian profile with a width of 4.25 meV and 5.13 meV, respectively. They are split by approximately 39 meV at 0 T. This splitting is determined by strain and quantum confinement effects.[30]

The related photoluminescence spectrum in the range from 2.78 to 2.85 eV consists of two lines (see Fig. 6.1 (a)). The high-energy emission line at $E_X = 2.8164$ eV stems from the recombination of neutral heavy-hole excitons. The less intense line, shifted to lower energy relative to the exciton (X), is attributed to a negatively charged

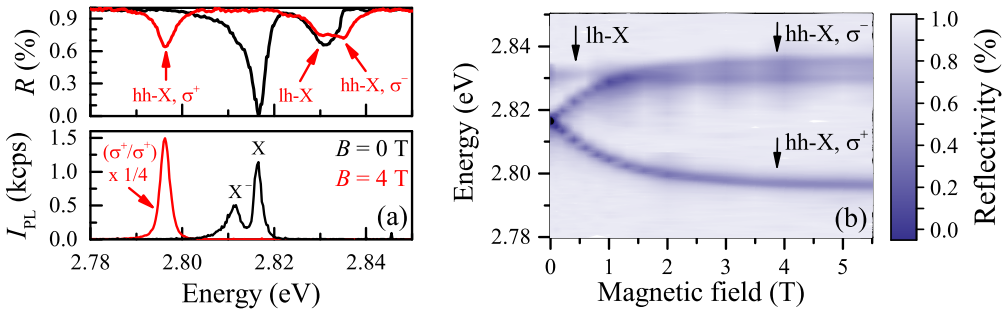

Figure 6.1: (a) White-light reflectivity spectrum and the related PL spectrum of the $Zn_{0.988}Mn_{0.012}Se$ QW with the resonances of the neutral excitons measured at $\theta = 0°$, in an ambient temperature of $T = 1.6$ K at $B = 0$ T (black colored line) and 4 T(red colored line). In the PL measurements, the sample is excited with a 405 nm Cube Laser ($E_{\text{PL-exc}} = 3.061$ eV) with low excitation density ($P \approx 7$ mW/cm^2). (b) Image plot of the magnetic field-dependent white light reflectivity spectrum of the neutral exciton resonance ($x = 0.012$, $\theta = 0°$).

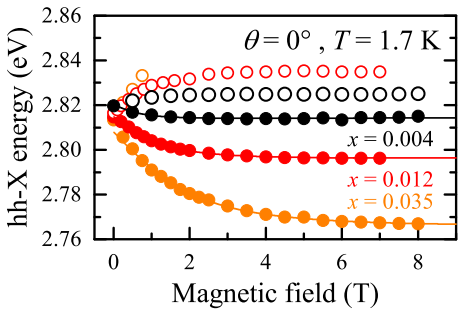

Figure 6.2: Energies of the hh-X reflectance resonances as function of the magnetic field in $Zn_{x-1}Mn_xSe$ QWs for different Mn concentrations x. Experimental data points for the hh-X with $j_z = -1$ (σ^-) are shown by open circles and for the hh-X with $j_z = +1$ (σ^+) by full circles. The error in the hh-X energy does not exceed the symbol size. Solid lines represent the best Brillouin function $\mathfrak{B}_{5/2}$ fit for the reflectance data points.

exciton (X^-) recombination ($E_{X^-} = 2.8313$ eV).[144,289,298] The binding energy of this complex is 5.1 meV. It is in good agreement with previous studies on ZnSe-based QW's.[60,299] According to literature, a positively charged exciton (X^+) is not present in these QW samples.[295,300] In comparison to the hh-X ground state resonance observed in reflectance, the PL of the X is redshifted by 0.3 meV. This small shift means that effects caused by a magnetic polaron formation, e.g. the nonmagnetic localization of excitons on alloy or their magnetic localization, do not essentially influence the properties of the structure.[30] Furthermore the low full width at half maximum of the X line, which amounts 2.25 meV, indicates a high structural quality of the sample.[30]

After the initial analysis of the spectral lines in PL and reflectance in zero field, now the scope is set on the magnetic field dependence. In the vicinity of an external magnetic field, neutral excitons in the (Zn,Mn)Se quantum well experience the giant Zeeman splitting, which results from the strong exchange interaction of the localized magnetic moments of the Mn ions with the localized carriers (see Chap. 2.3.3). Due to the giant Zeeman effect the hh-X and the lh-X ground state split into two bands as can be derived from the results in figure 6.1 (b). The splitting of the exciton resonances increases linearly at low magnetic fields and tends to saturate at higher field values. At $B = 5$ T the optically bright hh-X's are separated by 39 meV. The splitting arrangement of the exciton resonances is almost symmetric relative to the zero field positions. However, the splitting of the lh-X ground state is not dissolvable in the reflectance spectra. According to theory this Zeeman splitting energy is three times smaller than the one of the hh-X in exact Faraday geometry.[143,144] This would appear to explain why it is arduous to see the splitting in reflectance.

The reflectance and PL spectra measured at $B = 4$ T are depicted in figure 6.1 (a). In this regard, the low-energy resonance at $E = 2.7963$ eV is attributed to the

hh-X with the total angular momentum projection $j_z = +1$. Its optical transition is σ^+ polarized. On the other hand the high-energy resonance at $E = 2.8352$ eV stems from the hh-X with $j_z = -1$. Its optical transition is σ^- polarized. The results reveal strict polarization selection rules. They are valid for all studied (Zn,Mn)Se QW samples. They arise from the giant Zeeman splitting of the exciton states which strongly exceeds the inhomogeneous broadening of the exciton lines of ≈ 5.2 meV.[143,298]

A precise study of the reflectance is shown in Fig. 6.2, where the splitting of the hh-X is plotted versus the magnetic field for samples with three different Mn concentrations x. The results demonstrate that the splitting of the X ground state increases with the Mn concentration. For a better overview the hh-X separation energies δE^* at $B = 4$ T and 7 T and the zero field hh-X energy are depicted in table 6.2. From the evolution of the measurement data shown in figure 6.2 can be concluded that the hh-X splitting saturates at high magnetic fields in respect of all investigated (Zn,Mn)Se QW samples. However the magnetic field to reach the saturation increases with the Mn content. For instance, in the case of $x = 0.012$ the hh-X splitting fully saturates at $B = 3$ T whereas for $x = 0.035$ a field of $B = 8$ T is required.

In order to theoretically describe the giant Zeeman splitting of the hh-X and, thus, to model the energy shift of the exciton resonance, a commonly used approach for the description of QW excitons, which is discussed in chapter 2.3.4, is employed. In this regard the modified Brillouin function $\mathfrak{B}_{5/2}$ (see Eq. 2.85) is used to fit the experimental data obtained from an analysis of the reflectance spectra shown in Fig. 6.2. For each fit the parameters $S_{\text{eff}} = -0.804 + 0.364/(x + 0.109)$ and $T_0(x) = 47.2x - 281x^2 + 714x^3$ are calculated considering the functional dependencies of those parameters on the Mn content described by D. Keller et al.[30]. The modified Brillouin function is further used to determine the Mn spin temperature T_{Mn}, which is a general indicator for the heating of the Mn ion system. The values of S_{eff} and T_0 determined for the investigated samples as well as the values of T_{Mn} and the zero field hh-X energy resulting from the fit are collected in table 6.2. The results of the best regression calculation, where T_{Mn} and $E_{\text{X}}(B = 0)$ have been the only fitting parameters, are displayed by solid lines in Fig. 6.2. The data-points match well to the theoretical calculations revealing Mn temperatures between 2.80 K and 2.17 K. Furthermore, the results display a dependence of T_{Mn} on x. From the analyzed data it appears that the higher the Mn

sample No.	Mn content x	$E_X(B = 0)$ (eV)	$\delta E^*_{4\text{ T}}$ (meV)	$\delta E^*_{7\text{ T}}$ (meV)	T_{Mn} (K)	T_0 (K)	S_{eff}
#1	0.004	2.820 ± 0.001	11 ± 1	11 ± 1	2.80	0.18	2.42
#2	0.012	2.815 ± 0.001	38 ± 1	38 ± 1	2.59	0.52	2.20
#3	0.020	2.812 ± 0.001	55 ± 1	59 ± 1	2.31	0.84	2.02
#4	0.035	2.808 ± 0.001	85 ± 1	93 ± 1	2.17	1.34	1.72

Table 6.2: Results obtained from an analysis of the giant Zeeman splitting of the hh-X resonance shown by means of a fit with the modified Brillouin function $\mathfrak{B}_{5/2}$. (see Fig. 6.2).

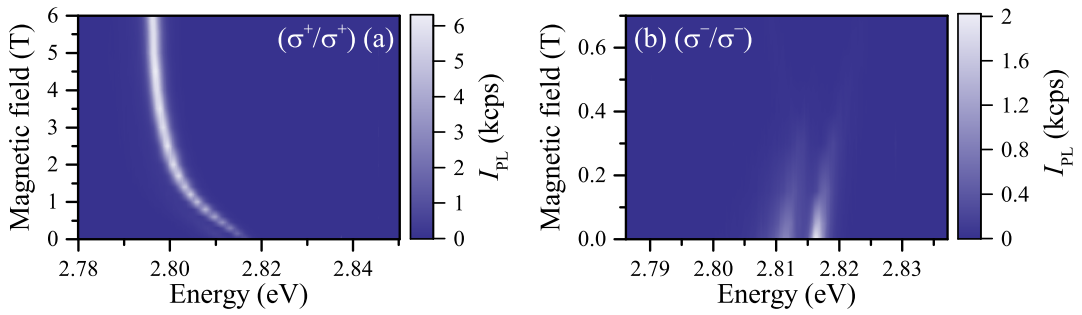

Figure 6.3: Image plots of the magnetic field-dependent giant Zeeman splitting of the X and X^- states in the $Zn_{0.988}Mn_{0.012}Se$ QW measured at $\theta = 0°$, in an ambient temperature of $T = 1.6$ K for the two co-circular polarization configurations (a) (σ^+/σ^+) and (b) (σ^-/σ^-). In these PL measurements, the sample is excited at $E_{\text{PL-exc}} = 3.061$ eV with low excitation density ($P \approx 7$ mW/cm^2).

content the lower the spin temperature. This is in good agreement with previous studies on $Zn_{1-x}Mn_xSe$/(Zn,Be)Se heterostructures.[30] D. Keller et al. inferred that this effect is attributed to a stronger coupling between the magnetic ion system and the lattice, by showing a strong decrease of the spin lattice relaxation time for higher Mn concentrations.[30]

Beyond that one observes that the reflectance signal is very sensitive to the photo-excitation density. Already a slightly larger illumination leads to a minor decrease of the Zeeman splitting in small magnetic fields. However, the mismatch abates with the field increasing, providing a slower saturation. Taking into account equation 2.90, it is highly likely that the photocarriers influence the spin temperature T_{Mn}. At higher excitation densities the number of photocarriers inside of the QW increases, elevating the flux of energy transmitted to the Mn system through direct and indirect exchange interaction and consequently heating the Mn system. The interaction between the different systems in DMS heterostructures and the resulting exchange of the energy, is outlined in chapter 2.3.5. Based on spin-flip exchange scattering and a coupling of the phonon and magnetic system, a reduction of the thermal average $\langle S_z \rangle$ of the Mn spin along the magnetic field direction z occurs, which in turn leads to a lowering of the Zeeman splitting.

After this brief review of the key characteristics of the reflectance properties of $Zn_{1-x}Mn_xSe$/(Zn,Be)Se heterostructures, the effects of the giant Zeeman splitting on the related photoluminescence are highlighted in the following. Since it turned out that by means of steady-state photo-excitation a heating of the magnetic ion system arises, the photo-excitation density (P_{exc}) in the conducting PL measurements is kept very low. In the presented results, unless otherwise described, P_{exc} amounts 0.016 W/cm^2.

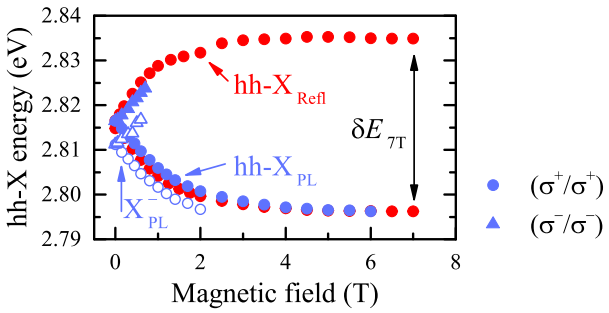

Figure 6.4: Energies of the hh-X resonances in reflectance (red circles) and PL (blue full (X) and open X^- circles/triangles) as function of the magnetic field measured at $\theta = 0°$, in an ambient temperature of $T = 1.6$ K. The PL is excited at $E_{\text{PL-exc}} = 3.061$ eV with low excitation density ($P \approx 7$ mW/cm^2) for the two co-circular polarization configurations (σ^+/σ^+) (circles) and (σ^-/σ^-) (triangles). The error in energy does not exceed the symbol size.

Similar to the observations in reflectance, the PL of the neutral exciton and the negativly charged exciton split, as shown in Fig. 6.3, when an external magnetic field is applied. Further can be observed that both excitonic bands reveal strict optical selection rules. In that respect, the optical transition of the low-energy X and X^- is σ^+ polarized whereas the high energy contribution is σ^- polarized. However, in the PL measurements negligibly small deviations from perfect selection rules are observed which steam from not impeccable polarization components in the experimental setup.

In Fig. 6.3 one can observe that the PL-intensity (I_{PL}) of the excitonic lines changes significantly with increasing field. While the overall integral intensity of the lower energy exciton PL (σ^+/σ^+) rises, the excitonic line (σ^-/σ^-) shifting to higher energy becomes weaker and finally diminishes at a field of $B = 0.7$ T. The intensity ratio of X and X^- changes with the magnetic field as well. In this regard the related trion PL can only be traced up to a field of $B = 2$ T in the underlying conditions of measurement. Above exclusively the X can be detected in the PL spectra, as shown in Fig. 6.3.

A survey of the exciton Zeeman splitting determined from reflectance and PL for the $Zn_{0.988}Mn_{0.012}Se$ QW sample is presented in Fig. 6.4. From the evolution of the measurement data it can be seen that the magnetic field-induced shift of the PL is of the same size as observed for the exciton resonance in reflectance. However, the shift of the X energy can be suppressed when P_{exc} increases. To deduce the Mn spin temperature from the conducting PL measurements the modified Brillouin function (see Eq. 2.85) is used to fit the experimental data. In this way a manganese temperature of $T_{Mn} = 2.73$ K is determined. This good agreement with the experimental values obtained in reflectance implies a very low heating effect of the Mn spin system. This results match very well with previous studies.[29,30]

In summary, on the basis of conducting PL and reflectance this chapter has outlined briefly the important optical characteristics of DMS's, highlighting the influence of the strong *sp-d* exchange interaction on the optical properties of $Zn_{1-x}Mn_xSe$ QWs. The origin of the resonance lines is clarified underlining their strict optical selection rules. Furthermore the high sensitivity to illumination, which manifests itself in a strong reduction of the Zeeman splitting, is highlighted for QW structures with diverse Mn concentrations. These observations are in good accordance with literature and provide essential information for a better understanding of the spin-flip Raman scattering studies presented in the following chapter.

Chapter 7

Resonant $3d$-electron spin-flip scattering in DMS

SFRS is a powerful tool to investigate magnetic phenomena presented by DMS's. SFRS on free electrons or those bound to donor states provides a direct access to the magnetic field induced electron spin splitting energy and, thus, allows one to study the s-d exchange interaction between the $3d$-electrons of the Mn^{2+} and the s-like electrons of the photo excited excitons.[289,301] However, up to now it is not investigated how far the nuclear quadrupole moments coupled with the electric field gradients at the magnetic ion sites impact the paramagnetic Mn^{2+} spin-flip resonances. In order to determine this impact, the SFRS technique is used to determine the dependence of the spin-flip scattering process on the optical power density, excitation energy, Mn-ion concentration as well as tilting angle between the magnetic field direction and quantum-well growth axis. In the process, it turned out that a significant quadrupole correction of a few tens of GHz affects the exchange interaction, leading consequently to a strong asymmetry of the scattering on the Stokes and anti-Stokes side. The origin and dependences of this energetic asymmetry are studied in-depth to gain a better understanding of the underlying mechanism.

Starting point in the first Sec. 7.1 are the circular polarization properties of the paramagnetic resonance spin-flip of single Mn^{2+} ions in Faraday geometry. Furthermore, the magnetic field dependence and resonance profiles of the spin-flip Raman line is demonstrated. In the subsections 7.1.1 and 7.1.2 the focus is set on the evaluation of the g factor and the angular dependence of the Mn^{2+} SF resonances as well as the investigation of interactions between nuclei and carrier spins by application of radio frequencies. In the following Sec. 7.2 the responsible SFRS mechanism in Faraday and tilted field geometries is described and validated. The last section of this chapter 7.3 addresses the energetic asymmetry between Stokes and anti-Stokes scattering which originates from a dynamic polarization of non-equilibrium manganese spins with high

spin temperatures. All the dependencies of the energetic asymmetry and the responsible mechanism are discussed in the subsections 7.3.1 to 7.3.6.

7.1 SFRS of single Mn^{2+} ions in $Zn_{1-x}Mn_xSe$ QWs

As described above SFRS is a powerful technique, providing information about the unique signatures of the underlying exchange interactions in DMS's. This approach is used to study spin-flips of single Mn^{2+} ions in $(Zn_{1-x}Mn_x)Se/(Zn,Be)Se$ QWs with low Mn concentrations ($x \leq 0.035$) in order to gain a deeper insight into the spin phenomena of II-VI semiconductors. The results, their interpretation and analysis are discussed in this section.

To get a first impression, in order to understand the mechanism of SFRS in these structures, initially a basic SFRS spectra of the first paramagnetic resonance spin-flips of single Mn^{2+} ions on the Stokes and anti-Stokes side is demonstrated in figure 7.1. It is shown for the co-circular (σ^+,σ^+), (σ^-,σ^-) and counter-circular (σ^-,σ^+), (σ^+,σ^-) polarization configurations. The spectra is measured at a temperature of $T = 1.6$ K and in a field of $B = 4$ T in Faraday geometry ($B \parallel z$). On the basis of the reflectance and PL analysis, which is discussed in chapter 6.2, the excitation energy is chosen in the way, that it is in quasi resonance with the bands of the low (Fig. 7.1 a) and high-energy (Fig. 7.1 b) X-PL at $B = 4$ T. It is set to $E_{exc} = 2.800$ eV and $E_{exc} = 2.828$ eV, respectively. For this excitations, multiple spin-flip Raman lines on the Stokes and anti-Stokes side are observed on top of a background contributed by PL. The Raman shift of the first paramagnetic resonance spin-flips shown in Fig. 7.1 on the Stokes and anti-Stokes side equals 444 ± 7 meV and 479 ± 9 meV, respectively. Taking into consideration the Zeeman splitting $|g|\mu_B B$, these Raman shifts correspond to a g factor of 1.92 ± 0.2 and 2.07 ± 0.3 for Stokes and anti-Stokes.

In previous resonant spin-flip Raman studies on DMS materials doped with Mn ions, it is shown that these Raman lines stem from spin-flips of the $3d$-electrons of the Mn^{2+} ions.[289] However, the priori determined g factor significantly differs from literature. Investigations of similar DMS structures, e.g. single quantum wells of $Cd_{0.76}Mn_{0.24}Te/Cd_{0.98}Mn_{0.02}Te$, have revealed a Mn^{2+} g factor of 1.997.[289] In ZnS and CdTe based semiconductor structures by means of electron spin resonance a g factor of 2.0025[298] and 2.010[302], respectively, is reported. This substantial discrepancy between experiment and literature is addressed in Sec. 7.3.

The circular polarization characteristics of the SFRS spectra reveal a lot about the underlying spin-flip processes. Therefore, next the focus is set on the analysis of the polarization properties of the Mn^{2+} spin-flip lines. As can be seen in Figs. 7.1 (a) and (b), the spin-flips demonstrate a strong polarization dependence. For resonant excitation of the low-energy X they are primarily polarized in the (σ^+,σ^+) configuration, whereas

an excitation of the high-energy X reveals the fully opposite polarization characteristic (σ^-,σ^-). Therefore, it can be concluded that for magnetic fields applied along the quantum-well growth axis z the spin-flip scattering is governed by strict optical selection rules. This observation overlaps well with the results gained from an analysis of the PL polarization properties in external magnetic fields (see Chap. 6.2, Fig. 6.3). In the conducting analysis of the PL, it is shown that due to the giant Zeeman splitting which exceeds the inhomogeneous broadening of the exciton lines, the optical transition of the low-energy X is fully σ^+ and the high-energy X is fully σ^- polarized. This polarization characteristic is clearly reflected in the resonant SFRS. However, the SFRS measurements allow one to observe very small deviations from perfect selection rules. For σ^+ excitation of the low-energy X a spin-flip line with a 110 times smaller intensity is detectable (see Fig. 7.1 (a)). It might be reasonable to assume that this negligible small contribution can stem from imperfections of the optical elements used for the analysis of the polarization.

Within the framework of this thesis, the strict optical selection rules are determined to be valid for all $Zn_{1-x}Mn_xSe$ QW samples with $x \geq 0.012$. Exclusively in the sample with the lowest Mn concentration ($x = 0.004$), this feature is not pronounced so well. The reason for this is the fact that the giant Zeeman splitting scales with the Mn content, leading to a far smaller splitting of the optically bright X resonances at $B = 4$ T, as it is depicted in table 7.2. In very diluted magnetic semiconductors, like in the case of the $Zn_{0.996}Mn_{0.004}Se$ QW, the giant Zeeman splitting does not fully exceed the inhomogeneous broadening of the exciton line ($\Delta E_{\text{Zeeman, X }(\sigma^+)} = 5$ meV $\approx \omega_{\text{X-FWHM}} = 5.1$ meV) what in turn leads to less strict optical selection rules. In Figs. 7.1 (a) and (b) one observes moreover that the intensity of the SF signals on the Stokes and anti-Stokes decisively diverges. For resonant excitation of the low-energy X in case

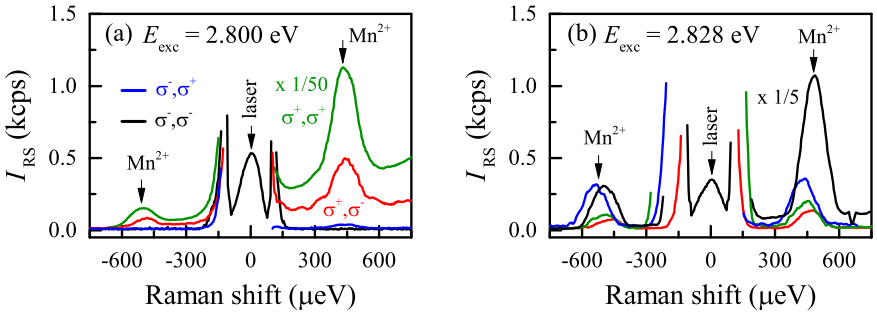

Figure 7.1: SFRS spectra of the first paramagnetic Mn^{2+} SF line ($n = 1$) in Faraday geometry at $B = 4$ T and $T = 1.8$ K for parallel and crossed circular polarizations measured at the lower ((a); $E_{exc} = 2.800$ eV) and higher ((b); $E_{exc} = 2.828$ eV) exciton resonances. The laser line is at zero Raman shift. The intensity of the (σ^+,σ^+) polarized SFRS spectrum in (a) is scaled by a factor of 1/50 whereas in (b) the (σ^-,σ^-) polarized SFRS spectrum is scaled by a factor of 1/5 for better visibility.

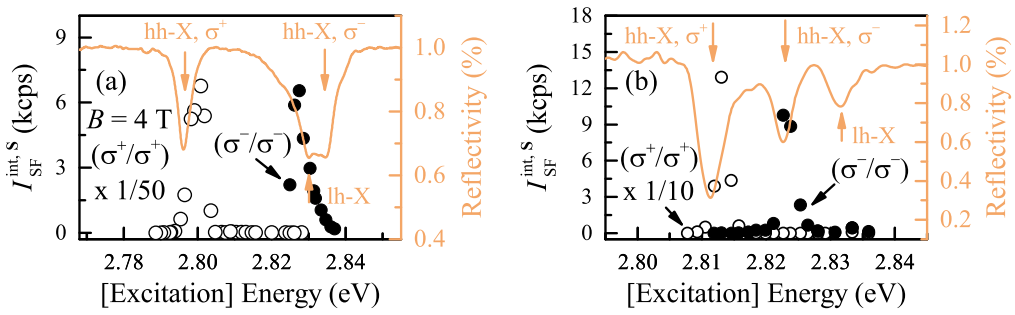

Figure 7.2: White-light reflectance spectra and SFRS resonance profiles of the first paramagnetic Mn^{2+} SF line ($n = 1$) measured at $B = 4$ T and $T = 1.6$ K in Faraday geometry. The data points with open circles display the results for (σ^+,σ^+) polarization configuration whereas the ones with full circles for (σ^-,σ^-). In (a) the results for the $Zn_{0.988}Mn_{0.012}Se$ QW are shown. The error in the integral SF intensity does not exceed the symbol size. In (a), the intensity of the (σ^+,σ^+) polarized SFRS resonance profile is scaled by a factor of 1/50 for better visibility. In (b) the results for the $Zn_{0.996}Mn_{0.004}Se$ QW are depicted. For better visibility, the intensity of the (σ^+,σ^+) polarized SFRS resonance profile is scaled by a factor of 1/10.

of (σ^+,σ^+) configuration the integral intensity of the the Mn^{2+} SFs differs by a factor of 300. The disparity depends on the spacing of the energy levels and, thus, scales with the magnetic field. In low fields the Stokes and anti-Stokes scattering intensities are of similar magnitude.

To distinguish the origin of the mechanism, which leads to the spin-flip scattering, spin-flip resonance profiles for the first paramagnetic resonance ($n = 1$) are investigated. The resonance profile of the $Zn_{1-x}Mn_xSe$ QW sample with $x = 0.004$ and $x = 0.012$ recorded at $B = 4$ T and the related reflectance spectra are shown in Figs. 7.2 (a) and (b). As described in the previous chapter 6.2, the two resonances observed in the reflectance spectra stem from the hh-X. For a better overview, they are highlighted in Fig. 7.2 by vertical arrows and their circular polarization of light is denoted by $\sigma^{\pm}$. As shown by the open (σ^+,σ^+) and closed circles (σ^-,σ^-), the maxima of the SF intensity profiles are in the vicinity of the heavy-hole exciton resonances. The energy values of those maxima, the differences $\Delta E_{\text{Reso-Refl}}$ between the SF maxima and the corresponding exciton resonances as well as the full width at half maximum of the SFRS resonance profile (ω_{Reso}) are summarized in table 7.2.

These depicted results show that the energy difference $\Delta E_{\text{Reso-Refl}}$ is not equal to zero. It increases for systems with higher Mn content and is affected strongly by the applied resonant power density of the exciting laser beam. The width of the resonance profiles fluctuates between 1.7 and 4.8 meV and does not show any dependence on the Mn concentration. These results are similar to the observations in photoluminescence. As described in chapter 6.2, a reduction of the giant Zeeman splitting occurs when the Mn system is excited with large light density, consequently leading to a heating of

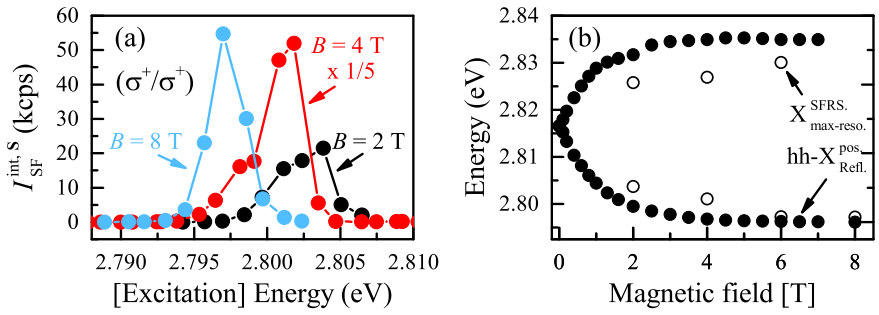

Figure 7.3: (a) Low energy SFRS resonance profile of the first paramagnetic Mn^{2+} SF line ($n = 1$) of the $Zn_{0.988}Mn_{0.012}Se$ QW sample measured at $B = 2$ T (black), 4 T (red) and 8 T (blue) for co-circular polarization configuration (σ^+,σ^+) in Faraday geometry. For better visibility, the data points are connected by straight lines and the SFRS resonance profile at $B = 4$ T is scaled by a factor of 1/5. (b) Energy positions of the SFRS profile maxima (open circles) and of the hh-X resonances in reflectance (full circles) as function of the magnetic field measured in Faraday geometry at $T = 1.6$ K. The error of the measurement data does not exceed the symbol size.

the Mn spin system. The same effect occurs, when the sample is excited resonantly. Therefore, it is reasonable to assume that the reduction of the giant Zeeman splitting observed in the resonance profile is caused due to resonant heating of the Mn system. To estimate the influence of this effect the Mn spin temperature needs to be determined. To achieve this, the maxima of the SF intensity profiles have been investigated for magnetic fields up to $B = 8$ T keeping the power density of the excitation at a constant value of 2.5 W/cm^2. The results for the $Zn_{0.988}Mn_{0.012}Se$ QW sample are shown in Figs. 7.3 (a) and (b).

The evolution of the measurement data shows that the SFRS resonance profile shifts with rising field to lower (higher) energies, for resonant excitation of the high (low)

	$x = 0.004$		$x = 0.012$		$x = 0.020$	$x = 0.035$
circ. pol. of hh-X	(σ^+)	(σ^-)	(σ^+)	(σ^-)	(σ^+)	(σ^+)
$E_{\text{Reso-max}}$ (eV)	2.8132	2.8232	2.8000	2.8275	2.7853	2.7716
$E_{\text{Refl-max}}$ (eV)	2.8116	2.8224	2.7963	2.8345	2.7804	2.7669
$\Delta E_{\text{Reso-Refl}}$ (meV)	1.6	−0.8	3.7	−7.0	4.9	4.7
ω_{Reso} (meV)	1.7	2.2	4.1	4.8	3.0	1.8

Table 7.1: The energy position of the SFRS profile maxima, the reflectance spectra maxima, the difference $\Delta E_{\text{Reso-Refl}}$ between the SF maxima and the corresponding exciton resonance as well as the full width at half maximum of the SFRS resonance profile (ω_{Reso}) shown for all studied $Zn_{1-x}Mn_xSe$ QW samples measured at $B = 4$ T and $T = 1.6$ K in Faraday geometry. The results for resonant excitation of the higher and lower energy hh-X are depicted by the circular polarization (σ^-) and (σ^+), respectively.

energy hh-X (σ^+/σ^+). The shift of the resonance profile peak is of similar magnitude as the giant Zeeman splitting of the exciton resonance (see Fig. 7.3 (b)). However the difference $\Delta E_{\text{Reso-Refl}}$ gradually diminishes with the field incresing. For instance, at $B = 8$ T, $\Delta E_{\text{Reso-Refl}}$ amounts about 1.1 meV whereas at $B = 4$ T, the difference is 3.3 times larger. Using the modified Brillouin function $\mathfrak{B}_{5/2}$ (see Eq. (2.85)) to model the estimated data in Fig. 7.3 (b), from the $E_{\text{Reso}}(B)$-dependence the Mn spin temperature is evaluated. For the low and high-energy X one obtains $T_{\text{Mn, X }(\sigma^+)} = 3.69$ K and $T_{\text{Mn, X }(\sigma^-)} = 6.33$ K, respectively. The Mn spin temperatures differs approximately by a factor of 2. Further it can be deduced from those results, that a resonant excitation of the high-energy hh-X leads to a larger energy difference than a resonant excitation of the low-energy hh-X at the same laser power. It is likely that the disparity between the two exciton bands arises from uniform heating efficiencies. It is conceivable that additional energy is transferred through phonon interaction to the Mn spin system, when the photo-excited X relaxes from the high (σ^-) to the low (σ^+) energy state. Since this effect leads to a decisive change of the resonance profile peak positions of the Mn^{2+} SF intensities, it is considered in all experimental investigations.

In summary, the preliminary studies on DMS $Zn_{1-x}Mn_xSe$ QWs have provided important information on the optical polarization properties and the excitation energy dependence of the first paramagnetic resonance spin-flip of single Mn^{2+} ions. It is clarified that the Mn^{2+}-SF processes are initiated at the heavy-hole exciton resonances and that due to the giant Zeeman splitting of the exciton states, the SFs reveal strict optical selection rules. Furthermore, a decisive heating of the Mn ion system is observable in case of resonant excitation of the exciton resonances. On the basis of those results in the following section the "effective" g factors of the Mn^{2+} spin-flips and the multiple spin-flip resonances in oblique magnetic field geometries will be the subject of discussion.

7.1.1 Magnetic field and angular dependence of the SFRS of single Mn^{2+} ions

One of the most investigated properties of DMS's, which attracted a lot of attention in recent years, is the exchange induced spin-splitting of effective mass states. The spin splitting being proportional to the macroscopic magnetization of d-spins, can become even in very diluted systems several times greater than the cyclotron energy. Since the magnetization of the manganese ions plays a important role in this process, in numerous preformed electron paramagnetic resonance (EPR) measurements the presence of magnetic ions in a given charge and spin state has been extensively researched. [192,303] In this regard, the hyper fine interaction between the electronic and the nuclear magnetic moments of Mn^{2+} ions are studied in particular. [303,304] With the intention of gaining new insights in optical manipulation algorithms, a further focus is placed on the exchange interactions between the magnetic ion and carrier spins. One common

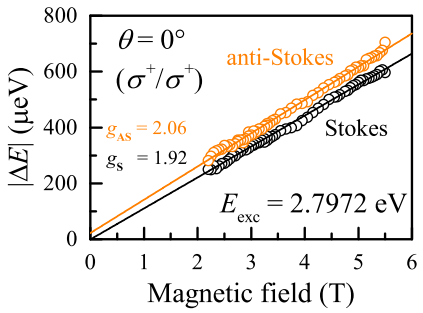

Figure 7.4: Raman shift of the first paramagnetic Mn^{2+} SF line ($n = 1$) on the Stokes and anti-Stokes side in dependence on the magnetic field in Faraday geometry. The depicted results pertain the $Zn_{0.988}Mn_{0.012}Se$ QW sample regarding an excitation of the low energy hh-X ($E_{exc} = 2.7972$ eV) in co-circular polarization configuration (σ^+,σ^+). The error in the Raman shift does not exceed the symbol size. The fitting (orange and black-colored) curves based on Eq. (2.35) show that the offset is negligible.

way to study those is by an analysis of the magnetic field and angular dependence characteristics of the SFRS of paramagnetic resonance SF of single Mn^{2+} ions. The results and analyses presented here are devoted to this issue. An exceptionally important parameter in this context is the manganese Landé factor, which describes the correlation between the angular momentum and the magnetic momentum. In previous studies, this value is estimated to $g = 1.997$ [289] in $Cd_{0.76}Mn_{0.24}Te/Cd_{0.98}Mn_{0.02}Te$ QWs. In comparison, electron spin resonance measurements (ESP) have led to a value of $g = 2.010$ in the same material [302]. However, a thorough analysis of single Mn^{2+} ions in $Zn_{1-x}Mn_xSe$ QWs has revealed that the Landé factor exhibits exceptional behavior. The "effective" g factor and the angular dependence of the Mn^{2+} SFs are presented next.

In order to determine the Landé factor of the $3d$-electrons of Mn^{2+} in $Zn_{1-x}Mn_xSe$ QWs, the Raman shift of the first paramagnetic resonance SF on the Stokes and anti-Stokes side is investigated for different field geometries and excitation conditions as a function of magnetic field. The results regarding a resonant excitation of the low energy hh-X ($E_{exc} = 2.7972$ eV) in co-circular polarization configuration in Faraday geometry ($\theta = 0°$) are shown in Fig. 7.4. As can be derived from these results, the absolute Raman shifts ($|\Delta E|$) of the Stokes and anti-Stokes SF lines show approximately linear magnetic field evolutions. It is further observable that the evaluated values fluctuate slightly. However, this fluctuation of the Raman shift is of the same order of magnitude as the measurement error and can, therefore, be neglected. In spite of this, a discrepancy between Stokes and anti-Stokes is monitored. In this manner, one observes a throughout smaller Raman shift on the Stokes side than on the anti-Stokes side. The energy difference between these Raman shifts, which is abbreviated in the following by δE, grows linearly with the magnetic field. In the first assessment, one can

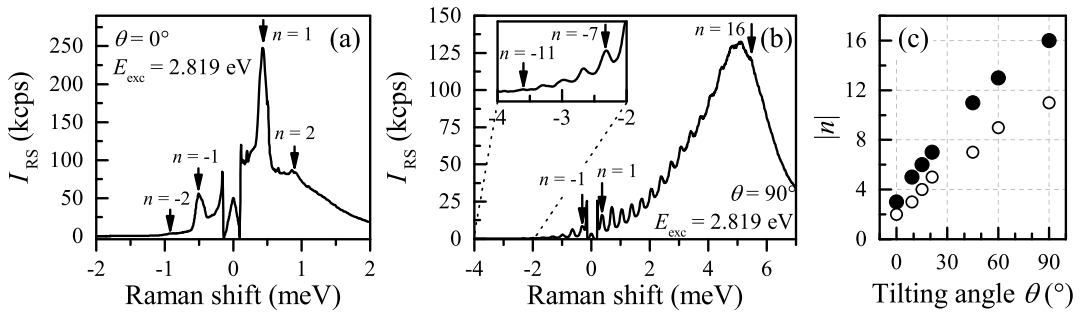

Figure 7.5: SFRS spectra of the paramagnetic Mn^{2+} SF lines in Faraday (a) and Voigt (b) geometry at $B = 4$ T and $T = 1.6$ K in co-circular polarization configuration (σ^+,σ^+). The depicted results pertain the $Zn_{0.988}Mn_{0.012}Se$ QW sample regarding a quasi resonant excitation of the low energy hh-X at $E_{exc} = 2.819$ eV. For better insight, in (b) the area near the eleventh resonance on the anti-Stokes side has been enlarged in the sub-figure. The Mn^{2+} SF resonance number on the Stokes and anti-Stokes are marked by arrows and their respective number is depicted. (c) Angular dependence of the maximal number ($|n|$) of detectable resonances on the Stokes (full circles) and anti-Stokes (open circles) side at $B = 4$ T and $T = 1.6$ K.

say that $|\delta E|$ increases by about 15 μeV per Tesla. To determine the corresponding Landé factors of the Stokes (g_{S}) and anti-Stokes (g_{AS}) SF, a linear least squares fit to the data according to Eq. (2.35) is conducted. This yields Landé factors of $g_{\mathrm{S}} = 1.92$ and $g_{\mathrm{AS}} = 2.06$. From a linear extrapolation of the experimental data a zero-field offset of $\Delta E_{\mathrm{off,\,S}} = -10 \pm 20$ μeV and $\Delta E_{\mathrm{off,\,AS}} = 25 \pm 20$ μeV is deducible. Since these offsets are in the range of the measurement error, they are negligible. The disparity between Stokes and anti-Stokes scattering, which is clearly prominent here, is investigated in the framework of this thesis in-depth under numerous aspects. The results and interpretations are presented in the Sec. 7.3.

So far, the description of the results has focused on the first paramagnetic scattering resonance. In order to provide a better understanding of the underlying SF-mechanism, the appearance of collective multiple higher order spin-flips within the Zeeman split of the Mn^{2+} ground state is discussed. In previous studies, the effect of multiple SFs, which appear near the exciton resonance, are thoroughly investigated. For instance, in $Cd_{0.98}Mn_{0.02}Te$ QWs and nonmagnetic $Cd_{0.76}Mn_{0.24}Te$ barriers, a large number of simultaneous spin-flips of Mn^{2+} ions has been detected and studied.[289] The investigation of $Zn_{1-x}Mn_xSe$ QWs has shown that a large number of resonances appears as well. The quantity of lines depends inter alia on the manganese ion concentration, the excitation resonance conditions and the field geometry. The influence of these factors is discussed below. However, the related Mn^{2+} spin-flip scattering mechanism has been discussed contrarily and could not be clarified up to now.[289,290,292,293]

The Figs. 7.5 (a) and (b) show SFRS spectra exhibiting the multiple SF signals at a magnetic field of 4 T in Faraday ($\theta = 0°$) and Voigt ($\theta = 90°$) geometry. The

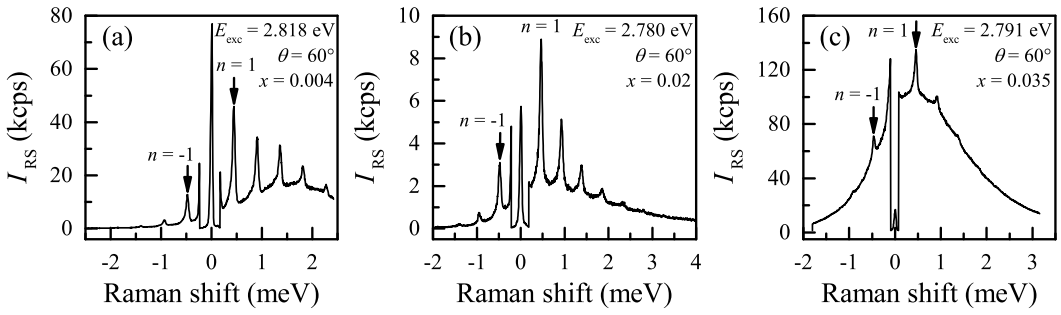

Figure 7.6: SFRS spectra of the paramagnetic Mn^{2+} SF lines in tilted field geometry ($\theta = 60°$) at $B = 4$ T and $T = 1.6$ K in co-circular polarization configuration (σ^+,σ^+). The depicted results pertain the $Zn_{1-x}Mn_xSe$ QW sample with $x = 0.004$ (a), $x = 0.02$ (b) and $x = 0.035$ (c) regarding a quasi resonant excitation of the low energy hh-X. The respective excitation energies are depicted in the figures. For better insight, the Mn^{2+} SF resonance with $n = 1$ is marked by arrows.

excitation energy is tuned to 2.819 eV, which is close to the low energy X resonance detected in PL spectra (see Chap. 6.2). In exact Faraday geometry (see Fig. 7.5 (a)), maximally $n = 3$ paramagnetic Mn^{2+} resonances on the Stokes side and $n = 2$ on the anti-Stokes side are observable. The energetic spacings between the resonances equals the Raman shift of the first SF line. However, the peak intensity of this overtones decreases with increasing number of resonances. For instance, in Faraday geometry, the second resonance SF on Stoke side ($n = 2$) has a 50 times lower intensity than the first ($n = 1$). This ratio changes as soon as the angle θ between the growth axis and B_{ext} is adjusted from 0° to 90°. θ significantly influences the number ($|n|$) of detectable resonances, as illustrated in Fig. 7.5 (c). The larger the angle, the more resonances are visible. In Voigt geometry, one can identify up to 11 paramagnetic Mn^{2+} resonances on the anti-Stokes side and up to 16 on the Stokes side. An exemplary SFRS spectra for Voigt geometry is shown in Fig. 7.5 (b). For better insight, the area near the eleventh resonance on the anti-Stokes side has been enlarged in the sub-figure.

A detailed investigation of the multiple higher order spin-flips has shown that an enhancement of the Raman signal intensity is triggered when the energy of either the ingoing or outgoing photon is equal to that of the exciton states at the given magnetic field. In case of a nonresonant excitation, the signal of the detectable overtones is much weaker. For this reason, in the spectra shown here the excitation energy is chosen in the way to maximize the number of SF resonances while at the same time preserving a monotonic decrease in their intensity.

However, not only the excitation conditions play an important role, but also the Mn^{2+} concentration x within the DMS heterostructure. In Fig. 7.6 (a)-(c), SFRS spectra are depicted, which have been acquired at an intermediate angle of $\theta = 60°$ for samples with different Mn^{2+} concentrations. Comparing the spectra with each other, it

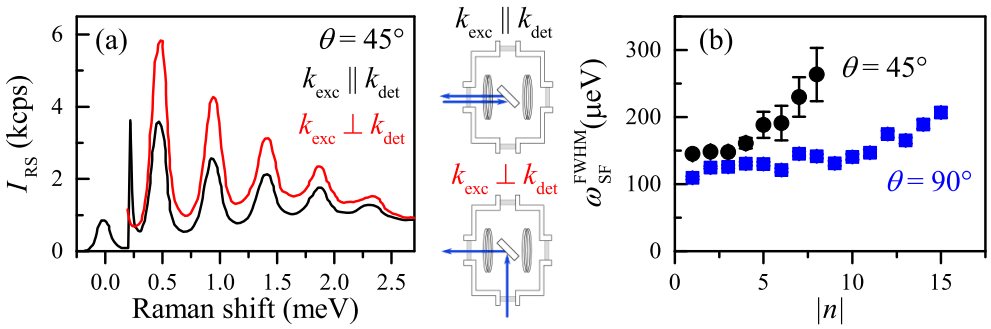

Figure 7.7: (a) Comparison of two Stokes-SFRS spectra of the paramagnetic Mn^{2+} SF lines for parallel (black curve) and perpendicular (red curve) laser light incidence with respect to the optical detection path. The two small schemes between Fig. (a) and (b) illustrate the principal course of light in this experiment. The depicted results pertain the $Zn_{0.988}Mn_{0.012}Se$ QW sample regarding a resonant excitation of the low energy hh-X at $E_{exc} = 2.7991$ eV measured at $B = 4$ T and $T = 1.6$ K in co-circular polarization configuration (σ^+,σ^+). (b) Dependence of the FWHM of the Mn^{2+} Stokes-SF line (ω_{SF}^{FWHM}) on the resonance number ($|n|$) in tilted ($\theta = 45°$) and Voigt geometry. This data originate from SFRS spectra measured at $B = 2.9$ T and $T = 1.6$ K in co-circular polarization configuration (σ^+,σ^+).

is immediately evident that for higher x there are significantly fewer resonances visible. At $x = 0.004$ one observes $n = 7$ resonances on the Stokes side, while at $x = 0.035$ it is only $n = 2$. From these results one concludes that a strong spatial confinement and low Mn^{2+} ion concentrations enhance the probability of observing a large number of multiple higher order spin-flips in QWs. Nevertheless, it should be noted at this point that the highest number of SF resonances for $\theta = 60°$ has been denoted at $x = 0.012$ ($n_S = 13$ and $n_{AS} = -9$).

A thorough analysis of the spin-flip profiles suggests that the SF halfwidth increases for higher n. In order to illustrate this more clearly, Fig. 7.7 (b) shows the SF halfwidth (ω_{SF}^{FWHM}) as a function of n at 45° and 90° for the ZnMnSe QW sample with $x = 0.012$. The evolution of the data shows that the width of the SFs depends on the angle θ as well as on the resonance number n. In both cases shown, the width of the SFs increases by a factor of two, whereby this occurs earlier with regard to smaller angles ($\theta = 45°$). Furthermore, it appears that the Mn^{2+}-SF halfwidth in Faraday geometry is much larger than in Voigt geometry. It differs approximately by 70 μeV.

To determine the influence of the propagation direction k of the excitation beam on the signal outcome, SF Stokes spectra in backscattering geometry ($k_{ext} \parallel k_{det}$) and for incident laser light perpendicular to the detection path ($k_{ext} \perp k_{det}$) are investigated. The resulting SFRS spectra are shown in Fig. 7.7 (a). The two small schemes shown in this figure illustrate the principal course of light in this experiment. While in the backscattering geometry the k-vector difference is maximal, for tilted incidence the k-

vector difference vanishes. Apart from slight differences in intensity, the two acquired Raman spectra in opposing geometries display no divergences. One can neither see a shift of the SF energy nor an energy separation between the different Mn^{2+} resonances.

In summary, the study of the g factor and the angular dependence of the Mn^{2+} SF resonances has provided substantial information for a better understanding of the SF mechanism. In this context, the results show a clearly visible difference between Stokes and anti-Stokes scattering, yielding Landé factors of $g_S = 1.92$ and $g_{AS} = 2.06$, respectively. Furthermore, an analysis of the multiple higher order spin-flips has revealed a strong dependence on the angle between the external magnetic field and the quantum well growth axis as well as on the Mn^{2+} ion concentration. A dependence on the k-vector of the incident beam could not be monitored.

The last open question before the SF mechanism is explained in-depth is whether nuclei are involved in the Mn SF process or not. In the interest of finding an answer to this issue, radio frequency measurements are carried out. The results of these are discussed in the subsequent section.

7.1.2 Interaction between nuclei and carriers in the SF-process investigated by application of radio frequencies

An established method to investigate the influence of nuclei on spin-flip processes is by means of radio-frequency (RF) measurements coupled with SFRS. Here, this method is used to check whether ^{55}Mn or ^{77}Se nuclei, which are embedded in the crystal structure, have an influence on the Mn SF process. In order to get an impression of the technique used, at the outset of this section the theoretical basics are introduced and subsequently the results of the experiments are discussed.

Radio frequencies are mainly used in the field of nuclear magnetic resonance (NMR). NMR is a physical phenomenon in which the atomic nuclei of a material absorb and emit electromagnetic alternating fields in a constant magnetic field. This technique is one of the standard methods for the investigation of atoms and molecules and is used primarily in the field of medical imaging diagnostics.[305] NMR is based on the Larmor precession of the nuclear spin around the axis of the magnetic field. Hereby the nuclei align their spin precision either parallel or anti-parallel and precess with their rotational eigenfrequency, which is given by:

$$\omega = \gamma B_0.$$

Here, ω is the frequency of precession, γ is the gyromagnetic ratio and B_0 is the strength of the external field at the location of the core. As one can derive from this equation, the resonance frequency is proportional to the strength of the magnetic field and to the gyromagnetic ratio of the magnetic dipole moment of the core. Analyzing the amplitude and especially the frequency of the magnetic resonance allows one to draw

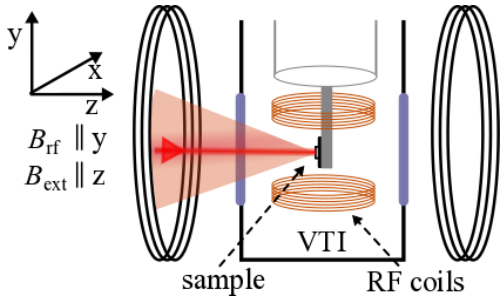

Figure 7.8: Scheme of the sample holder with a pair of small coils in Helmholtz configuration located in the variable temperature insert (VTI) of a split-coil superconducting magnet system. The laser excitation is illustrated by the red line. The scattered light from the sample is collimated by a plano-convex lens positioned in front of the cryostat. The radio frequency (RF) coils generate a magnetic field (B_{RF}) perpendicular to the external magnetic field as well as the growth axis.

detailed conclusions on the structure of the nuclei as well as on possible interactions with the immediate and wider atomic environment.

In order to study the nuclei which have aligned themselves in the presence of an external field, the nuclear spins have to be pertubated by employing an electro-magnetic pulse, for example in the form of radio frequencies. The necessary frequency to achieve this is dependent upon the magnetic field and nuclei of observation. In the case of the ZnMnSe heterostructure the main focus is on the ^{55}Mn and ^{77}Se nuclei. To address those nuclei RF fields are used, which are directed perpendicular to the growth axis (along the y-axis) using a pair of coils in Helmholtz configuration.

A scheme of the bottom part of the sample holder, illustrating the mounting of the sample and the position of the RF coils, is presented in Fig. 7.8. The RF coils are placed directly below and above the sample, and, thus, provide a homogeneous magnetic field in the vicinity of the sample. By driving a sinusoidal alternating current through the Helmholtz coils at the Larmor frequency, an oscillating magnetic field perpendicular to the external magnetic field as well as the growth axis is produced ($\vec{B}_{\mathrm{RF}} \perp \vec{B}(xz$-plane)). To provide the necessary RF power for the experiments, the RF signal from the arbitrary function generator (AFG, Tektronix AFG 3022) is amplified by a class AB RF amplifier with complementary transistor output stages. The effective RF-field strength is about 1 mT.

In contrast to typical NMR measurements, the result here is directly studied by means of resonant SFRS. With this approach, the influence on the SF process can be investigated directly. Any change in the spectrum is an indication of an interaction between the nuclei and Mn carriers.

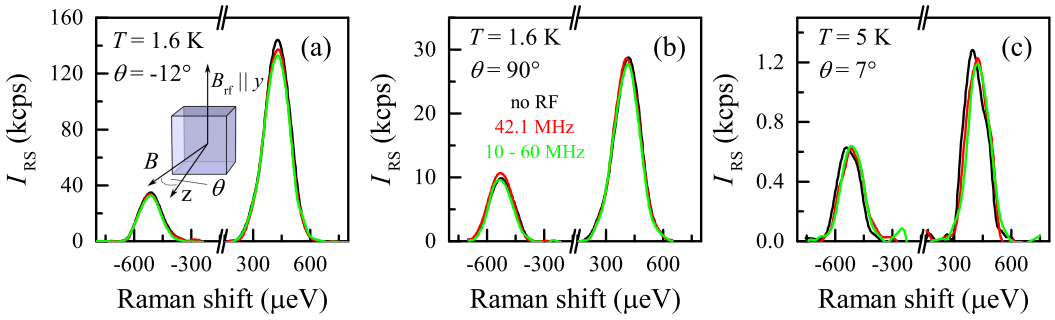

Figure 7.9: Dependence of the first paramagnetic Mn^{2+} SF line ($n = 1$) on the Stokes and anti-Stokes side on the application of RF-fields at $B = 4$ T in co-circular polarization configuration (σ^+,σ^+). The spectra are measured in tilted ($\theta = -12°$ (a), $\theta = 7°$ (c)) and Voigt (b) geometries at $T = 1.6$ K (a)-(b) and $T = 5$ K (c). The laser line at zero Raman shift is not shown in the spectra. The small insert in Fig. (a) illustrates the direction of RF field and the external magnetic field. The RF fields are directed perpendicular to the growth axis z. The effective RF-field strength is about 1 mT. The black spectra in each Fig. displays the SFRS spectra without applied RF fields. In the other two examples a frequency of 42.1 MHz (red curve) and a frequency sweep from 10 to 60 MHz with a repetition rate of 100 Hz (green curve) is used.

The SFRS spectra measured with and without applied RF fields at low ($T = 1.6$ K) and elevated ($T = 5$ K) temperatures in close to Faraday and Voigt geometry for the $Zn_{0.988}Mn_{0.012}Se$ QW sample are depicted in Figs. 7.9 (a)-(c). In the measurements, two different RF's has been used. On the one hand a frequency of 42.1 MHz has been applied, which is in resonance with the ^{55}Mn isotope with a nuclear spin of 5/2,[306] and on the other hand a frequency sweep from 10 to 60 MHz with a repetition rate of 100 Hz is used to depolarize simultaneously the ^{55}Mn and ^{77}Se (32.4 MHz) nuclear spin system.

However, as one can see in these results, the Mn^{2+} SF is insensitive to any applied RF fields. There is no distinct change in the energy shift, scattering intensity or shape of the spectra. A change of the sample bath temperature or the geometry does not induce any change, as well. The slight fluctuation of the SF intensities can be attributed to a heating of the lattice by means of nuclear magnetic resonance spin heating. However, since there is no evident change a possible interaction between nuclear and carrier spins in the Mn SF process can be excluded.

7.2 Mechanism of the Mn^{2+} spin-flip scattering

As mentioned above exchange interactions between the magnetic ion spins and carriers spins in II-Mn-VI semiconductor structures have been studied extensively in recent

years. DMS structures such as (Cd,Mn)Te/Cd(Mn,Mg)Te quantum wells have been thoroughly investigated, providing precious knowledge on Mn^{2+} spin-flip scattering in oblique magnetic field geometries. However, the spin-flip scattering mechanism is discussed contrarily and a unified description is not stated so far. Up to now there are several unsolved open issues which are dealt with in the framework of this thesis. The newly gained knowledge shall contribute to a better understanding of the mechanism and shall help to unite the different explanations in one common picture.

Based on the experimental results, which are discussed in the last sections, the spin-flip scattering mechanism of the Mn^{2+} ions is described in the following. Generally speaking, the scattering mechanism consists of two processes. In Faraday geometry the transitions between the six spin states of Mn^{2+} define the spin-flip characteristics whereas in oblique magnetic field geometries the scattering is governed by the presence of heavy-hole exciton polarons. In the following, the focus is first set on the mechanism in Faraday geometry and afterwards extend in regard of oblique field geometries.

The first important issue that is addressed in the course of investigation is the excitation energy dependence of the first paramagnetic resonance (see Sec. 7.1). It is crucial to determine whether trions are involved in the scattering process or exclusively the heavy-hole excitons. In a negative trion, the electron spins compensate each other and only the hole can interact with the Mn spin. The observation of trion linked spin-flip processes would, therefore, indicate that exclusively the holes are involved in the spin-flip process. However, the investigations of the excitation energy dependence showed that the SF processes are only initiated at the heavy-hole exciton resonances. Regarding a resonant negative trion (X^-) excitation spin-flips could not be instigated as can be clearly seen in Fig. 7.2. For this reason negative trions can be excluded in the mechanism. The influence of positive trions (X^+) can be ruled out as well, since those are not present in the studied QW samples.[295,300] The results demonstrate that the exciton electron plays a major role in the SF process.

The analysis of the SFRS polarization properties (see Sec. 7.1) revealed strict optical selection rules. The SF is predominantly co-polarized. This means that the polarization of the incident light is equal to that of the scattered light. These spin-flip polarization properties result from the giant Zeeman splitting of the exciton states which strongly exceed the inhomogeneous broadening of the exciton lines. For this reason, the electron and hole in the exciton have the same spin orientation before and after the Mn spin-flip process. This implies that in this SF process the exciton electron has to reverse its spin orientation either twice or not at all.

For the first case an at least fourth-order SF process has to be proposed. This is explainable, if an interaction with nuclei is considered. A scheme illustrating a possible fourth-order SF process is shown in Fig. 7.10. Here the spin-flips of the exciton electron are induced by the *sp-d* contact exchange interaction with the 3*d*-electrons of an Mn^{2+} ion reversing the spin of the conduction band electron. Immediately afterwards the

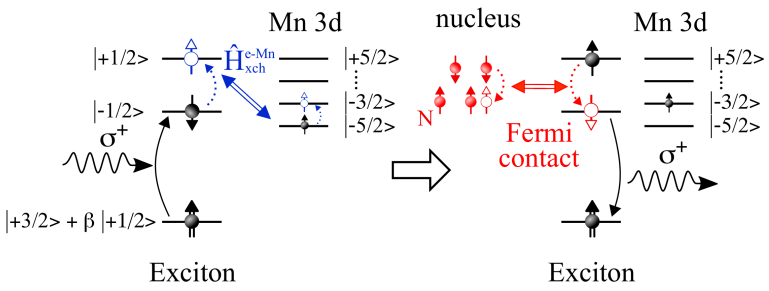

Figure 7.10: Model scheme of the fourth-order Mn^{2+}-SF scattering process in Faraday geometry in which the ^{55}Mn nuclei are involved. The resonant excitation is σ^+ polarized. Due to *sp-d* contact exchange interaction with the 3*d*-electrons of an Mn^{2+} ion and afterwards through Fermi contact hyperfine interaction with the ^{55}Mn nuclei the photo excited electron flips his spin twice. The scattered electron recombines in the last step emitting light with the same polarization as the incident. The energy difference between incoming and outgoing photon equals $\Delta E = \hbar\omega_{det} - \hbar\omega_{exc} = \mu_B\, g_{\mathrm{Mn}}\, B_{\mathrm{eff}}$.

exciton electron interacts through Fermi contact hyperfine interaction with the ^{55}Mn nuclei which causes the spin of the carrier to be reversed again. Finally, the electron and hole of the exciton recombine and emit polarized light equal to the incident light. However, this process can be excluded since the application of radio-frequency fields demonstrated that there is no interaction between nuclear and carrier spins involved in the spin-flip process (see Sec. 7.1.2). This leads to the conclusion that the spin orientation of the exciton electron remains fixed during the spin-flip process.

A possible way to explain the process in regard of a fixed spin orientation, is by an anisotropic *e-e* flip-stop exchange interaction [171] and the coherent rotation of the Mn spin ensemble around the exchange field generated by the photo excited hole spins. [307] The mechanism will be explained in more detail now. The overall spin-flip process is illustrated by the scheme in Fig. 7.11 whereas the intermediate interaction with the heavy holes is schematically shown in Fig. 7.12.

Before the arrival of the laser pulse, the Mn spins are preferentially aligned perpendicular to the applied magnetic field $B_z \parallel \vec{z}$. (see Fig. 7.12 (a)). Immediately following photo excitation, the electrons and heavy-holes of the exciton are spin polarized along the growth direction z. Now, due to the *sp-d* contact exchange interaction between the 3*d*-electrons of the Mn^{2+} ions and the conduction-band electron, a flip of the 3*d*-electron spin is initiated while leaving the spin of the exciton electron invariant. In other words, this can be depicted as a flip-stop exchange interaction. In the intermediate state of this scattering process, the total magnetization of the manganese spins precesses around the resulting field (B_{eff}), which is formed by a combination of the external magnetic field (B_{ext}) and the exchange field (B_{exch}) induced by heavy holes (see Fig. 7.12 (b)). The exchange field of the electron spin can be neglected here

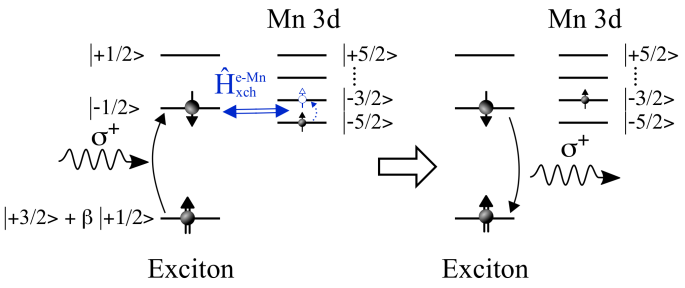

Figure 7.11: Model scheme of an anisotropic flip-stop exchange interaction process between the 3*d*-electrons of the Mn^{2+} ions and the conduction-band electron in Faraday geometry. The resonant excitation is σ^+ polarized. The exchange interaction leads to a flip of the Mn 3*d*-electron spin, while leaving the spin of the photoexcited electron invariant. In the intermediate state, the scattering of the electron induces a coherent rotation of the Mn spin ensemble around the exchange field generated by the heavy-hole spins. The scattered electron recombines in the last step emitting light with the same polarization as the incident. The energy of the outgoing photon equals $\Delta E = \mu_B\, g_{\mathrm{Mn}}\, B$.

due to its weaker coupling to the Mn sublattice.[307] The precession of the total Mn magnetization leads to a reduction of the exciton energy not altering the exciton spin orientation. After this exchange interaction, the exciton electron and hole recombine and emit polarized light equal to the incident. Now that the exciton is absent, the perturbed Mn magnetization remains precessing around the external field but the precession amplitude will decay with time (see Fig. 7.12 (c)). In this Raman scattering process the energy of the exciton decreases (increases) by the amount of energy needed for a single Mn spin-flip to be excited from $|-5/2>$ to $|-3/2>$. The shift in energy between the incident and emitted photon is, therefore, equal to an integer multiple n of the basic SF energy given by the Zeeman equation: $\Delta E = \mu_B\, g_{\mathrm{Mn}}\, B$, where g_{Mn} is the gyromagnetic ratio for the Mn^{2+} 3*d*-electrons.

In order for this process to be possible, the total angular momentum conservation must be lifted. This requires a spatial mismatch between the conduction band electrons and the manganese 3*d*-electron wave functions.[301] If one considers the formation of a magnetic polaron, as suggested in earlier studies[290], one can expect that within the exciton volume a spatial disproportion of the wave functions is probable. The efficiency of the anisotropic exchange interaction can be several orders of magnitude higher than that of an isotropic exchange interaction.[165,308]

It shall be emphasized at this point that the mechanism described here obviously does not negate the influence of the heavy holes. The given description is in no contrast to earlier studies. However, it takes into consideration that not only the heavy-holes are involved in the process.

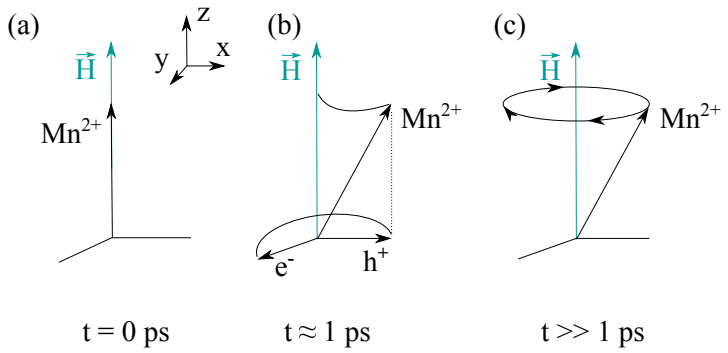

Figure 7.12: Model scheme of coherent rotation of the Mn^{2+} SF around the hole exchange field. (a) All Mn spins are oriented initially perpendicular to the applied magnetic field $B_z \parallel \vec{z}$. (b) Due to a flip-stop exchange interaction between the photo excited electron and the Mn $3d$-electron the Mn spin is tipped into x direction and starts to precess around the exchange field created by the heavy-holes. (c) Mn spins remain precessing around the applied field for long times. The figures are adapted from Ref. [307].

In tilted magnetic field geometries, where the external magnetic field is at an angle θ to the z axis, it is stated that the decrease in magnetization over time, results from the procession of the magnetization around B_{eff}, which is parallel to the angle θ. Here, the precession is given by the angular velocity $\omega_{ac} = \mu_B\, g_{\text{Mn}}\, B_{\text{eff}}/\hbar$.[289,290] This rotation model of Merkulov and Kavokin is used to describe the appearance of multiple spin-flip resonances in tilted magnetic field geometries.[24] However, it is not completely inconsistent with the results shown here, although it implies that multiple Mn^{2+} spin-flips are not observable in the anti-Stokes spectrum, when the projection of the total Mn spin on the external magnetic field is equal to its maximum value. The reason is that this only applies when the temperature of the Mn system is negligibly low ($T_{\text{Mn}} \approx T_{\text{bath}}$). Since our experiments show in exact Faraday geometry at least two paramagnetic Mn^{2+} spin-flips on the anti-Stokes side (see Sec. 7.1.1), in consideration of this model, this indicates a high Mn spin temperature. This is in good agreement with the results presented in this chapter. Due to resonant excitation of heavy-hole exciton resonances the temperature of the Mn system is raised significantly. From an analysis of the $E_{\text{Reso}}(B)$-dependence, one obtains effective Mn spin temperatures between 3.7 and 6.4 K. Therefore, it is obvious that this reaches the limits of the model proposed by Merkulov and Kavokin, which in turn leads to the consequence that paramagnetic spin-flip resonances are observed on the anti-Stokes side. Another aspect that should be mentioned here is the spin-lattice relaxation time, which is directly influencing the Mn spin temperature (see Sec. 2.3.5). As it has been shown in previous studies, the spin-lattice relaxation is slower in (Zn,Mn)Se QWs than in (Cd,Mn)Te QWs[300], resulting in a high Mn spin temperature induced through resonant exciton excitation.

Contrary to the Faraday geometry, in oblique magnetic fields one identifies a large number of paramagnetic Mn^{2+} resonances on the Stokes ($n_S = 16$) and anti-Stokes

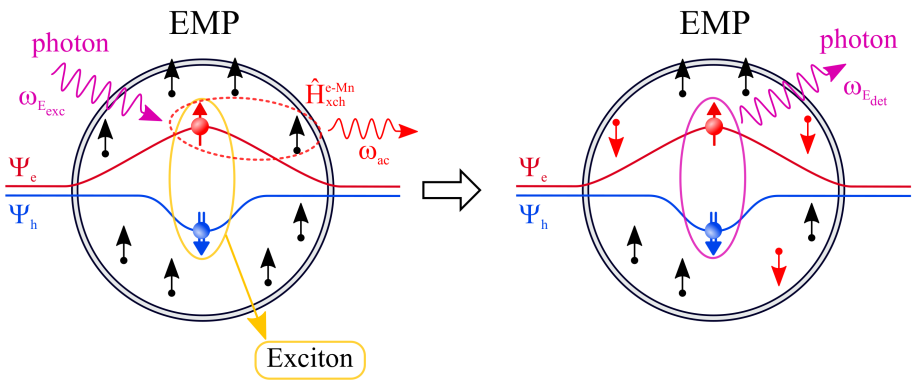

Figure 7.13: Model scheme illustrating the anisotropic flip-stop exchange interaction process between the 3*d*-electrons of the Mn^{2+} ions and an electron polaron in tilted geometries. The resonant excitation by a photon creates an exciton in whose nourishing environment several Mn spins align themselves perpendicular to the exciton electron. Due to the *sp-d* contact exchange interaction the exciton electron interacts with several Mn^{2+} ions changing their spin orientation. The scattered electron recombines in the last step emitting a photon with an energy, reduced by an integer multiple n, equal to the number of 3*d*-electron Mn spins, which are involved in the scattering process.

($n_{AS} = 11$) side. Obviously, this cannot be explained in terms of scattering processes involving just the six ($n_{\max} = 2S + 1$, with $S = 5/2$) spin states of a single Mn^{2+} ion states. It is self-evident that this has to be a collective effect involving numerous Mn^{2+} ions. It is considerable that the multiple paramagnetic resonance spin-flips result from the creation of a localized heavy-hole exciton formed by an electron hole pair belonging to the lowest subbands of spatial quantization.[289] This is described in the frame of an electron polaron (EP). A scheme illustrating the exciton-Mn exchange interaction is shown in Fig. 7.13.

To understand how the mechanism works, this segment focuses on describing the interaction between the EP with the 3*d*-electrons of the single Mn^{2+} ion states. The exciton and the magnetic Mn^{2+} ions, which are in the immediate vicinity of the exciton, are coupled by the *sp-d* contact exchange interaction (see Chap. 2.3.3). This interaction between the jth Mn ion and ith electron can be described by the Hamiltonian:

$$H_{\text{exch,e-Mn}} = \sum_{i,j,\sigma\sigma'} J_{ij}(R) S_{\sigma\sigma'} \cdot M c^{+}_{i,\sigma} c_{j,\sigma'}, \tag{7.1}$$

which involves the exchange matrix elements $J_{ij}(R)$, the Pauli spin matrices $S_{\sigma\sigma'}$ and the Mn spin operators.[155] As the results of an analysis of the SFRS spectra in oblique magnetic field geometries show, this interaction, does not reverse the spin of the exciton electron, since the polarization properties remain unchanged. This leads to the conclusion that this interaction is based on a flip-stop exchange interaction. During this

scattering process the exciton electron can interact with several Mn^{2+} ions. The total magnetization of these Mn ions, precesses around the effective magnetic field provided by the heavy holes of the EP, in turn reducing the energy of the EP by an integer multiple n equal to the number of $3d$-electron Mn spins involved. The energy ($\hbar\omega_{ac}$) of each Mn spin-flip excitation is passed on to the crystal lattice via acoustic phonons. This can in turn cause an increase of the Mn spin temperature. The shift in energy between the incident (ω_{exc}) and emitted photon (ω_{det}) is given by: $\Delta E = \hbar\omega_{det} = \hbar\omega_{exc} - n \cdot \hbar\omega_{ac}$.

The multiple Raman scattering depends strongly on the Mn doping concentration and on the magnetic field geometry, since spin-flip process of the exciton electron become more likely by magnetic-field-induced symmetry reduction. While in Faraday geometry the spin-flip of the exciton-electron is blocked by the Pauli exclusion principle, in tilted geometries, the in-plane component induces a mixing of the electron spin basis eigenstates leading to a reduction of the symmetry and in turn increasing the e-SFRS efficiency.[33,36] The maximum possible symmetry breaking by the applied field is achieved in Voigt geometry, thus, explaining the significantly enhanced *sp-d* exchange interaction, which results in a large number of excited Mn ions and, thus, in many multiple Mn^{2+} spin-flips.

The Mn concentration in the QW influences the number of Mn ions within the exciton interaction radius. On the one hand, this leads to an intensification of the *sp-d* exchange interaction, but on the other hand it also increases the number of counterproductive Mn-Mn interactions. In the case of high concentrations, this leads to a significant decrease of observable higher order spin-flips, as described in Sec. 7.1.1.

Summing up, the spin-flip scattering mechanism in $(Zn_{1-x}Mn_x)$Se/ (Zn,Be)Se QWs is governed by anisotropic flip-stop exchange interactions between the $3d$-electrons of the Mn^{2+} ions and the conduction band electrons and is influenced strongly by the heavy-hole induced exchange field in the intermediate state of the scattering process. In non-oblique field geometries the mechanism bases mainly on transitions between the six spin states of Mn^{2+} ions whereas in tilted magnetic field geometries it is exclusively describable by the formation of an electron magnetic polaron. As shown these explanations are in no contradiction to previous publications, as it is adequately clarified. The presented theoretical explanation of the mechanism is furthermore supported by the experimental results.

On the basis of the above described mechanism, the following section focuses on the energetic asymmetry observed in SFRS on Mn^{2+} ions. This peculiarity, which is monitored for the first time within a $Zn_{1-x}Mn_x$Se QW DMS structure, is thoroughly analyzed and discussed.

7.3 Asymmetric Mn^{2+} spin-flip resonances in DMS

In this section the focus is shifted to the energetically asymmetric Mn^{2+} spin-flip resonances in $Zn_{1-x}Mn_xSe$ QWs. After an extensive analysis of the Mn Landé factors it has turned out that a clear disparity between Stokes and anti-Stokes scattering in exact Faraday geometry yields effective g factors of $g_{Mn} = 1.96(2.06)$. Due to this significant difference in Raman scattering at high magnetic fields the Stokes and anti-Stokes spin-flip lines differ by several hundreds of μeV. It is to be assumed that the energetic asymmetry is created by a dynamic polarization of non-equilibrium manganese spins with high spin temperatures. The energy difference in the Mn^{2+} SF resonance energies between Stokes and anti-Stokes is displayed in the following by

$$\delta E = |\Delta E_{\mathrm{S}}| - |\Delta E_{\mathrm{AS}}|. \tag{7.2}$$

This asymmetry in the Mn spin-flip energies depends on several factors, e.g. the Mn ion concentration, laser power density, magnetic field strength as well as optical geometry. Each of these aspects is studied in detail. The results and associated interpretations are presented in the subsequent sections.

7.3.1 Dependence of the energetic asymmetry on the Mn-ion concentration

As it is revealed by an detailed analysis of the multiple higher order Mn^{2+} SFs in tilted geometries, the Raman signal intensity as well as the number of spin-flip overtones depends strongly on the concentration x of Mn impurities in the $Zn_{1-x}Mn_xSe$ QWs. To which degree this also affects the energetic asymmetry is discussed in this subsection. To analyze this dependence, three (Zn,Mn)Se QWs with different Mn ion concentrations are studied. The obtained results are further compared with SFRS measurements on a $Cd_{0.983}Mn_{0.017}Te$ QW. In regard of the experiment, all studied QW structures are excited respectively at their low-energy X resonance. The spin-flip Raman spectra showing the first paramagnetic resonance SF ($n = \pm 1$) measured at $B = 4$ T in Faraday geometry are depicted in Figs. 7.14 (a)-(d). The g factors of the respectively investigated QW samples are depicted in table 7.2. The values are determined by linear least square fit to magnetic field series in Faraday geometry (not shown here).

The QW sample with the weakest Mn ion concentration ($x = 0.004$) (see Fig. 7.14 (a)) reveals a very low asymmetry. Here the Stokes (S) and anti-Stokes (AS) Raman scattering lines have similar energy shifts of $\Delta E_{\mathrm{S}} = (466 \pm 4)$ μeV and $\Delta E_{\mathrm{AS}} = (-474 \pm 5)$ μeV yielding a asymmetry energy of $\delta E = (8 \pm 9)$ μeV. The corresponding g factor for a low- and high-energy X resonance excitation on the Stokes side equal approximately $g_{\text{X-low}} = 1.97 \pm 0.03$ and $g_{\text{X-high}} = 2.04 \pm 0.03$ (see Tab. 7.2). For comparison, in literature the Mn^{2+} resonance is characterized by a g factor of 2.0.[309] In terms of measurement accuracy, this corresponds well to the experimental results.

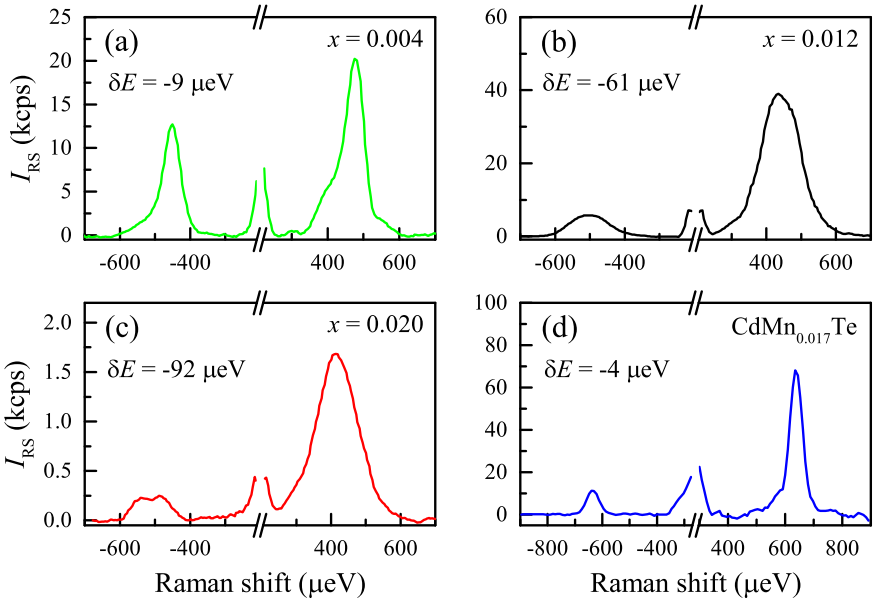

Figure 7.14: "(a)-(c) SFRS spectra of the first paramagnetic Mn^{2+} SF lines ($n = 1$) of the $Zn_{1-x}Mn_xSe$ QWs, excited at their low-energy hh-X resonances at $B = 4$ T and $T = 1.6$ K in co-circular polarization configuration (σ^+,σ^+). The excitation energies for each case are: (a) 2.812 eV, (b) 2.797 eV and (c) 2.792 eV. (d) SFRS spectrum for a (Cd,Mn)Te/(Cd,Mg)Te single QW with $x = 0.017$ measured at $B = 6$ T and $T = 1.6$ K. The laser line areas from -220 to $+220$ μeV are excluded from all plots. The backgrounds are subtracted from the spectra.

If the Mn concentration rises, it can be observed that the asymmetry increases gradually, as shown in Figs. 7.14 (b) and (c). In this regard, the QW sample with $x = 0.020$ reveals the highest asymmetry energy in Faraday geometry of $\delta E = (92 \pm 11)$ μeV. Here the Raman shifts on the Stokes and anti-Stokes side equal $\Delta E_S = (423 \pm 4)$ μeV ($g_S = 1.76 \pm 0.03$) and $\Delta E_{AS} = (-509 \pm 7)$ μeV ($g_{AS} = 2.13 \pm 0.03$), respectively. The asymmetry δE is 84 μeV greater than in the case of the (ZnMn)Se sample with the lowest Mn concentration. Furthermore, one can see that the Raman shift on the Stokes side decreases by 43μ eV while increasing on the anti-Stokes side by 41μ eV. The energetic shift to lower or higher energies is of the same magnitude. For the $Cd_{0.983}Mn_{0.017}Te$ QW sample, which is used for comparison purposes, one observes a negligible asymmetry energy of $\delta E = -4$ μeV. The SFRS spectra is shown in Fig. 7.14 (d). In the (Zn,Mn)Se sample with $x = 0.035$ no spin-flip could be detected in exact Faraday geometry. This is most likely caused by considerable broadening of the SF line due to enhanced Mn-Mn spin interactions. These manifest in fast Mn-spin coherence times and is characteristic for DMS structures with high Mn ion concentrations. [310]

Another noticeable feature of $Zn_{1-x}Mn_xSe$ QWs with raised Mn concentration is a considerable larger halfwidth (ω_{FWHM}) of the SF line. As one can see in the spec-

x	low-energy X resonance		high-energy X resonance	
	Stokes	anti-Stokes	Stokes	anti-Stokes
0.004	1.97 ± 0.03	1.98 ± 0.03	2.04 ± 0.03	2.04 ± 0.03
0.012	1.92 ± 0.02	2.06 ± 0.02	1.95 ± 0.03	2.05 ± 0.02
0.020	1.76 ± 0.03	2.13 ± 0.03	$(1.80 \pm 0.04)^*$	$(2.12 \pm 0.04)^*$

Table 7.2: Landé factor values for Stokes and anti-Stokes of the low- and high-energy X resonance in dependence on the Mn ion concentration. The g factors are determined from a linear least square fit to magnetic field series in Faraday geometry. Exclusively in the sample with $x = 0.020$ the spin-flip signal for resonant excitation of the high-energy X resonance is absent in Faraday geometry. For comparison purposes in this special case the g factor is determined in a small tilting angle of $\theta = 15°$.

tra shown in Figs. 7.14 (a)-(c), ω_{FWHM} grows with rising Mn concentration from $\omega_{\mathrm{FWHM}} = (45 \pm 5)$ μeV ($x = 0.004$) up to $\omega_{\mathrm{FWHM}} = (140 \pm 6)$ μeV ($x = 0.02$). This observation emphasizes the enhanced Mn-Mn spin interactions at higher Mn-doping levels. However, for the $Cd_{0.983}Mn_{0.017}Te$ QW sample, only a very small half-width of $\omega_{\mathrm{FWHM}}^{\mathrm{SF}} = (37 \pm 4)$ μeV is detectable even though the manganese content is $x = 0.017$.

From the g factor values listed in table 7.2, it is evident that the Mn concentration influences the disparity between Stokes and anti-Stokes Raman scattering. The g factor on the Stokes side decreases with rising Mn content while increasing on the anti-Stokes side. The results furthermore demonstrate that there is a negligible difference between an excitation of the low- or high-energy exciton. In both cases, the dependence of g on x is similar. However, the g factor for a resonant excitation of the high-energy X in the (Zn,Mn)Se sample with $x = 0.020$ could not be determined in exact Faraday geometry, since no spin-flip could be detected. The reason for the absence of a spin-flip signal is attributed to the very low signal intensity caused by the giant Zeeman splitting of the hh-X states. For the sake of comparison, g factors determined in a small tilting angle of $\theta = 15°$ are depicted in table 7.2. After clarifying to what extent the Mn concentration affects the energetic asymmetry, in the subsequent section the focus is set on the excitation energy dependence of δE.

7.3.2 Excitation energy dependence of the energetically asymmetric spin-flip resonances

The preliminary analysis of the SFRS resonance profile, described in Sec. 7.1.1, showed that the Mn^{2+}-SF processes are initiated at the heavy-hole exciton resonances. Furthermore, a decisive heating of the Mn spin system is identified leading to a slight decrease of the giant Zeeman splitting. The extent to which this affects the energetic asymmetry of the spin-flip resonances is investigated for the (Zn,Mn)Se QWs. The results and their analysis is discussed in the following.

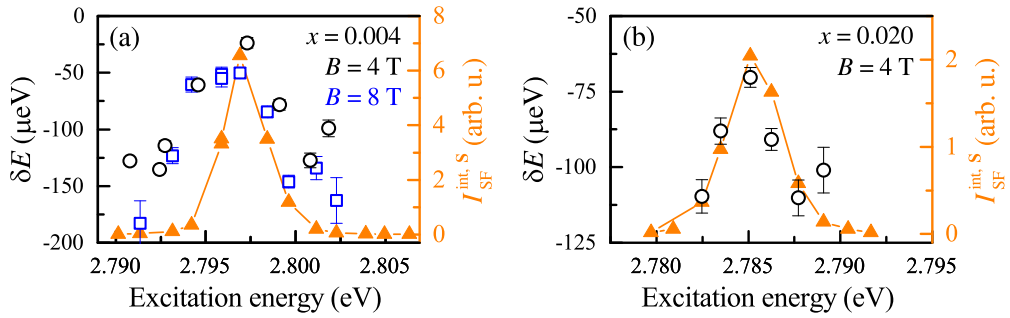

Figure 7.15: Difference δE between the energy shifts of the Stokes and anti-Stokes scattering lines of the first Mn^{2+}-SF paramagnetic resonance (left y-axis) and the integral intensity of the Mn^{2+}-SF on the Stokes side (right y-axis) in dependence on the excitation energy for the samples with a Mn content of $x = 0.004$ and $x = 0.012$. The data are obtained from SFRS measurements in Faraday geometry at $T = 1.6$ K for $B = 4$ T (black open circles) and 8 T (blue open circles).

In order to obtain a better understanding of the energetic asymmetry, the SFRS resonance profile of the $Zn_{1-x}Mn_xSe$ QW sample with a Mn concentration of $x = 0.004$, $x = 0.012$ and $x = 0.020$ are investigated. The QW structures are excited at their low-energy X resonance. In Figs. 7.15 (a), (b) and 7.16 (a) the asymmetry energy δE for the first spin-flip resonance (left y-axis) and the integral intensity of the spin-flip on the Stokes side (right y-axis) are shown as function of the excitation energy. The QW samples are studied in various magnetic fields.

In each case, the results demonstrate that δE is minimal around the hh-X resonance, while it becomes larger for quasi-resonant conditions. The overall evolution of the data reflects clearly the shape of the heavy-hole exciton resonance. For the (Zn,Mn)Se QW samples with $x = 0.004$ studied at $B = 4$ and 8 T in exact Faraday geometry, at the energy of maximal integral spin-flip intensity δE equals -23 μeV and -50 μeV, respectively (see Fig.7.15 (a)). For quasi-resonant conditions this value rises up to -127 μeV at 4 T and -182 μeV at 8 T. This corresponds to a total increase of 105 and 132 μeV. As one can see, the energetic asymmetry value grows for resonant excitation of the X by ≈ 27 μeV. The reason for this result is the magnetic field dependence of δE. As the analysis of the g factor in Faraday geometry has shown, δE increases linearly with the external magnetic field (see Fig. 7.4). This matches well with the depicted results here. For the QW sample with a Mn concentration of $x = 0.02$ studied at $B = 4$ T (see Fig.7.15 (b)), δE equals -68 μeV for resonant and -111 μeV for quasi-resonant conditions. Compared to the sample with less Mn content, the increase of δE to nonresonant excitation is significantly lower. The data show that the Mn content influences noticeably the energetic asymmetry, as it is demonstrated in the last section. In this regard, for resonant excitation of the exciton resonance, $|\delta E|$ differs by 45 μeV. One can see that for higher Mn content the $\delta E(E_{\mathrm{exc}})$-dependence shifts significantly to

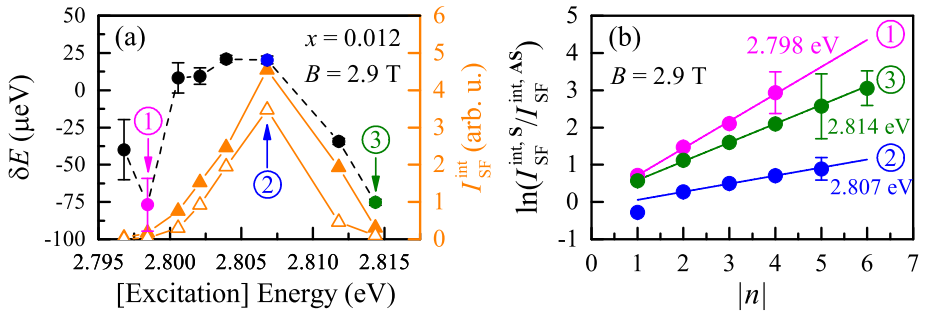

Figure 7.16: (a) Difference δE between the energy shifts of the Stokes and anti-Stokes scattering lines of the first Mn^{2+}-SF paramagnetic resonance (left y-axis) and the integral intensity of the Mn^{2+}-SF on the Stokes side (right y-axis) in dependence on the excitation energy for the sample with a Mn content of $x = 0.012$. The data are obtained from SFRS measurements in tilted geometry ($\theta = 6°$) at $T = 1.6$ K for $B = 2.9$ T. (b) Dependence of the logarithmic Stokes/anti-Stokes intensity ratio on the SF resonance number ($|n|$) for three different excitation energies. The excitation energies are: 2.798 eV (pink), 2.807 eV (blue) and 2.792 eV (green). The chosen excitation energies are numbered and additionally marked by arrows in the respective color. For each set of data points a linear least square fit is preformed. The fit results are depicted by solid lines.

larger negative values, as it is shown in Figs. 7.15 (a) and (b). In summary, one draws the conclusion from these two observations that the external magnetic field influences the strength of δE, whereas the Mn content determines the δE-offset.

It is important to note that the spectra presented for each case are just representative for a certain magnetic field strength. To provide a clear description of the associated Landé factors, it is necessary to investigate the Raman shift for multiple magnetic field series's. A detailed examination of these, evaluated from multiple regression analysis in Faraday geometry, is presented in table 7.2.

Another important aspect, which relates to the resonance profile, is the intensity ratio of Stokes and anti-Stokes. This is investigated for the (Zn,Mn)Se sample with a Mn concentration of $x = 0.012$ at $B = 2.9$ T. The measurement is carried out in close to Faraday geometry ($\theta = 6°$), to provide larger number multiple SFs on the Stokes and anti-Stokes side (see Fig. 7.16 (a)). Due to the slight change of the geometry an extraordinary behavior is evident. In this regard, a detailed analysis of the geometry dependence of the energetic asymmetry is presented in Sec. 7.3.3. Nevertheless, it is worthwhile to note that δE becomes positive for resonant excitation. At the energy of maximal integral spin-flip intensity it amounts $+23$ μeV. But similar as in the other cases, the overall evolution of the data reflects clearly the shape of the heavy-hole exciton resonance and the asymmetry increases to nonresonant conditions. For an excitation energy of $E_{\mathrm{exc}} = 2.798$ eV, δE reaches a maximum value of -78 μeV.

In Fig. 7.16 (b) the dependence of the logarithmic Stokes/anti-Stokes intensity ratio on the spin-flip resonance number ($|n|$) is shown for three different excitation energies. The chosen excitation energies are numbered and additionally marked by pink-, green- and blue-colors in Fig. 7.16(a).

The first distinctive feature one observes is a linear dependence of the logarithmic intensity ratio ($\ln(I^{\mathrm{int,S}}/I^{\mathrm{int,AS}})$) on n. For higher overtones, this ratio increases steadily, which means that the Raman scattering intensity decreases faster on the anti-Stokes side than on the Stokes side. The gradient of change differs markedly for the three highlighted excitation energies. A low (1) or high (3) excitation energy leads to large deviations between the Stokes and anti-Stokes SF line intensities, while for resonant excitation (2), the logarithmic ratio is comparably small and does not exceed a value of 1. It is obvious on the basis of these results, that the logarithmic ratio and δE are interdependent. One sees a clear enhancement of δE as soon as the proportion between Stokes and anti-Stokes rises.

One important detail to be emphasized here, is that, in the case of the first paramagnetic SF resonance ($|n| = 1$), the anti-Stokes SF line is even more intense than the Stokes line. This can be deduced from the negative logarithm which reaches a value of -0.3. However, a linear least square fit to the data indicates that this value deviates significantly from the linear progression. The fit results are shown by solid lines in Fig. 7.16(b). The deviation can be seen as a peculiarity of the first paramagnetic SF resonance.

In summary, the results presented in this section lead to the conclusion that the energetic difference between Stokes and anti-Stokes scattering depends strongly on the excitation resonance conditions as well as on the magnetic field strength. For resonant excitation of the exciton, the energy disparity δE is minimal whereas for quasi-resonant conditions it rises by a factor of three and reaches values of up to -180 μeV. This characteristic has been observed for all investigated ZnMnSe samples. However, the investigation of the (Zn,Mn)Se sample with intermediate Mn content in a slightly tilted geometry yielded unique results. For this reason, the strong dependence on the magnetic field geometry is studied carefully. The results and their analysis are presented in the next section.

7.3.3 Geometry and power dependence of the energetic asymmetry

To complete the overall picture of the underlying effect which causes the energetic asymmetry, the SFRS geometry and excitation power dependence of the paramagnetic resonance spin-flips are studied in-depth. In this context, many factors had to be considered. As it is observed, changes in the geometry or excitation power lead to a shift of the resonance profile, caused by a reduction of the giant Zeeman splitting due to increased spin temperature. Since δE depends strongly on the resonant excitation

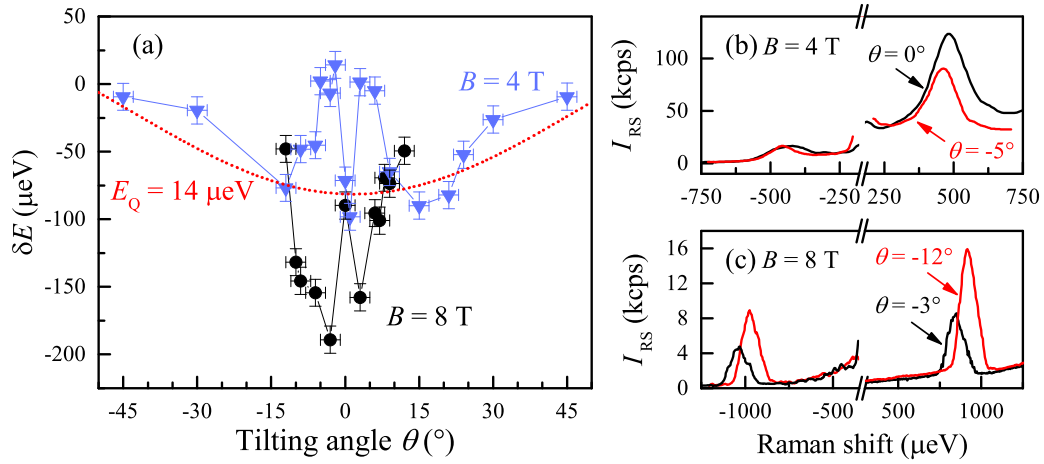

Figure 7.17: (a) Dependence of δE on the tilting angle θ measured for $B = 4$ T (blue triangles) and 8 T (black circles) in co-circular polarization configuration (σ^+,σ^+) at $T = 1.6$ K. Fit results on basis of Eq. (7.14) are shown by the solid curves. (b) SFRS spectra of the first paramagnetic Mn^{2+} SF lines ($n = 1$) at $B = 4$ T for $\theta = 0°$ and $-5°$. (c) SFRS spectra of the first paramagnetic Mn^{2+} SF lines at $B = 8$ T for $\theta = -3°$ and $-12°$. The laser line areas from -220 to $+220$ μeV in (a) and (b) are excluded from the plots. All depicted results pertain the $Zn_{0.988}Mn_{0.012}Se$ QW sample regarding a quasi resonant excitation of the low energy hh-X at $E_{exc} = 2.819$ eV.

conditions, repeated controls had to ensure that the initial conditions remained the same during all experiments.

As it became apparent in the last section, the discrepancy between the Stokes and anti-Stokes energy shifts depends significantly on the tilting angle θ. Already small deviations from exact Faraday geometry lead to strong decrease of δE. To analyze this more precisely, the (Zn,Mn)Se sample with a Mn content of $x = 0.012$ is studied carefully for several angles between Faraday and Voigt geometry at $B = 4$ and 8 T. The QW structure is excited resonantly at their low-energy X resonance. The energetic asymmetry of the first paramagnetic resonance spin-flips determined from the SFRS spectra for each angle is shown in Fig. 7.17 (a). Example spectra for some distinct angles are shown in Figs. 7.17 (b) and (c).

The first noticeable feature is the almost symmetric angular evolution of the data to zero tilting angle ($\theta = 0°$). However, the evolution of the data for $B = 4$ T and 8 T differs strongly from each other. For small tilting angles in very close Faraday geometry ($\theta \leq 3°$) both angular evolutions display strong contrary changes of δE. For instance, in exact Faraday geometry δE equals independent of the applied magnetic field ≈ -75 μeV. But as soon as the tilting angle between the growth and the external magnetic field axis changes, a discernible jump is visible, as depicted in Fig. 7.17 (b).

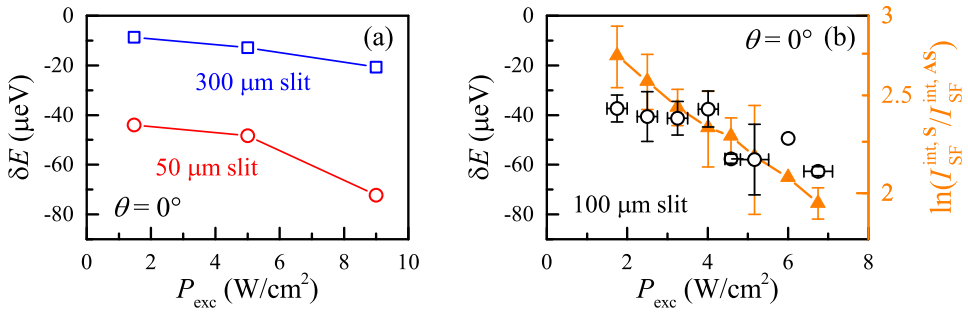

Figure 7.18: (a)Dependence of δE on the laser power density for different sizes of the intermediate cross slit. (b) δE (left y-axis) and the logarithmic SF intensity ratio between Stokes and anti-Stokes (right y-axis) as a function of the laser power density. The data are obtained from SFRS measurements in Faraday geometry at $T = 1.6$ K for $B = 4$ T. All depicted results pertain the $Zn_{0.988}Mn_{0.012}Se$ QW sample regarding a quasi resonant excitation of the low energy hh-X at $E_{exc} = 2.8054$ eV. The full sample area (300 μm diameter) is illuminated homogeneously by the laser spot.

For $B = 4$ T, δE reaches values of $\approx +15$ μeV whereas for $B = 8$ T, δE drops up to ≈ -189 μeV. In the further development, δE descends/ grows with increasing angle, respectively for 4 and 8 T. At about $\theta = 15°$ the evaluated data start to overlap. At this specific angle the energetic asymmetry amounts -85 μeV. From this point on, the value of δE continuously increases reaching $\approx +5$ μeV at $\theta = 45°$. In Voigt geometry (not shown here), the energetic asymmetry is positive and amounts $+35$ μeV for $B = 4$ T. The angular evolution will be theoretically discussed in the subsequent section.

It becomes apparent, that a slight variation of the angle leads to a significant change in the intensity ratio between Stokes and anti-Stokes as well (see Fig. 7.17 (b)). From $\theta = 0°$ to 5°, the SF intensity on the Stokes side rises by a factor of 1.5 while remaining unchanged on the anti-Stokes side. As discussed in the previous section, the logarithmic ratio and δE are interdependent. A change in the energetic asymmetry, therefore, has a direct effect on the intensity ratio as can be seen here. It is important to point out that during these series of measurements it is always ensured that the excitation energy is resonant with the hh-X resonance. In order to demonstrate, that this effect is caused just by the tilting angle, two spectra recorded at $B = 8$ T for $\theta = -3°$ and $-12°$ are shown in Fig. 7.17 (c). Even though the intensity ratio of Stokes and anti-Stokes in both example spectra is similar, one monitors a Raman shift of ≈ 52 μeV, respectively. This corresponds to a absolute change of δE by ≈ 104 μeV.

Besides the strong angular dependence, δE is also very sensitive to the excitation power density. As the brief analysis of the SFRS resonance profiles, described in chapter , showed, the excitation density influences the heating of the Mn spin system and, thus, the magnitude of the giant Zeeman splitting. Especially for a resonant excitation this is not to be disregarded. How far this effect in turn influences the energetic asymmetry

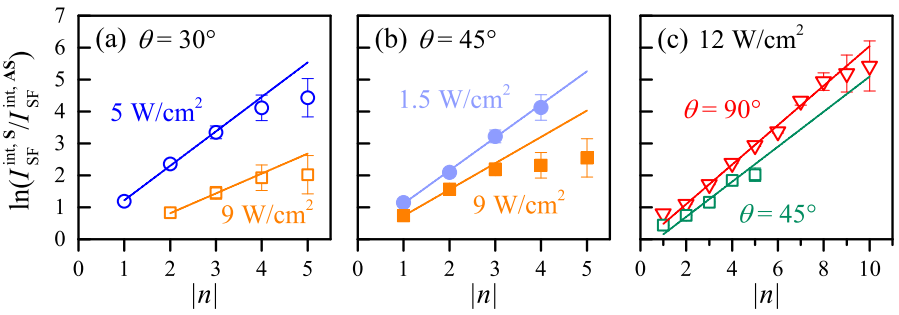

Figure 7.19: Dependence of the logarithmic intensity ratio on the resonance number n for different laser power densities at $\theta = 30°$ (a), $\theta = 45°$ (b & c) and $\theta = 90°$ (c). All depicted results pertain the $Zn_{0.988}Mn_{0.012}Se$ QW sample regarding a quasi resonant excitation of the low energy hh-X at $E_{exc} = 2.8054$ eV. The data are obtained from SFRS measurements at $T = 1.6$ K for $B = 4$ T. The size of the intermediate cross slit in these measurements is set to 100 μm. For each set of data points a linear least square fit for $n \leq 3$ is preformed. The fit results are depicted by solid lines.

is studied for the (Zn,Mn)Se sample with a Mn content of $x = 0.012$. In Fig. 7.18 (b) the energetic asymmetry energy for the first spin-flip resonance (left y-axis) and its logarithmic integral intensity ratio (right y-axis) are shown as function of the excitation density in exact Faraday geometry. From the evolution of this data can be deduced, that an increase of the laser power density results in an enhancement of δE, while the logarithmic intensity ratio decreases. In this regard, δE increases from -38 ± 3 μeV at $P_{\text{exc}} = 2$ W/cm^2 up to -62 ± 1 μeV at $P_{\text{exc}} = 9$ W/cm^2, while $\ln(I^{int,S}/I^{int,AS})$ decreases linearly from 3.5 ± 0.4 to 1.9 ± 0.2. These measurements are performed at an intermediate slit size of 100 μm. However, to determine to what extent the size of the illuminated area (A_{exc}) plays a role, the functional dependence of $\delta E(A_{\text{exc}},P_{\text{exc}})$ is studied. The result for exact Faraday geometry is shown in Fig. 7.18 (a). The analysis indicates that an increase of the illuminated area by a factor of 36 leads to noticeable reduction of the energetic asymmetry by a factor of 4.

To determine the influence of the excitation density on the Mn^{2+}-SF resonance number, the logarithmic intensity ratio of the SF overtones is investigated for different geometries. The results are depicted in Figs. 7.19 (a)-(c). For a tilting angle of $\theta = 30°$ and 45°, one derives from the functional dependence that the ratio between Stokes and anti-Stokes diminishes for higher excitation densities. However, this effect is stronger at 30° then 45°, as one can clearly observe comparing the Figs. 7.19 (a) and (b). The number of observable SFs is mainly determined by the angle. The excitation power has a relatively small impact on n. In the present measurement conditions, due to higher laser power the number can be effectively increased just by 1, as can be seen in Fig. 7.19 (b).

Another characteristic feature that appears for high optical excitation densities, is a deviation of the logarithmic intensity ratio from the linear dependence on n. To show this deviance, a linear least square fit to the data for $n \leq 3$ is preformed. The fit results are depicted by solid lines in Figs. 7.19 (a)-(c). Here, it is evident that in the case of high excitation densities the logarithmic ratio deviates from a linear dependence for $n \geq 4$. However, this effect is less prominent at higher tilting angles, as shown in Fig. 7.19 (c). In Voigt geometry one observes up to the 8th resonance that the logarithmic intensity ratio follows the linear dependence on n.

In summary, the SFRS geometry and excitation power dependence of δE has demonstrated a strong interdependence. The slightest change of the tilting angle θ reveals decisive changes of δE which additionally depend on the applied external magnetic field. The level of asymmetry between Stokes and anti-Stokes depends linearly on the excitation power density. These effects and observations and the reason for the difference between the Mn^{2+} Stokes and anti-Stokes SF energy shifts is discussed in the following section.

7.3.4 Quadruple spin splitting of non-thermalized Mn^{2+}-ions

The detailed experimental analysis of the energetically asymmetric Mn^{2+} spin-flip resonances in $Zn_{1-x}Mn_xSe$ QW's revealed several dependencies. It became apparent, as discussed in the previous sections, that δE displays significant changes concerning the Mn ion concentration, excitation power density, magnetic field strength as well as field geometry. These effects and their associated explanations are discussed and interpreted based on the theoretical background in the following. In this process, different possible explanations will be given and discussed to what extent they can be taken into consideration or which arguments speak against them.

The first possible approach to describe the disparity between the scattering processes on the Stokes and anti-Stokes side is by a nonlinear $E(k)$-dispersion of the exciton polaron. For a clear understanding, the basic idea behind this consideration will be briefly described. In general the exciton dispersion in a semiconductor can be interpreted within the effective-mass approximation as a consequence of the translational movement of the electron-hole pair. The related dispersion relation is then given by the equation:

$$E(k) = \frac{\hbar^2 k^2}{M} = \frac{\hbar^2 k^2}{m_e + m_h}.^{[71]} \tag{7.3}$$

Here M is the total band mass, which is the sum of the electron effective mass m_e and the hole effective mass m_h. Due to deviations from parabolicity, which can occur in the conduction and valence band of a semiconductor because of the interaction with the longitudinal optical phonons, corrections to the above-mentioned dispersion relation must be considered.[311,312] To give an example: In the investigation of the a-exciton in a CdS mass crystal , a pronounced asymmetry for Stokes and anti-Stokes scattering

is observed which results from a non-linear $E(k)$-dispersion due to strong scattering by longitudinal acoustic phonons.[313] However, we cannot apply this explanation to the (Zn,Mn)Se QW. Due to the spatial localization of the exciton polaron in the QW layer, the k_z-vector is not conserved. As a consequence, k-vector-dependent scattering events along the nonlinear dispersion curve are not defined. For this reason, any high- or low energy scattering would be greatly broadened.

An alternative way to explain the process would be via an Mn spin wave (magnon) with a nonlinear dispersion relation. However, this is not very probable in DMS QWs with very low Mn content, since a magnon needs at least two nearly adjacent Mn ions to be excited and even more to progress. In addition, in the case of a Mn spin wave excitation, the energy shift shall depend on the k-vector transfer.[314] This means, that the mechanism should show some effect depending on the optical detection path. In this regard, an in-depth study, which investigates the k-vector dependence in backscattering geometry ($k_{\mathrm{ext}} \parallel k_{\mathrm{det}}$) and for incident laser light perpendicular to the detection path ($k_{\mathrm{ext}} \perp k_{\mathrm{det}}$), is discussed in Sec. 7.1.1. While in the backscattering geometry the k-vector difference is maximum, it is absent for tilted incidence ($\theta = 45°$). However, the results highlight that neither a shift of the SF energy nor an energy separation between the different Mn^{2+} resonances occurs (see Fig. 7.7). This is a clear indication that Mn spin waves are not involved in the process.

Another solution to explain the energetic asymmetry between Stokes and anti-Stokes is by effects of internal exchange fields due to distant-neighbor exchange interactions.[315] In previous experiments on DMS structures with very low Mn concentrations ($x \leq 0.1$), namely $Cd_{0.95}Mn_{0.05}Se$ and $Zn_{0.95}Mn_{0.05}Se$, due to effects of Mn ion pair magnetization abrupt increases of internal fields as a function of the external field are monitored.[316] These magnetization steps lead to an increase of the total magnetic field. This in turn can influence the result of SFRS measurements. However, these effects are observed up to now only in magnetic fields above 10 T. But assuming these are also present here, a decisive zero-field offset in the magnetic field dependence of the Stokes and anti-Stokes SF energy shift shall be measurable. This is not the case in the studied (Zn,Mn)Se QWs, as it is shown in Sec. 7.1.1 (see Fig. 7.4). This means that internal exchange fields can also be excluded from the mechanism.

If one considers the amount of QWs embedded in the studied (Zn, Mn)Se samples, one might expect a coherent excitation of multiple excitons for each QW layer. It would seem obvious that each exciton, independently of the others, coherently generates Mn^{2+}-SF processes. Based on the fact that each QW is separated by a 20 nm thick (Zn,Be)Se barrier this would imply a phase shift between each QW, in turn leading to a dispersion in the Mn SFs along the growth direction z. Considering this possibility, no energetic asymmetry between Stokes and anti-Stokes shall be observable in samples with only one QW-layer. Since, a non-zero δE is measured for single and multiple QW structures, as shown in Sec. 7.3.1, this effect can be ruled out as well.

Since the different excluded approaches have shown that neither the exciton nor the exciton-electron can be responsible for the asymmetry of the Mn^{2+} spin-flip scattering processes, it is reasonable to assume that the effect comes exclusively from the crystal-field splitting of the $3d$-electron states of the incorporated Mn ions. It shall be noted that this assumption considers Mn ions in different non-equilibrium states in a most likely not homogenous Mn ion ensemble. In general, the Mn ion system inside of a DMS heterostructure is characterized by a specific heat capacity and spin temperature.[30] Assuming that all states of this system are in equilibrium and the spin temperature is small, the populated spin levels are concentrated at the lowest part of the energy spectrum. In this case, any scattering process would lead to the same energy shift for low- or high-energy corresponding to the crystal-field splitting of the respective part of the spectrum. However, this is not given for the studied (Zn,Mn)Se QWs, as it is shown by the analyzed data presented in this chapter.

Therefore, to calculate the Stokes and anti-Stokes Mn^{2+}-SF transitions in oblique magnetic field geometries, a general approach on the basis of the model proposed by Merkulov and Kavokin[24] is used. The model itself bases on the precession of the total magnetization of the manganese ions around a resulting field formed by a combination of an external field and an exchange field induced by heavy-holes in the intermediate state of the spin-flip scattering process. In general, the heavy-hole states are characterized by the spin $J_z = 3/2$ and, therefore, their Zeeman splitting in an external magnetic field amounts $3g^h_{\parallel}\mu_B B$. Here, $g^h_{\parallel}$ defines the anisotropic heavy-hole g value in Faraday geometry. In oblique field geometries, where B_{ext} is at an angle θ to the growth axis z, the heavy hole states remain unmixed, providing that these are well separated in energy from those of the light holes.[290] The exciton experiences in this configuration on one side the strong exchange field induced by the heavy holes ($B_{\text{exch}} \parallel z$) and on the other side the external field. The external field leads to a splitting of the exciton states into a higher and lower energy band which are characterized by the total angular momentum projection $j_z = \pm 1$. Here, due to the giant Zeeman effect in DMS's, a stabilization of the exciton spin projections is provided, as it is confirmed by the experimental observation of the strict optical selection rules of the Mn^{2+} SF lines.

As it is discussed in Sec. 7.2, the corresponding SF process is based on a flip-stop exchange interaction with the exciton electron, triggered by a pulse of the heavy-hole exchange field as it is described within the Merkulov and Kavokin model.[24] However, the stated model implies that multiple Mn^{2+} spin-flips are not observable in the anti-Stokes spectrum, which is in contradiction to the results presented here. This discrepancy is caused by the fact that this model only applies when the temperature of the Mn system is negligibly low. As it is highlighted in Sec. 7.2, the Mn temperature is greatly increased by resonant excitation of the heavy-hole exciton leading to significant deviations from the theoretically expected results. For this reason, instead of the semi-classical rotation model by Merkulov and Kavokin, in terms of a general approach, first the probability of spin-flips for each Mn ion is calculated and then the statistical distribution of the number of spin-flips in the Mn ion ensemble is evaluated,

including both positive and negative numbers corresponding to Stokes and anti-Stokes SFRS transitions. In this context, it is assumed that the pulse of the heavy-hole exchange field is short what implies that the spin-flip probability for each Mn ion is small. Furthermore, the occurrence of multiple spin-flips for the same Mn ion is not considered, even though it is symmetry-allowed. Finally, it should be noted that the approach shown below applies to both Faraday and oblique geometries, on condition that the exchange field amplitude is replaced by the matrix element of the anisotropic interaction.

Considering all remarks and assumptions, the transition probability between two levels $|m\rangle$ and $|m-1\rangle$ of a certain Mn ion spin is given by the perturbation theory:

$$W_{m,m-1} = W_{m-1,m} = \langle m|M_x|m-1\rangle^2 b_x^2 \tau/\hbar^2. \tag{7.4}$$

Here M_x is the Mn magnetic moment projection on the x axis perpendicular to the growth axis ($\vec{B} \parallel z$), b_x is the x-component of the exchange field amplitude and τ is the characteristic lifetime during which the exchange field is applied. In an ensemble of n Mn spins, the average number (p) of transitions that increase the Zeeman energy of the Mn spins, in turn leading to spin-flips on the Stokes (S) side, and those that decrease the energy, and, thus, leading to spin-flips on the anti-Stokes (AS) side, are equal to

$$p_{\mathrm{S}} = n \cdot \sum_m \rho_m W_{m,m-1} \tag{7.5}$$

$$p_{\mathrm{AS}} = n \cdot \sum_m \rho_{m-1} W_{m,m-1}. \tag{7.6}$$

In this context, ρ_m and ρ_{m-1} are the probabilities to find a Mn spin in state with the corresponding projection on the external field. When the Mn-spin system is thermalized at a certain spin temperature (T^*) the probability ρ_{m-1} of occupying the state $|m-1\rangle$ with the energy $E = \mu_B g_{\mathrm{Mn}} B$ weighted by the corresponding Boltzmann factor is given by:

$$\rho_{m-1} \propto \exp\left(\frac{-\mu_B g_{\mathrm{Mn}} B}{k_B T^*}\right). \tag{7.7}$$

Hence, the average can be expressed as follows:

$$p_{\mathrm{AS}} = n \cdot \sum_m \exp\left(\frac{-\mu_B g_{\mathrm{Mn}} B}{k_B T^*}\right) W_{m,m-1} = p_{\mathrm{S}} \cdot \exp\left(\frac{-\mu_B g_{\mathrm{Mn}} B}{k_B T^*}\right). \tag{7.8}$$

Because of the small spin-flip probability, the average number of transitions on the Stokes and anti-Stokes side is decisively smaller then the amount of Mn SFs in the ensemble ($p_{\mathrm{S}} \ll n$ and $p_{\mathrm{AS}} \ll n$). Therefore, random numbers of transitions up (n_{S}) and down (n_{AS}) in energy, obey the Poisson distribution:

$$P(n_{\mathrm{S}}) = \frac{p_{\mathrm{S}}^{n_{\mathrm{S}}}}{n_{\mathrm{S}}!} \exp\left(-p_{\mathrm{S}}\right) \tag{7.9}$$

$$P(n_{\mathrm{AS}}) = \frac{p_{\mathrm{AS}}^{n_{\mathrm{AS}}}}{n_{\mathrm{AS}}!}\exp\left(-p_{\mathrm{AS}}\right). \tag{7.10}$$

The distribution of the total number (L) of Zeeman energy quanta in an SFRS spectrum, is obtained from the Eqs. (7.9) and (7.10) by averaging over all possible configurations of transitions on the Stokes and anti-Stokes side:

$$P(L) = \sum_{n_{\mathrm{S}},n_{\mathrm{AS}}} P(n_{\mathrm{S}})P(n_{\mathrm{AS}})\delta_{L,n_{\mathrm{S}}-n_{\mathrm{AS}}} \tag{7.11}$$

$$= \left(\frac{p_{\mathrm{S}}}{p_{\mathrm{AS}}}\right)^{L/2} \cdot \sum_{K=0}^{\infty} \frac{(p_{\mathrm{S}}p_{\mathrm{AS}})^{|L|/2+K}}{(|L|+K)!\cdot K!}\exp\left(-(p_{\mathrm{S}}+p_{\mathrm{AS}})\right). \tag{7.12}$$

This equation can be used to calculate the SFRS spectrum theoretically. However, some conclusions can be drawn even without calculating $P(L)$. For example, one can derive from Eq. (7.12) that the ratio between the Stokes and anti-Stokes intensities with the same number equals to

$$\frac{P(L)}{P(-L)} = \left(\frac{p_{\mathrm{S}}}{p_{\mathrm{AS}}}\right)^{L}. \tag{7.13}$$

When the Mn spins are described by a spin temperature, then it follows from Eq. (7.8) that the ratio of the average number of transitions between Stokes and anti-Stokes ($p_{\mathrm{S}}p_{\mathrm{AS}}$) according to Eq. (7.7) is given by:

$$\ln\left(\frac{P(L)}{P(-L)}\right) = L\cdot\frac{\mu_B g_{\mathrm{Mn}} B}{k_B T^*}. \tag{7.14}$$

If this equation does not describe the experiment, it has to be assumed that the Mn spin system is not in an equilibrium state. Furthermore, if one cannot describe the experiment with Eq. 7.13 either, then this means that the Stokes and anti-Stokes SFRS spectra originate from different Mn ensembles with possibly different spin temperatures, which are caused by dynamic polarization of the non-equilibrium carriers and excitons.

If one compares these theoretical considerations with the experimental observations, one finds out, that most results can be modeled within the frame of 7.14. For example, the dependence of δE on the excitation energy, which is analyzed in detail in Sec. 7.3.2, revealed a clear linear dependence of the logarithmic intensity ratio ($\ln(I^{int,S}/I^{int,AS})$) on the number n of Mn^{2+}-SF resonances. This fact is shown obviously in Fig. 7.16. The theoretical model fits perfectly to the experimental results. In this regard, according to Eq. 7.14, from the slope of the resulting linear fits one can estimate the theoretical Mn spin temperature (T^*). From the evaluation of these results a spin temperature of $T^* = 25 \pm 4$ K for resonant excitation and $T^* = 5 \pm 1$ K for quasi-resonant excitation is determined. As can be derived from these observations the energetic asymmetry scales with T^*. In order to briefly recap, the study of the resonance profile demonstrated that for resonant excitation of the exciton, the energy disparity δE is minimal whereas for quasi-resonant conditions it rises significantly, reaching values of up to -180 μeV. If one

combines both results it becomes obvious that for high theoretical spin temperatures T^* the energetic disparity δE is very low.

In regard of high optical excitation densities, see Figs. 7.19 (a) and (b), the natural logarithm of the intensity ratio cannot be modeled by Eq. (7.14), since the evaluated data points deviate from the linear dependence on n. This occurs for $n \geq 4$, as it is highlighted in Sec. 7.3.3. Further, it is observed that for small n at a high laser power density, the differences in the Mn spin temperatures become larger than for weakly excited Mn ions. However, this effect is less prominent at higher tilting angles, as shown in Fig. 7.19 (c). Nonetheless, the observed deviations from the linear dependence imply that in case of high laser power densities the above described model cannot solely be used to explain the interactions. One can assume in this cases that the Mn spin system is not in an equilibrium state, meaning that there are different Mn ensembles with various spin temperatures involved in the process. However, in the experiments carried out, one always observes the total sum over a large number of excited Mn spins. The effect of energetic asymmetry get's averaged and in turn can decrease, the more Mn ion complexes are taken into consideration. This is particularly evident from the strong functional dependence of $\delta E(A_{\mathrm{exc}})$ on the size of the illuminated area. As it is discussed in the previous section, the analysis indicates that an increase of the illuminated area leads to a noticeable reduction of the energetic asymmetry. This result supports the theoretical consideration.

Since, as explained above, the process cannot be explained solely by the model of Mn spin temperature. A strong influence of dynamic polarization must be considered, based on a system of individual weakly interacting Mn ions in which the excited Mn ions have different polarizations, i.e. different spin orientations in respect to the external magnetic field. It is evident, according to the model of Merkulov and Kavokin, that the precession of the Mn spins around the effective magnetic field depends mainly on the orientation of the Mn spins. Assuming that the Mn spins occupy higher energy spin states after the spin-flip scattering process, i.e. $|+1/2\rangle$, $|+3/2\rangle$, $|-1/2\rangle$ etc., for example due to multiple exchange processes with photoexcited electrons or due to a higher initial energy, the spin orientation is reversed and, therefore, their magnetic moment is opposite to the external magnetic field. This leads to a change of the angular velocity and in turn influences the precession of the Mn spin, resulting in a change of the sign of the quadrupole correction and, thus, leading to the disparity between low and high energy scattering. The quadrupole correction is described in more detail later on in this section. This proposed process is very likely to occur when the number of photoexcited electrons (excitons) is high, as this increases the number of interactions with the Mn spins. Experimentally, this is supported by the fact that the energetic asymmetry increases with the excitation power density, as shown in Sec. 7.3.3. A similar effect of the formation of hot spin domains has been observed by Tyazhlov et al.[175] and has been theoretically analyzed by Kavokin and Malpuech.[317]

The following considerations concern the angular dependent quadrupolar shift which will be explained in the frame of the crystal-field splitting of $3d$-electrons of the Mn^{2+} ions. In general, Mn spins in a QW structure may experience quadrupole splitting. It is similarly to that in tetragonal crystals [318] which take the form of uniaxial quadrupole splitting. The spectrum of transition energies for a quadrupole-split spin in a strong external field is well-known [319]:

$$E_{m-1,m} = -\mu_B g_{\mathrm{Mn}} B + \hbar\omega_Q \cdot (m - 1/2) \cdot (3\cos^2(\phi) - 1). \tag{7.15}$$

Here θ is the angle between the magnetic field and the quadrupole axis, presumably coinciding with the growth axis, m is the spin quantum number of the $3d$-electron of the Mn^{2+}-ion and $\hbar\omega_Q$ is the quadrupole splitting energy. For non-equilibrium states, where the Mn spins have different spin orientations ($-5/2 \leq m \leq 5/2$), the quadrupole correction (see Eq. (7.3.4)) will have a different sign. In particular, positive values of m give rise mainly to anti-Stokes transitions whereas negative values of m lead to Stokes shifts.

To model the angular dependence of the energetic asymmetry, shown in Fig. 7.17 (a), a quadrupole term, obtained from second-order perturbation theory, is used, which is valid for field gradients with less than cylindrical symmetry. [319] In this way, the Eq. expands to

$$E_{m-1,m} = -\mu_B g_{\mathrm{Mn}} B + \hbar\omega_Q \cdot (m - 1/2) \cdot (3\cos^2(\phi) - 1 + \eta \cdot \sin^2(\theta)\cos(2\phi)), \tag{7.16}$$

$$\text{with } \eta = \frac{V_{XX} - V_{YY}}{V_{ZZ}}. \tag{7.17}$$

Here ϕ is the polar angle perpendicular to the plane (zx) and V_{ij} is a tensor which describes the electric field gradient. By means of Eq. (7.16), the evolution of the angular dependence of the energetic asymmetry can now be calculated. For sake of simplicity ϕ, which is negligibly small in the experiment, is set to zero. The best fit to the data for $m = 5/2$, neglecting the strongly deviating data points at small tilting angles at $B = 4$ T, is depicted by the dotted line in Fig. 7.17 (a). One obtains from this fit a quadrupole splitting energy of about 14 μeV (3.4 GHz). However, the complex behavior of $\delta E(\theta)$ at small tilting angles cannot be modeled by the quadrupole term. From the evolution of the data, it can be expected that the significant differences in close to Faraday geometry are due to magnetic field induced processes. An analysis of these is discussed in the following section.

In summary, it is shown in this section that the origin of the Stokes and anti-Stokes Mn^{2+}-SF transitions in diluted magnetic (Zn,Mn)Se QWs can be theoretically derived from a general approach on the basis of the model proposed by Merkulov and Kavokin. The energetic asymmetry is based on the crystal-field split spin states of the $3d$-electrons of Mn ions in a non-equilibrium magnetic state. In this regard, from the angular dependence of the difference between the Stokes and anti-Stokes Mn^{2+} spin-flip energies, a quadrupole splitting energy of about 14 μeV is evaluated. It turned

out that the value of the quadrupole correction and, thus, δE, are tunable through the optical pumping efficiency which also contributes greatly to the Mn spin heating. For Mn ions in a non-equilibrium magnetic state, the huge amount of spins with different spin orientations further manifests itself in the large number of multiple anti-Stokes Mn^{2+} SF lines, not observed in any previous studies.

Now, that it is clear how to describe the energetic asymmetry theoretically, in the upcoming section one further observation will be discussed, which is directly related to the paramagnetic Mn spin system. It is the occurrence of SFRS-intensity drops for specific external magnetic fields.

7.3.5 Resonantly enhanced spin-lattice relaxation of Mn^{2+} ions

In numerous previous studies the dynamics of spin-lattice relaxation in the magnetic Mn^{2+} ion system of DMS QWs are studied by means of optical methods.[30,174,295,300,320] It is discovered that the spin-lattice relaxation (SLR) of single Mn^{2+} ions is limited, as they only weakly interact with the lattice.[320,321]. However, it is completely opposite in Mn spin clusters. Here the Mn ions, which are in non-equilibrium states can relax really efficiently through clusters into equilibrium states while transferring their orbital momentum and energy to them.[174] In general, Mn spins in clusters are coupled anti-ferromagneticaly, providing control of the spin dynamics in DMS structure whereas paramagnetic single Mn ions contribute to the magneto-optical effects.[322] It is clear that the formation of a cluster depends heavily on the Mn-doping content. The more Mn ions are in the crystal, the larger is the number of clusters. The formation of tripple or higher order clusters is also possible.[315] In this section the focus is set on the optical detection of spin transfers between single Mn ions and Mn clusters in the $Zn_{0.988}Mn_{0.012}Se$ QW by means of SFRS.

The magnetic field dependences of the integral spin-flip intensities of the first paramagnetic Mn^{2+} SF line on the Stokes and anti-Stokes side studied in co-polarized configuration (σ^+/σ^+) are shown in Figs. 7.20 (a) and (b) for close to Faraday ($\theta = 7°$) and Faraday geometry ($\theta = 0°$), respectively. It shall be noted, that the excitation energy in these experiments is fixed at 2.7980 eV. Therefore, it cannot be excluded that the resonance conditions change with rising magnetic field strength during this measurement. The shift of the resonance profile amounts approximately 10 meV for increasing B from 2 to 8 T, as it is depicted in Fig. 7.3 (b).

As can be derived from the results shown in Figs. 7.20 (a) and (b), the SF intensity generally increases with increasing magnetic field strength. This is due to the enhanced magnetic confinement of the carriers, which leads to a shrinkage of the wave function and, thus, to high emission and scattering probabilities.[192] One noticeable feature in the evolution of the spin-flip intensity is the appearance of maxima at specific magnetic fields. For $\theta = 7°$ (see Fig. 7.20 (a)), one observes an increase of integral intensity at

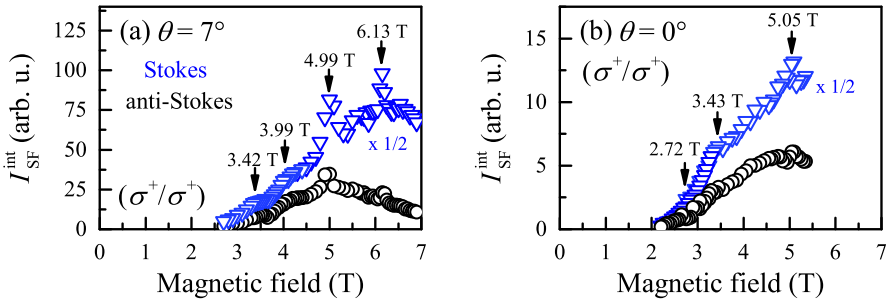

Figure 7.20: Integral intensity of the Stokes and anti-Stokes Mn^{2+} SF lines as a function of the magnetic field strength for close to Faraday ($\theta = 7°$) (a) and Faraday geometry ($\theta = 0°$) (b). All depicted results pertain the $Zn_{0.988}Mn_{0.012}Se$ QW sample regarding a quasi resonant excitation of the low energy hh-X at $E_{exc} = 2.7980$ eV. The data are obtained from SFRS measurements at $T = 1.6$ K for $P_{\text{exc}} = 9$ W/cm^2 in co-circular polarization configuration (σ^+,σ^+). The distinctive peaks in the evolution of the data are marked by arrows. The error in the Raman shift does not exceed the symbol size.

3.42, 3.99, 4.99 and 6.13 T, whereas in Faraday geometry (see Fig. 7.20 (b)), maxima of integral intensity appear at 2.72, 3.43 and 5.05 T. These distinctive peaks are marked by arrows in the figures. The SF intensity rises at these magnetic fields by about 24 %. However, comparing the results in both geometries, one can clearly see that some peaks disappear in Faraday geometry ($\theta = 0°$).

To distinguish, to what extent these enhancements of SFRS intensity alter the energy shift on the Stokes and anti-Stokes side, the energetic asymmetry and the natural logarithm of the intensity ratio between the first SF on the Stokes and anti-Stokes side are evaluated as a function of the applied magnetic field. The results are shown in Figs. 7.21 (a)-(d). In regard of the $\delta E(B)$-dependence, one observes generally a decrease of the asymmetry for decreasing magnetic field. From the first magnetic field dependence analysis preformed in Faraday geometry (see Sec. 7.1.1), it emerged from initial estimation that δE decreases by about 15 μeV/T. This is in good agreement with the evolution of the data shown in Fig. 7.21 (c). However, at the positions of integral intensity-maxima, δE as well as the logarithmic ratio ($\ln(I^{int,\,S}/I^{int,\,AS})$) obviously deviate from this linear behavior. The same applies to the measurement results in close to Faraday geometry. Here the deviations are even more evident. For instance, at $B = 2.89$ T at $\theta = 7°$, the energy difference between the Stokes and anti-Stokes Mn^{2+} SF lines increases abruptly from (-48 ± 2) μeV up to (-147 ± 3) μeV, whereas in Faraday geometry it rises from (-22 ± 2) μeV up to (-48 ± 3) μeV. For the sake of completeness, the places where significant changes of δE and the logarithmic intensity ratio in both geometries occur are: 2.39, 2.90, 3.39, 3.68, 3.94, 4.37, 5.01 and 6.18 T.

Based on literature (see Ref. [295]), exactly at these magnetic-field strengths, the spin states of the single Mn^{2+} ions and nearest-neighbor Mn ions, which are antifer-

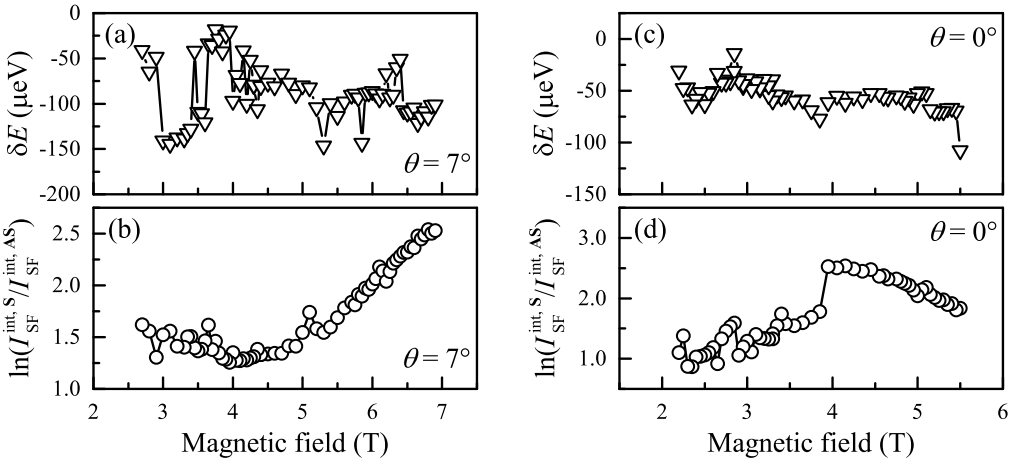

Figure 7.21: Dependence of δE and the logarithmic intensity ratio of Stokes and anti-Stokes on the external magnetic field strength for close to Faraday ($\theta = 7°$) (a & b) and Faraday geometry ($\theta = 0°$) (c & d). All depicted results pertain the $Zn_{0.988}Mn_{0.012}Se$ QW sample regarding a quasi resonant excitation of the low energy hh-X at $E_{exc} = 2.7980$ eV. The data are obtained from SFRS measurements at $T = 1.6$ K for $P_{\mathrm{exc}} = 9$ W/cm^2 in co-circular polarization configuration (σ^+,σ^+). The error in the Raman shift does not exceed the symbol size.

romagnetically coupled to pair or tripple clusters, are mixed. Due to this coupling non-equilibrium states can relax efficiently through clusters into equilibrium states, in turn leading to an increase in the probability of an Mn^{2+} spin-flip process. Since the effect bases on the amount of non-equilibrium states, to observe cusps, it is necessary to heat the Mn spin system above the bath temperature.[295] This is achieved, due to the efficient anisotropic spin exchange between the electrons of the photoexcited excitons and the localized 3d-electrons, which contributes to the Mn spin heating under resonant exciton excitation.

The strong changes of the energy shift for Stokes and anti-Stokes SF lines result from the relaxation of non-equilibrium into equilibrium states, and, thus, enhancing the SF scattering probability and, therefore, providing an great increase of the dynamic polarization of the non-equilibrium carriers. For this reason, δE displays an abrupt change at magnetic fields where the Mn ion-pair cluster level mixing occurs. This alteration can be about a hundred of μeV. In contrast to previous publications[289,290], it is shown here, that the interactions between single Mn ions and clusters also significantly influence the Mn^{2+} SF scattering probability.

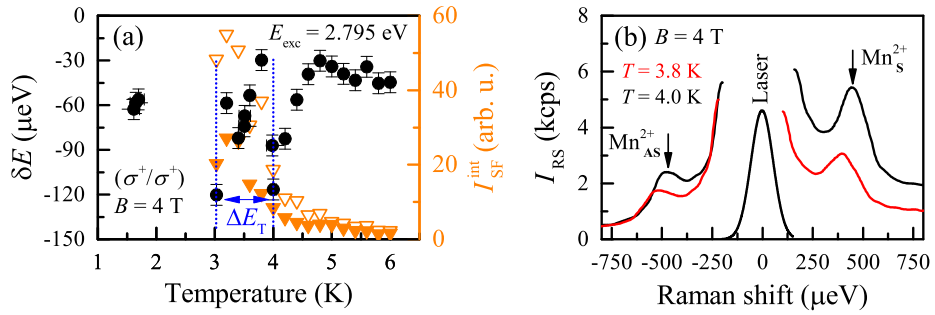

Figure 7.22: (a) Difference δE between the energy shifts of the Stokes and anti-Stokes scattering lines of the first Mn^{2+}-SF paramagnetic resonance (left y-axis) and their integral intensity (right y-axis) in dependence on the bath temperature. The measurements refer to the $Zn_{0.988}Mn_{0.012}Se$ sample regarding a resonant excitation of the low energy hh-X at E_{exc} = 2.795 eV. The data are obtained from SFRS measurements in Faraday geometry at T = 1.6 K for B = 4 T and P_{exc} = 5 W/cm^2. (b) SFRS spectra of the first paramagnetic Mn^{2+}-SF lines ($n = 1$) for T = 3.8 and 4 K. The laser line is found at zero Raman shift.

7.3.6 Temperature dependence of the SFRS on Mn^{2+} ions

The results presented so far have demonstrated that spin interactions and dynamics between the photo-injected carriers and the embedded manganese ions in DMS strongly depend on the heating of the Mn ion system, i.e. the number of non-equilibrium states. A large number of non-equilibrium states enhances the value of the quadrupole correction and, thus, the quadrupole splitting, manifesting itself in multiple anti-Stokes Mn^{2+} SF lines and a significant energy difference between Stokes and anti-Stokes scattering. However, it has not yet been clarified to what extent the bath temperature can influence the spin interactions and dynamics. In recent years, a variety of time-resolved optical techniques have been developed and applied to investigate the dynamic spin behavior at elevated temperatures.[307,323–325] For instance, in the DMS (Ga,Mn)As the transverse in-plane g factor of electrons is studied in a wide range of temperature, yielding g factors of about 0.2 - 0.3.[326] In this regard, an increase of the spin relaxation with increasing magnetic field strength is observed, originating from enhanced p-d exchange interaction between the heavy-holes and the localized magnetic ion spins.[326] However, the free Mn^{2+} spin splitting g factor is stated to be independent of temperature.[307] How far this also applies for the $Zn_{1-x}Mn_xSe$ QWs is discussed in the following.

To study the spin interactions between the photo-carriers and the Mn^{2+} ions, the asymmetry energy δE and integral intensity of the Mn^{2+} SF resonances are studied in a temperature range from T = 1.5 up to 6 K in Faraday geometry. During this investigation, the exciton resonance is excited resonantly at E_{exc} = 2.795 eV, with a laser power density of P_{exc} = 5 W/cm^2. In Fig. 7.22 (a) the asymmetry energy δE for the first spin-flip resonance (left y-axis) and its integral intensity on the Stokes and anti-

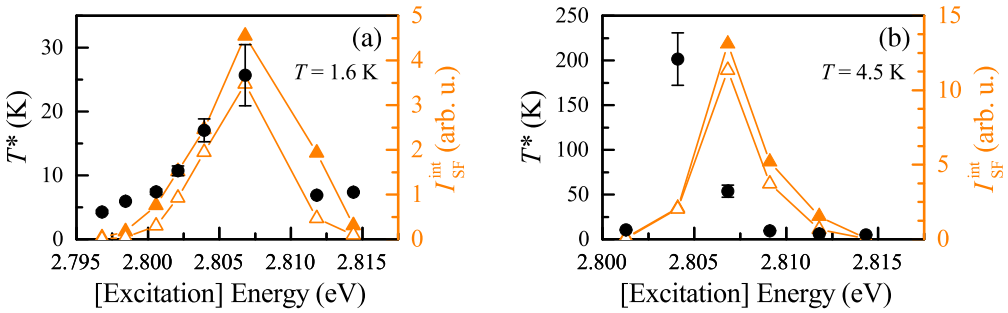

Figure 7.23: Theoretical Mn spin temperature T^* (left y-axis) and integral SF intensity of the first paramagnetic SF resonance on the Stokes and anti-Stokes side (right y-axis) in dependence on the excitation energy. The measurements refer to the $Zn_{0.988}Mn_{0.012}Se$ sample. The data are obtained from SFRS measurements in tilted field geometry ($\theta = 45°$) at $T = 1.6$ K and 4.5 K for $B = 2.9$ T and $P_{exc} = 5$ W/cm^2 in co-circular polarization configuration (σ^+,σ^+).

Stokes side (right y-axis) are shown as function of the bath temperature (T_{bath}). As can be seen in the evolution of this data, the Mn^{2+} SF Stokes and anti-Stokes intensities are strongly sensitive to the temperature. They are most intensive at temperatures below 2 K, whereby their absolute value differs from each other considerably. For $T_{bath} = 6$ K the intensities are three orders of magnitude smaller than at 1.6 K, whereas above 6 K the SFs almost disappear. Over the complete temperature range, the SF scattering efficiency stays twice as high as on the anti-Stokes side. In comparison, the δE dependence displays a more complex behavior. Between 3 and 3.8 K, one observes a linear decrease of δE from 119 μeV down to 28 μeV. However, at 4 K the energetic asymmetry abruptly increases back to 117 μeV. This pronounced change of δE is clearly noticeable in the SFRS spectrum, as can been seen in the exemplary SFRS spectra measured at 3.8 and 4 K shown in Fig. 7.22 (b). The Raman shift on the Stokes and anti-Stokes side changes here symmetrically by ≈ 58 μeV. After this sharp increase of δE at 4 K, with rising temperature the symmetry decreases again linearly down to 31 μeV at 5 K. From that point δE converges towards a constant value of ≈ 45 μeV. The energy-difference between the highest (3 K) and lowest (3.8 K) δE value amounts 91 μeV. Since the temperature is directly proportional to the energy: $E = k_B T$, the quantity of energy can be calculated, which is added to the system when the bath temperature increases by 1 K. This corresponds to: $\Delta E_T = |E_{T=4\,K} - E_{T=3\,K}| = 90\,\mu$eV. This corresponds pretty well to the change of δE in this temperature range. The same effect repeats between 4 and 5 K. Here, δE changes by 86 μeV. In general, the results of this study show that a change of the bath temperature leads to alterations of both δE and the integral intensity.

As the bath temperature and the Mn spin temperature are closely linked to each other, it is of particular interest to investigate this interdependence in more detail. To do so the linear dependence of the logarithmic intensity ratio ($\ln(I^{int,\,S}/I^{int,\,AS})$)

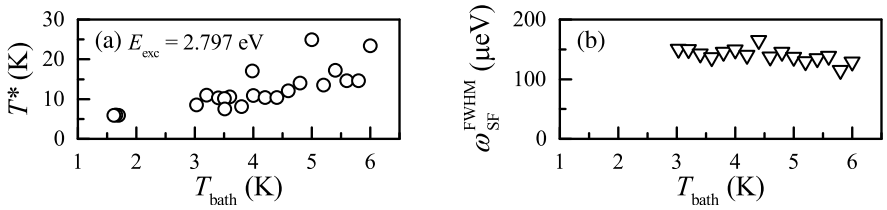

Figure 7.24: Dependence of the spin temperature T^* (a) and the FWHM of the first Mn^{2+} SF resonance on the Stokes side (ω_{SF}^{FWHM}) (b) on the bath temperature T_{bath}. The measurements refer to the $Zn_{0.988}Mn_{0.012}Se$ sample regarding a resonant excitation of the low energy hh-X at $E_{exc} = 2.795$ eV. The related SFRS spectra are measured in tilted field geometry ($\theta = 45°$) at $B = 2.9$ T and $P_{exc} = 5$ W/cm^2 in co-circular polarization configuration (σ^+,σ^+). The errors of T^* and ω_{SF}^{FWHM} do not exceed the symbol size.

on the number n of Mn^{2+}-SF resonances is explored further. From the slope of the resulting linear evolutions, according to Eq. (7.14), one can approximately estimate the theoretical Mn spin temperature (T^*). The dependence of T^* (left y-axis) on the excitation energy as well as the respective SF integral intensity on the Stokes and anti-Stokes side (right y-axis) for $T_{bath} = 1.6$ and 4.5 K at $B = 2.9$ T in tilted geometries ($\theta = 45°$) are illustrated in Fig. 7.23 (a) and (b). The results demonstrate that T^* is maximal around the exciton resonance, while becoming weak for quasi-resonant conditions. However, for $T_{bath} = 4.5$ K one data point ($E_{exc} = 2.8035$ eV) obviously diverges from this behavior. This occurs because the natural logarithm of the intensity ratio deviates from the linear dependence on n. As already mentioned in Sec. 7.3.4, this behavior implies that the Mn spin system is not in an equilibrium state, and, therefore, the model can be treated just for a approximate estimation of the Mn spin temperature. In this regard, for resonant excitation ($E_{exc} = 2.8071$ eV) one obtains from the evaluation of the data a theoretical Mn spin temperature of $T^* = (26 \pm 4)$ K ($T_{bath} = 1.6$ K) and (54 ± 5) K ($T_{bath} = 4.5$ K). For nonresonant excitation ($E_{exc} = 2.8122$ eV) T^* decreases down to (6.9 ± 0.5) K and (9.1 ± 0.7) K, respectively.

To further develop the interdependence of the Mn spin and bath temperature, T^* and the FWHM of the first Mn^{2+} SF resonance (ω_{SF}^{FWHM}) are studied precisely between 1.6 and 6 K. The results for nonresonant excitation are depicted in Figs. 7.24 (a) and (b). In general, one observes an increase of T^* as function of the bath temperature. For instance, at $T_{bath} = 1.6$ K the theoretical spin temperature amounts $T^* = (6.9 \pm 0.5)$ K, while rising up to $T^* \approx (15 \pm 1)$ K at 6 K. However, there are significant discrepancies in the evolution of the data. As explained above these are based on deviations from the theoretical model used for description of the experimental observations. Considering the FWHM of the Mn^{2+} SF line, the evolution of the data demonstrates that the temperature does not significantly alters the SF width. Between 3 and 6 K, it remains stable at about 150 μeV.

As the overall results indicate, the scattering efficiency, the energetic asymmetry as well as the related theoretical spin temperature are very sensitive to the ambient temperature. Already small changes of T_{bath} lead to noticeable alterations of these factors. From the evaluated results, one can draw the conclusion that the number of non-equilibrium states is increasing with temperature, leading to a change of δE. However, the energetic asymmetry does not exclusively rise with the number of non-equilibrium states. In fact, one can observe that the temperature compensates the energetic asymmetry up to a certain degree, but experiences a significant jump back to high asymmetry for slightly greater ambient temperatures, as shown in Fig. 7.22. These observations imply that the quadrupolar shift is temperature dependent and, therefore, cannot be explained solely within the model presented in Sec. 7.3.4. The phenomenological model has to be extended by a nonmonotonic $\delta E(T_{\mathrm{bath}})$ dependence to describe properly an overheated magnetic-ion spin system of small ion concentration.

7.4 Conclusion

The second experimental part of this thesis has addressed, on the one hand, the impact of nuclear quadrupole moments coupled with the electric field gradients at the magnetic ion sites on the paramagnetic Mn^{2+} spin-flip resonances and, on the other hand, the occurrence of a significant quadrupole correction of a few tens of GHz that affects the exchange interaction, leading consequently to a strong asymmetry of the scattered light frequency in the DMS based on II-VI compound $Zn_{1-x}Mn_xSe$.

It is demonstrated that the spin-flip scattering mechanism in (Zn,Mn)Se is governed by anisotropic flip-stop exchange interactions between the $3d$-electrons of the Mn^{2+} ions and the conduction band electrons and is influenced strongly by the heavy-hole induced exchange field in the intermediate state of the scattering process. In the absence of an external magnetic field the mechanism is mainly based on transitions of the $(3d)^5$ manganese electrons between the six spin states of the $^6S_{5/2}$-multiplet. Here, the induction of a spin-flip of one $3d$-electron leads to an excited state of the d-shell with the total spin $S = 3/2$ and non-zero total angular momentum. In contrast to the expectations based on the parity rule and spin conservation, optical transitions between these excited states and the ground state are electric dipole active due to the lack of inversion symmetry of the tetrahedral crystal field and the mixing of $S = 5/2$ and $S = 3/2$ states by spin-orbit interaction. It is further demonstrated that the Mn^{2+}-SF processes are initiated at the heavy-hole exciton resonances, moreover, revealing strict optical selection rules, which is attributed to the giant Zeeman splitting of the exciton states. Furthermore, the results highlight a decisive difference between Stokes and anti-Stokes scattering, yielding Landé factors of $g_{\mathrm{S}} = 1.92$ and $g_{\mathrm{AS}} = 2.06$, respectively.

The origin of the Stokes and anti-Stokes Mn^{2+}-SF asymmetric transitions in DMS can be theoretically derived from a general approach on the basis of the model proposed

by Merkulov and Kavokin. The energetic asymmetry is based on the crystal-field split spin states of the $3d$-electrons of Mn ions in a non-equilibrium magnetic state. In this regard, from the angular dependence of the difference between the Stokes and anti-Stokes Mn^{2+} spin-flip energies, a quadrupole splitting energy of about 14 μeV is evaluated. It is further demonstrated that the quadrupole correction and, thus, δE, are tunable through the optical pumping efficiency which also contributes greatly to the Mn spin heating. The huge amount of spins with different spin orientations, in a non-equilibrium magnetic state, manifests itself in the large number of multiple anti-Stokes Mn^{2+} SF lines, not observed in any previous studies. One draws the conclusion that the strong changes of the energy shift for Stokes and anti-Stokes SF lines result from the relaxation of non-equilibrium into equilibrium states, thus enhancing the SF scattering probability and, therefore, providing an great increase of the dynamic polarization of the non-equilibrium carriers. For this reason, δE displays an abrupt change at magnetic fields where the Mn ion-pair cluster level mixing occurs. It is worthwhile to note that δE can reach values about a hundred of μeV.

Part IV

Spin-flip Raman scattering in CdSe colloidal nanocrystals

Among the most direct effects of reducing the size of materials to the nanometer range is the occurrence of quantization effects due to restricted electron movement. The spatial restriction of carriers in a semiconductor leads to a phenomenon well known as quantum confinement [327]. The impact of this effect differs for various materials, as it is determined by the materials composition and structure. In this regard, the spatial expansion of excitons in low dimensional semiconductors is defined by the exciton Bohr radius (a_0). Depending on the chosen material, a_0 ranges from ≈ 2 to ≈ 50 nm. [118] By varying the nanostructure size, due to the quantum confinement effect, the wavelength of the optical emission of semiconductors can be influenced. [328] An essential aspect of nanosciences, which has led to enormous research efforts and great advances in recent decades [119,328–330], is to understand the origin of quantum confinement and its influence on the electronic and spin properties of semiconductor nanostructures. Colloidal nanocrystals (NCs) are one of the well-known semiconductor nanostructures that have been theoretically and experimentally thoroughly investigated for this purpose. Their unique size- and shape-dependent optoelectronic properties revealed their great potential for application in lasers [40–42], optical amplifiers [40], light emitting devices [42,43], biomedical imaging [44] and photocatalysis [45,46].

Currently, there is considerable interest in the study of strongly anisotropic nanocrystals, with one dimension remarkably smaller than the other two. These structures are called colloidal two-dimensional nanoplatelets (NPLs). They combine the advantages of size-tunable electronic properties, similar to those of QWs formed by molecular beam epitaxy, with vast reactive surfaces enabling the realization of emissive luminescent-sensing varnishes. [331] Precise studies of their electronic structure revealed that they possess large exciton and biexciton binding energies which give rise to stimulated emission from biexcitons even at room temperature. [332] Embedding these NPLs in surface-emitting microcavities it is even possible to achieve continuous-wave pumped stimulated emission or lasing. [332] Particularly the remarkable optical properties of NPLs, which can be controlled precisely by their atomic thickness, aroused major interest. [333,334] In general, NPLs present an extremely narrow emission spectrum with full-width at half-maximum less than 40 meV at room temperature. [333] A large variety of materials can be synthesized as NPLs allowing one to tune the emission wavelength from blue to the far infrared range.

One noticeable milestone in current research has been the experimental and theoretical discovery of the dark exciton, which forms the exciton ground state in CdSe NPLs. These dark excitons strongly affect the exciton dynamics, lifetimes, and photoluminescence in NCs. [335,336] However, recent research has shown that at low temperatures NCs, e.g. CdSe/CdS QDs [47], can be charged under illumination, leading to formation of negatively charged excitons in their ground state which can recombine within a few nanoseconds. This optical charging of the colloidal NCs allows one to create resident carriers in the NPLs that can be optically addressed, controlled and manipulated. [48] For developing optical manipulation algorithms, the study and understanding of the spin related phenomena, such as the exchange interaction between

the resident carriers and photogenerated exciton, is of central importance. For that purpose, electron-electron spin exchange interactions are investigated by the method of spin-flip Raman scattering. This technique is suitable to provide information about the spin structure, their symmetries and spin interactions. For instance, it is used in previous studies to investigate the electron g factor of negatively charged excitons in dense and diluted CdSe/CdS colloidal nanoplatelets with thick shells [337], yielding an electron g factor of 1.68 ± 0.02 independent on the density of NPLs. With the goal of achieving even more knowledge about the spin properties of the resident electrons in CdSe NPLs in the framework of this thesis these structures are investigated further by means of the SFRS technique in terms of NPL-thickness, selection rules, geometry and temperature dependence. A special feature that became apparent, here, is the presence of double spin-flip Raman scattering resonances. Previously, such resonances are observed experimentally in CdS [338] and are explained theoretically basing on the interaction of impurity spin states with virtually bound exciton states. [339] To the best of our knowledge, the observation of such resonances in NPLs has not been observed so far. This part IV of the thesis addresses exactly this issue in prospect of contributing to a better understanding.

Chapter 8

Double spin-flip Raman scattering in CdSe nanoplatelets

Spin-flip Raman scattering is a new technical approach to study spin phenomena in NCs. Several previous studies have focused mainly on the analysis of the PL and time-resolved PL in order to determine the structural properties of the colloidal NCs such as the bright-dark energy splitting and the radiative lifetimes of the two lowest exciton fine structure states.[336,337,340] However, spin interactions between the resident carriers and photogenerated excitons have not been characterized so far. Particularly the observation of double spin-flip scattering resonances in CdSe NPLs is still yet unexplored.

To provide an insight into the scientific field of NCs and the experimental techniques used to study these materials, in Sec. 8.1 the experimental approach, the synthesis of CdSe NPLs and the influence of confinement on the electronic and optical properties of NCs is described. Moreover, on the basis of preliminary PL measurements the formation of dark and bright exciton states and the formation of magnetic polarons in NPLs is discussed. In the following Sec. 8.2 the focus is set on the SFRS in NPLs. Here, the circular polarization properties of the spin-flip scattering, the g factor, the SFRS angular and temperature dependence are discussed. The responsible spin-flip scattering mechanisms in Faraday and tilted field geometries are described and validated in Sec. 8.3. The Chapter is concluded with Sec. 8.4.

8.1 Experimental approach and structural properties of nanocrystals

Various optical approaches can be used to investigate the spin dynamics and spin interactions in colloidal two-dimensional NPLs. The most commonly used methods

are reflectivity, transmission and photoluminescence spectroscopy. For instance, these methods have been used to study the properties of dangling-bond magnetic polarons (DBMPs) in 2.8 nm diameter CdSe colloidal NCs in temperature range from 2 up to 20 K.[340] The studies revealed that each DBMP is composed of a dark exciton and about 60 dangling-bond spins.[340] This particular property of NPLs, combined with its outstanding optical characteristics, makes these structures promising candidates for investigating the interactions between photo-induced excitons and the resident electrons. In this regard, a suitable technique to explore the interactions and the structural properties of these NCs is spin-flip Raman spectroscopy. The general experimental approach and the major advantages of this technique are presented in detail in chapter 3. However, colloidal NCs require special treatment and certain experimental conditions. In order to meet these requirements, the experimental setup had to be adapted. All modifications of the setup and the synthesis of CdSe NPLs are briefly described in the subsections 8.1.1 and 8.1.2. An important topic in this context is the influence of confinement on the electronic and optical properties of NCs. This issue is addressed theoretically in subsection 8.1.3. On the basis of preliminary PL measurements the alteration of optical properties induced by strong confinement, the formation of dark and bright excitonic states and, thus, the formation of magnetic polarons in NPLs is described in the last subsection 8.1.4.

8.1.1 Experimental approach

A common method to characterize semiconductor nanostructures is PL spectroscopy. The advantages and benefits of this nondestructive spectroscopic technique are highlighted throughout the previous chapters. In general PL spectroscopy bases on the generation of excitons by nonresonant laser excitation and the detection of their luminescence, after the electron makes a transition from the valence band to the conduction band. The analysis of the polarization and spectral characteristics of the emitted PL provides information about the electronic properties and recombination characteristics of the sample under study. However, in view of a nonresonant excitation of colloidal NPLs, this technique has a major disadvantage. Due to the shape and size dispersion of the NPLs and the fact that the laser energy is greater than the energy of the lowest absorption resonance, the resulting PL spectrum of NPLs is strongly inhomogeneous broadened. Hence, in order to study the exciton fine-structure or phonons inside the NCs, it is important to tune the laser energy in resonance with just a small fraction of NPLs. This selective excitation of only a few NPLs leads to significantly narrower lines in the PL spectrum.[328,341] In this context, recent studies on CdSe NPLs have demonstrated that for quasi resonant excitation the emission spectrum of a single NPL becomes very narrow (FWHM < 400 μeV) at low bath temperatures ($T_{\mathrm{bath}} < 20$ K), while its width increases strongly up to room temperature. The dominant mechanism responsible for this is attributed to the exciton-phonon interactions.[341]

Since the resonant and nonresonant excitation of CdSe NCs provides equally important but distinct information about their electronic characteristics, two different approaches are used for investigation of their radiative properties. For a rough analysis of the polarization and spectral characteristics of the emitted PL the sample structures are excited nonresonantly with a continuous wave semiconductor laser (Coherent Cube) with a photon energy of $E_{\text{PL-exc}} = 3.061$ eV. The energy is chosen in the way that the colloidal NPLs are excited above the energy band-gap. To avoid unwanted heating, the laser power density in this experiments is reduced by natural gradient filters down to 20 mW/cm^2. The scheme of the experimental setup is shown in Fig. 3.4.
In order to investigate the exciton fine-structure of the CdSe NPLs, the NPL samples are excited resonantly either by an argon-ion laser with a photon energy of $E_{\text{PL-exc}} = 2.808$ eV (2.497 eV) or by a Nd:YVO_4 laser (Coherent, Verdi V10) with a photon energy of $E_{\text{PL-exc}} = 2.33$ eV. In the case of quasi resonant excitation, the choice of the laser mainly depends on the sample under investigation. The reason for this is that slight changes in the NPL composition/structure lead to major changes of the NPL optical and electronic properties and, thus, to a significant shift of its absorption and PL. To maintain the resonance condition, the laser is chosen in the way that the lowest absorption resonance is excited resonantly. To avoid unwanted heating of the sample, like in the case of nonresonant excitation, the intensity of the laser beam is attenuated by a neutral gradient filter to about 6 W/cm^2. During intensity-sensitive measurements demanding a stable laser power, the power density is additionally monitored with a power meter which has been inserted in the laser beam.

To study the spin related phenomena, i.e. the exchange interaction between the resident carriers and photogenerated excitons, the technique of SFRS is used. Similar to the examination of the resonantly excited PL, it is necessary for SFRS to excite the colloidal structures resonantly at the exciton resonance. To achieve this the same excitation sources are used. The measurements are performed at high magnetic fields up to 10 T and at low temperatures ranging from 1.6 to 17 K. The Raman spectra are measured in backscattering configuration in Faraday and oblique geometries, where the magnetic field B and NPL crystal axis c enclosed an angle of θ within the xz-plane. In Faraday configuration ($\theta = 0°$) the polarization of the incident (scattered) light is set (read) by a Glan-Thompson prism combined with a quarter-wave retardation plate. Since in Voigt geometry the optical selection rules are lifted, the quarter-wave retardation plates are changed to half-wave retardation plates, in order to study the cross-linear polarization. The circular and linear polarization characteristics of the SFRS spectra are described by the abbreviated expression ($\sigma^{+/-}/\sigma^{+/-}$) or ($\pi^{\text{H/V}}/\pi^{\text{H/V}}$). Here, $\sigma^{+/-}$ and $\pi^{\text{H/V}}$ designate the circular and linear polarization of the incident and scattered light, which is determined by the angular momentum projection on the propagation direction of the incident light.

A more detailed description of the basic experimental setup is provided in chapter 3. The next section focuses on the synthesis and structural properties of the CdSe NPL ensembles.

8.1.2 Synthesis and structural properties of CdSe nanocrystals

The CdSe nanoplatelets that are investigated in the framework of this thesis belong to the group of nanoparticles, which form one of the most important classes of nanomaterials. They are zero-dimensional structures with just a few nanometers in size. Because of their small size, these nanoparticles are comparable to molecules, revealing unique structural properties, which clearly differ from those of bulk crystals.[342] In general, the size-dependent properties of nanoparticles include electronic, optical, magnetic, and chemical characteristics.[343] When their size reaches the regime of the exciton Bohr radius, due to the quantum confinement effect, the wavelength of their optical emission is greatly influenced.[328] For this reason, by simply varying their size, one can modify the absorption and emission energies without changing their chemical composition.[344]

Nanometersized platelets can be fabricated by different techniques. The most widely known manufacturing processes are mechanical exfoliation[346–348], liquid exfoliation[349], chemical vapour phase epitaxy[350] or wet-chemical synthesis[351,352]. The last mentioned has become very popular in the past few years in the manufacture of NCs, as it is very easy to accomplish and, therefore, suitable for mass production. By means of this method, 2D colloidal nanocrystals or nanoplatelets can be synthesized with different thicknesses quantified by just one CdSe monolayer.[352,353] This method of wet-chemical synthesis bases on the solution phase decomposition of cadmium myristate and selenium mesh precursors in the presence of a hot non coordinating solvent and an acetate salt.[353] This technique is precisely described in Ref. [353]. By the correct dosage of the chemicals and salts involved, one achieves with this kind of synthesis technique CdSe platelets with lateral dimensions between 6 to 50 nm with a zinc-blende crystal structure.[353] After the synthesis these NPLs are dispersed in a solvent. By simply drop-casting the concentrated NPL solutions onto a silicon substrate, the samples are prepared for optical measurements. Characteristic transmission electron microscope (TEM) image of the studied NPLs are shown in Figs. 8.1 (a) to (c). As it

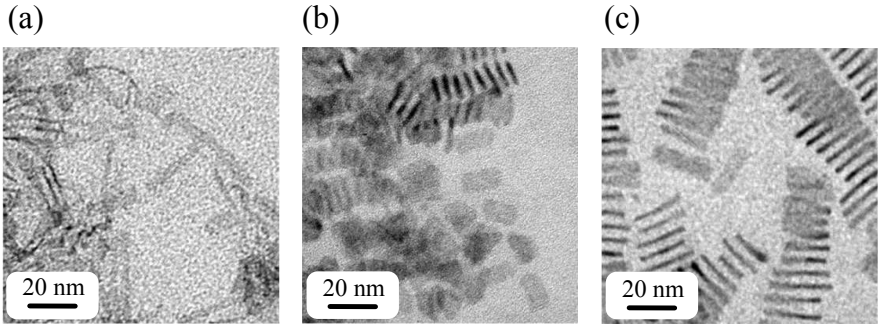

Figure 8.1: TEM images of the studied NPLs with 3 ML (a), 4 ML (b), and 5 ML (c). Adapted from Ref. [345].

sample name	Thickness (no. ML)	(nm)	Lateral size (nm^2)	Exciton emission (X^0) max. (eV)	width (meV)	$\Delta E_{X^0-X^{LO}}$ (meV)
3ML	3	0.91	6 x 40	2.829	20.3	45
4ML	4	1.22	8 x 16	2.499	17.1	18
5ML	5	1.52	7 x 30	2.329	15.5	26

Table 8.1: Technological and optical parameters of the CdSe nanoplatelets.

is shown, the NPLs orient randomly on the substrate surface and, furthermore, tend to stack into small groups. The CdSe NPLs have an in-plane size of approximately a few nanometers and a thickness of just a few monolayers.[353,354] The exact lateral sizes of the NPLs are listed in Tab. 8.1. These types of NC structures consist typically of a core surrounded by numerous ligands. Colloidal cores can be additionally overcoated by a second material serving as a shell of small lattice mismatch and with larger band-gap. This shell confines the excited carriers in the core and shields these from defects on the surface of the NC, which can act as carrier traps and, thus, improve radiation-free processes consequently reducing the quantum yield.[48] The great difference between QDs and NPLs arises from their unique morphologies and morphology-dependent surface ligand bondings. In this regard, recent studies have demonstrated that the soft ligands not only increase the stability of NPLs, but also improve their elastic strength and fracture toughness.[355,356]

In the framework of this thesis various CdSe nanoplatelets, which were grown at the Laboratoire de Physique et d'Etude des Matériaux in Paris by Prof. Dr. B. Dubertret's group, are investigated. The study focuses on CdSe platelets having in-plane sizes of 6 x 40 nm, 8 x 16 nm, and 7 x 30 nm and a thicknesses, i.e. amount of monolayers (ML), of 0.91 nm (3 ML), 1.22 nm (4 ML), and 1.52 nm (5 ML) of CdSe and an additional layer of Cd atoms, to ensure that both sides of the NPLs are Cd-terminated. These NPLs are synthesized without an outer shell. All technological and optical parameters of the studied samples are summarized in Tab. 8.1.

As outlined above, in terms of optical measurements, the NPLs are prepared by drop-casting the NC solution onto a silicon substrate. In order to ensure the best possible measurement conditions, immediately after the preparation of the specimens, these are immediately inserted into a magnet cryostat and cooled down to $T_{\mathrm{bath}} = 1.6$ K. This procedure ensures that a structural degradation of the NCs and/or irreversible modification of their surface is mostly prevented. The degradation of CdSe NPLs caused by elevated temperatures or great laser excitation densities is a well-known characteristic of NCs. It is typically accompanied by steady PL intensity degradation and a change of the PL profile and polarization characteristics. Particularly for this reason, it is necessary to prevent the use of high excitation power densities in the corresponding SFRS measurements. In Sec. 8.2.2 of this chapter, the influence of NC degradation on the resonant SFRS efficiency is explored in detail.

8.1.3 Confinement effects in CdSe nanocrystals

The description of the optical exciton states in low-demnsional structures depends mainly on the boundary conditions of the system. These conditions differ strongly between quantum dots and quantum wells. At first glance, it would appear reasonable to compare NPLs with quantum dots. However, the colloidal structures are considerably larger than an MBE grown QD, which leads to dissimilar electronic and optical properties. While a QD is a quasi-zero-dimensional system with discrete states, the NPL displays rather the features of a two-dimensional system similar to a QW. Within a QW, the photo-excited electron-hole pairs (excitons) are confined just in one dimension, but can move freely in the other two.[100] A well-known and thoroughly studied example are epitaxial QWs. Chemically produced equivalents of these are colloidal CdSe nanoplatelets, which can be grown with monolayer precision[353,354], as it is described in the previous section. However, NPLs have significantly smaller lateral expansions than epitaxial QWs, what causes that the electronic properties of their lowest exciton states differ. Nonetheless, previous studies demonstrated that the optical feautures, e.g. the photoluminescence characteristics, of NPLs are very similar to those of epitaxial QWs.[48,357–359]

NPLs can be seen as an intermediate structure between QWs and QDs. Therefore, the correct approach to describe the relevant exciton states must take into account the peculiarities of both types of low dimensional systems. In regard of a general QW-approach, one will obviously assume that the Coulomb interaction between the electrons and holes dominates in comparison to the confinement. However, this is exactly the opposite for QDs where the confinement is a crucial factor. The extent to which the external dimensions of a NPL, which define the strength of the Coulomb interaction and confinement influence the optical exciton states in a NPL, is described and simulated theoretically by M. Richter in previous publications.[360] For better understanding of the interdependence, the most important aspects of this theory are briefly recapitulated in the following.

The starting point of the theoretical derivation by M. Richter[360] is a Wannier type model system being used to obtain the four-dimensional exciton wave functions for in-plane motion. This description is based on the four-dimensional stationary Schrödinger equation of the envelope function ($\psi(\rho_e,\rho_h)$), which describes the exciton in-plane motion:

$$\left[-\frac{\hbar^2}{2m_e}\Delta_{\perp e} - \frac{\hbar^2}{2m_h}\Delta_{\perp h} + V_{c,e}(\rho_e) + V_{c,h}(\rho_h) + U_{\mathrm{coul}}(\rho_e - \rho_h)\right]\psi(\rho_e,\rho_h) = E\psi(\rho_e,\rho_h). \tag{8.1}$$

This Schrödinger equation encloses the motion ($-\frac{\hbar^2}{2m_{e\,(h)}}\Delta_{\perp e\,(h)}$) and the confinement potentials ($V_{c,e\,(h)}(\rho_{e\,(h)})$) of the electrons in the conduction band and holes in the valence band, and the Coulomb potential ($U_{\mathrm{coul}}(\rho_e - \rho_h)$) between them. Here, m_e and m_h stand for the effective masses of electrons and holes, respectively. For thin two

dimensional NPLs, the modified Coulomb potential [361] is given by:

$$U_{\mathrm{coul}}(\rho) = 1/[4\pi\epsilon_0(2\epsilon_{r,\mathrm{out}}\rho_0)] \left\{ \ln\left[\frac{\rho}{\rho+\rho_0}\right] + [\gamma - \ln(2)]\, e^{-\rho/\rho_0} \right\}, \tag{8.2}$$

with $\rho_0 = z_0\epsilon_r/(2\epsilon_{r,\mathrm{out}})$. Here, z_0 describes the platelet thickness, ϵ_r the platelet material, $\epsilon_{r,\mathrm{out}}$ the solvent that surrounds the platelet, and γ the Euler constant.

As discussed above, the interplay of Coulomb and confinement potential are the most important parameters that determine the properties of the lowest exciton states. To differentiate between them generally two regimes have to be taken into consideration, namely the strong confinement regime and the Coulomb dominated regime. In the case of strong confinement the confinement potential restricts decisively the motion of electron and holes determining fully the shape of the wave function. Assuming the Coulomb interaction is negligibly small ($U_{\mathrm{coul}}(\rho_e - \rho_h) \ll V_{c,e}(\rho_e) + V_{c,h}(\rho_h)$), the Schrödinger equation (8.1) can be factorized into a separate Schrödinger equation for the electron and hole:

$$\left[-\frac{\hbar^2}{2m_e}\Delta_{\perp e} + V_{c,e}(\rho_e)\right]\psi_e(\rho_e) = E\psi_e(\rho_e), \tag{8.3}$$

$$\left[-\frac{\hbar^2}{2m_h}\Delta_{\perp h} + V_{c,h}(\rho_h)\right]\psi_h(\rho_h) = E\psi_h(\rho_h). \tag{8.4}$$

The exciton states are determined by the eigenfunctions of the electrons and holes. The related energy eigenvalues ϵ_e and ϵ_h, which can be derived from the two motion equations (8.3) and (8.4), define the exciton energy. However, the energy is also affected markedly by the Coulomb coupling. Even though Coulomb interaction has only a minor influence on the exciton wave function shape, it leads to a significant shift of the exciton energy. This shift is given in first-order perturbation theory by:

$$\epsilon_{\mathrm{coul}} = \int d^2\rho_e \int d^2\rho_h \; |\psi_e(\rho_e)|^2 \; U_{\mathrm{coul}}(\rho_e - \rho_h) \; |\psi_h(\rho_h)|^2 .\,^{[360]} \tag{8.5}$$

Herewith one obtains for the total energy of the exciton $E_{\mathrm{total}} = \epsilon_e + \epsilon_h + \epsilon_{\mathrm{coul}}$.

Theoretical simulations and calculations [360] have shown that the assumption of a strong confinement is only justified if the dimensions of an NPL are below 21 nm x 7 nm. For larger platelets, the confinement becomes weaker, whereby the Coulomb coupling predominantly determines the exciton wave function. In this case, the electrons and holes of the bound exciton states are characterized by a correlated motion. The correlated motion of the carriers can be expressed by the relative coordinates $r = \rho_e - \rho_h$ and the center of mass $R = m_e\rho_e + m_h\rho_h$ with the overall mass $M = m_e + m_h$ ($\psi(\rho_e,\rho_h) \rightarrow \psi(r,R)$). Using the factorization ansatz ($\psi(r,R) = \psi(r) \cdot \psi(R)_{\mathrm{COM}}$), the wave function can be rewritten to a product of the eigenfunction $\psi(r)$ and the center of mass function $\psi(R)_{\mathrm{COM}}$. The product of these two wave functions depends on the selected eigenfunction $\psi_{r,n}(r)$ and $\psi_{\mathrm{COM},m}(R)$. These eigenfunctions are characterized

by the quantum numbers n of the relative wave function and m of the COM motion. Using the above described factorization ansatz for a selected eigenfunction $\psi_{r,n}(r)$, one obtains by equation (8.1) the full Schrödinger equation [100,362]:

$$\left[-\frac{\hbar^2}{2m_r}\Delta_r - \frac{\hbar^2}{2M}\Delta_R + U_{\text{coul}}(r) + V_{c,e}(R + \frac{m_h}{M}r) + V_{c,h}(R - \frac{m_e}{M}r)\right]\psi_{r,n}(r)\psi_{\text{COM},n}(R)$$

$$= E\psi_{r,n}(r)\psi_{\text{COM},n}(R). \tag{8.6}$$

By means of this equation one can derive the overall energy $E^{\text{COM}}_{n,m}$ of an exciton state in dependence on the quantum numbers n and m. This eigen-energy is given by $E^{\text{COM}}_{n,m} = E_{r,n}+E_{\text{COM},n,m}$. [360] In comparison to the strong confinement regime, here, the energy is defined mainly by the correlated motion of the exciton bound electrons and holes inside the NPL. Previous studies have theoretically devised that the impact of confinement is negligible in platelets with lateral dimensions higher then 21 nm x 7 nm. With regard to the colloidal NC studied in this thesis, both types of NPL structures are present. Due to the particularly large lateral size of the 3 ML (6 nm x 40 nm) and 5 ML (7 nm x 30 nm) NPLs, these can be assigned to QW like structures in which the Coulomb interaction prevails the confinement strength. However, in the case of the 4 ML NPLs (8 nm x 16 nm) the lateral size is so small that one may expect QD like properties, since the strong confinement will obviously surpass the Coulomb interaction. However, this explanations are theoretically only applicable for the lowest energy exciton states and, therefore, have to be used with care for quantitive and qualitative analysis. [360]

In conclusion, geometric confinement in low dimensional semiconductor structures leads to an enhancement of short range contact interactions between the involved carriers, e.g. exciton, electrons and holes. This effect can be ascribed to shrinkage of carrier wave functions which in turn increase the localized charge density and, therefore, the interaction efficiency between the carriers. The confinement volume is inversely proportional to the interaction rate and, thus influencing particularly the optical properties of NCs.

8.1.4 Magnetic polaron formation in CdSe colloidal nanocrystals

The study of the electronic structure and carrier dynamics in low-dimensional colloidal NCs is based on the characterization of their optical properties which can be influenced, e.g. by the geometric confinement. As described in the previous section, strong confinement leads to a shrinkage of the carrier wave functions which leads to an enhancement of the electron-hole exchange interaction and, therefore, alters the radiative characteristics in nanocrystals. In this case, besides optically accessible bright excitonic states, the NCs also exhibit a variety of dark excitonic states. The energy of these may even be lower than the bright states, and, thus, determining the exciton dynamics, lifetimes, and photoluminescence characteristics. [363] Although the formation of dark

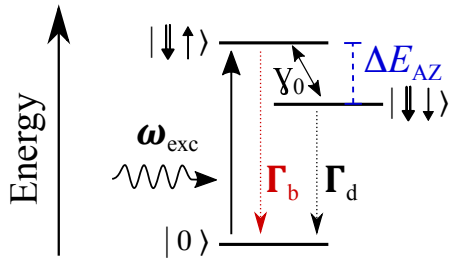

Figure 8.2: Model schemes of the bright-dark exciton level alignment. Shown are the unexcited state $|\,0\rangle$ and the two lowest states of the band-edge exciton fine structure $|\Downarrow\uparrow\rangle$ and $|\Downarrow\downarrow\rangle$. The resonant excitation (ω_{exc}) is σ^- polarized. Γ_b and Γ_d are the recombination rates of dark and bright excitons ($\Gamma_d \ll \Gamma_b$), respectively. ΔE_{AZ} denotes the energy of the bright-dark exciton splitting and γ_0 describes the bright-to-dark spin–flip rate induced by a thermal mixing of bright and dark excitons. Adapted from Ref. [48,340].

excitons in NPL has been discovered many years before, the mechanisms, which enable its radiative recombination are still not fully clarified. In the scope of this section the main mechanisms, which are yielding the radiative dark exciton recombination are discussed.

The radiative recombination of a dark exciton can be simply described by a three-level system.[364,365] A scheme illustrating this model is depicted in Fig. 8.2. The model is composed of the unexcited state $|\,0\rangle$ and the two lowest states of the band-edge exciton fine structure $|\Downarrow\uparrow\rangle$ and $|\Downarrow\downarrow\rangle$ which represent the excited exciton states. The energy separation ΔE_{AZ} between them particularly depends on the applied magnetic field as well as the NC size and shape.[335] The first excited state ($|\Downarrow\uparrow\rangle$) with an angular momentum of $\Delta L = \pm 1$ is optically active (bright). On the contrary, the lowest exciton ground state ($|\Downarrow\downarrow\rangle$) in NCs is a twofold degenerate dark state with an angular momentum projection on the NC wurtzite axis of $\Delta L = \pm 2$.[335] It is termed dark, because its radiative recombination is in principle forbidden in the electric dipole approximation. The reason is that the angular momentum is not conserved during a transition from the excited dark state to the vacuum state. With regard to the dipole approximation, only an angular momentum of $\Delta L = \pm 1$ can be emitted by a single photon and, therefore, the momentum conservation requirement is not fulfilled. In this context, a decay over two photons is conceivable, but the probability of such a second order process is very low and is, therefore, to be neglected.

On the basis of these theoretical limitations the dark exciton state shall experience an infinite lifetime. However, previous studies on NCs have demonstrated that this does not apply, since the radiative decay of the optically inactive dark exciton can occur via a phonon assisted momentum-conserving transition. Here, the dark and bright exciton states are coupled via longitudinal acoustic (LA) or optical phonons (LO). Alternatively, also an external magnetic field can be used to couple these states.

In the case of phonon driven interaction, in the decay process the phonon takes a part of the momentum leading to a charge carrier spin-flip ($|\Downarrow\downarrow\rangle \rightarrow|\Downarrow\uparrow\rangle$) and afterwards to an emission of a photon from the bright exciton state. This process is fulfilling the angular momentum conservation rule, facilitating the radiative decay of the dark exciton.[340,366,367] This mechanism is evidenced by the presence of strong LO and LA phonon replica in fluorescence line narrowing (FLN) experiments.[48,328] Furthermore, FLN studies have revealed that in an external magnetic field the emission of the zero phonon line increases, and, thus, also the recombination of dark excitons.[368,369] Accordingly, it is demonstrated that magnetic fields lead to an activation of the dark exciton and, therefore, have a significant influence on the decay mechanism. Moreover, the observation of a zero phonon line in absence of an external magnetic field has raised the question about the presence of internal fields yielding the decay process. Despite many studies which have been devoted to this issue, a final explanation could not yet be provided.[369]

An important factor associated with the recombination of excitons is the decay time. In low dimensional semiconductors the decay time can differ significantly between optically-allowed and -forbidden states. A good example of this are indirect band-gap (In,Al)As/AlAs quantum dots in which after resonant optical excitation a formation of an indirect-in-momentum-space exciton occurs, whose radiative lifetime exceeds several hundreds of microseconds and is, therefore, far longer than that of direct bright excitons.[36] It behaves similarly in colloidal CdSe NCs where the radiative lifetime of the dark excitonic states is several orders higher than that of the bright states. The dependence of their exciton populations on the decay time has been investigated comprehensively in the past.[328,336,340] Solving a two rate equation and utilizing it to model the experimental bi-exponential photoluminescence intensity decays yielded time evolutions of $\tau_b \approx 150$ s and $\tau_d \approx 2500$ s for the bright and dark exciton states, respectively.[340] However, their decay times as well as their exciton state populations depend greatly on the temperature. Previous studies have shown that for higher temperatures, the decay times become shorter and the relative PL intensity ratio between dark and bright states changes, reflecting the thermal progressiv population of the bright excitons.[340] For low temperatures the thermal activation is suppressed and recombination stems solely from the dark exciton ground state via a phonon assisted transition.

Beside the phonon driven mixing of dark and bright exciton states, the similarity between the effects of temperature and of magnetic field on the dark exciton recombination have led to the conclusion of a new mechanism similar to a magnetic polaron formation which has been found in diluted magnetic semiconductors (see Chap. III). On the basis of the observations, it is assumed that the mechanism in colloidal CdSe NPLs bases on the interaction of photogenerated excitons with the local carriers, orienting their magnetic moments along the NC axis (c-axis). With rising temperature these magnetic moments become arbitrarily oriented leading to an overall internal magnetic field perpendicular to the c-axis, in turn causing a mixing of dark and bright exciton states. However, unlike diluted magnetic semiconductors, CdSe NCs do not contain any

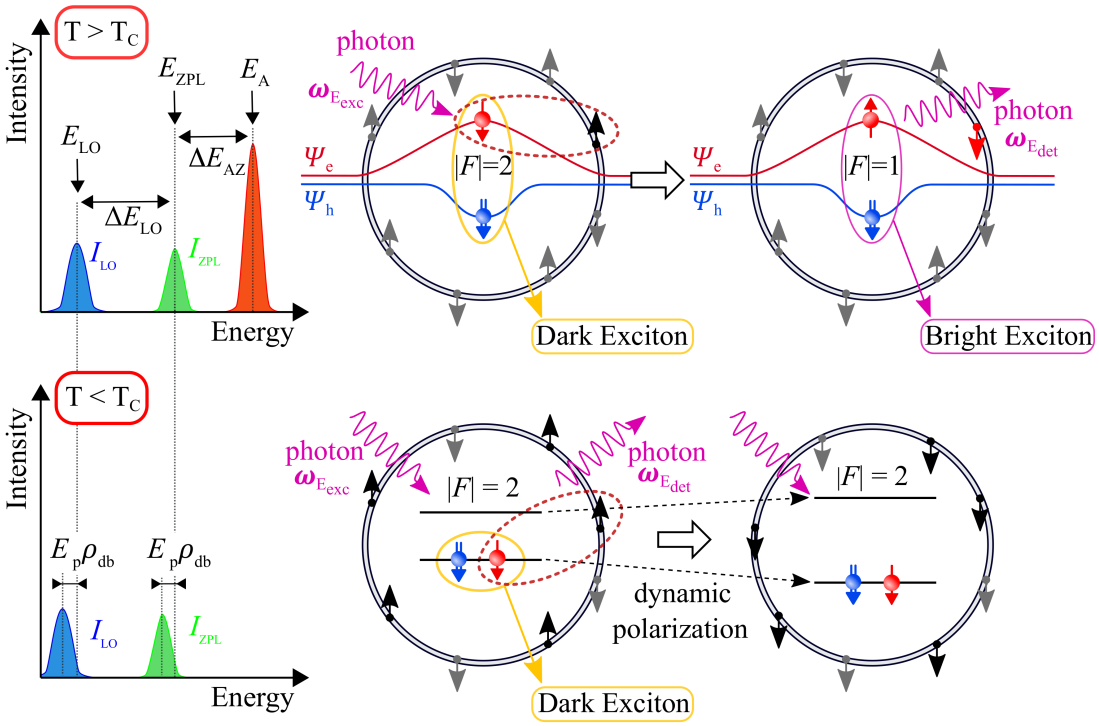

Figure 8.3: Scheme of the dark exciton radiative decay via dangling bond spin flip-flop assisted recombination (right) and the respective lines in the emission spectra (left) for two temperature regimes. For $T > T_c$: The radiative decay of the dark exciton is triggered by a virtual spin flip-flop transition between the exciton bound electron and the DBS. Subsequently the bright exciton recombines radiatively. Above T_c the DBSs are not polarized. The PL spectrum is composed of the bright (E_A) and the dark exciton (E_{ZPL}) as well as their corresponding phonon replica (E_{LO}) of the dark exciton. The related energy shifts are described by ΔE_{LO} and ΔE_{AZ}. For $T < T_c$: The dangling bond assisted recombination results in the dynamic polarization of DBSs and the consequential formation of a DBMP. Due to the polarization of the DBSs the ZPL and the phonon replica shift towards lower energies ($E_p\rho_{db}$). Adapted from Ref. [340,366].

magnetic impurities. It is, therefore, assumed that the exciton interacts with the spins of the surface dangling bonds leading to the formation of a dangling-bond magnetic polaron (DBMP).[335,336,340,366,368] The existence of dangling bonds at the NC surface and their magnetic properties have been highlighted by superconducting quantum interference device measurements in previous studies.[370]

The dangling bond assisted recombination of the dark exciton is shown schematically in Fig. 8.3. Here, the radiative decay of the dark exciton is based on a spin flip-flop virtual transition to the bright exciton and the bright exciton consequential radiative decay. This process obviously presupposes that the system is above a criti-

cal temperature T_c at which the dangling bond spins (DBSs) are not polarized. The arbitrary orientation of the dangling bond spins leads to an admixture of the bright and dark exciton states which in turn yields the dark exciton decay. For this to be possible, it is necessary that in the vicinity of the exciton there are always DBSs which could assist in the recombination process. In this regard, it is worthwhile to note that as long as T exceeds T_c the DBMP is not fully formed, since the magnetic moments of the DBSs become immediately arbitrarily oriented due to LA-phonon interaction.[366] The interaction with dangling bond spins occurs predominantly for the electron, since the wave-function Ψ_e is more delocalized due to its lower effective mass than the hole wave-function Ψ_h.

In the predicted FLN spectra for $T > T_c$, the emission is dominated by the bright (E_A, red spectra) and dark excitons (E_{ZPL}, green spectra) as well as their corresponding phonon replica (E_{LO}, blue spectra). The shift of the dark-exciton line is denoted by ΔE_{AZ} and particularly depends on the applied magnetic field as well as the NC size and shape. The energy difference between the zero phonon line and the first LO-phonon replica is given by ΔE_{LO}. The relative intensities, i.e. the emission yield strength, of the dark and bright exciton depend on the efficiency of the DBS-assisted and LO-phonon-assisted recombination.[340]

When the system is cooled down below T_c each spin flip-flop virtual transition to the bright exciton results in a DBS dynamic polarization as it is schematically shown in Fig. 8.3 ($T < T_c$). In this case, the temperature is no longer sufficient enough to decisively influence the dangling bond magnetic moments what consequently leads to the formation of a DBMP. Due to the dynamic polarization of the DBSs the bright–dark exciton splitting ΔE_{AZ} increases, in turn shifting the dark-exciton line as well as the LO-phonon replica towards lower energies. The energy shift is given by $E_p \rho_{db}$. Here, E_p denotes the DBMP binding energy of a fully polarized DBS system and $\rho_{db} = (N_{db}^- - N_{db}^+)/(N_{db}^- + N_{db}^+)$ describes the dangling bond polarization degree with $N_{db}^{\pm}$ indicating the relative number of DBSs with spin-up (+) and spin-down (−) orientation. The dynamic polarization of the DBSs further leads to a redistribution of the dark-exciton and LO-phonon line intensities. At low temperatures the LO-phonon-assisted transition becomes more intense than the dark exciton related zero phonon line, since the amount of matching DBSs which could assist in the dark exciton recombination decreases due to a higher polarization degree.

As the descriptions above have highlighted, clear signatures of the way how the radiative dark exciton recombination occurs can be observed well in FLN experiments. Therefore, for the first characterization of the three different CdSe NPLs which are studied within the framework of this thesis, PL spectra for different excitation conditions are recorded.

In regard of a rough analysis of the spectral characteristics these structures are excited nonresonantly ($E_{PL\text{-}exc} = 3.061$ eV) at a temperature of $T = 1.6$ K in the

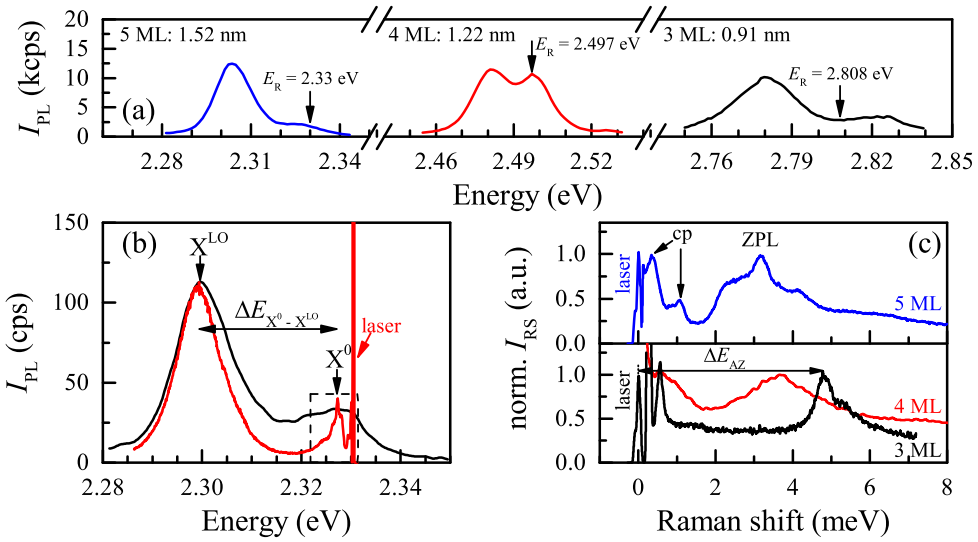

Figure 8.4: (a) PL spectra of the studied CdSe NPLs with 3 ML (black), 4 ML (red), and 5 ML (blue) measured at $T = 1.6$ K and $B = 0$ T. To obtain the PL spectra these structures are excited nonresonantly at $E_{\text{PL-exc}} = 3.061$ eV. The arrows mark the resonant excitation energies used in the spin-flip Raman measurements. (b) FLN spectrum of the 5 ML NPLs for resonant excitation at $E_{\text{exc,5 ML}} = 2.33$ eV ($P_{\text{exc}} = 0.5$ W/cm^2) (red) and PL spectrum under nonresonant excitation (black). Both spectra are measured at $T = 1.6$ K and $B = 0$ T. The emission of the exciton (X^0) and LO-phonon replica (X^{LO}) are indicated by arrows. Their energy difference is described by $\Delta E_{X^0 - X^{LO}}$. (c) Raman spectra of the NPLs with 3 ML (black), 4 ML (red), and 5 ML (blue) measured for resonant excitation at $E_{\text{exc}} = 2.33$ eV, 2.497 eV, and 2.808 eV, respectively. The laser line is at zero Raman shift. Acoustic phonons (cp) are marked by arrows.

absence of an external field. The resulting PL spectra are shown in Fig. 8.4 (a). Each spectra is composed of two lines with a gaussian shape, whereby the high-energy one is attributed to the emission of the exciton (X^0). The binding energy of excitons is approximately given by the Stokes shift between the absorption and PL line. In two-dimensional CdSe NPLs the exciton binding energy is estimated to amount $200 - 300$ meV.[357] This value lies between binding energy estimated for bulk CdSe (10 meV) and CdSe QDs ($500 - 1000$ meV) (see Ref. [371] and references therein).

The origin of the low-energy line in the PL spectrum is to the best of our knowledge still unknown. However, recent studies assume that this feature could either stem from LO-phonon assisted exciton recombination, the emission of a charged excitons (X^+ or X^-), or the recombination of a ground exciton state.[341,345,359] Numerous and comprehensive experiments and analyses of the absorption and recombination dynamics in CdSe NPLs suggest that this secondary feature might be a charged exciton.[345] It is worthwhile to mention here that the Gaussian shape of the two lines in the PL spectra

at $T = 6$ K is symmetric evidencing that the NPLs are evenly distributed across the emission spectrum. Depending on the thickness of the CdSe NPLs the shift between the exciton and this secondary line varies from 45 to 18 meV. The corresponding FWHM of the exciton line ranges from 15.5 to 20.3 meV. A summary of the exact spectral positions of the exciton emission lines as well as its FWHM and the shift of the low energy line $\Delta E_{X^0-X^{\mathrm{LO}}}$ are depicted in Tab. 8.1. The analysed PL spectra indicate a clear dependence of the NPL thickness on the emission energy. With increasing number of ML, i.e. increasing NPL thickness, the exciton energy gradually shifts to lower energies while its FWHM decreases. A detailed analysis of the magnetic-field induced degree of circular polarization and the PL dynamics of the exciton will not be explained in more detail here, since it goes beyond the scope of this thesis. However, these issues are precisely described in recent publications.[345,372]

After this rough analysis of the PL spectral characteristics, next the focus is set on the properties of the high-energy exciton emission line, i.e. the fine structure of the band edge exciton. In order to investigate these properties, FLN experiments are carried out in which the photon energy of the laser excitation is tuned in resonance with the neutral exciton. The selective excitation energies used in these experiments to study the NPLs are summarized in Sec. 8.1.1 and for a better overview their spectral positions are highlighted by vertical arrows in the PL spectrum in Fig. 8.4 (a). The resulting FLN spectra of the 5 ML NPLs under resonant excitation (2.3305 eV, red line) as well as the under nonresonant excitation acquired PL spectrum (black line) are shown in Fig. 8.4 (b). As can be clearly seen in the FLN spectrum, the broad exciton peak turns into several narrow lines. The energy separation between these lines and the low-energy line ($\Delta E_{X^0-X^{\mathrm{LO}}}$) amounts 25.2 meV. This relative energy corresponds well to the result of the nonresonant PL measurement and is furthermore similar to the energy of a LO phonon ($E_{LO} = 25$ meV) reported in the literature.[328] Nevertheless, the exact origin of this line is still unclear as it is stated above.

The comparison of the relative intensities of the spectral lines in the FLN spectra, shows that the low-energy line clearly dominates at a temperature of 6 K. Assuming that this line is the contribution of a LO-phonon, one can draw the conclusion that the optical phonon assisted transitions play an important role for dark exciton radiative recombination as it is described theoretically above. A change of the relative intensity ratio to the favor of the ZPL by increasing temperature or magnetic field emphasizes this observation.[345]

For a more detailed analysis of the PL in the vicinity of the laser line, FLN spectra of the 3 ML, 4 ML, and 5 ML NPLs are studied in detail. The laser excitation energies are set to 2.808 eV, 2.497 eV, and 2.330 eV, respectively. The results are depicted in Fig. 8.4 (c). The x-scale indicates the red shift of the PL with respect to the laser excitation energy. The resonant excitation of the NPLs yields as stated above the creation of several emission lines. In each spectrum the line with the highest PL intensity can be attributed to the zero-phonon line (ZPL) which provides information

about the bright-dark exciton splitting. Its shift equals about 3.2 meV in the 5 ML, 3.8 meV in the 4 ML, and 4.8 meV in the 3 ML NPLs. As one can derive from these results, the bright-dark exciton splitting, which is proportional to the exciton resonance energy, i.e. the band-gap energy, is inversely proportional to the NPL thickness. In this regard, spectrally-resolved PL decay measurements in which the emission line maximum of the PL spectrum is compared for $t = 0$ and $t \to \infty$, yielding a bright-dark splitting energy of (5.5 ± 0.5) meV for the 4 ML and (4.0 ± 0.5) meV for the 5 ML NPLs.[345]

The FLN spectra in Fig. 8.4 (c) exhibits additional side peaks (cp) at relatively lower and higher energies. These are suggested to be confined acoustic phonon modes or acoustic phonon replicas of the dark and bright excitons.[345] The phonon modes depend strongly on the temperature and, therefore, have a significant influence on the shape of the PL spectrum. The temperature dependence is the subject of discussion in Sec. 8.2.1. In addition, the acoustic phonon background creates a great challenge in spin-flip scattering experiments, as it overlaps with the SFRS signal and consequently makes its detection more difficult.

In summary, on the basis of theory and conducting PL measurements this section has outlined briefly the important optical characteristics of CdSe NPLs, highlighting the dark exciton recombination process via DBSs and longitudinal phonons. In this regard, the influence of confinement, caused by selective sample properties, e.g. NPL size and shape, and secondary parameters, such as temperature and magnetic field, on the emission spectra is discussed. Furthermore, the origin of the PL lines is clarified underlining interrelationships and particularities. The focus in the following section is set on the study of spin related phenomena by the method of SFRS.

8.2 Resonant electron spin-flip Raman scattering in CdSe nanoplatelets

As highlighted in the previous chapters, the SFRS technique delivers information on Zeeman splittings of carriers and excitons, by providing the immediate measurement of a carrier's g factor, and on the selection rules, which give insight into the spin structure of exciton complexes, their symmetries and spin interactions.[33] SFRS, therefore, represents a suitable tool to study and coherently manipulate spins, e.g. of resident electrons or holes.[36,138,337,338] This approach is used to study the electron spin-flip scattering under resonant excitation of the band edge exciton in colloidal CdSe NPLs. The results, their interpretation and analysis are discussed in this section.

To provide a first impression, of how SFRS is reflected in NPLs, initially basic SFRS spectra on the Stokes and anti-Stokes side are demonstrated in Figs. 8.5 (a) and (b). These results pertain to the 4 ML CdSe NPLs and are measured at a bath-temperature of $T = 2.5$ K in an external magnetic field of $B = 5$ T in Voigt ($B \perp$c-axis, (a)) and

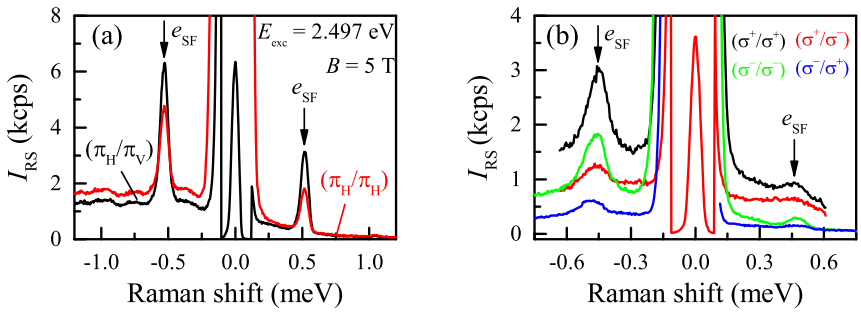

Figure 8.5: SFRS spectra of the CdSe NPLs with 4 ML measured in Voigt (B ⊥c-axis) (a) and Faraday geometry (B ∥c-axis) (b) at $B = 5$ T and $T = 2.5$ K for parallel and crossed circular polarizations. The exciton is excited resonantly at $E_{\mathrm{exc,4\ ML}} = 2.497$ eV ($P_{\mathrm{exc}} = 6$ W/cm^2). The laser line is at zero Raman shift. The intensities of the electron spin-flip Raman lines (marked by arrows) in Faraday geometry are significantly smaller than in the Voigt geometry.

Faraday geometry (B ∥c-axis, (b)). Since in the tilted geometries the optical selection rules are lifted, the polarization is changed from the circularly polarized to the cross-linearly polarized configuration. The SFRS spectra are shown in Fig. 8.5 (a) for the parallel- and cross-linear polarization denoted as ((π_H,π_H), (π_H,π_V)), and in Fig. 8.5 (b) for the co-circular ((σ^+,σ^+), (σ^-,σ^-)) and the counter-circular ((σ^-,σ^+), (σ^+,σ^-)) polarization configurations. On the basis of the PL analysis, which is briefly discussed in Sec. 8.1.4, the excitation energy is chosen in the way, that it is in resonance with the exciton (X^0) emission line at $B = 5$ T. Thus, the laser photon energy is set to $E_{exc} = 2.497$ eV. For this excitation energy, Raman lines on the Stokes and anti-Stokes side are observed on top of a background contributed by PL or acoustic phonons. These Raman lines stem from spin-flips of bound electrons, as it has been highlighted in previous resonant spin-flip Raman studies on wide band-gap CdS semiconductors and colloidal CdSe NPLs.[31,33,61,337]

With regard to an accurate analysis of the SFRS properties, in the following the focus is set on the evaluation of the electron spin-flip Raman shifts in Voigt and Faraday geometry. A rough comparison of the related SFRS spectra reveals that the Raman shifts of the scattered light clearly differ between both geometries. In the case of Faraday the shift of the electron spin-flip lines on the Stokes and anti-Stokes side equals independently of the co- or cross-circular polarization configurations 445 ± 7 μeV and 465 ± 10 μeV, respectively. On the contrary, in Voigt geometry the Raman shift for cross and parallel linear polarization amounts 530 ± 2 μeV on the Stokes side and 514 ± 8 μeV on the anti-Stokes side. From this, one derives that the Raman shift obviously increases by approximately 70 ± 20 μeV changing from Faraday to Voigt geometry. Taking into consideration the Zeeman splitting $|g|\mu_B B$, the Raman shifts correspond to a g factor of 1.53 ± 0.02 for Faraday and 1.83 ± 0.03 for Voigt. This weak anisotropy of the electron g factor, however, does not apply for all studied NPL

structures. For comparison, the e-SFRS in colloidal CdSe NPLs with 5 monolayers is investigated throughly. The resulting SFRS spectra, regarding a resonant excitation of X^0 (E_{exc} = 2.33 eV) are presented in Fig. 8.6. This spectra are measured in an external magnetic field of $B = 6$ T at $T = 1.6$ K. The results highlight that regardless of the chosen geometry the Raman shift equals (609 ± 10) μeV which corresponds to an electron g factor of 1.75 ± 0.04. In contrast to the 4 ML NPLs the g factor in the 5 ML NPLs is isotropic. To gain further information and to be able to explain these observations, an analysis of the polarization properties is necessary.

In general, the circular polarization properties of the SFRS spectra provide important information about the underlying spin structure and spin interactions in a low dimensional semiconductor. Therefore, next the focus is set on the analysis of the SFRS polarization properties in colloidal NPLs starting in Faraday geometry. As can be seen in Fig. 8.5 (b), for resonant excitation of X^0 the spin-flips are predominantly co-polarized, whereby the strongest signal is measured in (σ^+,σ^+) configuration on the Stokes side. From the analysis of the SFRS spectra it is evident that the SF intensity on the anti-Stokes side is significantly smaller than on the Stokes side. However, the relative ratio of the SFRS intensities ($I^{+/+} : I^{+/-} : I^{-/+} : I^{-/-}$) between the different polarizations remain identical regarding scattering to higher and lower energies. Here, the ratio equals $(1 : 0.23 : 0.18 : 0.71)$. In the first instance, one can describe the optical selection rules for the 4 ML NPLs as more or less strict. However, in comparison with the SFRS on 5 ML NPLs, it appears that the optical selection rules are rather disturbed. The SFRS spectra reveal in all polarization configurations practically no differences between the spin-flip Raman lines, concerning relative intensities, FWHM or energy shift. The relative ratio of the SFRS intensities equals in each case about $(1 : 0.73 : 0.97 : 0.89)$.

In the following, the attention is directed towards Voigt geometry. The analysis of the SFRS polarization properties in Voigt highlights exclusively in the 4 ML NPLs a perceptible difference between cross- and parallel-polarization. Here, the relative scattering intensity between cross and parallel polarization configuration differs by a factor of 1.7. The maximum e-SFRS intensity is present in the (π_H,π_V) configuration. As noted above, the SFRS in NPLs with 5 ML reveals once again deviating polarization properties. Here, the relative SFRS intensity in both polarization configurations is similar. The relative scattering intensity differs only by a factor of 1.08 to the favor of (π_H,π_H). Further, it is worth to note that for cross linear configuration one observes a decisive increase of the PL background. However, independent of polarization and geometry the gaussian shape of the spin-flip Raman lines remains unaltered.

Before going into deeper analysis of the SFRS in colloidal NPLs, next the focus first will be directed towards a further particular feature of CdSe NPLs, which is discovered in the course of investigations. It concerns the observation of an additional SF line in the Raman spectrum. For a better overview, this feature is highlighted in Fig. 8.6 by vertical arrows. This secondary scattering line appears on the Stokes side as well as on the

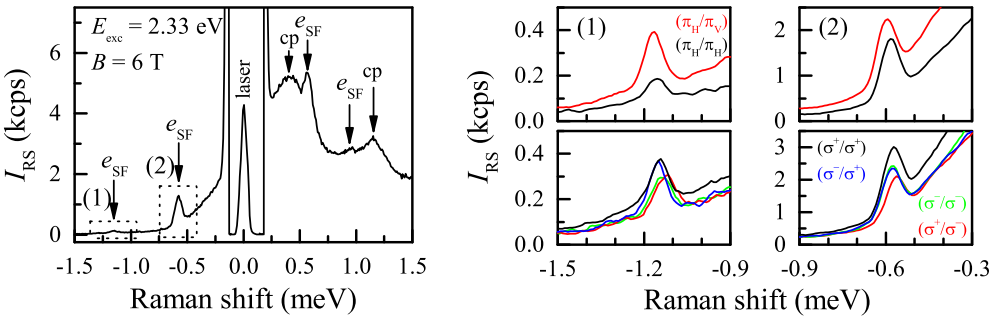

Figure 8.6: Shown left is the SFRS spectrum of the CdSe NPLs with 5 ML measured in Faraday geometry (B ‖c-axis) at $B = 6$ T and $T = 1.5$ K regarding a resonant excitation of the exciton at $E_{\mathrm{exc,5\ ML}} = 2.33$ eV. The electron spin-flip line (e_{SF}) and the acoustic phonons (cp) are marked by vertical arrows. The region (1) and (2) are shown enlarged on the right hand side in the e-SFRS anti-Stokes spectra. These spectra are measured in Voigt (upper panels) and Faraday (lower panels) geometry in parallel and crossed circular polarizations.

anti-Stokes side and has twice the Raman shift of the first SF line ($\Delta E_{2-SF} = 1.14$ meV, $\Delta E_{1-SF} = 0.57$ meV). Considering the Zeeman-splitting $|g|\mu_B B$, the corresponding g factor amounts in first approximation 3.25 ± 0.06. Since its SFRS intensity is rather small, it represents a great experimental challenge to distinguish it from the background contributed by PL and acoustic phonons (cp). The relative intensity ratio between the first e-SF line and the secondary Raman line amounts 10 to 1. As the analysis of SFRS spectra in Voigt and Faraday geometry proves, the related g factor is isotropic in the 5 ML NPLs. With regard to the polarization properties, in Faraday geometry they prove to be similar to those of the first SF-line. Here, the relative ratio of the SFRS intensities equals $(1 : 0.94 : 0.93 : 0.97)$, indicating that the selection rules are disturbed as it is the case for the electron spin-flip line. However, in Voigt geometry, a predominant scattering signal for cross-linear polarization configuration (π_H,π_V) is evident. In comparison to parallel-polarization (π_H,π_H), the relative scattering intensity for (π_H,π_V) is raised by a factor of 2.1. In terms of SFRS polarization properties, this particularity is the only difference between the two spin-flip Raman lines.

From these first results one can conclude that the scattering mechanism which is responsible for the higher-order spin-flip scattering processes must be closely related to the spin-flip of the X^0 bound electron. This assumption is supported by the fact that the polarization properties are almost identical and the g factor of the second order spin-flip is exactly twice as large. However, in order to be able to provide a accurate description of the origin and SFRS mechanism, an analysis of the magnetic field and angular dependence is essential. This issue is addressed in the following section.

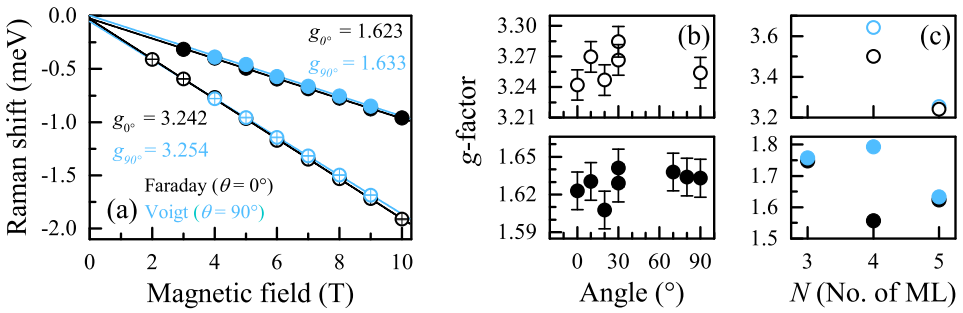

Figure 8.7: (a) Raman shift of the first and second order spin-flip scattering line on the anti-Stokes side as function of the magnetic field, measured in Faraday (black) and Voigt geometry (blue). The depicted results pertain the 5 ML NPLs regarding a resonant excitation of the exciton at $E_{\mathrm{exc,5\ ML}} = 2.33$ eV at $T = 1.5$ K for co-circular polarization configuration (σ^+,σ^+). The error in the Raman shift does not exceed the symbol size. The fitting (blue and black-colored) curves based on Eq. (2.35) show that the offset is negligible. (b) Angular dependence of the electron g factors of the first (lower panel) and second order (upper panel) electron spin-flip Raman lines. For each adjusted angle the g factor is evaluated from an SFRS magnetic field series. (c) Landé factor as a function of the CdSe monolayers measured at $T = 1.6$ K in Faraday geometry. For each NPL structure the laser photon energy is tuned into resonance with the exciton.

8.2.1 Magnetic field and angular dependence of the SFRS in CdSe NPLs

With the intention to distinguish the origin of the SFRS processes in CdSe NPLs, next the focus is set on the study of magnetic field and geometry dependence of the e-SFRS. An exceptionally important parameter in this context is the Landé factor of the electron (g_e), which describes the correlation between angular momentum and magnetic momentum. In a previous study on CdSe NPLs the g factor is estimated to $g_{\mathrm{e}} = 1.69 \pm 0.02$.[337] These studied NPLs had a lateral size of 5 nm x 30 nm, a total thickness of (18 ± 1) nm, and are covered by a 1.2 nm-thick CdSe core and a (8.4 ± 0.5) nm-thick CdS shell. However, to the best of our knowledge a thorough magnetic field study of the electron g factor tensors and the higher order electron spin-flip Raman contribution has not yet been carried out for colloidal nanostructures. A precise analysis of the electron g factor dependence on the NPL thickness is also not tackled. The results and analyses devoted to this issues are presented in detail below.

In order to determine the g factor of the electron in the 5 ML CdSe NPLs, the dependence of the spin-flip Raman shifts on the magnetic field are studied for different magnetic field geometries. The results regarding a resonant excitation of X^0 ($E_{\mathrm{exc}} = 2.330$ eV) in Faraday ($\theta = 0°$, black circles) and Voigt geometry ($\theta = 90°$, blue circles) are shown in Fig. 8.7 (a). To measure the electron spin-flip Raman line in Faraday the polarization configuration is set to (σ^+,σ^+), whereas in Voigt the parallel-linear

polarization configuration (π_H,π_H) is used.

As can be derived from the depicted results, the Raman shifts of the anti-Stokes SF lines demonstrate linear magnetic field evolutions. With increasing magnetic field strength B, the first (1) and second (2) spin-flip Raman line linearly shift to lower energies, as described by the Zeeman term $|g_\mathrm{e}|\mu_\mathrm{B}B$. In this regard, the Raman shift for Faraday and Voigt geometry differs only marginally. The fluctuation of the evaluated values is of the same order of magnitude as the measurement error. As it is discussed in chapter 2.1.5 the Raman shift is described by a longitudinal and transverse g factor value. Thus, the interrelationship between the g factor and the tilting angle θ is expressed by the equation:

$$g(\theta) = \sqrt{(g^{\parallel}\cos(\theta))^2 + (g^{\perp}\sin(\theta))^2}. \tag{8.7}$$

In order to determine the corresponding g factors of the electron (closed circles) and second order spin-flip Raman line (open circles), a linear least squares fit to the data according to Eq. (2.35) is conducted. This yields Landé factors of $g_1^{\parallel} = (1.623 \pm 0.002)$, $g_2^{\parallel} = (3.242 \pm 0.002)$ for Faraday and $g_1^{\perp} = (1.633 \pm 0.003)$, $g_2^{\perp} = (3.254 \pm 0.002)$ for Voigt geometry. Thus, the difference between both geometries equals $\Delta g_1 = g_1^{\parallel} - g_1^{\perp} = 0.010 \pm 0.005$ for the electron and $\Delta g_2 = 0.012 \pm 0.004$ for the second order Raman line. For instance, this small values highlight the fact that both g factors are isotropic with regard to the 5 ML CdSe NPLs. From a linear extrapolation of the experimental data a zero-field offset of $\Delta E_{\mathrm{off,Faraday}} = (1 \pm 2)$ μeV and $\Delta E_{\mathrm{off,Voigt}} = (3 \pm 3)$ μeV is deducible. Since these offsets are in the range of the measurement error, one can conclude that the Raman shift offset equals zero in absence of an external field.

A comparison of the evaluated g factor values of both investigated spin-flip Raman lines demonstrates that the higher order spin-flip Raman line exhibits exactly twice the Raman shift of the first. This characteristic seems to be independent of the chosen geometry. To analyze the SFRS geometry dependence more precisely and, thus, describe the g factor tensor, the dependence of the spin-flip Raman line shifts on the angle between the magnetic field direction and c-axis is studied carefully. In this respect, for each adjusted angle a magnetic field series is measured, investigating the Raman shift as a function of the magnetic field, in order to determine the corresponding g factor. The results are presented in Fig. 8.7 (b). The angular dependence reveals that the g factor values only slightly fluctuate between Faraday and Voigt geometry. In case of the electron, the value varies between 1.605 and 1.642, whereas for the second order spin-flip Raman line, it ranges from 3.241 up to 3.285. This result emphasizes that the geometry has almost no influence on the g factors. In addition, it is worth to mention, that the SFRS intensity does not vary as a function of angle (not shown here).

As discussed above, the dimensions of a NPL have a considerable impact on the optical properties of the material. Therefore, in order to determine to what extent the thickness of a NPL can alter the SFRS properties, the g factors of the highlighted

spin-flip Raman lines are studied as a function of the number of CdSe monolayers. In this context, all the samples listed in the Tab. 8.1 are studied. For each NPL structure the laser photon energy is tuned into resonance with the exciton. The SFRS spectra are measured in Faraday (black) and Voigt (blue) geometry. The results are depicted in Fig. 8.7 (c). From the evolution of the data can be concluded that the g factor decreases with rising number of monolayers, i.e. increasing NPL thickness. The thickness in turn is inversely proportional to the exciton resonance energy as it is shown in Fig. 8.4. The fact that the electron g factor smoothly varies with energy underlines that it is mostly determined by the band-gap which becomes smaller for an increasing number of monolayers. This dependence is well known for (In,Ga)As/GaAs QDs and is studied by means of SFRS on resident electrons before. [138,249]

It is important to note here that a second order SF line is not be observed in the CdSe NPLs composed of 3 monolayers. Furthermore, a weak deviation is monitored in the case of the 4 ML NPLs. A reason for this deviation may be attributed to the small lateral size (8 nm x 16 nm) of the NPLs which yields QD-like properties as it has been discussed in Sec. 8.1.3. A weak anisotropy is characteristic of the electron g factor in QDs. [251] Thus, this may serve as an explanation for the discrepancy between the g factors in Voigt and Faraday.

In summary, the study of the magnetic field and geometry dependence of the SFRS in NPLs provided important information on the g factor tensors of both studied spin-flip Raman lines and, thus, on the SFRS processes. In addition, it is demonstrated that the lateral size of the NPL as well as its thickness affect the value of the corresponding g factor. Hence, already a minor change of a NPL dimension can be used to adjust their optical properties. In this context, a further important parameter that defines the optical properties of a NPL is the temperature. To what degree and how the temperature influences the SFRS in NPLs is discussed in the following section.

8.2.2 Temperature dependence of the SFRS in CdSe NPLs

The temperature is a crucial parameter in colloidal nanostructures as it influences the spin interactions and in turn the decay dynamics. In this regard, previous studies have demonstrated the formation of DBMPs at low temperatures which occur due to optical orientation of the dangling-bond spins that result from dangling-bond-assisted radiative recombination of spin-forbidden dark excitons (see Sec. 8.1.4). [340] This process demands the system to be below a critical temperature at which the DBSs are not polarized. However, if the temperature increases, the arbitrary orientation of DBSs evoked by phonon interaction causes an admixture of the bright and dark exciton states which in turn yields the dark exciton decay and consequently changes the PL characteristics. [340] However, the impact of temperature on the e-SFRS in NPLs has not yet been investigated in literature. Nevertheless, it is well known that coherent phonons can establish an interconnection between quantum states in nanostructures. [229,373] Furthermore, the

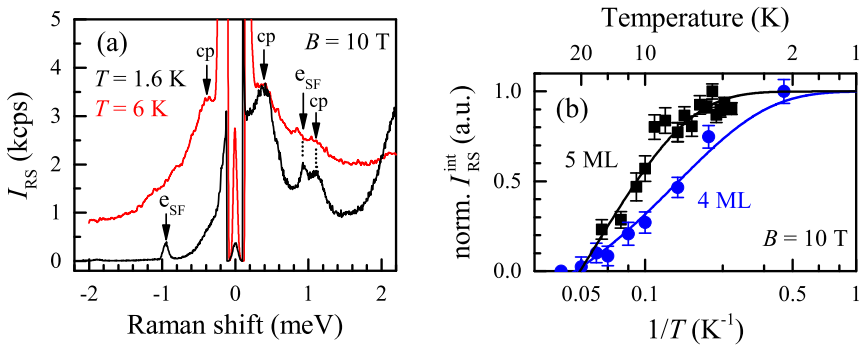

Figure 8.8: (a) SFRS spectrum of the CdSe NPLs with 5 ML in Faraday geometry (B ‖c-axis) at $B = 10$ T for $T = 1.6$ K (black) and 6 K (red). The spectra is measured regarding a resonant excitation of the exciton at $E_{\mathrm{exc,5\ ML}} = 2.33$ eV ($P_{\mathrm{exc}} = 8$ W/cm^2) in co-circular (σ^+,σ^+) polarization configuration. The electron spin-flip lines (e_{SF}) and the acoustic phonons (cp) are marked by vertical arrows. (b) Normalized integral intensity of the first electron spin-flip Raman line on the anti-Stokes side as a function of the inverse bath temperature ($1/T$). The integral intensity is normalized to the values measured at $T = 2.2$ K. The depicted results pertain the 5 ML (black) and 4 ML (blue) NPLs regarding a resonant excitation of the exciton at $E_{\mathrm{exc}} = 2.33$ eV and 2.497 eV, respectively. The shown fitting (blue and black-colored) curves are based on the Arrhenius-like equation (Eq. (8.9)).

interaction probability between light and matter depends immanently on phonons as it is the case in Raman scattering. As shown in this thesis phonons play a significant role in many spin related phenomena as they can be used to trigger a flip and thereby orient a spin in any imaginable way. In order to understand the spin-phonon interactions in colloidal nanostructures, the study of the temperature-dependent changes in the e-SFRS is of great importance. The results and analyses presented here are devoted to this issue. The main focus is on the investigation of temperature and excitation power dependence of the e-SFRS.

To demonstrate initially the changes which are caused by an temperature increase, the e-SFRS in 5 ML CdSe NPLs is carefully studied for low ($T = 1.6$ K) and slightly elevated temperatures ($T = 6$ K). The Stokes and anti-Stokes SFRS spectra measured in co-circular polarization configuration (σ^+,σ^+) at $B = 10$ T ($B \parallel c$-axis) are presented in Fig. 8.8 (a). It becomes apparent, that a variation of T leads to a significant increase of the emission background which superimposes markedly with the SFRS signal. Below $T = 2$ K the intensity of the electron spin-flip Raman lines is relatively strong ($\approx$ 120 cps), while the peak intensity significantly drops to about 40 cps at 6 K. Above $T = 18$ K, the first e-SFRS signal cannot be monitored any further. With respect to the second-order SF line, it is under no circumstances possible to detect it above 2 K. For this reason, the temperature dependence analysis presented below refers exclusively to the first electron SF.

The intensity ratio between Stokes $I_{SF}^{\mathbf{S}}$ and anti-Stokes $I_{SF}^{\mathbf{AS}}$ of the first electron spin-flip Raman line is stable throughout the whole temperature range. Using this ratio the temperature of the photogenerated electron (T_e) can be estimated. The intensity ratio is given by

$$\frac{I_{SF}^{\mathbf{S}}}{I_{SF}^{\mathbf{AS}}} = \left(\frac{\Delta E_\mathrm{SF}}{k_\mathrm{B} T_\mathrm{e}}\right). \tag{8.8}$$

Here, ΔE_SF denotes the Raman shift which correspond to transitions between exciton spin-sublevels. In reference to the SFRS spectrum shown in Fig. 8.8 (a), which has been measured at 1.6 K for $B = 10$ T, the temperature of the photogenerated electron yields $T_\mathrm{e} = (2.1 \pm 0.5)$ K. Within the frame of the measurement error this is in good agreement with the surrounding bath temperature, highlighting that the electrons involved in the SFRS processes are in thermal equilibrium with the lattice.

In the SFRS spectrum shown in Fig. 8.8 (a), one observes that between 1.6 K and 6 K the absolute Raman shift of about (960 ± 20) μeV remains unchanged. To illustrate the temperature dependence of the Raman shift more clearly, in Fig. 8.9 (a) the g factor is presented as a function of temperature. The results pertain to the 5 ML CdSe NPLs. It becomes apparent that the g factor remains almost unaltered throughout the full temperature range. The mean value equals 1.65 ± 0.02. The small deviations at $T = 11$ and 16 K can be attributed to a measurement inaccuracy caused by a very low signal to background ratio at higher temperatures. The fact that the Raman shift is insensitive to the sample temperature indicates a thermally robust SFRS mechanism.

Turning now the attention to the SFRS background (see Fig. 8.8 (a)), which is mainly attributed by acoustic phonon scattering and resonant PL, one monitors that the peak intensity of the acoustic phonon modes (cp), which are clearly distinguishable at $T = 1.6$ K, decreases with rising lattice temperature. For $T > 6$ K the width of these acoustic phonon modes becomes decisively enhanced. The formation of new phonon modes at higher temperatures is facilitated as well, as can be seen on the anti-Stokes side of the Raman spectrum. However, the Raman shift of these phonon lines does not alter at higher temperatures.

To further analyze the temperature dependence of the e-SFRS, the integral intensity (I_SF) of the first electron-SF on the anti-Stokes side is studied as a function of the lattice temperature in the range from 1.6 up to 17 K for the 4 and 5 ML NPLs. The results are presented in Fig. 8.8 (b). The measurements are done in Faraday geometry at $B = 10$ T. The evolution of the data demonstrates that the e-SFRS intensity decreases steadily with rising temperature independent of the NPL thickness or lateral size. The spin-flip Raman lines are most intensive at temperatures below 2 K. At $T = 7$ K (4 ML NPLs) and 10 K (5 ML NPLs) the integral SFRS intensities decrease to about 50% of the maximum value. Above $T = 17$ K, the e-SFRS can no longer be monitored.

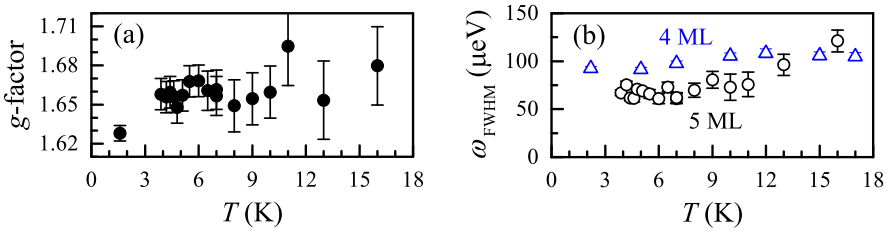

Figure 8.9: Dependence of the g factor (a) and the FWHM of the first e-SF line on the anti-Stokes side ($\hbar\omega_{\mathrm{FWHM}}$) (b) on the bath temperature (T). The measurements refer to the 4 and 5 ML NPLs. The related SFRS spectra are measured in Faraday geometry at $B = 10$ T and $P_{\mathrm{exc}} = 8$ W/cm^2 in co-circular polarization configuration (σ^+,σ^+). The error of ω_{FWHM} does not exceed the symbol size.

The temperature-dependent SFRS intensities follow the Arrhenius-like exponential equation:

$$I_{\mathrm{RS}} = I_0 \exp\left(-\frac{\epsilon}{k_{\mathrm{B}}T}\right). \tag{8.9}$$

Here, I_0 describes the intensity amplitude, k_{B} the Boltzmann constant, and ϵ the activation energy of the SFRS process. Using the Arrhenius-like equation to model the temperature dependence of the SFRS intensity, one can distinguish the activation energy of the e-SFRS. The resulting exponential fits after Eq. (8.9) are illustrated in Fig. 8.8 (b) by solid lines. The fittings of the e-SFRS data yield activation energies of $\epsilon_{4\ \mathrm{ML}} = 0.61$ meV and $\epsilon_{5\ \mathrm{ML}} = 1.42$ meV. It can be concluded that the activation energies of the e-SFRS processes increase with growing NPL thickness, i.e. decreasing band-gap energy. However, ϵ cannot be attributed to the exciton binding energy in NPLs, since it amounts $200 - 300$ meV for CdSe NPLs.[345] It is also not comparable with the DBMP binding energy which amounts about (5.5 ± 0.5) meV in the 4 ML and (4.0 ± 0.5) meV in the 5 ML NPLs (see Sec. 8.1.4).[337,345] On the contrary, the activation energies coincide well with the FWHM of the exciton ZPL which do not exceed 1.4 meV (see Fig. 8.4). In general, the localization potential of a QW or QD as well as potential fluctuations at the interfaces, define the line width of the ZPL.[374] For this reason, the activation energy of the e-SFRS processes can be assumed to describe the localization energy of the exciton complex in a NPL.

In the full temperature range the shape of the spin-flip Raman line is well described by a Gaussian profile. An analysis of this profile provides information about the electron spin-flip Raman line width which is of particular interest, since it allows one to draw conclusions about the g factor dispersion and lifetime of the intermediate scattering state. As depicted in Fig. 8.8 (b), the width of the electron spin-flip Raman line in the 5 ML NPLs increases from about 75 μeV at 4 K up to 120 μeV at 16 K. The situation is slightly different for the 4 ML NPLs, where no significant change of the FWHM is observable. Here, the mean value of the FWHM equals (105 ± 15) μeV, which is

very similar to the laser line FWHM. The roughly identical average spin-flip Raman line widths of both investigated NPL structures indicate that the g factor dispersion is almost independent of the platelet thickness. The evaluated widths can be used to approximate the lifetime of the intermediate scattering state which is defined by the carrier-phonon interaction. The respective lifetime in the 4 ML NPLs approximately equals $\tau_{\mathrm{4ML,e}} = \hbar/\omega_{\mathrm{FWHM}} \approx 6$ ps. On the contrary in the 5 ML NPLs it ranges from $\tau^{\mathrm{4K}}_{\mathrm{4ML,e}} \approx 9$ ps at 4 K down to $\tau^{\mathrm{16K}}_{\mathrm{4ML,e}} \approx 5$ ps at 16 K.

8.2.3 Power dependence of the SFRS in CdSe NPLs

Another crucial aspect in the analysis of the SFRS is the power density of excitation. As has been demonstrated in the previous parts of this thesis, strong laser power principally leads to an increase of the local lattice temperature and, thus, a reduction in the exciton lifetime as well as delocalization of the resident electrons. Further, laser-induced heating enhances the density of thermal phonons which can violate spin-flip processes. For this reason, the SFRS is very sensitive to the temperature, and already a minor local heating can reduce the SFRS intensity. However, depending on the SFRS mechanism, thermal phonons can also enhance spin manipulation and in turn amplify the SFRS efficiency, as has been shown for (In,Ga)As/GaAs QDs (see Chap. 4.2). In the following the impact of the power density P_{exc} of the resonant excitation on the SFRS processes in NPLs will be highlighted. To illustrate briefly how an increase in power density affects the e-SF line, SFRS spectra in the vicinity of the first electron spin-flip on the Stokes side are presented in Fig. 8.10 (a) exemplarily for three different excitation densities. The spectra are measured in co-polarized configuration (σ^+,σ^+) at $T = 1.6$ K for $B = 7$ T in Faraday geometry. One observes that with increasing excitation power the scattering intensity as well as the acoustic phonon background rise. For instance, one can monitor that the peak intensity of the SF line increases from $I^{\mathbf{S}}_{SF} = (100 \pm 10)$ cps at $P_{\mathrm{exc}} = 6$ W/cm^2 up to $I^{\mathbf{S}}_{SF} = (300 \pm 10)$ cps at $P_{\mathrm{exc}} = 22$ W/cm^2, while the gaussian shape and the FWHM of the e-SF line remain unaltered. Furthermore, the maximum of the SF-line does not demonstrate a power-dependent energy shift. The absolute Raman shift remains unchanged at about (680 ± 10) μeV.

To further analyze this power dependence, the peak-intensity ($I^{\mathbf{S}}_{SF}$) and FWHM of the first electron spin-flip Raman line on the Stokes side are presented in Figs. 8.10 (b) and (c) as a function of the excitation power. For comparison purposes, the acoustic phonon scattering background (aSPB) intensity (I_{aPSB}) at the position of the e-SF maximum is estimated from the SFRS spectra. The results are enclosed in Fig.8.10 (c). As can be derived from the evolution of the data, the e-SF intensity and the scattering background intensity reveal a linear increase with P_{exc}. Only for high power densities ($P_{\mathrm{exc}} > 25$ W/cm^2), a saturation of the e-SF is observable. However, the e-SF width of about (80 ± 10) μeV remains unaltered. It is important to stress here that the ratio between $I^{\mathbf{S}}_{SF}$ and I_{aPSB} is almost independent from P_{exc}.

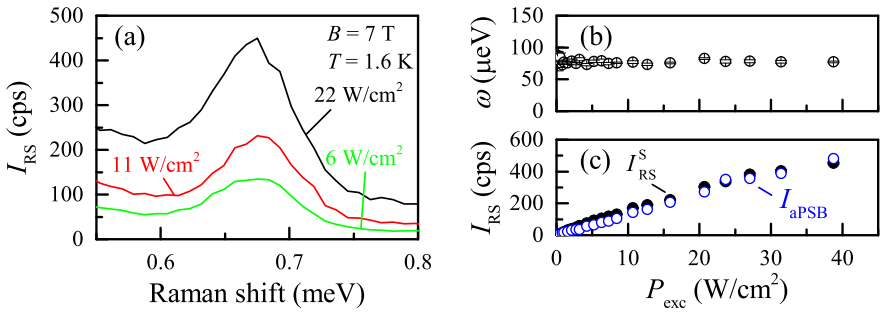

Figure 8.10: (a) SFRS spectra of the CdSe NPLs with 5 ML in the range of the first electron SF for $P_{\mathrm{exc}} = 6$ W/cm^2 (green), 11 W/cm^2 (red), and 22 W/cm^2 (black). The spectra are measured in Faraday geometry at $B = 7$ T and $T = 1.6$ K for co-circular (σ^+,σ^+) polarization configuration. (b) Dependence of the FWHM of the first e-SF line on the anti-Stokes side on the excitation power density P_{exc}. The error of $\hbar\omega_{\mathrm{FWHM}}$ does not exceed the symbol size. (c) Peak intensity of the first electron spin-flip Raman line and the acoustic phonon scattering background (aSPB) intensity (I_{aPSB}) at the position of the e-SF maximum on the anti-Stokes side as a function of P_{exc}.

On the basis of these results, one can draw the conclusion that the generation of thermal phonons induced by high excitation power densities facilitates the SFRS processes. However, the results further indicate a process counteracting the enhancement of the coherent SFRS which provokes a saturation of $I^{\mathbf{S}}_{SF}$ for very high excitation powers. The effect that prevents a further increase in SFRS intensity is the structural degradation of NPLs. It is well known from previous studies that strong laser excitation not only provides a heating of the sample but also triggers an irreversible modification of the NPL surface. For instance, the degradation of NPLs can be monitored via the steady decrease of X^0 PL intensity over time. Depending on the NPL composition, i.e. NPL dimensions, shell thickness, and material, as well as on the lattice temperature and excitation energy, this process can proceed faster or slower. It is important to note, here, that the degradation of platelets is also apparent in the SFRS. In order to show this the intensity of the e-SFRS on the Stokes side for an excitation with high laser power density ($P_{\mathrm{exc}} = 60$ W/cm^2) is studied over a long period of time. For this purpose repeating fast SFRS spectra are measured at $T = 1.6$ K and $B = 6$ T ($B \parallel c$-axis). The measurement period of a single spectrum is about 40 s. The approximate time delay between the measurement (n) and ($n + 1$) amounts about 200 s. Further, the laser is not turned off in between the measurements, in order to study the consequences of continuous illumination. The evaluated e-SFRS peak intensities are shown in Fig. 8.11 as a function of the elapsed time. These results highlight that with elapsing time t the e-SFRS intensity markedly decreases from $\approx (455 \pm 10)$ cps at $t = 0$ s down to $\approx (250 \pm 10)$ cps at $t = 1200$ s. The corresponding FWHM as well as the Raman shift do not demonstrate any alteration (not shown here). Moreover, one observes that the structural degradation of NPLs driven by high laser power is irreversible, since the e-

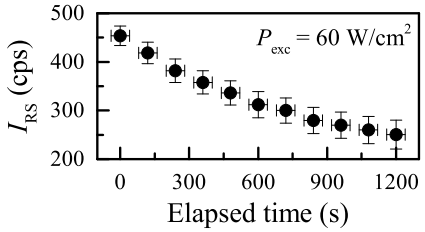

Figure 8.11: Peak intensity of the first electron spin-flip Raman line as a function of elapsed time regarding a resonant excitation of the exciton with high power density ($P_{\mathrm{exc}} = 60$ W/cm^2). The depicted results pertain the 5 ML NPLs. The related spectra are measured at $B = 7$ T and $T = 1.6$ K for co-circular (σ^+,σ^+) polarization configuration. The measurement period of a single spectrum is about 40 s and the delay time between two measurements amounts 200 s.

SFRS intensity could not be restored even after keeping the sample in the darkness for several hours. The decisive influence of high laser power density is taken into account in all the underlying studies and for this reason a moderate excitation power is used to study the NPLs.

Before the SF mechanism will be explained in-depth, the following section briefly addresses the open question to what extent additional unpolarized laser illumination with energies, which exceed considerably the band-gap energy, influences the electron spin-flip scattering in CdSe NPLs.

8.2.4 Impact of additional high-energy illumination on the e-SFRS in NPLs

High-energy illumination, which is used in addition to the resonant SFRS, can be an essential factor in influencing the SFRS mechanism. As described in chapter 5, it is demonstrated for (In,Ga)As/GaAs QDs that the application of an quasi resonant excitation in the WL in addition to the resonant SFRS can provide a coupling of carrier spins to the surrounding nuclear spin bath.[21] As a consequence a dynamic nuclear spin polarization occurs which can be monitored through the Overhauser shift of the electron spin-flip Raman line. Moreover, by additional high-energy illumination the e-SFRS can considerably be enhanced.[21,33] However, it may also result in local heating, which in turn decreases the exciton lifetime and violates the electron spin-flip scattering. The extent to which the generation of additional carriers by high-energy illumination influences the resonant e-SFRS in CdSe NPLs will be discussed in the following. All results presented below refer to the 4 ML NPLs.

To study the impact of additional high-energy illumination the e-SFRS is investigated for simultaneous resonant and above barrier excitation. Concerning the resonant

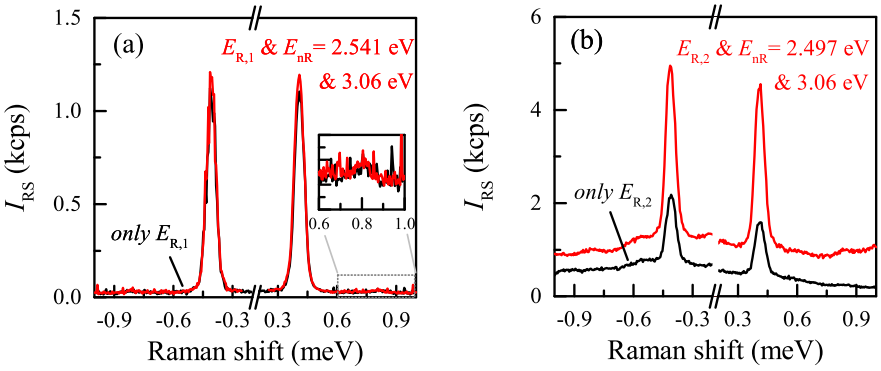

Figure 8.12: SFRS spectra of the CdSe NPLs with 4 ML for quasi-resonant ($E_{\mathrm{R},1} = 2.497$ eV) (a) and resonant ($E_{\mathrm{R},2} = 2.497$ eV) (b) excitation, with (red) and without (black) simultaneous above-barrier illumination ($E_{\mathrm{nR}} = 3.06$ eV). The spectra are measured at $B = 5$ T and $T = 2.5$ K for co-circular (σ^+,σ^+) polarization configuration in Faraday geometry. The inset in (a) demonstrates the weak intensity of the second order spin-flip line and the induced change by above-barrier illumination.

excitation two cases are studied in detail. On the one hand, when the excitation is in resonance with X^0 ($E_{\mathrm{R},2} = 2.497$ eV) and on the other hand, when it is at excitation energies slightly above ($E_{\mathrm{R},1} = 2.541$ eV). The resulting Raman spectra for resonant excitation only (black line) and under simultaneous above-barrier illumination (red line) measured at $T = 1.6$ K and $B = 5$ T ($B \parallel c$-axis) in co-circular polarization configuration (σ^+,σ^+) are presented in Fig. 8.12 (a) and (b). The photon energy of the above-barrier illumination is set in these measurements to $E_{\mathrm{nR}} = 3.06$ eV and the respective power density $P_{\mathrm{nR}} = 3$ W/cm^2.

When the NPLs are excited only resonantly a first and a second order spin-flip Raman line are observed on the Stokes and anti-Stokes side on top of the PL background. Independent of the chosen excitation energy their Raman shift equals $|\Delta E_{\text{e-SF}} \approx 420|$ μeV and $|\Delta E_{\text{2-SF}} \approx 845|$ μeV, respectively. The relative intensity ratio between the electron spin-flip Raman line and the secondary Raman line amounts approximately $1 : 0.03$. If one compares the absolute intensity and width of the SF lines on the Stokes and anti-Stokes side, it appears that they are similar. The relative scattering intensities $I_{SF}^{\mathbf{S}}$ and $I_{SF}^{\mathbf{AS}}$ differ marginally by a factor of 1.02. Furthermore, one can deduce from the SFRS spectra that the background is less prominent for quasi-resonant excitation conditions. This indicates that it is most likely originating from resonant PL.

Considering now the simultaneous illumination with above-barrier photons, one observes a distinct difference between the SFRS spectra concerning resonant and quasi-resonant excitation. In the latter case (see Fig. 8.12(a)), the SF intensity of the first and second order SF line increase just marginally by a factor of 1.1. The Raman shift,

width and ratios of the SF lines remain unchanged. In the case of resonant excitation (see Fig. 8.12(b)) the SF intensity rises on the Stokes side as well as on the anti-Stokes side by a factor of 2.5. However, the intensity ratio between the SF lines scattered to higher and lower energies does not change. Moreover, from an analysis of the spectra can be derived that the Raman shift and width do not alter, but the PL background decisively increases.

Overall, these results indicate that due to above barrier illumination the spin-flip scattering efficiency gets enhanced but only for resonant excitation conditions, i.e. the photon energy is in resonance with X^0. As elaborated in Chapter 4.2, the influence of an additional higher energy excitation can be elucidated via the SFRS intensity which is in general described by the product $I_{\mathrm{SF}} \propto I_{\mathrm{i}} W_{\mathrm{em}} \tau_{\bar{\mathrm{j}}} W_{\mathrm{SF}} \tau_{\mathrm{j}} W_{\mathrm{abs}}$ (see Eq. (4.5)). The intensity of the resonant incident light I_{i} is kept constant during the experiments and can be, therefore, neglected as an influencing factor. The absorption W_{abs} and emission W_{em} probabilities, which depend on the excitonic resonance energies, do not change either in case of additional nonresonant excitation in the studied NPLs. Due to high energy illumination the background carrier concentration rises and, in turn, the probability of trion formation. This can lead to a shortening of the exciton lifetime τ_j which consequently would reduce the spin-flip scattering intensity. However, the SFRS process can also be accelerated by electrons which relax from continuum states directly into the intentionally undoped QW structures of a NPL. These electrons may interact with optical or acoustic phonons, shifting the phonon density of states in energy, so that resonant carrier spin-phonon scattering may become more efficient. These theoretical considerations overlap well with the experimental results highlighting that the increase of the e-SFRS efficiency may mainly be attributed to additional electrons in the QW ground states of NPLs.

8.3 Mechanism of multiple Raman scattering in NCs

As mentioned above colloidal NCs are one of the best-known semiconductor nanostructures that have been theoretically and experimentally thoroughly investigated in the recent years. Particularly the formation of the dark exciton, which forms the exciton ground state in CdSe NPLs, strongly affecting the exciton dynamics, lifetimes, and photoluminescence properties, has been in the spotlight of research. However, although it is well known that via the dark exciton the possibility of optically charging colloidal NCs is provided, allowing one to create resident carriers that can be optically addressed, controlled and manipulated, the spin interactions are not yet fully exploited and a description of the spin interactions is not stated so far. However, the newly gained knowledge provided by SFRS studies shall contribute to a better understanding of the spin-related phenomena in NPLs and, thus, give the possibility to characterize the SF mechanism.

Based on the experimental results, which are discussed in the previous sections, the spin-flip scattering mechanism in NPLs will be described in the following. In this context, the explanations are developed on the basis of earlier SFRS studies on NCs and material related QW structures. For instance, the feature of double SFRS is experimentally investigated in wide band-gap CdS semiconductors and later theoretically explained.[338,339] In order to elaborate the mechanism sequentially, the focus will be set initially on the first order electron spin-flip and afterwards expanded to incorporate double spin-flip processes. Herein, different model schemes of electric dipole allowed spin-flip Raman processes in exciton complexes will be compared to the experimentally determined scattering mechanisms.

It is important to note that there is a prevailing assumption at the moment how this SFRS process may be established, exciton and resident electron

An important aspect in the description of the SFRS process are as mentioned above the selection rules for electric dipole transitions. These can be principally derived from the circularly polarized Raman spectra. However, all observations indicate disturbed selection rules of the SFRS. In NPLs this violation is attributed to two factors. On one hand the orientation of NPLs on the substrate layer and on the other hand the lateral size of the NPLs. Both aspects may influence the optical properties of nanostructures. The orientation of the NPLs is essential as it contributes to a violation of the optical selection rules in the SFRS process. In an ensemble of randomly oriented NPLs there will always be platelets with their c-axis aligned in the direction of the external magnetic field or perpendicular to it. Thus, SFRS on a carrier is expected to be observed regardless of the selected geometry as long as its g factor is not remarkably anisotropic. In the case of a heavy hole for instance, one would assume that, because of its anisotropic g factor, the SFRS signal is significantly smeared out and cannot be distinguished from the acoustic phonon background.

The orientation of NPLs in the investigated CdSe samples is absolutely arbitrary. The NPLs can be aligned either vertically, horizontally or tilted (see Fig. 8.1). A stacking of the NPLs is also possible, as it is shown by PL analysis combined with small angle X-ray diffraction in previous studies.[341] D. Tessier et al. reported that due to stacking of NPLs an additional emission line ($\Delta E_{X^0-X^{\mathrm{LO}}} \approx 25$ meV) appears in PL which is independent of the NPLs size, thickness, and amount of surface ligands. It is pointed out, that the emission line has the same fluorescence lifetime and properties as the band-gap exciton and is, therefore, identified as an optical phonon line.[341] As these studies demonstrate, the orientation of NPLs on the substrate surface plays a crucial role for the optical properties. Interpreting the SFRS polarization characteristics on this basis, one might reasonably assume that only in regard of the 4 ML sample (see Fig. 8.5) the orientation of NPLs is less arbitrary, since the optical polarization properties are more defined. Here, one can observe that the spin-flip Raman line is very weak in Faraday geometry but becomes stronger, when the magnetic field is tilted into Voigt geometry. This is well comparable with the SFRS properties of resident

electrons in (In,Ga)As/GaAs singly charged epitaxial QDs described in chapter II. In those structures the dots have a well defined orientation, i.e. the heavy-hole quantization axis is parallel to the growth axis, resulting in strict optical selection rules. The concordances in the experimental results emphasizes the assumption that the NPLs are predominantly oriented horizontally in the 4 ML CdSe NPLs. The absence of strict optical selection rules in the 5 ML NPLs implies that the platelets there are more randomly oriented.

Apart from the orientation of NPLs, their lateral size has a decisive impact on the optical properties as well. As discussed in Sec. 8.1.3, in platelets with smaller lateral dimensions, due to a shrinkage of the carrier wave functions the localized charge density increases, yielding the short range contact interactions between the involved carriers, e.g. exciton band electrons and holes. It is highlighted that in structures with lateral dimensions lower then 7 nm x 21 nm the strong confinement prevails the Coulomb interaction. Since the 4 ML NPLs have a lateral size of 8 nm x 16 nm, it is to be expected that the optical properties, which are mainly determined by the strong confinement, are comparable to those of a QD. For the 3 ML (6 nm x 40 nm) and 5 ML (7 nm x 30 nm) NPLs the size is twice larger and, therefore, the impact of confinement is smaller than the Coulomb interaction. These structures rather exhibit the characteristics of QWs. The experimentally observable difference in the optical properties that occurs between the smaller 4 ML and the larger 5 ML NPLs may, therefore, be explained by the stronger confinement which is predominant in QD structures.

Since the 4 ML NPLs display rather strict optical selection rules, the SFRS process will be retraced in the following on their example. As has been experimentally shown, the SFs are predominantly observed in the co-circular polarization configurations (σ^+,σ^+) and (σ^-,σ^-). This means that the polarization of the incident light is equal to that of the scattered light. Hence, the electron and hole have the same spin orientation before and after the spin-flip process, implying that the electron or hole have to reverse their spin orientation either twice or not at all. It is important to note that there are two prevailing assumption at the moment on how this SFRS process may be established. These will be briefly illustrated below and subsequently compared with the experimental results.

In the case of an interaction in which the spin orientation of the electron has to be reversed twice an at least fourth-order SF process has to be proposed. This is explainable, if an interaction with electrons at a neighboring impurity site and/or with dangling bond spins is considered. However, unlike diluted magnetic semiconductors, the studied CdSe NCs do not contain any magnetic impurities.[337,340,345] Thus, the SFRS process could proceed as follows. After photo excitation, e.g. by circularly polarized light (σ^+), the electron and heavy-hole of the exciton ($|\Uparrow\downarrow\rangle$) become spin polarized along the crystal direction c. Now, due to interaction with an acoustic phonon a single spin-flip of the electron occurs leading to a intermediate dark exciton state ($|\Uparrow\uparrow\rangle$) whose optical annihilation is forbidden in the electric dipole approximation. The

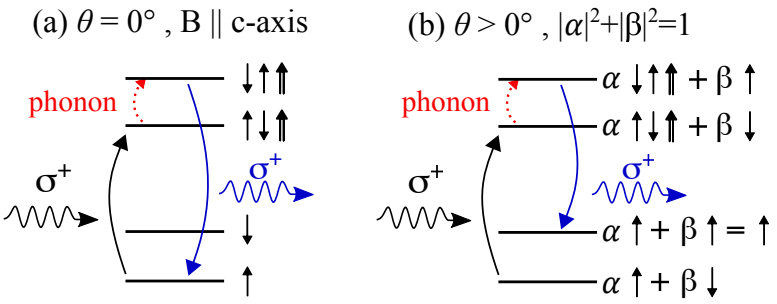

Figure 8.13: Model schemes of electric dipole allowed SFRS anti-Stokes-processes in a negative trion for Faraday (a) and tilted magnetic field geometries (b). The tilting of the magnetic field direction $\vec{B}$ with respect to the c-axis leads to a mixing of the electron states and hole states, thus, allowing single spin-flip Raman processes. In this regard, the mixing coefficients α and β depend on the tilting angle θ between $\vec{B}$ and c-axis. The resonant excitation is σ^+ polarized. In the negative trion the electron spin is scattered due to isotropic flip-flop exchange interaction between the resident and the exciton bound electron. The frequency shift between incident and scattered photon which defines the Raman shift on the anti-Stokes side is greater zero ($\omega_{\mathrm{in}} - \omega_{\mathrm{out}} > 0$) only for tilted geometries .

subsequent interaction with dangling bond spins or electrons at a neighboring impurity sides, e.g. electrons in neighboring NPLs, based on a spin flip-flop virtual transition reverses the spin of the electron back to the initial state. This process is described in the frame of the magnetic polaron formation in Sec. 8.1.4 and is schematically illustrated in Fig. 8.3. After this exchange interaction, the exciton, i.e. electron and hole pairs, annihilate and emit polarized light equal to the incident. In this Raman scattering process the energy of the exciton decreases (increases) by the amount of energy needed for a single dangling bond or impurity-electron spin-flip to be triggered. The shift in energy between the incident and emitted photon is given by the Zeeman equation: $\Delta E = \mu_{\mathrm{B}} g_{\mathrm{DBS}} B$, where g_{DBS} is the gyromagnetic ratio for the dangling bond or impurity-electron.

This SFRS model bases primarily on the exchange interaction between the electron and the DBSs. Hence, the Raman shift is defined by the DBS g factor, which shall not depend on the thickness of the NPLs, i.e. the size of the energy band-gap, since it is independent of the QW structure. However, this is in contradiction with the experimental observations, which have highlighted that the g factor is inverse proportional to the NPL thickness (see Sec. 8.2.1). Moreover, implying that DBSs are the main constituent, the SFRS intensity shall decrease for low temperatures, since each spin flip-flop virtual transition to the bright exciton shall result in a DBS dynamic polarization which in turn leads to the formation of a DBMP.[340,345,369] A decrease of the SFRS intensity for low T is not monitored.

Another approach to explain the mechanism is by SFRS of resident electron spins. This implies the formation of negative trions, i.e. the optically excited exciton state is bound to a resident electron in the NPL, as suggested by E. N. Economou et al. in a previous publication on multiple SFRS in CdS semiconductors.[339] The SFRS mechanism is shown schematically in Fig. 8.13 (a). For resonant excitation of a negative singlet trion with circularly polarized light (σ^+) the resident electron will occupy the spin-up and the photo-electron the spin-down state. The trion state with the total angular momentum projection $L = +3/2$ can be then expressed by $|+3/2, -1/2, +1/2\rangle = |\Uparrow\downarrow\uparrow\rangle$. Since in this spin configuration a single spin-flip of the electron is forbidden by Pauli exclusion principle, only an isotropic flip-flop exchange interaction between the resident and exciton electron may occur. However, this interaction would not alter the spin configuration of the trion. Therefore, in Faraday geometry an electron spin-flip will not be experimentally observable. The situation changes for magnetic field directions tilted with respect to the c-axis, and, thus, leading to a mixing of the electron and hole states, as it is described in Sec. 4.1. According to Eq. (4.2), in a tilted magnetic field, the spin state of the resident electron can be written as $\alpha\,|\uparrow\rangle \pm \beta\,|\downarrow\rangle$ with the mixing coefficients α and β. The SFRS mechanism is presented schematically in Fig. 8.13 (b). Assuming a circularly polarized excitation (σ^+) only one component in the superposition state can be excited to a trion resulting in $\alpha\,|\Uparrow\downarrow\uparrow\rangle + \beta\,|\downarrow\rangle$. Hereafter, an electron spin-flip in the second component may occur mediated by isotropic exchange interaction between the resident electron and the photo-excited electron. The intermediate state can be written as $\alpha\,|\Uparrow\uparrow\downarrow\rangle + \beta\,|\uparrow\rangle$. When the hole spin has remained unaffected during this scattering process, annihilation of the exciton yields the emission of a photon with obviously the same polarization as the incident. As a result, the resident spin has become oriented ($|\uparrow\rangle$). In this Raman scattering process the energy between the incident and emitted photon is given by $\Delta E = \mu_\mathrm{B} g_\mathrm{e} B$ with g_e describing the electron g factor. The transition amplitude depends on the projection of the resident electron spin state on the c-axis and, thus, the intensity exhibits an angular dependence of the form $\propto \sin^2(\theta)$.

The experimental observations pertaining the 4 ML NPLs are in good agreement with the later proposed SFRS model. For instance, the angular dependence has highlighted that the electron spin-flip Raman line which is predominant in the co-circular polarization is very weak in Faraday geometry but becomes stronger, when the magnetic field is tilted into Voigt geometry. As explained above, the tilting of the magnetic field direction with respect to the c-axis leads to a mixing of the electron and hole states and, therefore, the exchange efficiency between the resident and photogenerated electrons increases. The proposed SFRS is moreover underlined by the two-beam SFRS experiment which has shown that the scattering intensity is influenced by the number of additional resident electrons provided by additional above-barrier illumination. In regard of the temperature dependence of the e-SFRS, it is shown that the spin-flip scattering intensity decreases steadily with rising temperature. This may be explained by the thermally induced dissociation of the trions and the pure trion dephasing suppressing the e-SFRS. Furthermore, the lifetime of a trion in a specific spin state is expected to shorten with increasing temperature due to additional scattering.

After elaboration of the SFRS mechanism of the first order electron spin-flip, next the focus is set on the double spin-flip process. In contrast to the single spin-flip transition, the experimentally observed double spin-flips involve a spin interaction of the trion in the intermediate scattering process with either a second resident electron inside the same NPL or with an electron at a neighboring impurity site, e.g. a neighboring NPL. This interaction between the second electron and the photogenerated electron is mediated by exchange coupling. In order for this process to be possible the exciton wave function has to overlap with the resident electrons. In the case of a second electron inside the same NPL the exciton wave function overlap is obviously given. Considering electrons in neighboring NPLs the seperation distance plays a crucial role. Since the dimensions of an NPL are in the nm range, the overlapping of the wave functions is possible for two adjacent platelets. Especially in the case of stacked NPLs the approximate distance amounts less then 1 nm. Obviously the trion in the intermediate scattering process can couple to more than just one additional resident electron and, thus, give rise to even higher-order spin-flip processes. However, in the investigation of SFRS in CdSe NPLs it is not possible to see more than two spin-flips on the Stokes or anti-Stokes side.

The multi spin-flip process can be described theoretically [339] in terms of the applied field B along the crystal axis direction by the spin-dependent part of the Hamiltonian:

$$B = -\sum_{ij} J_{ij}\vec{S}_i \cdot \vec{S}_j - g\mu_{\mathrm{B}}\vec{B}\sum_i \vec{S}_i. \tag{8.10}$$

Here, J describes the exchange interaction between spins in adjacent NPLs. One can derive from Eq. (8.10) that the energy difference corresponding to a single spin-flip process is given by

$$\Delta E_1 = g\mu_{\mathrm{B}}B + J_{\mathrm{T}}. \tag{8.11}$$

In this context, $J_{\mathrm{T}} = \sum_{i\neq 1} J_{i1}$ denotes the total exchange interaction between the photogenerated and all adjacent spins. Thus, the energy difference involving spin-flips at two adjacent sites can be expressed by

$$\Delta E_2 = 2g\mu_{\mathrm{B}}B + \sum_{i\neq 1,2}(J_{i1} + J_{2i}) = 2\cdot\Delta E_1 - 2\,J_{12}. \tag{8.12}$$

This equation states that the shift of the second order SF must be twice as large as that of the first, reduced by the exchange interaction between the two involved spin states. Furthermore, this description indicates that the line broadening of both spin-flips should be due to the random distribution of both J_{T} and J_{12} approximately equal. By means of the Eq. (8.11) further the Raman scattering cross section for the first order scattering process can be evaluated. [31,339] Hence, it is expressed as follows:

$$\left(\frac{\mathrm{d}\sigma}{\mathrm{d}\Omega}\right)_1 \propto \frac{1}{(\hbar\omega_1 - \hbar\omega_0)^2}, \quad \Delta\hbar\omega = \Delta E_1. \tag{8.13}$$

In this context, ω_1 is the incoming light frequency and ω_0 denotes the frequency of the trion in the intermediate scattering process. The change of frequency due to scattering

is described by $\Delta\hbar\omega$. By means of standard perturbation theory, the Raman cross section for the second order spin-flip process can be calculated to:

$$\left(\frac{\mathrm{d}\sigma}{\mathrm{d}\Omega}\right)_2 \propto \frac{1}{(\hbar\omega_1 - \hbar\omega_0)^2} \cdot \frac{V^2}{(\hbar\omega_1 - \hbar\omega_0 - g\mu_\mathrm{B}B)^2}, \quad \Delta\hbar\omega = 2\,\Delta E_1 - 2\,J_{12}. \tag{8.14}$$

Here, V denotes the strength of the multi spin-flip process between the photogenerated exciton and electrons in nearby NPLs. The last equation obviously indicates that for resonant excitation of the trion ($\hbar\omega_1 = \hbar\omega_0$) the intensity of the second order SF line shall vary significantly, since it reveals a strong dependence on the external magnetic field.

Comparing these theoretical considerations with the experimental observations, one finds out, that most results can be modeled within the frame of the Eqs. (8.11) and (8.12). For instance, the analysis of the magnetic field dependence has highlighted that the Raman shift of the second order Raman line is almost exactly twice as large as the Raman shift of the first order electron spin-flip. In this regard, the experiments have yielded Landé factors in Faraday geometry pertaining the 5 ML NPLs of $g_1^{\parallel} = (1.623 \pm 0.002)$ and $g_2^{\parallel} = (3.242 \pm 0.002)$. Accordingly, the total exchange interaction J_{12} equals (0.1 ± 0.1) μeV/T. This value indicates that the interaction between spins of two adjacent platelets is negligible. However, a different result is obtained in regard of the 4 ML NPLs in which the g factor of the first order Raman line revealed a slight anisotropy. Here, the g factors in Faraday geometry equal $g_1^{\parallel} = (1.53 \pm 0.02)$ and $g_2^{\parallel} = (3.49 \pm 0.02)$. Hence, the exchange interaction J_{12} amounts (13 ± 1) μeV/T. The reason for this enhanced exchange interaction between two adjacent spins may be attributed to the smaller lateral size of the 4 ML NPLs in which the confinement potential restricts decisively the motion of electron and holes determining fully the shape of the wave function.

The theoretical calculations have further indicated that both the shape and width of the first and second order SF lines shall be comparable. This is observed and confirmed experimentally as described in Sec. 8.2. In this regard, it is shown that both SF lines have a gaussian shape with a FWHM of approximately (55 ± 10) μeV. Moreover, it is demonstrated that the shape is independent of the NPL properties, geometry, or magnetic field strength.

It is worth to note, that additional above-barrier illumination does not alter the frequency shift of the second order SF line. However, due to the optically induced increase in the resident electron concentration which facilitates the formation of negative trions, the electron-SFRS becomes more probable and in turn the SFRS intensity increases. However, this does not apply if the incident photon energy is not in resonance with the exciton.

8.4 Conclusion

The spin-flip Raman scattering of resident electrons is studied for resonant excitation of charged excitons in CdSe nanoplatelets. In this respect, the mechanism of the spin-flip scattering is discussed on the basis of its polarization properties as well as angular, temperature and magnetic field dependencies. Moreover, the influence of quantum confinement and electron spin state mixing in a tilted magnetic field geometry is elaborated. In order to theoretically describe the studied scattering processes different types of model schemes of scattering mechanisms are introduced and compared with the experimental results. The analysis revealed that at the exciton resonance an isotropic exchange interaction induces the electron spin-flip scattering. The scattering mechanism is based on isotropic exchange interaction between resident electrons and photo-excited electrons. As a result of the scattering process the resident electron spins become oriented.

In addition to the spin-flip of a single electron, higher order spin-flips are observed. The multiple spin-flip Raman scattering involves a spin interaction of the charged excitons with additional resident electrons localized in either the same NPL or in neighboring NPLs. This interaction is attributed to the exchange coupling and its strength depends on the overlap of the involved carrier wave functions. It is important to note at this point that acoustic phonons may also have an influence on this process, as evidenced by a large number of confined phonons in the Raman spectrum. Furthermore, the multiple spin-flip Raman scattering is very sensitive to the lattice temperature and seems to be present only in NPLs with small band-gap energy.

The longitudinal and transverse electron g factors of the first and second order spin-flips are determined. It is shown that the lateral size of NPLs as well as their thickness influences the g factor value and angular dependence. In the case of small lateral NPL dimensions, the electron g factor becomes anisotropic and the exchange interaction between two adjacent neighboring impurity spins enhances. Due to the random orientation of NPLs on the substrate surface the selection rules for electric dipole transitions are disturbed and, therefore, electron spin-flip Raman scattering can be monitored also in Faraday geometry. The application of additional above-barrier illumination enhances the efficiency of electron spin-flip scattering by increasing the resident electron concentration.

Symbols and abbreviations

Symbol	Meaning
$\hat{a}, \hat{a}^\dagger$	Annihilation and creation operators for an electron
a_B	Bohr radius
a	Lattice constant
Å	Ångström (unit), 1 Å = 0.1 nm
a_t	Lattice constant of ternary materials
AFM	Atomic force microscopy
As	Arsenic
a.u.	Arbitrary units
$\hat{b}, \hat{b}^\dagger$	Annihilation and creation operators for a phonon
$\vec{B}$	Magnetic field vector
B_N	Nuclear hyperfine field
$\mathfrak{B}_J(x)$	Brillouin-function
c	Speed of light in vacuum, 2.9979×10^8 m/s
$\hat{c}, \hat{c}^\dagger$	Annihilation and creation operators for a photon
CB	Conduction band
CCD	Charge-coupled device
Cd	Cadmium
cm^{-1}	Inverse centimeter (unit), 1 $\mathrm{cm}^{-1} \approx 123.9841$ μeV
cps	Counts per second
CW	Continuous wave
CZ	Czerny-Turner
$D_{e,h}$	Deformation potential constant
$\Delta_\text{hh-lh}$	Splitting between heavy-hole and light-hole band
Δ_SO	Split-off energy

Symbol	Meaning
Δ_{sf}	Splitting between heavy-hole and light-hole band
Δ_{Z}	Zeeman splitting of the spin sublevels
Δ_{Zeeman}	Giant Zeeman splitting
ΔE_{OS}	Overhauser shift
$D_{\mathrm{0D}}(E)$	Density of states in a quantum dot
$D_{\mathrm{1D}}(E)$	Density of states in a quantum wire
$D_{\mathrm{2D}}(E)$	Density of states in a quantum well
$D_{\mathrm{3D}}(E)$	Density of states in a bulk semiconductor
DFT	Density functional theory
DMS	Dilute magnetic semiconductor
DOS	Density of states
det	Detection
e	Electron
e	Elementary charge, 1.6022×10^{-19} C
$\vec{e}$	Polarization unit vector
E	Energy
E_{exchange}	Exchange energy
E_{F}	Fermi energy
E_{g}	Band gap energy
E_{γ}	Surface energies
$E_{\mathrm{n,l}}$	Fock-Darwin energy
E_{off}	Zero-field offset energy
E_{R}	Resonant excitation energy
E_{nR}	Nonresonant excitation energy
ν_{S}	Scattering efficiency
eV	Electron volt (unit), 1 eV = 1.6022×10^{-19} J
exc	Excitation
f	Focal length
$f_{n,k}$	Oscillator strength
FD	Fock-Darwin
FWHM	Full width at half maximum
g	Landé factor
g_0	Free electron Landé factor, $g_0 \approx 2.0023$
g_{e}	Electron Landé factor
Ga	Gallium
Γ-point	Center of the Brillouin zone at $\vec{k} = 0$
γ_i	Kohn-Luttinger Hamiltonian parameter (i = 1,2,3)

Symbol	**Meaning**
Γ_i	Irreducible representation (point group specific)
Γ_{rad}	Radiative decay rate
Γ_{ET}	Total energy transfer rate
GTP	Glan-Thompson prism
h	Hole
$\hbar$	Reduced Planck constant, $\hbar = \frac{h}{2\pi} \approx 6.5821 \times 10^{-16}$ eVs
$\hbar\omega_0$	Lateral confinement energy
hh	Heavy-hole
$\hat{H}$	Hamiltonian
$\hat{H}_0$	Unperturbed Hamiltonian
$\hat{H}_{\mathrm{DM}}$	Dzyaloshinsky-Moriya exchange Hamiltonian
$\hat{H}_{\text{e-R}}$	Electron-radiation interaction Hamiltonian
$\hat{H}_{\text{e-ph}}$	Electron-hole-lattice interaction Hamiltonian
H_{exchange}	Spin Hamiltonian describing the electron-hole exchange interaction
$\hat{H}_{sp\text{-}d}$	*sp-d* exchange Hamiltonian
$\hat{H}_{\mathrm{SO}}$	Spin orbit interaction Hamiltonian
$\hat{H}_{\mathrm{T}}$	Total Hamiltonian
$\hat{H}_{\mathrm{Z}}$	Zeeman Hamiltonian
I^-; I^+	σ^+, σ^+ polarized PL intensity
In	Indium
I_{RS}	Scattering intensity
J	Total angular momentum (J=L+s)
K	Kelvin (unit)
$\vec{k}$	Wave vector
k_{B}	Boltzmann constant, 8.6173×10^{-5} eV/K
κ	Orientational average of dipoles
l	Orbital angular momentum quantum number
L	Orbital angular momentum
λ	Wavelength
λ_{B}	De Broglie wavelength
$\mathrm{L}^{\lvert l\rvert}_{n+\lvert l\rvert}(\xi)$	Laguerre polynomials
LDA	Local density approximation
lh	Light-hole
$\bigtriangledown$	Laplacian operator

Symbol	Meaning
$\vec{M}$	Magnetization vector
m_0	Free electron mass, 9.1094×10^{-31} kg
m^*	Effective mass
m_{e}^*; m_{hh}^*; m_{lh}^*	Effective mass of electron, heavy-hole and light-hole
m_v; m_c	Effective masses of the valence and conduction band
m_J	Total angular momentum quantum numbers
M_{if}	Scattering matrix between initial and final states
MBE	Molecular beam epitaxy
Mg	Magnesium
Mn	Manganesse
N	Nitrogen
n	Radial quantum number
ν	Refractive index
N_{A}	Numerical aperture
N_f	f-number
NC	Nanocrystal
NPL	Nanoplatelet
NSP	Nuclear spin polarization
ω	Frequncy
Ω	Frequency of an elementary excitation (e.g. phonon)
ω	Cyclotron frequncy
ω_i	Frequency of an incident photon
P	Laser power (density)
$\vec{p}$	Momentum operator
PL	Photoluminescence
PMT	Photomultiplier tube
ψ	Wave function
$\vec{r}$	Position vector in Cartesian coordinates x,y,z
R	Quantum dot radius
ρ	Radial coordinate
μ_r	Relative permeability
RKKY	Ruderman-Kittel-Kasuya-Yosida (interaction)
$R_{n,l}(\rho)$	Radial wave function
S	Sulfur
s; s_z	Spin quantum number; its projection along z-axis
S_{eff}	Effective spin

Symbol	**Meaning**
σ_α	Pauli spin matrix ($\alpha = x,y,z$)
σ^+; σ^-	Left-handed, right-handed circular polarization
Se	Selenium
SHG	Second harmonic generation
SFRS	Spin-flip Raman scattering
t	Time
T^-; T^+	Positive trion, negative trion
T	Temperature
T_0	Antiferromagnetic temperature
Te	Tellurium
θ	Angle between magnetic field and growth axis
$u_{n,\vec{k}}(\vec{r})$	Bloch-wavefunctions
μ_B	Bohr magneton, 5.7884×10^{-5} eV/T
$\vec{q}$	Wave vector of an elementary excitation
QD	Quantum dot
QW	Quantum well
V	Volume, or potential (with index)
ϑ	Solid angle
VB	Valance band
VTI	Variable temperature insert
WL	Wetting layer
w_{if}	Scattering rate between initial and final states
x	Mn concentration
X^-; X^+	Negatively charged exciton, positively charged exciton
χ_s	Spin part of the electron wave function
$\hat{\chi}_m$	Magnetic susceptibility
$\hat{\chi}_\mathrm{Dia}$	Magnetic susceptibility in diamagnets
$\hat{\chi}_\mathrm{Para}$	Magnetic susceptibility in paramagnets
Zn	Zinc
ζ	Scattering cross section

List of Figures

List of Tables

Bibliography

[1] J. E. Lilienfield, *Method and apparatus for controlling electric current*, U.S. Patent 1745175 Canada (1925).

[2] M. A. Nielson and I. L. Chuang, *Quantum Computation and Quantum Information*, University Press, Cambridge, U.K. (2000).

[3] F. Giannazzo, G. Grecco, F. Roccaforte, and S. S. Sonde, *Vertical Transistors Based on 2D Materials: Status and Prospects*, Crystals **8** (2018).

[4] G. E. Moore, *Progress in digital integrated electronics*, IEEE Int. Electron Devices Meeting **21**, 11 (1975).

[5] C. D. M. Donegá, ed., *Nanoparticles: Workhorses of Nanoscience*, Springer-Verlag Berlin Heidelberg (2014).

[6] W. Gerlach and O. Stern, *Über die Richtungsquantelung im Magnetfeld*, Annalen der Physik **379**, 673 (1924).

[7] W. König, *Beobachtung des Zeeman'schen Phänomens*, Annalen der Physik **298**, 240 (1987).

[8] P. A. M. Dirac, *The quantum theory of the electron*, Proc. R. Soc. A **117**, 610 (1928).

[9] W. Pauli, *The Connection Between Spin and Statistics*, Phys. Rev. **58**, 716 (1940).

[10] G. E. Uhlenbeck, *FIFTY YEARS OF SPIN: Personal reminiscences*, Physics Today (American Institute of Physics) **29**, 43 (1976).

[11] K. Takanashi, *Fundamentals of Magnetoresistance Effects*, in *Spintronics for Next Generation Innovative Devices*, edited by K. Sato and E. Saitoh, chap. 1, Wiley & Sons Ltd (2016).

[12] G. Binasch, P. Grünberg, F. Saurenbach, and W. Zinn, *Enhanced magnetoresistance in layered magnetic structures with antiferromagnetic interlayer exchange*, Phys. Rev. B **39**, 4828 (1989).

[13] S. Datta and B. Das, *Electronic analog of the electro-optic modulator*, Appl. Phys. Lett. **56**, 665 (1990).

[14] A. S. Sheremet, O. V. Kibis, A. V. Kavokin, and I. A. Shelykh, *Datta-and-Das spin transistor controlled by a high-frequency electromagnetic field*, Phys. Rev. B **93**, 165307 (2016).

[15] L. L. Chang, L. Esaki, and R. Tsu, *Resonant tunneling in semiconductor double barriers*, Appl. Phys. Lett. **24**, 593 (1974).

[16] R. Dingle, W. Wiegmann, and C. H. Henry, *Quantum States of Confined Carriers in Very Thin $Al_xGa_{1-x}As$-GaAs-$Al_xGa_{1-x}As$ Heterostructures*, Phys. Rev. Lett. **33**, 827 (1974).

[17] E. L. Ivchenko, *Optical Spectroscopy of Semiconductor Nanostructures*, Alpha Science International Ltd., Harrow (2005).

[18] R. C. Temple, M. McLaren, R. M. D. Brydson, B. J. Hickey, and C. H. Marrows, *Long spin lifetime and large barrier polarisation in single electron transport through a CoFe nanoparticle*, Sci. Rep. **6** (2016).

[19] Y.Yamamoto, *Optically Controlled Semiconductor Spin Qubits and Indistinguishable Single Photons for Quantum Information Processing*, in *Comprehensive Semiconductor Science and Technology*, vol. 2, p. 400, Elsevier (2011).

[20] Y.Hirayama, *Contact Hyperfine Interactions in Semiconductor Heterostructures*, in *Comprehensive Semiconductor Science and Technology*, vol. 2, p. 68, Elsevier (2011).

[21] J. Debus, D. Kudlacik, V. F. Sapega, D. Dunker, P. Bohn, F. Paßmann, D. Braukmann, J. Rautert, D. R. Yakovlev, D. Reuter, A. D. Wieck, and M. Bayer, *Nuclear spin polarization in the electron spin-flip Raman scattering of singly charged (In,Ga)As/GaAs quantum dots*, Phys. Rev. B **92**, 195421 (2015).

[22] T. Östreich, K. Schönhammer, and L. J. Sham, *Theory of Spin Beatings in the Faraday Rotation of Semiconductors*, Phys. Rev. Lett. **75**, 2554 (1995).

[23] R. Fiederling, M. Keim, G. Reuscher, W. Ossau, G. Schmidt, A. Waag, and L. W. Molenkamp, *Injection and detection of a spin-polarized current in a light-emitting diode*, Nature **402**, 787 (1999).

[24] K. V. Kavokin and I. A. Merkulov, *Multispin Raman paramagnetic resonance: Quantum dynamics of classically large angular momenta*, Phys. Rev. B **55**, R7371(R) (1997).

[25] K. V. Kavokin, *Coherent dynamics of localized spins coupled with a twodimensional hole gas in diluted-magnetic quantum wells*, Phys. Rev. B **59**, 9822 (1999).

[26] D. Loss and D. P. DiVincenzo, *Quantum computation with quantum dots*, Phys. Rev. A **57**, 120 (1998).

[27] m. Oestreich, J. Hübner, D. Hägele, P. J. Klar, W. Heimbrodt, and W. W. Rühle, *Spin injection into semiconductors*, Appl. Phys. Lett. **74**, 1251 (1999).

[28] J. Gaj, R. Galazka, and M. Nawrocki, *Giant exciton Faraday rotation in $Cd_{1-x}Mn_xTe$ mixed crystals*, Sol. Stat. Commun. **25**, 193 (1978).

[29] B. König, I. A. Merkulov, D. R. Yakovlev, W. Ossau, S. M. Ryabchenko, M. Kutrowski, T. Wojtowicz, G. Karczewski, and J. Kossut, *Energy transfer from photocarriers into the magnetic ion system mediated by a two-dimensional electron gas in (Cd,Mn)Te/(Cd,Mg)Te quantum wells*, Phys. Rev. B **61**, 16870 (2000).

[30] D. Keller, D. R. Yakovlev, B. König, W. Ossau, T. Gruber, A. Waag, and L. W. Molenkamp, *Heating of the magnetic ion system in (Zn,Mn)Se/(Zn, Be)Se semimagnetic quantum wells by means of photoexcitation*, Phys. Rev. B **65**, 035313 (2001).

[31] D. G. Thomas and J. J. Hopfield, *Spin-Flip Raman Scattering in Cadmium Sulfide*, Phys. Rev. **175**, 1021 (1968).

[32] A. V. Koudinov, Y. G. Kusrayev, D. Wolverson, L. C. Smith, J. J. Davies, G. Karczewski, and T. Wojtowicz, *Giant modulation of resonance Raman scattering from (Cd,Mn)Te quantum wells by secondary illumination*, Phys. Rev. B **79**, 241310(R) (2009).

[33] J. Debus, D. Dunker, V. F. Sapega, D. R. Yakovlev, G. Karczewski, T. Wojtowicz, J. Kossut, and M. Bayer, *Spin-flip Raman scattering of the neutral and charged excitons confined in a CdTe/(Cd,Mg)Te quantum well*, Phys. Rev. B **87**, 205316 (2013).

[34] V. F. Sapega, T. Ruf, M. Cardona, K. Ploog, E. L. Ivchenko, and D. N. Mirlin, *Resonant Raman scattering due to bound-carrier spin flip in $GaAs/Al_xGa_{1-x}As$ quantum wells*, Phys. Rev. B **50**, 2510 (1994).

[35] A. A. Sirenko, V. I. Belitsky, T. Ruf, M. Cardona, A. I. Ekimov, and C. Trallero-Giner, *Spin-flip and acoustic-phonon Raman scattering in CdS nanocrystals*, Phys. Rev. B **58**, 2077 (1998).

[36] J. Debus, T. S. Shamirzaev, D. Dunker, V. F. Sapega, E. L. Ivchenko, D. R. Yakovlev, A. I. Toropov, and M. Bayer, *Spin-flip Raman scattering of the Γ-X mixed exciton in indirect band gap (In,Al)As/AlAs quantum dots*, Phys. Rev. B **90**, 125431 (2014).

[37] T. G. Spiro, *Biological applications of resonance Raman spectroscopy: haem proteins*, Proc. R. Soc. A **345**, 1 (1975).

[38] Q. Jin, M. Li, B. Polat, S. K. Paidi, A. Dai, A. Zhang, J. V. Pagaduan, I. Barman, and D. H. Gracias, *Frontispiz: Mechanical Trap Surface-Enhanced Raman Spectroscopy for Three-Dimensional Surface Molecular Imaging of Single Live Cells*, Angewandte Chemie **129**, 3880 (2017).

[39] M. I. Dyakonov, ed., *Spin Physics in Semiconductors*, vol. 157, Springer Berlin Heidelberg (2008).

[40] D. Bimberg and U. W. Pohl, *Quantum dots: promises and accomplishments*, Mater. Today **14**, 388 (2011).

[41] F. Garcia-Santamaria, Y. Chen, J. Vela, R. D. Schaller, J. A. Hollingsworth, and V. I. Klimov, *Suppressed Auger recombination in "giant" nanocrystals boosts optical gain performance*, Nano Lett. **9**, 3482 (2009).

[42] G. Konstantatos and E. H. Sargent, *Colloidal quantum dot optoelectronics and photovoltaics*, Cambridge University Press, Cambridge (2013).

[43] Y. Shirasaki, G. J. Supran, M. G. Bawendi, and V. Bulovic, *Emergence of colloidal quantum-dot light-emitting technologies*, Nat. Photon. **7**, 13 (2013).

[44] T. L. Doane and C. Burda, *The unique role of nanoparticles in nanomedicine: Imaging, drug delivery and therapy*, Chem. Soc. Rev. **41**, 2885 (2012).

[45] T. O'Connor, M. S. Panov, A. Mereshchenko, A. N. Tarnovsky, R. Lorek, D. Perera, G. Diederich, S. Lambright, P. Moroz, and M. Zamkov, *The effect of the charge-separating interface on exciton dynamics in photocatalytic colloidal heteronanocrystals*, ASC Nano **6**, 8156 (2012).

[46] E. H. Sargent, *Colloidal quantum dot solar cells*, Nat. Photon. **6**, 133 (2012).

[47] C. Javaux, B. Mahler, B. Dubertret, A. Shabaev, A. V. Rodina, A. L. Efros, D. R. Yakovlev, F. Liu, M. Bayer, G. Camps, L. Biadala, S. Buil, X. Quelin, and J.-P. Hermier, *Altmetric: 4Citations: 98More detail Article Thermal activation of non-radiative Auger recombination in charged colloidal nanocrystals*, Nature nanotchnology **8**, 206 (2013).

[48] B. Siebers, *Spectroscopy of excitons in CdSe/CdS colloidal nanocrystals*, Ph.D. thesis, TU Dortmund (2015).

[49] J. Debus, *Spin-flip Raman scattering in low-dimensional semiconductors*, Ph.D. thesis, TU Dortmund (2012).

[50] O. Gywat, H. Krenner, and J. Berezovsky, eds., *Spins in Optically Active Quantum Dots: Concepts and Methods*, Wiley-Vch, Weinheim (2010).

[51] D. Bimberg, ed., *Semiconductor Nanostructures*, Springer-Verlag Berlin Heidelberg (2008).

[52] C. Buss, R. Pankoke, P. Leisching, J. Cibert, R. Frey, and C. Flytzanis, *Giant Photoinduced Excitonic Faraday Rotation in CdTe/$Cd_{1-x}Mn_x$Te Multiple Quantum Wells*, Phys. Rev. Lett. **78**, 4123 (1997).

[53] C. Kittel, *Einführung in die Festkörperphysik*, 13th edn., Oldenbourg Wissenschaftsverlag, München (2002).

[54] S. V. Gaponenko, *Introduction to Nanophotonics*, Cambridge University Press, Cambridge (2010).

[55] M. A. Lampert, *Mobile and Immobile Effective-Mass-Particle Complexes in Nonmetallic Solids*, Phys. Rev. Lett. **1**, 450 (1958).

[56] G. Finkelstein, H. Shtrikman, and I. Bar-Joseph, *Negatively and positively charged excitons in GaAs/$Al_xGa_{1-x}As$ quantum wells*, Phys. Rev. B **53**, R1709 (1995).

[57] J. Frenkel, *On the Transformation of light into Heat in Solids. I*, Phys. Rev. **37**, 17 (1931).

[58] M. Hayashi and K. Katsuki, *Absorption spectrum of cuprous oxide*, J. Phys. Soc. Japan **5**, 380 (1950).

[59] G. H. Wannier, *The Structure of Electronic Excitation Levels in Insulating Crystals*, Phys. Rev. **52**, 191 (1937).

[60] G. V. Astakhov, D. R. Yakovlev, V. P. Kochereshko, W. Ossau, J. Nürnberger, W. Faschinger, and G. Landwehr, *Charged excitons in ZnSe-based quantum wells*, Phys. Rev. B **60**, R8485 (1999).

[61] P. A. Fleury and J. F. Scott, *Spin-Flip Raman Scattering from Conduction Electrons in CdS and ZnSe*, Phys. Rev. B **3**, 1979 (1971).

[62] F. Schwabl, *Quantum Mechanics*, vol. 4, Springer-Verlag Berlin Heidelberg (2007).

[63] D. B. Williams and C. B. Carter, *Bloch Waves*, in *Transmission Electron Microscopy*, Springer, Boston, MA (2009).

[64] F. Meier and B. Zakharchenya, eds., *Optical Orientation*, 1st edn., North Holland (1984).

[65] J. E. Bernard and A. Zunger, *Electronic structure of ZnS, ZnSe, ZnTe, and their pseudobinary alloys*, Phys. Rev. B **36**, 3199 (1987).

[66] C. S. Wang and B. M. Klein, *First-principles electronic structure of Si, Ge, GaP, GaAs, ZnS, and ZnSe. I. Self-consistent energy bands, charge densities, and effective masses*, Phys. Rev. B **24**, 3393 (1981).

[67] C. F. Klingshirn, *Semiconductor Optics*, 4th edn., Springer, Berlin (2012).

[68] E. O. Kane, *Energy band structure in p-type germanium and silicon*, J. Chem. Phys. Solids **1** (1956).

[69] P. Y. Yu and M. Cardona, *Fundamentals of Semiconductors: Physics and Materials Properties*, 4th edn., Springer, Heidelberg/ Dordrecht/London/New York (2010).

[70] H. W. Streitwolf, *Gruppentheorie in der Festkörperphysik*, Akademische Verlagsgesellschaft Geest & Portig K.G., Leipzig (1967).

[71] P. Bassani and G. P. Parravicini, *Electron States and Optical Transitions in Solids (Science of Solid State Monographs)*, Pergamon Press (1975).

[72] P. A. M. Dirac, *On the Theory of Quantum Mechanics*, in *Proceedings of the Royal Society of London A: Mathematical, Physical and Engineering Sciences*, 112.762, p. 661 (1926).

[73] S. Schulz, *Electronic and Optical Properties of Quantum Dots: A Tight-Binding Approach*, Ph.D. thesis, University of Bremen (2007).

[74] A. A. Lipovskii, E. V. Kolobkova, and V. D. Petrikov, *Effect of spin-orbit splitting on electron-hole transitions in microscopic CdS and CdTe crystals*, Phys. Sol. State **40**, 794 (1998).

[75] *A Dictionary of Physics*, 6th edn., Oxford University Press (2009).

[76] A. G. Thompson, M. Cardona, K. L. Shaklee, and J. C. Woolley, *Electroreflectance in the GaAs-GaP*, Alloys. Phys. Rev. **146**, 601 (1966).

[77] M. A. Kastner, *Artificial Atoms*, Phys. Today **46**, 24 (1993).

[78] M. A. Reed, *Quantum Dots*, Sci. Am. **268**, 118 (1993).

[79] K. K. Likharev and T. Claeson, *Single electronics*, Sci. Am. **266**, 80 (1992).

[80] V. Vijayakrishnan, A. Chainani, D. D. Sarma, and C. N. R. Rao, *Metal-Insulator Transitions in Metal Clusters: A High-Energy Spectroscopy Study of Pd and Ag Clusters*, J. Phys. Chem. **96**, 8679 (1992).

[81] P. A. Sabatier, *Top-down and Bottom-up Approaches to Implementation Research: A Critical Analysis and Suggested Synthesis*, Jnl. Publ. Pol. **6**, 21 (1986).

[82] R. G. Hobbs, N. Petkov, and J. D. Holmes, *Semiconductor Nanowire Fabrication by Bottom-Up and Top-Down Paradigms*, Chem. Mater. **24**, 1975 (2012).

[83] H. Dislich and E. Hussmann, *Amorphous and crystalline dip coatings obtained from organometallic solutions: Procedures, chemical processes and products*, Thin Solid Films **77**, 129 (1981).

[84] M. A. Herman and H. Sitter, *Molecular Beam Epitaxy*, Springer-Verlag Berlin Heidelberg/ New York (1989).

[85] A. Y. Cho and J. R. Arthur, *Molecular Beam Epitaxy*, Prog. Solid State Chem. **10**, 157 (1975).

[86] R. Murri, ed., *Silicon Based Thin Film Solar Cells*, Bentham e Books (2013).

[87] V. A. Shchukin, N. N. Ledentsov, and D. Bimberg, *Epitaxy of nanostructures*, Springer-Verlag Berlin Heidelberg (2004).

[88] T. Schmidt and E. Bauer, *Interfactant-mediated quasi-Frank–van der Merwe growth of Pb on Si(111)*, Phys. Rev. B **62**, 15815 (2000).

[89] L. Benning and G. Waychunas, *Nucleation, Growth, and Aggregation of Mineral Phases: Mechanisms and Kinetic Controls*, in *Kinetics of Water-Rock Interaction*, edited by S. Brantley, J. Kubicki, and A. White, p. 259, Springer, New York, NY (2008).

[90] P. Harrison and A. Valavanis, *Quantum Wells, Wires and Dots: Theoretical and Computational Physics of Semiconductor Nanostructures*, 4th edn., John Wiley & Sons, Ltd (2016).

[91] I. N. Stranski and L. Krastanow, *Zur Theorie der orientierten Ausscheidung von Ionenkristallen aufeinander*, Akademie der Wissenschaften Wien Klasse IIb **146**, 797 (1938).

[92] M. Grundmann, J. Christen, N. N. Ledentsov, J. Böhrer, D. Bimberg, S. S. Ruvimov, P. Werner, U. Richter, U. Gösele, J. Heydenreich, V. M. Ustinov, A. Y. Egorov, A. E. Zhukov, P. S. Kop'ev, and Z. I. Alferov, *Ultranarrow Luminescence Lines from Single Quantum Dots*, Phys. Rev. Lett. **74**, 4043 (1995).

[93] J. M. Moison, F. Houzay, F. Barthe, and L. Leprince, *Self-organized growth of regular nanometer-scale InAs dots on GaAs*, Appl. Phys. Lett. **64**, 196 (1994).

[94] D. Leonard, K. Pond, and P. M. Petroff, *Critical layer thickness for self-assembled InAs islands on GaAs*, Phys. Rev. B **50**, 11687 (1994).

[95] N. Liu, J. Tersoff, O. Baklenov, A. L. H. Jr., and C. K. Shih, *Nonuniform Composition Profile in $In_{0.5}Ga_{0.5}As$ Alloy Quantum Dots*, Phys. Rev. Lett. **84**, 334 (2000).

[96] M. Fox, *Optical Properties of Solids*, Oxford Master Series in Physics, 2nd edn., Oxford University Press, Oxford/New York (2010).

[97] F. M. Peeters and O. Hipólito, *Low Dimensional Semiconductors Structures*, Brazilian J. Phys. **22**, 183 (1992).

[98] M. Sachs, *Solid State Theory*, McGraw-Hill Book Company, New York (1963).

[99] D. Bohm, *Quantum Theory*, Dover Publications, New York (1951).

[100] H. Haug and S. W. Koch, *Quantum Theory of the Optical and Electronic Properties of Semiconductors*, 5th edn., World Scientific (2009).

[101] A. Rogalski, K. Adamiec, and J. Rutkowski, *Narrow-gap Semiconductor Photodiodes*, vol. 77, SPIE Press (2000).

[102] M. Sugawara, *Self-Assembled InGaAs/GaAs Quantum Dots. Semiconductors and Semimetals*, vol. 60, Academic Press Inc. (1999).

[103] A. D. Yoffe, *Low-dimensional systems: Quantum size effects and electronic properties of semiconductor microcrystallites (zero-dimensional systems) and some quasi-two-dimensional systems*, Adv. in Phys. **51:2**, 799 (2002).

[104] E. Berkowicz, D. Gershoni, G. Bahir, A. C. Abare, S. P. DenBaars, and L. A. Coldren, *Optical Spectroscopy of InGaN/GaN Quantum Wells*, Phys. Sol. State (b) **216**, 291 (1999).

[105] T. Grange, *Electron transport in quantum wire superlattices*, Phys. Rev. B **89**, 165310 (2014).

[106] V. A. Sablikov and B. S. Shchamkhalova, *Electron transport in a quantum wire with realistic Coulomb interaction*, Phys. Rev. B **58**, 13847 (1998).

[107] A. Wojs, P. Hawrylak, S. Fafard, and L. Jacak, *Electronic structure and magneto-optics of self-assembled quantum dots*, Phys. Rev. B **54**, 5604 (1996).

[108] O. Stier, M. Grundmann, and D. Bimberg, *Electronic and optical properties of strained quantum dots modeled by 8-band $k \cdot p$ theory*, Phys. Rev. B **59**, 5688 (1999).

[109] C. Pryor, *Eight-band calculations of strained InAs/GaAs quantum dots compared with one-, four-, and six-band approximations*, Phys. Rev. B **57**, 7190 (1998).

[110] D. Bimberg, M. Grundmann, and N. N. Ledentsov, *Quantum Dot Heterostructures*, Wiley & Sons Ltd, Chichester (1999).

[111] P. C. Sercel and K. J. Vahala, *Analytical formalism for determining quantum-wire and quantum-dot band structure in the multiband envelope-function approximation*, Phys. Rev. B **42**, 3690 (1990).

[112] M. Grundmann, O. Stier, and D. Bimberg, *InAs/GaAs pyramidal quantum dots: Strain distribution, optical phonons, and electronic structure*, Phys. Rev. B **52**, 11969 (1995).

[113] F. B. Pedersen and Y.-C. Chang, *Energy levels of one and two holes in parabolic quantum dots*, Phys. Rev. B **53**, 1507 (1996).

[114] T. K. Ng, *Generalized Hohenberg-Kohn theorem and effective Hamiltonian of a quantum system*, Phys. Rev. B **44**, 2407(R) (1991).

[115] P. Hohenberg and W. Kohn, *Inhomogeneous Electron Gas*, Phys. Rev. **136**, B864 (1964).

[116] F. M. Peeters, *Magneto-optics in parabolic quantum dots*, Phys. Rev. B **42**, 1486 (1990).

[117] L. Quiroga, D. R. Ardila, and N. F. Johnson, *Spatial correlation of quantum dot electrons in a magnetic field*, Sol. Stat. Commun. **86**, 775 (1993).

[118] A. P. Alivisatos, *Perspectives on the physical chemistry of semiconductor nanocrystals*, J. Phys. Chem. **100**, 13226 (1996).

[119] A. L. Efros and M. Rosen, *The electronic structure of semiconductor nanocrystals*, Annu. Rev. Mater. Sci. **30**, 475 (2000).

[120] Y. Wang and N. Herron, *Nanometer-sized semiconductor clusters: materials synthesis, quantum size effects, and photophysical properties*, J. Phys. Chem. **95**, 525 (1991).

[121] G. W. Bryant, *Excitons in quantum boxes: Correlation effects and quantum confinement*, Phys. Rev. B **37**, 8763 (1988).

[122] E. K. Zavoisky, *Relaxation of liquid solutions for perpendicular fields*, J. Phys. U.S.S.R. **9**, 211 (1945).

[123] G. K. Narula, K. S. Narula, and V. K. Gupta, *Materials Science*, Tata McGraw-Hill Education (1989).

[124] H. W. van Kesteren, E. C. Cosman, W. A. J. A. van der Poel, and C. T. Foxon, *Fine structure of excitons in type-II GaAs/AlAs quantum wells*, Phys. Rev. B **41**, 5283 (1990).

[125] E. Blackwood, M. J. Snelling, R. T. Harley, S. R. Andrews, and C. T. B. Foxon, *Exchange interaction of excitons in GaAs heterostructures*, Phys. Rev. B **50**, 14246 (1994).

[126] M. Bayer, O. Stern, A. Kuther, and A. Forchel, *Spectroscopic study of dark excitons in $In_xGa_{1-x}As$ self-assembled quantum dots by a magnetic-field-induced symmetry breaking*, Phys. Rev. B **61** (2000).

[127] V. V. Belykh, D. R. Yakovlev, J. J. Schindler, E. A. Zhukov, M. A. Semina, M. Yacob, J. P. Reithmaier, M. Benyoucef, and M. Bayer, *Large anisotropy of electron and hole g factors in infrared-emitting InAs/InAlGaAs self-assembled quantum dots*, Phys. Rev. B **93**, 125302 (2016).

[128] N. A. Bruce and P. A. Maksym, *Quantum states of interacting electrons in a real quantum dot*, Phys. Rev. B **61**, 4718 (1999).

[129] D. Pfannkuche and R. R. Gerhardts, *Quantum-dot helium: Effects of deviations from a parabolic confinement potential*, Phys. Rev. B **44**, 13132 (1991).

[130] P. A. Maksym and T. Chakraborty, *Quantum dots in a magnetic field: Role of electron-electron interactions*, Phys. Rev. Lett. **65**, 108 (1990).

[131] A. Babinski, M. Potemski, S. Raymond, J. Lapointe, and Z. R. Wasilewski, *Fock-Darwin spectrum of a single InAs/GaAs quantum dot*, Phys. Stat. Sol. (c) **3**, 3748 (2006).

[132] O. Voskoboynikov, C. P. Lee, and O. Tretyak, *Spin-orbit splitting in semiconductor quantum dots with a parabolic confinement potential*, Phys. Rev. B **63**, 165306 (2001).

[133] P. Hawrylak, *Excitonic artificial atoms: Engineering optical properties of quantum dots*, Phys. Rev. B **60**, 5597 (1999).

[134] P. A. Maksym, L. D. Hallam, and J. Weis, *Models of quantum dots*, Physica B **212**, 213 (1995).

[135] E. L. Ivchenko and G. E. Pikus, *Superlattices and Other Heterostructures*, Springer Berlin Heidelberg (1997).

[136] M. Bayer, G. Ortner, O. Stern, A. Kuther, A. A. Gorbunov, A. Forchel, P. Hawrylak, S. Fafard, K. H. andT. L. Reinecke, S. N. Walck, J. P. Reithmaier, F. Klopf, and F. Schäfer, *Fine structure of neutral and charged excitons in self-assembled In(Ga)As/(Al)GaAs quantum dots*, Phys. Rev. B **65**, 195315 (2002).

[137] W. Heisenberg, *Zur Theorie des Ferromagnetismus*, Zeitschrift für Physik A: Hadrons and Nuclei **49**, 619 (1928).

[138] J. Debus, V. F. Sapega, D. Dunker, D. R. Yakovlev, D. Reuter, A. D. Wieck, and M. Bayer, *Spin-flip Raman scattering of the resident electron in singly charged (In,Ga)As/GaAs quantum dot ensembles*, Phys. Rev. B **90**, 235404 (2014).

[139] J. Debus, D. Kudlacik, P. Waldkirch, V. F. Sapega, S. Scholz, A. Ludwig, A. D. Wieck, and M. Bayer, *Efficiency enhancement of the coherent electron spin-flip Raman scattering through thermal phonons in (In,Ga)As/GaAs quantum dots*, Phys. Rev. B **95**, 201303(R) (2017).

[140] A. L. Rogach, T. A. Klar, J. M. Lupton, A. Meijerink, and J. Feldmann, *Energy transfer with semiconductor nanocrystals*, J. Mater. Chem. **19**, 1208 (2009).

[141] T. Förster, *Energieumwandlung und Fluoreszenz*, Naturwissenschaften **33**, 166 (1946).

[142] H. Kett, W. Gebhardt, U. Krey, and J. Furdyna, *Magnetic phases of a Heisenberg spin glass in strong magnetic fields: High field faraday rotation in $Cd_{1-x}Mn_xTe$*, J. Magn. Magn. Mater. **25**, 215 (1981).

[143] J. K. Furdyna, *Diluted magnetic semiconductors*, J. Appl. Phys. **64**, R29 (1988).

[144] J. Gaj, *Magnetooptical Properties of Large-Gap Diluted Magnetic Semiconductors*, in *Semiconductors and Semimetals*, edited by J. K. Furdyna and J. Kossut, vol. 25, pp. 275–309, Academic Press Inc (1988).

[145] T. Dietl and H. Ohno, *Dilute ferromagnetic semiconductors: Physics and spintronic structures*, Rev. Mod. Phys. **86**, 187 (2014).

[146] C.-Y. Yeh, Z. W. Lu, S. Froyen, and A. Zunger, *Zinc-blende-wurtzite polytypism in semiconductors*, Phys. Rev. B **46**, 10086 (1992).

[147] M. Averous and M. Balkanski, *Semimagnetic Semiconductors and Diluted Magnetic Semiconductors*, Springer Science & Business Media (2012).

[148] J. K. Furdyna and J. K. Kossut, *Semiconductors and semimetals: Diluted magnetic semiconductors*, vol. 25, Academic Press (1988).

[149] P. G. Riewald and K. H. V. Vlack, *Deformation and fracture of MnTe and MnSe-MnTe solid solutions*, J. Am. Chem. Soc. **53**, 219 (2006).

[150] M. Aven and J. S. Prewer, eds., *Physics and chemistry of II-VI compounds*, North Holland Publishing Company (1967).

[151] R. W. G. Wykoff, *Crystal Structures*, vol. 1, Wiley-Vch, Weinheim (1971).

[152] A. R. Denton and N. W. Ashcroft, *Vegard's law*, Phys. Rev. A **43**, 3161 (1991).

[153] T. Kente and S. D. Mhlanga, *Gallium nitride nanostructures: Synthesis, characterization and applications*, J. Crystal Growth **444**, 55 (2016).

[154] A. Franciosi, S. Chang, R. Reifenberger, U. Debska, and R. Riedel, *Resonant photoemission from $Cd_{1-x}Mn_xSe$: A probe of Mn 3d character and hybridization*, Phys. Rev. B **32**, 6682 (1985).

[155] J. A. Gaj and J. Kossut, eds., *Introduction to the Physics of Diluted Magnetic Semiconductors*, vol. 144, Springer Series in Materials Science (2010).

[156] A. Abragam and B. Bleaney, *Electronic paramagnetic resonance of transition ions*, Clarendon, Oxford (1970).

[157] J. K. Furdyna, M. Dobrowolska, and H. Luo, *Semiconductors, Diluted Magnetic*, in *Scientific Computing by Numerical Methods to Separation Processes*, edited by G. L. Trigg, vol. 17 of *Encyclopedia of Applied Physics*, chap. 13-B, p. 373, Wiley-Vch, Weinheim (1996).

[158] J. S. Griffith, *The theory of transition-metal ions*, 1st edn., Cambridge University Press, Cambridge (1961).

[159] P. Weiss, *L'hypothèse du champ moléculaire et la propriété ferromagnétique*, Journal de Physique Théorique and Appliquée **6**, 661 (1907).

[160] N. W. Ashcroft and N. D. Mermin, *Solid state physics*, Holt, Rinehart and Winston, New York (1976).

[161] J. Kossut and W. Dobrowolski, *Diluted magnetic semiconductors*, vol. 7 of *Handbook of Magnetic Materials*, North-Holland, Amsterdam (1993).

[162] R. R. Galazka, S. Nagata, and P. H. Keesom, *Paramagnetic-spin-glass-antiferromagnetic phase transitions in $Cd_{1-x}Mn_xTe$ from specific heat and magnetic susceptibility measurements*, Phys. Rev. B **22**, 3344 (1980).

[163] A. K. Bhattacharjee, G. Fishman, and B. Coqblin, *Virtual bound state model for the exchange interaction in semimagnetic semiconductors such as $Cd_{1-x}Mn_xTe$*, Physica B **117-118**, 449 (1983).

[164] J. Blinowski and P. Kacman, *Kinetic exchange in diluted magnetic semiconductors*, Phys. Rev. B **46**, 12298 (1992).

[165] C. Rice, L. C. Smith, J. J. Davies, D. Wolverson, M. Wiater, G. Karczewski, and T. Wojtowicz, *Exchange interactions in $Cd_{1-x}Mn_xTe$ wide quantum wells*, Phys. Rev. B **86**, 155318 (2012).

[166] A. Twardowski, M. von Ortenberg, M. Demianiuk, and R. Pauthenet, *Magnetization and exchange constants in $Zn_{1-x}Mn_xSe$*, Sol. Stat. Commun. **51**, 849 (1984).

[167] B. E. Larson, K. C. Hass, H. Ehrenreich, and A. E. Carlsson, *Theory of exchange interactions and chemical trends in diluted magnetic semiconductors*, Phys. Rev. B **37**, 4137 (1988).

[168] F. Seitz and D. Turnbull, eds., *Solid state physics*, vol. 14, Elsevier (1963).

[169] K. Yosida, *Magnetic properties of Cu-Mn alloys*, Phys. Rev. **106**, 893 (1957).

[170] P. Kacman, *Spin interactions in diluted magnetic semiconductors and magnetic semiconductor structures*, Semiconductor Science and Technology **16**, R25 (2001).

[171] G. E. Marques, *Diluted Magnetic Semiconductor heterostructures*, in *Diluted Magnetic Semiconductors*, edited by M. K. Jain, pp. 465–498, World Scientific (1991).

[172] J. Gaj, R. Planel, and G. Fishman, *Relation of magneto-optical properties of free excitons to spin alignment of Mn^{2+} ions in $Cd_{1-x}MnxTe$*, Solid State Commun. **29**, 435 (1979).

[173] B. König, U. Zehnder, D. R. Yakovlev, W. Ossau, T. Gerhard, M. Keim, A. Waag, and G. Landwehr, *Magneto-optical properties of $Zn_{0.95}Mn_{0.05}Se/Zn_{0.76}Be_{0.08}Mg_{0.16}Se$ quantum wells and $Zn_{0.91}Mn_{0.09}Se/Zn_{0.972}Be_{0.028}Se$ spin superlattices*, Phys. Rev. B **60**, 2653 (1999).

[174] D. Scalbert, *Spin-lattice relaxation in diluted magnetic semiconductors*, Phys. Status Solidi B **193**, 189 (1996).

[175] M. G. Tyazhlov, V. D. Kulakovskii, A. I. Filin, D. R. Yakovlev, A. Waag, and G. Landwehr, *Mn spin domains in highly photoexcited (Cd,Mn)Te/(Cd,Mg)Te quantum wells*, Phys. Rev. B **59**, 2050 (1999).

[176] V. D. Kulakovskii, M. G. Tyazhlov, A. I. Filin, D. R. Yakovlev, A. Waag, and G. Landwehr, *Hierarchy of relaxation times in the system of Mn-ion spins in photoexcited semimagnetic quantum wells*, Phys. Rev. B **54**, R8333 (1996).

[177] H. Krenn, W. Zawadzki, and G. Bauer, *Optically Induced Magnetization in a Dilute Magnetic Semiconductor: $Hg_{1-x}Mn_xTe$*, Phys. Rev. Lett. **55**, 1510 (1985).

[178] D. D. Awschalom, J. Warnock, and S. von Molnár, *Low-Temperature Magnetic Spectroscopy of a Dilute Magnetic Semiconductor*, Phys. Rev. Lett. **58**, 812 (1987).

[179] C. V. Raman, *A new radiation**, Indian J. Phys. **2**, 387 (1928).

[180] G. Landsberg and L. Mandelstam, *Eine neue Erscheinung bei der Lichtstreuung in Krystallen*, Naturwiss. **16**, 557 (1928).

[181] M. Cardona, ed., *Light Scattering in Solids*, vol. 8, Springer-Verlag Berlin Heidelberg (1975).

[182] L. Zhang and Q. Niu, *Angular Momentum of Phonons and the Einstein-de Haas Effect*, Phys. Rev. Lett. **112**, 085503 (2014).

[183] D. A. Garanin and E. M. Chudnovsky, *Angular momentum in spin-phonon processes*, Phys. Rev. B **92**, 024421 (2015).

[184] M. A. Kanehisa and M. Balkanski, *Resonant Secondary Emission Spectroscopy*, Phys. Stat. Sol. (b) **102**, 67 (1980).

[185] F. J. Dyson, *Heisenberg Operators in Quantum Electrodynamics - I*, Phys. Rev. **82**, 428 (1951).

[186] S. Rudin, T. L. Reinecke, and B. Segall, *Temperature-dependent exciton linewidths in semiconductors*, Phys. Rev. B **42**, 11218 (1990).

[187] C. Kittel, *Quantum Theory of Solids*, Wiley, New York (1963).

[188] J. T. Devreese, ed., *Polarons in Ionic Crystals and Polar Semiconductors*, North-Holland, Amsterdam (1972).

[189] X. B. Zhang, T. Taliercio, S. Kolliakos, and P. Lefebvre, *Influence of electron-phonon interaction on the optical properties of III nitride semiconductors*, J. Phys. Condens. Matter. **13**, 7053 (2001).

[190] J. Puls, M. Rabe, H.-J. Wünsche, and F. Henneberger, *Magneto-optical study of the exciton fine structure in self-assembled CdSe quantum dots*, Phys. Rev. B **60**, R16303 (1999).

[191] G. E. Pikus and F. G. Pikus, *The mechanism of heavy and light hole mixing in GaAs/AlAs superlattices*, Solid State Commun. **89**, 319 (1994).

[192] J. Jedrzejewski, ed., *Condensed Matter Physics in the Prime of the 21st Century: Phenomena, Materials; Ideas, Methods*, World Scientific Publishing Co Pte Ltd (2008).

[193] L. Schultheis, M. D. Sturge, and J. Hegarty, *Photon echoes from two-dimensional excitons in GaAs-AlGaAs quantum wells*, Appl. Phys. Lett. **47**, 995 (1985).

[194] A. V. Koudinov, Y. G. Kusrayev, B. P. Zakharchenya, D. Wolverson, J. J. Davies, T. Wojtowicz, G. Karczewski, and J. Kossut, *Spin-flip Raman scattering in semimagnetic quantum wells with in-plane anisotropy: Analysis of the intermediate states*, Phys. Rev. B **67**, 115304 (2003).

[195] W. H. Weber and R. Merlin, eds., *Raman Scattering in Materials Science*, Springer-Verlag Berlin Heidelberg (2000).

[196] M. Born and E. Wolf, *Principles of optics*, Pergamon Press Ltd., Oxford (1986).

[197] J. Satterly, *The physical properties of solid and liquid helium*, Rev. Mod. Phys. **8**, 347 (1936).

[198] W. R. C. Coode-Adams, *The Refractive Index of Quartz*, Proc. R. Soc. Lond. A **117**, 209 (1927).

[199] D. T. F. Marple, *Refractive index of ZnSe, ZnTe, and CdTe*, J. Appl. Phys. **35**, 539 (1964).

[200] M. P. Lisitsa, L. F. Gudymenko, V. N. Malinko, and S. F. Terekhova, *Dispersion of the Refractive Indices and Birefringence of CdS_xSe_{1-x} Single Crystals*, Phys. Status Solidi B **31**, 389 (1969).

[201] Jobin Yvon, *Technical Manual - Ramanor U1000 Monochromator, Version 3* (1988).

[202] A. B. Shafer, L. R. Megill, and L. Droppleman, *Optimization of the Czerny-Turner Spectrometer*, J. of the optical society of america **54** (1964).

[203] H. Rhee and T. Joo, *Noncollinear phase matching in fluorescence upconversion*, Opt. Lett. **30**, 96 (2005).

[204] R. Petit, ed., *Electromagnetic Theory of Gratings*, Springer-Verlag Berlin Heidelberg (1980).

[205] Tekhnoscan Laser Systems, Novosibirsk, *T&D-scan laser system - Instruction manual* (2010).

[206] J. Eichler and H. J. Eichler, *Laser - Bauformen, Strahlführung, Anwendungen*, Springer-Verlag Berlin Heidelberg (2006).

[207] Thorlabs, *Liquid Crystal Noise Eaters - User Guide* (2015).

[208] V. M. Axt and T. Kuhn, *Femtosecond spectroscopy in semi-conductors: a key to coherences, correlations and quantum kinetics*, Rep. on Progress in Phy. **67**, 433 (2004).

[209] S. K. Sundaram and E. Mazur, *Inducing and probing nonthermal transitions in semiconductors using femtosecond laser pulses*, Nature Mater. **1**, 217 (2002).

[210] R. D. Averitt and A. J. Taylor, *Ultrafast optical and far-infrared quasiparticle dynamics in correlated electron materials*, J. Phys. Cond. Mater. **14**, R1357 (2002).

[211] Y. T. Wang, C. W. Luo, and T. Kobayashi, *Understanding Multiferroic Hexagonal Manganites by Static and Ultrafast Optical Spectroscopy*, Adv. in Cond. Mat. Phys. **2013**, 1 (2013).

[212] S. W. Brown, T. A. Kennedy, D. Gammon, and E. S. Snow, *Spectrally resolved Overhauser shifts in single $GaAs/Al_xGa_{1-x}As$ As quantum dots*, Phys. Rev. B **54**, 17339(R) (1996).

[213] A. I. Tartakovskii, ed., *Quantum Dots: Optics, Electron Transport and Future Applications*, Cambridge University Press, Cambridge (2012).

[214] D. D. Awschalom, N. Samarth, and D. Loss, *Semiconductor Spintronics and Quantum Computation*, Springer (2002).

[215] T. Brandes, *Coherent and collective quantum optical effects in mesoscopic systems*, Phys. Rep. **408**, 315 (2005).

[216] D. Y. Sharvin and Y. V. Sharvin, *Magnetic-flux quantization in a cylindrical film of a normal metal*, JETP Lett. **34**, 272 (1981).

[217] A. Greilich, D. R. Yakovlev, A. Shabaev, A. L. Efros, I. A. Yugova, R. Oulton, V. Stavarache, D. Reuter, A. Wieck, and M. Bayer, *Mode Locking of Electron Spin Coherences in Singly Charged Quantum Dots*, Science **21**, 341 (2006).

[218] D. Press, T. D. Ladd, B. Zhang, and Y. Yamamoto, *Complete quantum control of a single quantum dot spin using ultrafast optical pulses*, Nature **456**, 218 (2008).

[219] A. Ebbens, D. N. Krizhanovskii, A. I. Tartakovskii, F. Pulizzi, T. Wright, A. V. Savelyev, M. S. Skolnick, and M. Hopkinson, *Optical orientation and control of spin memory in individual InGaAs quantum dots*, Phys. Rev. B **72**, 073307 (2005).

[220] E. Poem, O. Kenneth, Y. Kodriano, Y. Benny, S. Khatsevich, J. E. Avron, and D. Gershoni, *Optically Induced Rotation of an Exciton Spin in a Semiconductor Quantum Dot*, Phys. Rev. Lett. **107**, 087401 (2011).

[221] B. Urbaszek, X. Marie, T. Amand, O. Krebs, P. Voisin, P. Maletinsky, A. Högele, and A. Imamoglu, *Nuclear spin physics in quantum dots: An optical investigation*, Rev. Mod. Phys. **85**, 79 (2013).

[222] I. A. Merkulov, A. L. Efros, and M. Rosen, *Electron spin relaxation by nuclei in semiconductor quantum dots*, Phys. Rev. B **65**, 205309 (2002).

[223] L. Besombes, K. Kheng, L. Marsal, and H. Mariette, *Acoustic phonon broadening mechanism in single quantum dot emission*, Phys. Rev. B **63**, 155307 (2001).

[224] S. Adachi, N. Yatsu, R. Kaji, S. Muto, and H. Sasakura, *Decoherence of exciton complexes in single InAlAs quantum dots measured by Fourier spectroscopy*, Appl. Phys. Lett. **91**, 161910 (2007).

[225] A. Greilich, M. Wiemann, F. G. G. Hernandez, D. R. Yakovlev, I. A. Yugova, M. Bayer, A. Shabaev, A. L. Efros, D. Reuter, and A. D. Wieck, *Robust manipulation of electron spin coherence in an ensemble of singly charged quantum dots*, Phys. Rev. B **75**, 233301 (2007).

[226] F. G. G. Hernandez, A. Greilich, F. Brito, W. Wiemann, D. R. Yakovlev, D. Reuter, A. D. Wieck, and M. Bayer, *Temperature-induced spin-coherence dissipation in quantum dots*, Phys. Rev. B **78**, 041303(R) (2008).

[227] P. C. Maurer, G. Kucsko, C. Latta, L. Jiang, N. Y. Yao, S. D. Bennett, F. Pastawski, D. Hunger, N. Chisholm, M. Markham, D. J. Twitchen, J. I. Cirac, and M. D. Lukin, *Room-temperature quantum bit memory exceeding one second*, Science **336**, 1283 (2012).

[228] M. Widmann, S.-Y. Lee, T. Rendler, N. T. Son, H. Fedder, S. Paik, L.-P. Yang, N. Zhao, S. Yang, I. Booker, A. Denisenko, M. Jamali, S. A. Momenzadeh, I. Gerhardt, T. Ohshima, A. Gali, E. Janzén, and J. Wachtrup, *Coherent control of single spins in silicon carbide at room temperature*, Nature Mater. **14**, 164 (2015).

[229] H. Gotoh, H. Sanada, H. Yamaguchi, and T. Sogawa, *Modifying exciton optical properties in quantum dots with coherent phonons induced by ultrafast optical pulses*, Appl. Phys. Lett. **103**, 112104 (2013).

[230] W. G. van der Wiel, S. D. Franceschi, J. M. Elzerman, T. Fujisawa, S. Tarucha, and L. P. Kouwenhoven, *Electron transport through double quantum dots*, Rev. Mod. Phys. **75**, 1 (2002).

[231] A. C. Johanson, J. R. Petta, J. M. Taylor, A. Yacoby, M. D. Lukin, C. M. Marcus, M. P. Hanson, and A. C. Gossard, *Triplet-singlet spin relaxation via nuclei in a double quantum dot*, Nature **435**, 925 (2005).

[232] O. N. Jouravlev and Y. V. Nazarov, *Electron Transport in a Double Quantum Dot Governed by a Nuclear Magnetic Field*, Phys. Rev. Lett. **96**, 176804 (2006).

[233] F. H. L. Koppens, K. C. Nowack, and L. M. K. Vandersypen, *Spin Echo of a Single Electron Spin in a Quantum Dot*, Phys. Rev. Lett. **100**, 236802 (2008).

[234] K. Ono and S. Tarucha, *Nuclear-Spin-Induced Oscillatory Current in Spin-Blockaded Quantum Dots*, Phys. Rev. Lett. **92**, 256803 (2004).

[235] T. Kobayashi, K. Hitachi, S. Sasaki, and K. Muraki, *Observation of Hysteretic Transport due to Dynamic Nuclear Spin Polarization in a GaAs Lateral Double Quantum Dot*, Phys. Rev. Lett. **107**, 216802 (2011).

[236] E. A. Chekhovich, M. N. Makhonin, A. I. Tartakovskii, A. Yacoby, H. Bluhm, K. C. Nowack, and L. M. K. Vandersypen, *Nuclear Spin Effects in Semiconductor Quantum Dots*, Nature Mater. p. 494 (2013).

[237] D. Gammon, S. W. Brown, E. S. Snow, T. A. Kennedy, D. S. Katzer, and D. Park, *Nuclear Spectroscopy in Single Quantum Dots: Nanoscopic Raman Scattering and Nuclear Magnetic Resonance*, Science **277**, 85 (1997).

[238] R. I. Dzhioev and V. L. Korenev, *Stabilization of the Electron-Nuclear Spin Orientation in Quantum Dots by the Nuclear Quadrupole Interaction*, Phys. Rev. Lett. **99**, 037401 (2007).

[239] W. Yang and R.-B. Liu, *Quantum many-body theory of qubit decoherence in a finite-size spin bath*, Phys. Rev. B **78**, 085315 (2008).

[240] M. S. Rudner and L. S. Levitov, *Self-Polarization and Cooling of Spins in Quantum Dots*, Phys. Rev. Lett. **99**, 036602 (2007).

[241] M. Eto, T. Ashiwa, and M. Murata, *Current-Induced Entanglement of Nuclear Spins in Quantum Dots*, J. Phys. Soc. Japan **73**, 307 (2004).

[242] P. Maletinsky, C. W. Lai, A. Badolato, and A. Imamoglu, *Nonlinear dynamics of quantum dot nuclear spins*, Phys. Rev. **75**, 035409 (2007).

[243] M. N. Makhonin, A. I. Tartakovskii, A. B. Van'kov, I. Drouzas, T. Wright, J. Skiba-Szymanska, A. Russell, V. I. Fal'ko, M. S. Skolnick, H.-Y. Liu, and M. Hopkinson, *Long nuclear spin polarization decay times controlled by optical pumping in individual quantum dots*, Phys. Rev. B **77**, 125307 (2008).

[244] H. Bluhm, S. Foletti, I. Neder, M. Rudner, D. Mahalu, V. Umansky, and A. Yacoby, *Dephasing time of GaAs electron-spin qubits coupled to a nuclear bath exceeding* 200 μs, Nature Phys. **7**, 109 (2011).

[245] D. Gammon, A. L. Efros, T. A. Kennedy, M. Rosen, D. S. Katzer, D. Park, S. W. Brown, V. L. Korenev, and I. A. Merkulov, *Electron and Nuclear Spin Interactions in the Optical Spectra of Single GaAs Quantum Dots*, Phys. Rev. Lett. **86**, 5176 (2001).

[246] H. Haug, *Optical Nonlinearities and Instabilities in Semiconductors*, Elsevier (2012).

[247] M. Y. Petrov, I. V. Ignatiev, S. V. Poltavtsev, A. Greilich, A. Bauschulte, D. R. Yakovlev, and M. Bayer, *Effect of thermal annealing on the hyperfine interaction in InAs/GaAs quantum dots*, Phys. Rev. B **78**, 045315 (2008).

[248] T. Nakaoka, T. Saito, J. Tatebayashi, and Y. Arakawa, *Size, shape, and strain dependence of the g factor in self-assembled In(Ga)As quantum dots*, Phys. Rev. B **70**, 235337 (2004).

[249] A. Schwan, B.-M. Meiners, A. B. Henriques, A. D. B. Maia, A. A. Quivy, S. Spatzek, S. Varwig, D. R. Yakovlev, and M. Bayer, *Dispersion of electron g-factor with optical transition energy in (In,Ga)As/GaAs self-assembled quantum dots*, Appl. Phys. Lett. **98**, 233102 (2011).

[250] A. Greilich, D. R. Yakovlev, and M. Bayer, *Optical Generation and Control of Quantum Coherence in Semiconductor Nanostructures*, chap. 6, pp. 85–127, Springer, Berlin (2010).

[251] I. A. Yugova, A. Greilich, E. A. Zhukov, D. R. Yakovlev, M. Bayer, D. Reuter, and A. D. Wieck, *Exciton fine structure in InGaAs/GaAs quantum dots revisited by pump-probe Faraday rotation*, Phys. Rev. B **75**, 195325 (2007).

[252] D. Richards and B. Jusserand, *Spin energetics in a GaAs quantum well: Asymmetric spin-flip Raman scattering*, Phys. Rev. B **59**, R2506 (1999).

[253] H. Kurtze, D. R. Yakovlev, D. Reuter, A. D. Wieck, and M. Bayer, *Hyperfine interaction mediated exciton spin relaxation in (In,Ga)As quantum dots*, Phys. Rev. B **85**, 195303 (2012).

[254] K. P. O'Donnell and X. Chen, *Temperature dependence of semiconductor band gaps*, Appl. Phys. Lett. **58**, 2924 (1991).

[255] Y. P. Varshni, *Temperature dependence of the energy gap in semiconductors*, Physica **34**, 149 (1967).

[256] E. C. L. Ru, J. Fack, and R. Murray, *Temperature and excitation density dependence of the photoluminescence from annealed InAs/GaAs quantum dots*, Phys. Rev. B **67**, 245318 (2003).

[257] E. B. Flagg, J. W. Robertson, S. Founta, W. Ma, M. Xiao, G. J. Salamo, and C.-K. Shih, *Direct evidence of interlevel exciton transitions mediated by single phonons in a semiconductor quantum dot using resonance fluorescence spectroscopy*, Phys. Rev. Lett. **102**, 097402 (2009).

[258] B. J. Witek, R. W. Heeres, U. Perinetti, E. P. A. M. Bakkers, L. P. Kouwenhoven, and V. Zwiller, *Measurement of the g-factor tensor in a quantum dot and disentanglement of exciton spins*, Phys. Rev. B **84**, 195305 (2011).

[259] P. Borri, W. Langbein, U. Woggon, V. Stavarache, D. Reuter, and A. D. Wieck, *Exciton dephasing via phonon interactions in InAs quantum dots: Dependence on quantum confinement*, Phys. Rev. B **71**, 115328 (2005).

[260] I. Favero, A. Berthelot, G. Cassabois, C. Voisin, C. Delalande, P. Roussignol, R. Ferreira, and J. M. Gérard, *Temperature dependence of the zero-phonon linewidth in quantum dots: An effect of the fluctuating environment*, Phys. Rev. B **75**, 073308 (2007).

[261] C. Hermannstädter, N. A. Jahan, J.-H. Huh, H. Sasakura, K. Akahane, M. Sasaki, and I. Suemune, *Inter-dot coupling and excitation transfer mechanisms of telecommunication band InAs quantum dots at elevated temperatures*, New. J. Phys. **14**, 023037 (2012).

[262] A. Musial, G. Sek, A. Marynski, P. Podemski, J. Misiewicz, A. Löffler, S. Höfling, S. Reitzenstein, J. P. Reithmaier, and A. Forchel, *Temperature dependence of photoluminescence from epitaxial InGaAs/GaAs quantum dots with high lateral aspect ratio*, Acta Physica Polonica A **120**, 883 (2011).

[263] J. Berezovsky, M. H. Mikkelsen, N. G. Stoltz, L. A. Coldren, and D. D. Awschalom, *Picosecond Coherent Optical Manipulation of a Single Electron Spin in a Quantum Dot*, Science **320**, 349 (2008).

[264] Y. Wu, E. D. Kim, X. Xu, J. Cheng, D. G. Steel, A. S. Bracker, D. Gammon, S. E. Economou, and L. J. Sham, *Selective Optical Control of Electron Spin Coherence in Singly Charged GaAs-$Al_{0.3}Ga_{0.7}As$ Quantum Dots*, Phys. Rev. Lett. **99**, 097402 (2007).

[265] A. J. Ramsay, S. J. Boyle, R. S. Kolodka, J. B. B. Oliveira, J. Skiba-Szymanska, H. Y. Liu, M. Hopkinson, A. M. Fox, and M. S. Skolnick, *Fast optical preparation, control, and readout of a single quantum dot spin*, Phys. Rev. Lett. **100**, 197401 (2008).

[266] G. Moody, M. E. Siemens, A. D. Bristow, X. Dai, A. S. Bracker, D. Gammon, and S. T. Cundiff, *Exciton relaxation and coupling dynamics in a GaAs/AlGaAs quantum well and quantum dot ensemble*, Phys. Rev. B **83**, 245316 (2011).

[267] R. V. Cherbunin, K. Flisinski, I. Y. Gerlovin, I. V. Ignatiev, M. S. Kuznetsova, M. Y. Petrov, D. R. Yakovlev, D. Reuter, A. D. Wieck, and M. Bayer, *Resonant nuclear spin pumping in (In,Ga)As quantum dots*, Phys. Rev. B **84**, 041304(R) (2011).

[268] D. Paget, G. Lampel, B. Sapoval, and V. I. Safarov, *Low field electron-nuclear spin coupling in gallium arsenide under optical pumping conditions*, Phys. Rev. B **15**, 5780 (1977).

[269] K. Flisinski, I. Y. Gerlovin, I. V. Ignatiev, M. Y. Petrov, S. Y. Verbin, D. R. Yakovlev, D. Reuter, A. D. Wieck, and M. Bayer, *Optically detected magnetic resonance at the quadrupole-split nuclear states in (In,Ga)As/GaAs quantum dots*, Phys. Rev. B **82**, 081308(R) (2010).

[270] I. Favero, G. Cassabois, R. Ferreira, D. Darson, C. Voisin, J. Tignon, C. Delalande, G. Bastard, P. Roussignol, and J. M. Gérard, *Acoustic phonon sidebands in the emission line of single InAs/GaAs quantum dots*, Phys. Rev. B **68**, 233301 (2003).

[271] S. I. Erlingsson, Y. V. Nazarov, and V. I. Fal'ko, *Nucleus-mediated spin-flip transitions in GaAs quantum dots*, Phys. Rev. B **64**, 195306 (2001).

[272] S. Adachi, R. Kaji, S. Furukawa, Y. Yokoyama, and S. Muto, *Nuclear spin depolarization via slow spin diffusion in single InAlAs quantum dots observed by using erase-pump-probe technique*, Appl. Phys. **111**, 103531 (2012).

[273] A. Greilich, A. Shabaev, D. R. Yakovlev, A. L. Efros, I. A. Yugova, D. Reuter, A. D. Wieck, and M. Bayer, *Nuclei-Induced Frequency Focusing of Electron Spin Coherence*, Science **317**, 1896 (2007).

[274] P.-F.Braun, B. Urbaszek, T.Amand, X. Marie, O. Krebs, B. Eble, A. Lemaitre, and P. Voisin, *Bistability of the nuclear polarization created through optical pumping in $In_{1-x}Ga_xAs$ quantum dots*, Phys. Rev. B **74**, 245306 (2006).

[275] J. Skiba-Szymanska, E. A. Chekhovich, A. E. Nikolaenko, A. I. Tartakovskii, M. N. Makhonin, I. Drouzas, M. S. Skolnick, and A. B. Krysa, *Overhauser effect in individual $InP/Ga_xIn_{1-x}P$ dots*, Phys. Rev. B **77**, 165338 (2008).

[276] E. A. Chekhovich, M. N. Makhonin, K. V. Kavokin, A. B. Krysa, M. S. Skolnick, and A. I. Tartakovskii, *Pumping of Nuclear Spins by Optical Excitation of Spin-Forbidden Transitions in a Quantum Dot*, Phys. Rev. Lett. **104**, 066804 (2010).

[277] T. S. Sosnowski, T. B. Norris, H. Jiang, J. Singh, K. Kamath, and P. Bhattacharya, *Rapid carrier relaxation in $In_{0.4}Ga_{0.6}As/GaAs$ quantum dots characterized by differential transmission spectroscopy*, Phys. Rev. B **57**, 9423(R) (1998).

[278] R. R. Galazka, *Proc. XIV Int. Conf. Phys. Semicond.*, Inst. Phys. Conf. Ser. **43**, 133 (1979).

[279] O. Krebs, E. Benjamin, and A. Lemaître, *Magnetic anisotropy of singly Mn-doped InAs/GaAs quantum dots*, Phys. Rev. B **80**, 165315 (2009).

[280] J. van Bree, P. M. Koenraad, and J. Fernández-Rossier, *Single-exciton spectroscopy of single Mn doped InAs quantum dots*, Phys. Rev. B **78**, 165414 (2008).

[281] Y. Léger, L. Besombes, J. Fernández-Rossier, L. Maingault, and H. Mariette, *Electrical Control of a Single Mn Atom in a Quantum Dot*, Phys. Rev. Lett. **97**, 107401 (2006).

[282] L. Besombes, Y. Leger, J. Bernos, H. Boukari, H. Mariette, J. P. Poizat, T. Clement, J. Fernández-Rossier, and R. Aguado, *Optical probing of spin fluctuations of a single paramagnetic Mn atom in a semiconductor quantum dot*, Phys. Rev. B **78**, 125324 (2008).

[283] C. L. Gall, L. Besombes, H. Boukari, R. Kolodka, J. Cibert, and H. Mariette, *Optical Spin Orientation of a Single Manganese Atom in a Semiconductor Quantum Dot Using Quasiresonant Photoexcitation*, Phys. Rev. Lett. **102**, 127402 (2009).

[284] M. Goryca, T. Kazimierczuk, M. Nawrocki, A. Golnik, J. A. Gaj, and P. Kossacki, *Optical Manipulation of a Single Mn Spin in a CdTe-Based Quantum Dot*, Phys. Rev. Lett. **103**, 087401 (2009).

[285] C. L. Gall, R. S. Kolodka, C. L. Cao, H. Boukari, H. Mariette, J. Fernández-Rossier, and L. Besombes, *Optical initialization, readout, and dynamics of a Mn spin in a quantum dot*, Phys. Rev. B **81**, 245315 (2010).

[286] D. E. Reiter, T. Kuhn, and V. M. Axt, *All-Optical Spin Manipulation of a Single Manganese Atom in a Quantum Dot*, Phys. Rev. Lett. **102**, 177403 (2009).

[287] S. A. Crooker, D. A. Tulchinsky, J. Levy, D. D. Awschalom, R. Garcia, and N. Samarth, *Enhanced Spin Interactions in Digital Magnetic Heterostructures*, Phys. Rev. Lett. **75**, 505 (1995).

[288] J. J. Baumberg, D. D. Awschalom, N. Samarth, H. Luo, and J. K. Furdyna, *Spin Beats and Dynamical Magnetization in Quantum Structures*, Phys. Rev. Lett. **72**, 717 (1994).

[289] J. Stühler, G. Schaack, M. Dahl, A. Waag, G. Landwehr, K. V. Kavokin, and I. A. Merkulov, *Multiple Mn^{2+}-Spin-Flip Raman Scattering at High Fields via Magnetic Polaron States in Semimagnetic Quantum Wells*, Phys. Rev. Lett. **74**, 2567 (1995).

[290] L. C. Smith, J. J. Davies, D. Wolverson, M. Lentze, J. Geurts, T. Wojtowicz, and G. Karczewski, *Dependence of multiple Mn^{2+} spin-flip Raman scattering in quantum wells on the magnetic field direction*, Phys. Rev. B **77**, 115341 (2008).

[291] J. Bao, A. V. Bragas, J. K. Furdyna, and R. Merlin, *Optically induced multispin entanglement in a semiconductor quantum well*, Nature Mater. **2**, 175 (2003).

[292] J. Stühler, M. Hirsch, G. Schaack, and A. Waag, *Raman spectroscopy of the paramagnetic spin flip in $Cd_{1-x}Mn_xTe$, the role of band-gap excitons as intermediate states, and optically detected electron-nuclear double resonance*, Phys. Rev. B **49**, 7345 (1994).

[293] M. Hirsch, R. Meyer, and A. Waag, *Excitons as intermediate states in spin-flip Raman scattering of electrons bound to donors in $Cd_{1-x}Mn_xTe$ epilayers*, Phys. Rev. B **48**, 5217 (1993).

[294] A. Petrou, D. L. Peterson, S. Venugopalan, R. R. Galazka, A. K. Ramdas, and S. Rodriguez, *Raman scattering study of the magnetic excitations in diluted magnetic semiconductors in the presence of an external magnetic field*, Phys. Rev. B **27**, 3471 (1983).

[295] J. Debus, V. Y. Ivanov, S. M. Ryabchenko, D. R. Yakovlev, A. A. Maksimov, Y. G. Semenov, D. Braukmann, J. Rautert, U. Löw, M. Godlewski, A. Waag, and M. Bayer, *Resonantly enhanced spin-lattice relaxation of Mn^{2+} ions in diluted magnetic (Zn,Mn)Se/(Zn,Be)Se quantum wells*, Phys. Rev. B **93**, 195307 (2016).

[296] M. K. Kneip, *Magnetization Dynamics in Diluted Magnetic Semiconductor Heterostructures*, Ph.D. thesis, TU Dortmund (2008).

[297] V. Kolkovsky, *Planar nanostructures made of diluted magnetic semiconductors - epitaxial growth and transport properties*, Ph.D. thesis, Polish Academy of Sciences (2008).

[298] L. M. Matarrese and C. Kikuchi, *Paramagnetic Resonance absorption of Mn^{++} in single crystals of zincblende*, J. Phys. Chem. Solids. **1**, 117 (1956).

[299] G. V. Astakhov, V. P. Kochereshko, D. R. Yakovlev, W. Ossau, J. Nürnberger, W. Faschinger, and G. Landwehr, *Oscillator strength of trion states in ZnSe-based quantum wells*, Phys. Rev. B **62**, 10345 (2000).

[300] M. K. Kneip, D. R. Yakovlev, M. Bayer, A. A. Maksimov, I. I. Tartakovskii, D. Keller, W. Ossau, L. W. Molenkamp, and A. Waag, *Spin-lattice relaxation of Mn ions in ZnMnSe/ZnBeSe quantum wells measured under pulsed photoexcitation*, Phys. Rev. B **73**, 045305 (2006).

[301] E. L. Ivchenko, *Exchange interaction and scattering of light with reversal of the hole angular momentum at an acceptor in quantum-well structures*, Sov. Phys. Solid State **34**, 254 (1992).

[302] J. Lambe and C. Kikuchi, *Paramagnetic Resonance of CdTe: Mn and CdS: Mn*, Phys. Rev. **119**, 1256 (1960).

[303] D. Khokhlov, ed., *Lead Chalcogenides: Physics and Applications*, vol. 18, CRC Press (2002).

[304] T. Story, C. H. W. Swüste, P. J. T. Eggenkamp, H. J. M. Swagten, and W. J. M. de Jonge, *Electron Paramagnetic Resonance Knight Shift in Semimagnetic (Diluted Magnetic) Semiconductors*, Phys. Rev. Lett. **77**, 2802 (1996).

[305] J. Venselaar, A. S. Meigooni, D. Baltas, and P. J. Hoskin, *Comprehensive Brachytherapy: Physical and Clinical Aspects - Imaging in medical diagnosis and therapy*, Taylor & Francis (2012).

[306] B. E. Sturgeon, J. A. Ball, D. W. Randall, and R. D. Britt, *^{55}Mn electron spin echo ENDOR of Mn^{2+} complexes*, J. Phys. Chem. **98**, 12871 (1994).

[307] S. A. Crooker, D. D. Awschalom, J. J. Baumberg, F. Flack, and N. Samarth, *Optical spin resonance and transverse spin relaxation in magnetic semiconductor quantum wells*, Phys. Rev. B **56**, 7574 (1997).

[308] K. V. Kavokin, *Symmetry of anisotropic exchange interactions in semiconductor nanostructures*, Phys. Rev. B **69**, 075302 (2004).

[309] L. Marton, ed., *Advances in Electronis and Electron Physics*, vol. 24, Academic Press Inc (1968).

[310] S. A. Crooker, J. J. Baumberg, F. Flack, N. Samarth, and D. D. Awschalom, *Terahertz Spin Precession and Coherent Transfer of Angular Momenta in Magnetic Quantum Wells*, Phys. Rev. Lett. **77**, 2814 (1996).

[311] D. C. Mattis and J. P. Gallinar, *What is the Mass of an Exciton?*, Phys. Rev. Lett. **53**, 1391 (1984).

[312] J. P. Gallinar and D. C. Mattis, *Effect of exciton hopping upon the mass of an exciton*, Phys. Rev. B **32**, 4914 (1985).

[313] G. Winterling and E. Koteles, *Resonant Brillouin scattering near the a exciton in CdS*, Sol. Stat. Commun. **23**, 95 (1977).

[314] A. Stasch, *Raman scattering from spin-flip and magnon excitations in magnetic semiconductors*, J. Phys. C: Solid State Phys. **16**, 4057 (1983).

[315] B. E. Larson, K. C. Hass, and R. L. Aggarwal, *Effects of internal exchange fields on magnetization steps in diluted magnetic semiconductors*, Phys. Rev. B **33**, 1789 (1986).

[316] Y. Shapira, S. Foner, D. H. Ridgley, K. Dwight, and A. Wold, *Technical saturation and magnetization steps in diluted magnetic semiconductors: Predictions and observations*, Phys. Rev. B **30**, 4021 (1984).

[317] A. Kavokin and G. Malpuech, *Formation of spin domains in semimagnetic quantum wells: Theory*, Phys. Rev. B **68**, 205206 (2003).

[318] A. Abragam and B. Bleaney, *Electron paramagnetic resonance of transition ions*, Oxford University Press, Oxford (2012).

[319] A. Abragam, *The principles of nuclear magnetism, Chapter VII*, Oxford University Press, Oxford (1983).

[320] M. Blume and R. Orbach, *Spin-Lattice Relaxation of S-State Ions: Mn^{2+} in a Cubic Environment*, Phys. Rev. **127**, 1587 (1962).

[321] Y. G. Semenov, *Interaction of a Localized Spin Moment with Phonons Due to the Exchange Scattering of Virtual Carriers in Semiconductors*, Phys. Status Solidi B **2**, 717 (1987).

[322] Y. Shapira, *Magnetization steps in dilute magnetic semiconductors (invited)*, J. Appl. Phys. **67**, 5090 (1990).

[323] V. F. Sapega, M. Moreno, M. Ramsteiner, L. Däweritz, and K. Ploog, *Electronic structure of Mn ions in (Ga,Mn)As diluted magnetic semiconductor*, Phys. Rev. B **66**, 075217 (2002).

[324] V. F. Sapega, M. Ramsteiner, O. Brandt, L. Däweritz, and K. H. Ploog, *Hot-electron photoluminescence study of the (Ga,Mn)As diluted magnetic semiconductor*, Phys. Rev. B **73**, 235208 (2006).

[325] J. M. Kikkawa, I. P. Smorchkova, N. Samarth, and D. D. Awschalom, *Room-Temperature Spin Memory in Two-Dimensional Electron Gases*, Science **277**, 1284 (1997).

[326] R. Zhou, B. Q. Sun, X. Z. Ruan, H. H. Luo, Y. Ji, W. Z. Wang, F. Zhang, and J. H. Zhao, *Temperature dependence of effective g factor in diluted magnetic semiconductor (Ga,Mn)As*, J. Appl. Phys. **103**, 053901 (2008).

[327] R. Rossetti and L. Brus, *Electron-hole recombination emission as a probe of surface-chemistry in aqueous CdS colloids*, J. Phys. Chem. **86**, 4470 (1982).

[328] M. Nirmal, C. B. Murray, and M. G. Bawendi, *Fluorescence-line narrowing in CdSe quantum dots: Surface localization of the photogenerated exciton*, Phys. Rev. B **50**, 2293 (1994).

[329] C. D. M. Donega, *Synthesis and properties of colloidal heteronanocrystals*, Chem. Soc. Rev. **40**, 1512 (2011).

[330] V. I. Klimov, *Spectral and dynamical properties of multiexcitons in semiconductor nanocrystals*, Annu. Rev. Phys. Chem. **58**, 635 (2007).

[331] M. Lorenzon, S. Christodoulou, G. Vaccaro, J. Pedrini, F. Meinardi, I. Moreels, and S. Brovelli, *Reversed oxygen sensing using colloidal quantum wells towards highly emissive photoresponsive varnishes*, Nature Commun. **6**, 6434 (2015).

[332] J. Q. Grim, S. Christodoulou, F. D. Stasio, R. Krahne, R. Cingolani, L. Manna, and I. Moreels, *Continuous-wave biexciton lasing at room temperature using solution-processed quantum wells*, Nature nanotchnology **9**, 891 (2014).

[333] S. Ithurria, M. D. Tessier, B. Mahler, R. P. S. M. Lobo, B. Dubertret, and A. L. Efros, *Colloidal nanoplatelets with two-dimensional electronic structure*, Nature Mater. **10**, 936 (2011).

[334] D. J. Norris, A. L. Efros, M. Rosen, and M. G. Bawendi, *Size dependence of exciton fine structure in CdSe quantum dots*, Phys. Rev. B **53**, 16347 (1996).

[335] A. L. Efros, M. Rosen, M. Kuno, M. Nirmal, D. J. Norris, and M. Bawendi, *Band-edge exciton in quantum dots of semiconductors with a degenerate valence band: Dark and bright exciton states*, Phys. Rev. B **54**, 4843 (1996).

[336] M. Nirmal, D. J. Norris, M. Kuno, M. G. Bawendi, A. L. Efros, and M. Rosen, *Observation of the "Dark Exciton" in CdSe Quantum Dots*, Phys. Rev. Lett. **75**, 3728 (1995).

[337] E. V. Shornikova, L. Biadala, D. R. Yakovlev, D. H. Feng, V. F. Sapega, N. Flipo, A. A. Golovatenko, M. A. Semina, A. V. Rodina, A. A. Mitioglu, M. V. Ballottin, P. C. M. Christianen, Y. G. Kusrayev, M. Nasilowski, B. Dubertret, and M. Bayer, *Electron and Hole g-Factors and Spin Dynamics of Negatively Charged Excitons in CdSe/CdS Colloidal Nanoplatelets with Thick Shells*, Nano Lett. **18(1)**, 373 (2018).

[338] J. F. Scott and T. C. Damen, *Anomalous Double Spin-Flip Raman Scattering in CdS, and a Visible Spin-Flip Laser*, Phys. Rev. Lett. **29**, 107 (1972).

[339] E. N. Economou, J. Ruvalds, and K. L. Ngai, *Theory of Multiple Spin-Flip Raman Scattering in Semiconductors*, Phys. Rev. Lett. **29**, 110 (1972).

[340] L. Biadala, E. V. Shornikova, A. V. Rodina, D. R. Yakovlev, B. Siebers, T. Aubert, M. Nasilowski, Z. Hens, B. Dubertret, A. L. Efros, and M. Bayer, *Magnetic polaron on dangling-bond spins in CdSe colloidal nanocrystals*, Nature nanotchnology (2017).

[341] M. D. Tessier, L. Biadala, C. Bouet, S. Ithurria, B. Abecassis, and B. Dubertret, *Phonon Line Emission Revealed by Self-Assembly of Colloidal Nanoplatelets*, ASC Nano **7**, 3332 (2013).

[342] J. Jortner and C. N. R. Rao, *Nanostructured advanced materials. Perspectives and directions**, Pure Appl. Chem. **74**, 1491 (2002).

[343] C. N. R. Rao, P. J. Thomas, and G. U. Kulkarni, *Nanocrystals: Synthesis, Properties and Applications*, vol. 1, Springer-Verlag Berlin Heidelberg (2007).

[344] D. Talapin, J.-S. Lee, M. V. Kovalenko, and E. V. Shevchenko, *Prospects of Colloidal Nanocrystals for Electronic and Optoelectronic Applications*, Chem. Rev. **110**, 389 (2010).

[345] E. V. Shornikova, L. Biadala, D. R. Yakovlev, V. F. Sapega, Y. G. Kusrayev, A. A. Mitioglu, M. V. Ballottin, P. C. M. Christianen, V. V. Belykh, M. V. Kochiev, N. N. Sibeldin, A. A. Golovatenko, A. V. Rodina, N. A. Gippius, A. Kuntzmann, Y. Jiang, M. Nasilowski, B. Dubertret, and M. Bayer, *Addressing the exciton fine structure in colloidal nanocrystals: the case of CdSe nanoplatelets*, Nanoscale **10**, 646 (2018).

[346] K. S. Novocelov, A. K. Geim, S. V. Morozov, D. Jiang, Y. Zhang, S. V. Dubonos, I. V. Grigorieva, and A. A. Firsov, *Electric Field Effect in Atomically Thin Carbon Films*, Science **306**, 666 (2004).

[347] K. S. Novoselov, D. Jiang, F. Schedin, T. J. Booth, V. V. Khotkevich, S. V. Morozov, and A. K. Geim, *Two-dimensional atomic crystals*, Proc. Natl. Acad. Sci. USA **102**, 10451 (2005).

[348] H. Li, J. Wu, Z. Y. Yin, and H. Zhang, *Preparation and applications of mechanically exfoliated single- and multi-layer MoS_2 and WSe_2 nanosheets*, Acc. Chem. Res. **47**, 1067 (2014).

[349] V. Nicolosi, M. Chhowalla, M. G. Kanatzidis, M. S. Strano, and J. N. Coleman, *Liquid exfoliation of layered materials*, Science **340**, 1226419 (2013).

[350] X. Li, W. Cai, J. An, S. Kim, J. Nah, D. Yang, R. Piner, A. Velamakanni, I. Jung, E. Tutuc, S. K. Banerjee, L. Colombo, and R. S. Ruoff, *Large-Area Synthesis of High-Quality and Uniform Graphene Films on Copper Foils*, Science **324**, 1312 (2009).

[351] D. Yoo, M. Kim, S. Jeong, J. Han, and J. Cheon, *Chemical synthetic strategy for single-layer transition-metal chalcogenides*, J. Am. Chem. Soc. **136**, 14670 (2014).

[352] J. S. Son, J. H. Yu, S. G. Kwon, J. Lee, J. Joo, and T. Hyeon, *Colloidal synthesis of ultrathin two-dimensional semiconductor nanocrystals*, Adv. Mater. **23**, 3214 (2011).

[353] S. Ithurria and B. Dubertret, *Quasi 2D Colloidal CdSe Platelets with Thicknesses Controlled at the Atomic Level*, J. Am. Chem. Soc. **130**, 16504 (2008).

[354] M. Pelton, S. Ithurria, R. D. Schaller, D. S. Dolzhnikov, and D. V. Talapin, *Carrier Cooling in Colloidal Quantum Wells*, Nano Lett. **12**, 6158 (2012).

[355] B. Zhou, G. Xiao, X. Yang, Q. Li, K. Wang, and Y. Wang, *Pressure-dependent optical behaviors of colloidal CdSe nanoplatelets*, Nanoscale **7**, 8835 (2015).

[356] Z. W. Wang, X. D. Wen, R. Hoffmann, J. S. Son, R. Li, C. C. Fang, D. M. Smilgies, and T. Hyeon, *Photoluminescence Up-conversion of CdSe/ZnS Core/shell Quantum Dots under High Pressure*, Proc. Natl. Acad. Sci. USA **107**, 17119 (2010).

[357] R. Benchamekh, N. A. Gippius, J. Even, M. O. Nestoklon, J.-M. Jancu, S. Ithurria, B. Dubertret, A. L. Efros, and P. Voisin, *Tight-binding calculations of image-charge effects in colloidal nanoscale platelets of CdSe*, Phys. Rev. B **89**, 035307 (2014).

[358] A. W. Achtstein, A. Schliwa, A. Prudnikau, M. Hardzei, M. V. Artemyev, C. Thomsen, and U. Woggon, *Electronic Structure and Exciton–Phonon Interaction in Two-Dimensional Colloidal CdSe Nanosheets*, Nano Lett. **12**, 3151 (2012).

[359] A. W. Achtstein, R. Scott, S. Kickhöfel, S. T. Jagsch, S. Christodoulou, G. H. Bertrand, A. V. Prudnikau, A. Antanovich, M. Artemyev, I. Moreels, A. Schliwa, and U. Woggon, *p-State Luminescence in CdSe Nanoplatelets: Role of Lateral Confinement and a Longitudinal Optical Phonon Bottleneck*, Phys. Rev. Lett. **116**, 116802 (2016).

[360] M. Richter, *Nanoplatelets as material system between strong confinement and weak confinement*, Phys. Rev. Mat. **1**, 016001 (2017).

[361] T. C. Berkelbach, M. S. Hybertsen, and D. R. Reichman, *Theory of neutral and charged excitons in monolayer transition metal dichalcogenides*, Phys. Rev. B **88**, 045318 (2013).

[362] R. Zimmermann, E. Runge, and V. Savona, *Quantum Coherence Correlation and Decoherence in Semiconductor Nanostructures*, pp. 89–165, Academic Press Inc. (2003).

[363] A. Naeem, F. Masia, S. Christodoulou, I. Moreels, P. Borri, and W. Langbein, *Giant exciton oscillator strength and radiatively limited dephasing in two-dimensional platelets*, Phys. Rev. B **91**, 121302(R) (2015).

[364] L. Biadala, Y. Louyer, P. Tamarat, and B. Lounis, *Direct observation of the two lowest exciton zero-phonon lines in single CdSe/ZnS nanocrystals*, Phys. Rev. Lett. **103**, 037404 (2009).

[365] O. Labeau, P. Tamarat, and B. Lounis, *Temperature dependence of the luminescence lifetime of single CdSe/ZnS quantum dots*, Phys. Rev. Lett. **90**, 257404 (2003).

[366] A. Rodina and A. L. Efros, *Magnetic Properties of Nonmagnetic Nanostructures: Dangling Bond Magnetic Polaron in CdSe Nanocrystals*, Nano Lett. **15**, 4214 (2015).

[367] L. Biadala, Y. Louyer, P. Tamarat, and B. Lounis, *Band-Edge Exciton Fine Structure of Single CdSe/ZnS Nanocrystals in External Magnetic Fields*, Phys. Rev. Lett. **105**, 157402 (2010).

[368] E. Johnston-Halperin, D. D. Awschalom, S. A. Crooker, A. L. Efros, M. Rosen, X. Peng, and A. P. Alivisatos, *Spin spectroscopy of dark excitons in CdSe quantum dots to 60 T*, Phys. Rev. B **63**, 205309 (2001).

[369] A. Rodina and A. L. Efros, *Radiative recombination from dark excitons in nanocrystals: Activation mechanisms and polarization properties*, Phys. Rev. B **93**, 155427 (2016).

[370] M. Seehra, P. Dutta, S. Neeleshwar, Y. Y. Chen, C. L. Chen, S. W. Chou, C. C. Chen, C. L. Dong, and C. L. Chang, *Size-controlled ex-nihilo ferromagnetism in capped CdSe quantum dots*, Adv. Mater. **8**, 1656 (2008).

[371] J. M. Elward and A. Chakraborty, *Effect of Dot Size on Exciton Binding Energy and Electron–Hole Recombination Probability in CdSe Quantum Dots*, J. Chem. Theory Comput. **9 (10)**, 4351 (2013).

[372] F. Liu, L. Biadala, A. V. Rodina, D. R. Yakovlev, D. Dunker, C. Javaux, J.-P. Hermier, A. L. Efros, B. Dubertret, and M. Bayer, *Spin dynamics of negatively charged excitons in CdSe/CdS colloidal nanocrystals*, Phys. Rev. B **88**, 035302 (2013).

[373] A. M. Barth, S. Lüker, A. Vagov, D. E. Reiter, T. Kuhn, and V. M. Axt, *Fast and selective phonon-assisted state preparation of a quantum dot by adiabatic undressing*, Phys. Rev. B **94**, 045306 (2016).

[374] D. Dragoman and M. Dragoman, *Optical Characterization of Solids*, Springer Science & Business Media (2002).

List of Publications

(1) J. Debus, D. Kudlacik, V. F. Sapega, D. Dunker, P. Bohn, F. Paßmann, D. Braukmann, J. Rautert, D. R. Yakovlev, D. Reuter, A. D. Wieck, and M. Bayer.

Nuclear spin polarization in the electron spin-flip Raman scattering of singly charged (In,Ga)As/GaAs quantum dots.

Phys. Rev. B **92**, 195421 (2015).

(2) J. Debus, D. Kudlacik, P. Waldkirch, V. F. Sapega, S. Scholz, A. Ludwig, A. D. Wieck, and M. Bayer.

Efficiency enhancement of the coherent electron spin-flip Raman scattering through thermal phonons in (In,Ga)As/GaAs quantum dots.

Phys. Rev. B **95**, 201303(R) (2017).

(3) I. A. Akimov, M. Salewski, I. V. Kalitukha, S. V. Poltavtsev, J. Debus, D. Kudlacik, V. F. Sapega, N. E. Kopteva, E. Kirstein, E. A. Zhukov, D. R. Yakovlev, G. Karczewski, M. Wiater, T. Wojtowicz, V. L. Korenev, Yu. G. Kusrayev, and M. Bayer.

Direct measurement of the long-range p-d exchange coupling in a ferromagnet-semiconductor Co/CdMgTe/CdTe quantum well hybrid structure.

Phys. Rev. B **96**, 184412 (2017).

(4) J. Debus, D. Kudlacik, V. F. Sapega, T. S. Shamirzaev, D. R. Yakovlev, D. Reuter, A. D. Wieck, A. Waag, and M. Bayer.

Basic Requirements of Spin-Flip Raman Scattering on Excitonic Resonances and Its Modulation through Additional High-Energy Illumination in Semiconductor Heterostructures.

Phys. Sol. State **60**, 1611 (2018).

(5) J. Jadczak, J. Kutrowska-Girzycka, P. Kapuscinski, J. Debus, D. Kudlacik, D. Schmidt, Y. S. Huang, M. Bayer, and L. Bryja.

Observation of three-particle complexes in WS_2 monolayers.

Condensed Matter - Mesoscale and Nanoscale Physics, arXiv:1612.04122 (2016).

(6) D. Kudlacik, J. Debus, K. V. Kavokin, C. Lüders, K. Barthelmi, J. J. Schindler, H. Moldenhauer, P. Waldkirch, V. F. Sapega, D. R. Yakovlev, D. Reuter, A. Waag, and M. Bayer.

Asymmetric Mn^{2+} spin-flips in (Zn,Mn)Se/(Zn,Be)Se quantum wells due to quadrupole splitting of the Mn^{2+} spin states.

In preparation for submission to Phys. Rev. B.